Dimensionality-Driven Metal-Insulator Transition in Spin-Orbit-Coupled $SrIrO_3$

Dissertation zur Erlangung des
naturwissenschaftlichen Doktorgrades der
Julius-Maximilians-Universität Würzburg

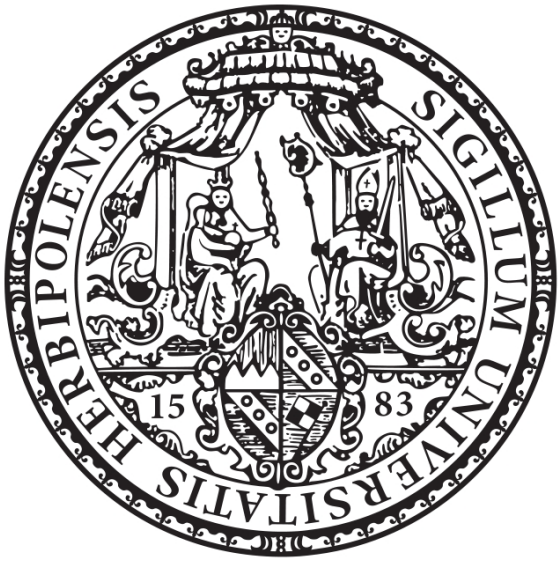

vorgelegt von

Philipp Schütz

aus

Fulda

Würzburg, 2020

Eingereicht am 12.2.2020

bei der Fakultät für Physik und Astronomie

1. Gutachter: Prof. Dr. Ralph Claessen

2. Gutachter: Prof. Dr. Matthias Bode

3. Gutachter: Prof. Dr. Andrea Caviglia

der Dissertation

Vorsitzender: Prof. Dr. Jens Pflaum

1. Prüfer: Prof. Dr. Ralph Claessen

2. Prüfer: Prof. Dr. Matthias Bode

3. Prüfer: Prof. Dr. Giorgio Sangiovanni

4. Prüfer: Prof. Dr. Andrea Caviglia

im Promotionskolloquium

Tag des Promotionskolloquiums: 24.9.2020

Doktorurkunde ausgehändigt am: 7.10.2020

Abstract

In the past decades correlated-electron physics due to strong Coulomb interactions and topological physics caused by band inversion often induced by strong spin-orbit coupling have been the workhorses of solid state research. While commonly considered as disparate phenomena, it was realized in the early 2010s that the interplay between the comparably strong Coulomb and spin-orbit interactions in the $5d$ transition metal oxides may result in hitherto unforeseen properties.

The layered perovskite Sr_2IrO_4 has attracted special attention due to the observation of an unconventional Mott-insulating phase and predictions of exotic superconductivity. Less is known about its three-dimensional counterpart $SrIrO_3$, since rather than the cubic perovskite structure it adopts the thermodynamically stable hexagonal polymorph thereof. This thesis therefore sets out to establish the synthesis of epitaxially stabilized perovskite $SrIrO_3$ by pulsed laser deposition and to investigate its electronic and magnetic structure by state-of-the-art x-ray spectroscopy techniques.

In this endeavor the appropriate thermodynamic conditions for the growth of high-quality $SrIrO_3$ are identified with a focus on the prevention of cation off-stoichiometry and the sustainment of layer-by-layer growth. In the thus-optimized films the cubic perovskite symmetry is broken by a tetragonal distortion due to epitaxial strain and additional cooperative rotations of the IrO_6 octahedra. As a consequence of the thermodynamic instability of the IrO_2 surface layer, the films unexpectedly undergo a conversion to a SrO termination during growth.

In an attempt to disentangle the interplay between spin-orbit and Coulomb interaction the three-dimensional electronic structure of perovskite $SrIrO_3$ is investigated in a combined experimental and theoretical approach using soft x-ray angle-resolved photoelectron spectroscopy and *ab initio* density functional theory calculations. The experimentally found metallic ground state hosts coherent quasiparticle peaks with a well-defined Fermi surface and is theoretically described by a single half-filled band with effective total angular momentum $J_{\text{eff}} = 1/2$ only upon incorporation of a sizeable local Coulomb repulsion and – to a lesser extent – the broken cubic crystal symmetry in the film.

Upon reduction of the $SrIrO_3$ thickness below a threshold of four unit cells the scales are tipped in favor of a Mott-insulating phase as the on-site Coulomb repulsion surmounts the diminishing kinetic energy upon transition into the two-dimensional regime. Concomitantly, a structural transition occurs because the corner-shared octahedral network between substrate and film imposes constraints upon the IrO_6 octahedral rotations in the thin-film limit. The striking similarity between the quasi-two-dimensional spin-orbit-induced Mott insulator Sr_2IrO_4 and SrO-terminated $SrIrO_3$ in the monolayer limit underlines the importance of dimensionality for the metal-insulator transition and possibly opens a new avenue towards the realization of exotic superconductivity in iridate compounds.

Whether the analogy between $SrIrO_3$ in the two-dimensional limit and its Ruddlesden-Popper bulk counterparts extends to their complex magnetic properties ultimately remains an open question, although no indications for a remanent (anti)ferromagnetic order were found. The unprecedented observation of an x-ray magnetic circular dichroism at the O K-absorption edge of iridium oxides in an external magnetic field promises deeper insights into the intricate connection between the $J_{\text{eff}} = 1/2$ pseudospin state, its hybridization with the oxygen ligand states and the magnetic order found in the Ruddlesden-Popper iridates.

Zusammenfassung

In den vergangenen Jahrzehnten waren die Physik korrelierter Elektronen aufgrund starker Coulomb- sowie topologische Physik aufgrund durch Spin-Bahn-Wechselwirkung induzierter Bandinversion die Zugpferde der Festkörperforschung. Während diese zuvor gemeinhin als disjunkt wahrgenommen wurden, setzte sich Anfang der 2010er Jahre die Einsicht durch, dass das Zusammenspiel der ähnlich starken Coulomb- und Spin-Bahn-Wechselwirkung in $5d$ Übergangsmetalloxiden zu unvorhergesehenen Eigenschaften führen kann.

Bedingt durch die Entdeckung einer unkonventionellen Mott-isolierenden Phase sowie Vorhersagen exotischer Supraleitung wurde dem geschichteten Perowskit Sr_2IrO_4 besondere Aufmerksamkeit zuteil. Über dessen dreidimensionales Pendant $SrIrO_3$ ist weniger bekannt, da es anstelle der kubischen Perowskitstruktur eine thermodynamisch stabilere polymorphe Gitterstruktur annimmt. Ziel dieser Thesis ist daher die Synthese von epitaktisch stabilisiertem Perowskit-$SrIrO_3$ mittels gepulster Laserablation sowie die Untersuchung dessen elektronischer und magnetischer Struktur mit modernsten Röntgenspektroskopiemethoden.

In diesem Bestreben werden zunächst die thermodynamischen Bedingungen für das Wachstum von qualitativ hochwertigem $SrIrO_3$ mit dem Fokus auf der kationischen Stöchiometrie sowie dem Erreichen lagenweisen Schichtwachstums identifiziert. In derart optimierten Filmen wird die kubische Symmetrie von einer tetragonalen Verzerrung aufgrund epitaktischer Verspannung sowie von kooperativen Verdrehungen der IrO_6 Oktaeder gebrochen. Während des Wachstums findet infolge der thermodynamischen Instabilität der obersten IrO_2 Lage eine Umwandlung zu einer SrO-Terminierung der Oberfläche statt.

Mit dem Ziel das Zusammenspiel von Spin-Bahn- und Coulomb-Wechselwirkung in $SrIrO_3$ zu entwirren wird dessen dreidimensionale elektronische Struktur in Kombination von winkelaufgelöster Photoelektronenspektroskopie im weichen Röntgenbereich und *ab initio* Dichtefunktionaltheorie untersucht. Der experimentell beobachtete metallische Grundzustand weist kohärente Quasiteilchenzustände mit wohldefinierter Fermifläche auf und wird theoretisch durch ein halbgefülltes Band mit effektivem Gesamtdrehmoment $J_{\text{eff}} = 1/2$ beschrieben, sofern eine substanzielle lokale Coulombabstoßung sowie - in geringerem Maße - die gebrochene kubische Symmetrie berücksichtigt werden.

Bei Schichtdicken unterhalb von vier Einheitszellen neigt sich das Gleichgewicht zugunsten einer Mott-isolierenden Phase, da die lokale Coulombabstoßung die im Zweidimensionalen reduzierte kinetische Energie zunehmend überwiegt. Gleichzeitig findet ein struktureller Übergang statt, da das Netzwerk aus Sauerstoffoktaedern deren Rotationen in dünnen Filmen Randbedingungen auferlegt. Die verblüffende Ähnlichkeit zwischen dem quasi-zweidimensionalen Mott-Isolator Sr_2IrO_4 und SrO-terminiertem Monolagen-$SrIrO_3$ unterstreicht die Bedeutung der Dimensionalität für den Metall-Isolator-Übergang und eröffnet neue Möglichkeiten zur Realisierung exotischer Supraleitung in Iridaten.

Die Frage, ob sich die Analogie zwischen $SrIrO_3$ im zweidimensionalen Limes und den quasi-zweidimensionalen Ruddlesden-Popper-Iridaten auf deren komplexe magnetische Eigenschaften erstreckt, bleibt schlussendlich offen, gleichwohl keine Hinweise auf eine remanente (anti-)ferromagnetische Ordnung hindeuten. Die bisher erste Beobachtung eines magnetischen Zirkulardichroismus an der O K-Absorptionskante eines Iridiumoxids in einem externen Magnetfeld verspricht tiefere Einsichten in den komplexen Zusammenhang zwischen dem $J_{\text{eff}} = 1/2$ Pseudospin-Zustand, dessen Hybridisierung mit den Valenzzuständen der Sauerstoffliganden sowie der magnetischen Ordnung in Iridatverbindungen.

Contents

List of Figures

List of Tables

List of Acronyms

2DES Two-Dimensional Electron System

AFM Atomic Force Microscopy

ARPES Angle-Resolved Photoemission/Photoelectron Spectroscopy

DFT Density Functional Theory

DMFT Density Mean-Field Theory

DOS Density of States

EDC Energy Distribution Curve

FFT Fast Fourier Transform

FIB Focused Ion Beam

FWHM Full Width at Half Maximum

FY Fluorescence Yield

GGA Generalized Gradient Approximation

HAADF High-Angle Annular Dark Field

HRTEM High-Resolution Transmission Electron Microscopy

IMFP Inelastic Mean Free Path

LEED Low-Energy Electron Diffraction

LHB Lower Hubbard Band

LSAT $La_{0.3}Sr_{0.7}Al_{0.65}Ta_{0.35}O_3$

MBE Molecular Beam Epitaxy

MIT Metal-Insulator Transition

PES Photoemission/Photoelectron Spectroscopy

PLD Pulsed Laser Deposition

RHEED Reflection High-Energy Electron Diffraction

RIXS Resonant Inelastic X-ray Scattering

RSM Reciprocal Space Mapping

SAED Selected-Area Electron Diffraction

SEM Scanning Electron Microscopy

SOC Spin-Orbit Coupling

STEM Scanning Transmission Electron Microscopy

SLS Swiss Light Source

SX Soft X-ray

TEM Transmission Electron Microscopy

TEY Total Electron Yield

UHB Upper Hubbard Band

UHV Ultrahigh Vacuum

UPS Ultraviolet Photoemission/Photoelectron Spectroscopy

XAS X-ray Absorption Spectroscopy

XLD X-ray Linear Dichroism

XMCD X-ray Magnetic Circular Dichroism

XPS X-ray Photoemission/Photoelectron Spectroscopy

XRD X-ray Diffraction

Chapter 1

Introduction

Two of the central threads of solid state research in the last decades have been correlated-electron physics resulting from electron-electron interactions [1] and topological physics due to a nontrivial band topology often induced by strong spin-orbit coupling [2]. The former is concerned with physical phenomena which go beyond the mean-field approximation in conventional band theory (i.e., Hartree-Fock or density functional theory), which successfully describes many semiconductors and simple metals composed of light main-group elements, highlighted gray in the periodic table in Fig. 1.1. Short-range electron-electron interactions, often described by the strong local Coulomb repulsion U between electrons occupying the same orbital at the same lattice site, result in a plethora of fascinating phenomena including Mott localization, quantum criticality, high-temperature superconductivity or the formation and long-range ordering of local magnetic momenta [1, 3]. Most prominently, the diverse properties of $3d$ transition metal oxides, highlighted blue in Fig. 1.1, originate from the enhanced electronic correlations in spatially confined d orbitals, as opposed to the rather delocalized s or p shells.

The second thread experienced a tremendous boost of research activity following the theoretical proposal of topological insulators in 2005 [4]. At its core the nontrivial band topology in these materials is due to the inversion of the usual ordering of the conduction and valence bands, which is typically driven by strong spin-orbit coupling, i.e., the relativistic interaction between a particle's spin and its motion inside a potential [5]. While spin-orbit coupling has traditionally been considered as small perturbation in solids, its magnitude is drastically increased in heavy elements due to their strong core potential and may therefore qualitatively change the electronic structure [2]. Until recently, research on topological insulators has been focused on solids with heavy s- and p-electron elements like Bi, Pb, Sb, Hg, and Te, highlighted red in Fig. 1.1, where electronic correlations are negligible.

Upon descending the periodic table from the $3d$ to the $4d$ and $5d$ transition metals, there are essentially two competing trends [6]. On the one hand, the local Coulomb repulsion U and hence the importance of electronic correlations decreases due to the enhanced spatial extent of the d orbitals as seen from their radial distribution $r^2 R_{nl}^2(r)$ in Fig. 1.1. On the other hand, the spin-orbit coupling strength λ increases significantly with the atomic number Z. Since the opposing trends of U and λ lead to a comparable order of magnitude in some of the heavy $5d$ elements, highlighted in yellow in Fig. 1.1, their interplay is expected to open new avenues for exotic physical behavior. In Fig. 1.1 these general trends are summarized in a generic phase diagram in terms of the relative strength of electronic interactions U/t and spin-orbit coupling λ/t with respect to the hopping integral t [6]. Whereas

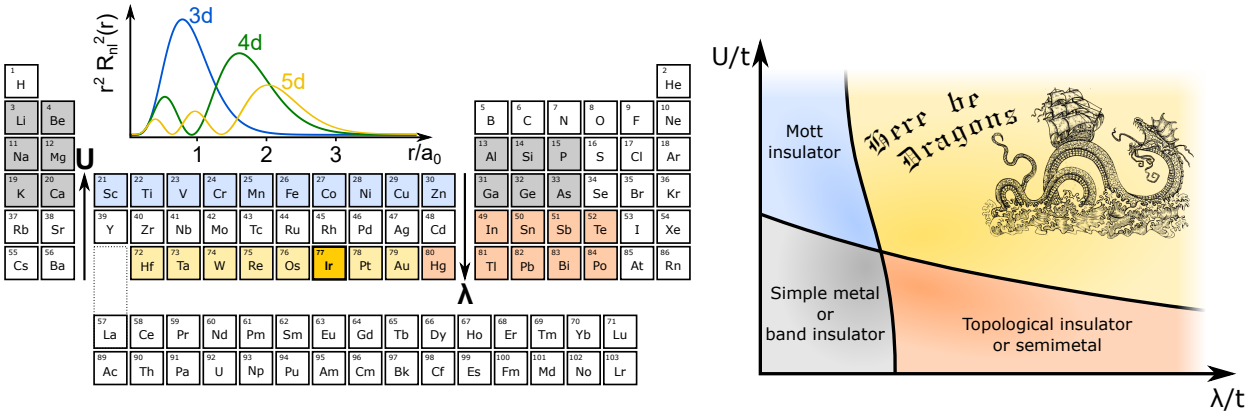

Figure 1.1: Whereas simple metals and semiconductors composed of light main-group elements (gray) are successfully described by band theory, the mean-field approaches break down for $3d$ transition metal oxides (blue) due to enhanced electron correlations. Spin-orbit coupling (λ) becomes important for heavy elements and can induce topological physics found in the heavy main-group elements (red). In the $5d$ transition metal oxides (yellow) λ becomes comparable to the reduced on-site Coulomb repulsion as a result of the extended radial charge distribution $r^2R^2(r)$. In iridium oxides, the interplay between the two comparably strong phenomena is expected to give rise to novel exotic physics. *Phase diagram adapted with permission from Ref. [6]. Copyright © (2014) by Annual Reviews. All rights reserved.*

the strong-coupling limits have been thoroughly investigated for both U and λ (albeit not necessarily comprehensively understood), the yellow part of the phase diagram is essentially *terra incognita* despite predictions of various exotic ground states.

Within the last decade, the heavy $5d$ transition metal oxides, in particular a number of iridium and osmium oxide compounds, have attracted significant attention, as their on-site Coulomb and spin-orbit interactions were found to be of a similar order of magnitude $U \approx \lambda \approx 0.5\,\mathrm{eV}$ [6]. Depending on the lattice symmetry (e.g., hexagonal, pyrochlore, spinel-related and perovskite-related [6]) and other intricacies (e.g., crystal field splittings and exchange interactions), these materials can exhibit a variety of exotic insulating or metallic ground states and are therefore tentatively positioned near the boundary between the four quadrants of the phase diagram.

One of the most prominent examples is the prototypical system Sr_2IrO_4, which has been reported to host a so-called spin-orbit-driven Mott-insulating state, that is promoted by the lifted orbital degeneracy of the t_{2g} manifold due to the entanglement of orbital and spin degrees of freedom in the presence of strong spin-orbit coupling and a large crystal field [7]. Its quasi-two-dimensional layered-perovskite structure with corner-shared IrO_6 octahedra hosts a square lattice of antiferromagnetically aligned $J_{\mathrm{eff}} = 1/2$ pseudospins [8, 9] reminiscent of the isostructural La_2CuO_4, which is the parent material of a family of cuprate high-temperature superconductors [1,10]. Indeed, Sr_2IrO_4 is considered a promising candidate for exotic superconductivity [11, 12] since it reproduces much of the fermiology of hole-doped cuprates, e.g., the formation of Fermi arcs [13] and a d-wave gap [14], upon electron doping.

Sr_2IrO_4 is the quasi-two-dimensional end member (n = 1) of the homologous Ruddlesden-

Popper series $Sr_{n+1}Ir_nO_{3n+1}$, which essentially consists of n perovskite layers, intercalated by SrO layers and laterally shifted against each other such that no Ir-O-Ir bonds persist between neighboring $[SrIrO_3]_n$ blocks [15]. In its sister compounds (n > 1) the hopping integral t of the charge carriers increases as function of dimensionality (via n), i.e., less confinement, and diminishes the prevalence of the on-site Coulomb interaction, eventually resulting in the breakdown of the Mott-insulating state [16]. However, the thermodynamical instability of the Ruddlesden-Popper iridates for n > 2 and, in particular, the metallic three-dimensional end member $SrIrO_3$ (n = ∞) [17] impedes a systematic investigation of the dimensionality and necessitates an alternative synthesis route, e.g., by epitaxial stabilization in form of thin films.

This thesis sets out to establish the heteroepitaxy of phase-pure $SrIrO_3$ thin films by pulsed laser deposition with full control of the film thickness on the atomic scale. In an attempt to mimic the bulk Ruddlesden-Popper iridates the evolution of the electronic and magnetic structure of $SrIrO_3$ is thereupon investigated upon transition from the three- to the two-dimensional thin-film limit. To this end the importance of spin-orbit coupling, electronic correlations and kinetic energy is investigated in a combined experimental and theoretical approach. It is found that the structural, electronic and magnetic degrees of freedom are intricately interwoven and cooperatively determine the system's ground state upon reduction of the dimensionality. In particular, the striking resemblance found for $SrIrO_3$ in the monolayer limit and bulk Sr_2IrO_4, the potential parent material for exotic superconductivity, opens a promising experimental avenue towards electron doping without the introduction of disorder, possibly pushing the system into a novel spin-orbit-driven superconducting phase.

Outline of this thesis

In Chapter 2 the theoretical background of the interplay between spin-orbit coupling and electronic correlations in iridium oxides and the properties of the relevant material systems are summarized. Chapter 3 introduces the thin-film growth technique and the employed characterization methods for the structural, electronic and magnetic properties. Chapter 4 summarizes the perils and pitfalls to be avoided for heteroepitaxy of high-quality, phase-pure $SrIrO_3$ thin films by pulsed laser deposition, thereby laying the groundwork for their following investigation. In Chapter 5 the electronic structure of metallic $SrIrO_3$ is analyzed by comparison between soft x-ray angle-resolved photoemission spectroscopy data and *ab initio* density functional theory calculations. Chapter 6 is concerned with the evolution of the electronic structure as function of dimensionality, as investigated by valence-band and core-level photoemission spectroscopy. Finally, the magnetic properties as function of film thickness are addressed in Chapter 7 by x-ray magnetic dichroism in x-ray absorption spectroscopy measurements. All chapters are organized such that they are self-containing and can be read independently.

Chapter 2

Iridium oxides – theoretical background and real materials

In the last decades $3d$ transition metal oxides have been in the focus of solid state research due to their extraordinary properties, which continue to puzzle physicists to the present day [18]. Amongst others, the plethora of remarkable phenomena comprises unconventional superconductivity with high critical temperature, colossal magnetoresistance, metal-insulator transitions, quantum criticality and complex magnetic orders [1]. Most of these phenomena are regarded as manifestations of strong electronic correlations, which arise from the large short-range Coulomb and exchange interactions among the valence electrons and result in the breakdown of conventional band theory.

Only weakly correlated electronic behavior is expected in the $4d$ and $5d$ transition metal oxides, since the intra-atomic Coulomb repulsion becomes progressively weaker due to the increasing radial extent of the d orbitals upon descending the periodic table. In contrast, the relativistic spin-orbit interaction follows the opposite trend and reaches a comparable order of magnitude in some heavy $5d$ compounds. Following the conjecture that the interplay of crystal field effects, intersite hopping, on-site Coulomb repulsion and spin-orbit coupling promises novel electronic behavior, the interest in $5d$ transition metal oxides – and particularly iridium oxides – saw a sharp rise within the last decade. Theoretically, a manifold of exotic electronic and magnetic phases has been predicted, among them topological states (Axion insulators, Weyl semimetals,...), quantum spin liquids and unconventional superconductivity [6].

In the following chapter an introduction to the rich physics of perovskite-related iridium oxides is given. Starting with a brief review of the effect of strong spin-orbit coupling on $5d$ electrons in the presence of a cubic crystal field, the concept of the spin-orbit-induced Mott-insulating state is established. After the introduction of the idealized perovskite lattice and its structural derivatives, the electronic, magnetic and structural properties of the known members of the Ruddlesden-Popper strontium iridates are outlined and compared to those of artificial superlattices mimicking their layered structure. Finally, the importance of dimensionality on the electronic ground state properties is discussed.

2.1 Interplay of electronic correlations and strong spin-orbit coupling in 5*d* transition metal oxides

Atomic iridium ($Z = 77$) has the electronic configuration $[\mathrm{Xe}]4f^{14}5d^{7}6s^{2}$ with the $5d$ and $6s$ subshells participating in chemical bonding. In iridium oxides the low-energy properties of iridium are therefore governed by the d orbitals, which can be written as linear combinations of the eigenstates $|l, m_l\rangle$ of the orbital angular momentum and its z-component, denoted by the orbital quantum number $l = 2$ and the magnetic quantum numbers $m_l = -2, ..., +2$, respectively, as depicted in Fig. 2.1 (a):

$$d_{xy} = \frac{1}{i\sqrt{2}}\left(|2,2\rangle - |2,-2\rangle\right), \quad d_{yz} = \frac{-1}{i\sqrt{2}}\left(|2,1\rangle + |2,-1\rangle\right), \quad d_{xz} = \frac{-1}{i\sqrt{2}}\left(|2,1\rangle - |2,-1\rangle\right)$$
$$d_{x^2-y^2} = \frac{1}{\sqrt{2}}\left(|2,2\rangle + |2,-2\rangle\right), \quad d_{z^2} = |2,0\rangle \tag{2.1}$$

In contrast to the spherical symmetry in a free atom, the electrostatic potential in iridium oxides is not rotationally invariant, since the iridium ion is surrounded by oxygen anions, which lower the symmetry and thereby break the degeneracy of the d-states. In an idealized cubic perovskite structure, the iridium ion is octahedrally coordinated by six nearest-neighbor oxygen ligands (O_h point group symmetry, cf. Fig. 2.1 (b)), which are described as negative point charges in the crystal field theory. In this picture the d levels are split into a doubly degenerate e_g and a triply degenerate t_{2g} sublevel as a result of the different electrostatic repulsion from the crystal field, since the respective orbital lobes are directed between or at the ligand ions. Beyond the bare electrostatic repulsion, the orbital overlap between transition metal d and oxygen p orbitals also leads to an orbital hybridization and formation of antibonding and bonding molecular orbitals between the symmetry-equivalent p_i and d_i subshells as described by the ligand field theory. As depicted in Fig. 2.1 (c) the orbital symmetries of the e_g and t_{2g} states result in strong σ- and weak π-bonding with the adjacent oxygen ligands, respectively, and therefore in a different energy splitting. The degeneracy of the e_g and t_{2g} manifolds is lifted if the octahedral symmetry is further reduced by an increasing complexity of the crystalline structure, e.g., by the presence of octahedral rotations or tetragonal distortions.

In all Ruddlesden-Popper iridates $\mathrm{Sr_{n+1}Ir_nO_{3n+1}}$ the iridium ion is tetravalent and adopts a $5d^5$ configuration. The filling of the d orbitals by the five valence electrons is determined by the competition between the intra-atomic Hund's coupling and the crystal field splitting [19]. In iridium oxides the latter dominates over the Hund's coupling due to the strong overlap between the $5d$ and $2p$ orbitals, such that the five electrons adopt a low-spin $S = 1/2$ configuration in the t_{2g} subshell [20].

Spin-orbit coupling (SOC) is the interaction between the orbital motion of an electron and its spin, which results from relativistic quantum mechanics [5]:

$$H_{\mathrm{SOC}} = -\frac{\hbar e}{4m^2c^2}\,\boldsymbol{\sigma}\cdot\left[\boldsymbol{\nabla}V(\mathbf{r})\times\mathbf{p}\right] \tag{2.2}$$

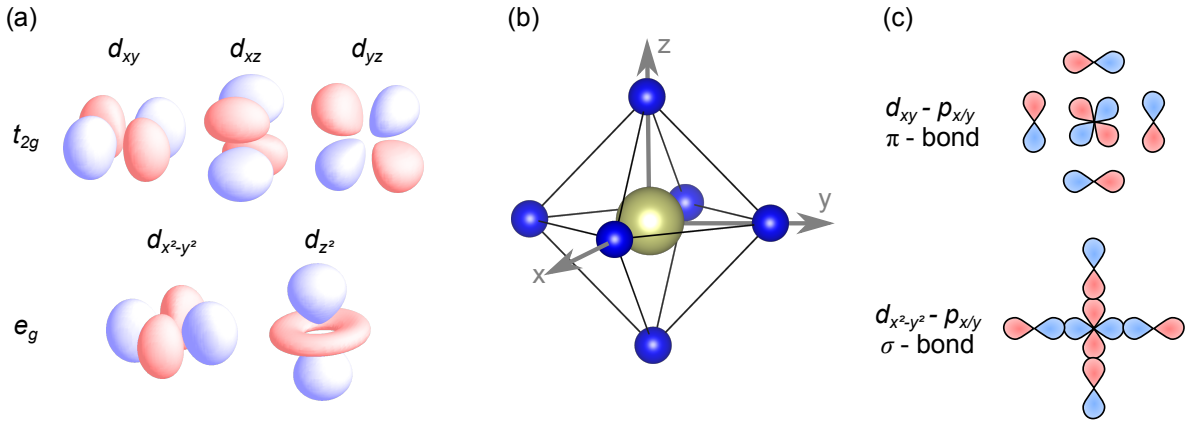

Figure 2.1: (a) Angular part of the atomic d orbitals represented as linear combinations of the eigenstates with orbital angular momentum quantum number $l = 2$ and magnetic quantum number m_l. The subshells are divided into t_{2g} and e_g orbitals according to their group-theoretical irreducible representations (T_2 and E). (b) Octahedral coordination of the transition metal cation (yellow) by six oxygen ligand anions (blue) in an idealized perovskite structure.[a] (c) The orbital symmetries of e_g and t_{2g} states result in stronger and weaker orbital overlap with their adjacent oxygen ligand orbitals and therefore in the formation of σ- and π-bonds, respectively.

[a] All lattice drawings within this thesis have been produced using the free software VESTA [21].

Here, $\boldsymbol{\sigma}$ denotes the Pauli matrix vector, $\mathbf{p}$ the electron momentum, $V(\mathbf{r})$ the electrostatic potential, $\hbar$ Planck's constant, c the speed of light and m_e the electron mass. For a single electron in an atom with the spherical potential $V(r) = \frac{Z\,e}{4\pi\epsilon_0}\frac{1}{r}$ (Z: atomic number, r: radial distance) the coupling between the orbital and spin angular momenta $\mathbf{l} = \mathbf{r} \times \mathbf{p}$ and $\mathbf{s} = \frac{\hbar}{2}\boldsymbol{\sigma}$ becomes

$$H_{\mathrm{SOC}} = \xi\ \mathbf{l}\cdot\mathbf{s}, \quad \text{with} \quad \xi = \frac{1}{8\pi m_e^2 c^2 \epsilon_0}\frac{Ze^2}{r^3}, \tag{2.3}$$

The resulting spin-orbit splitting is given by

$$E_{\mathrm{SOC}} = \langle H_{\mathrm{SOC}} \rangle = \frac{Z^4 e^2 \hbar^2}{16\pi m_e^2 c^2 \epsilon_0}\left(\frac{j(j+1) - l(l+1) - s(s+1)}{l\,(l+1/2)\,(l+1)\,a_0^3\,n^3}\right) \tag{2.4}$$

with a_0 the Bohr radius, n the principal quantum number and j, l, s the quantum numbers of the total, orbital and spin angular momenta. Accordingly, the magnitude of the spin-orbit interaction is proportional to Z^4 and inversely proportional n^3. For a many-electron atom the spin-orbit Hamiltonian is obtained by summing over all electrons

$$H_{\mathrm{SOC}} = \sum_i \xi_i \mathbf{l}_i \cdot \mathbf{s}_i \approx \lambda\,\mathbf{L}\cdot\mathbf{S} \tag{2.5}$$

where $\mathbf{L}$ and $\mathbf{S}$ denote the total orbital and spin angular momenta. In any real many-electron system the dependence on the atomic number Z will deviate from Eq. 2.4 due to screening of the nuclear charge from other electrons. Nonetheless, the SOC monotonically increases

with Z and, while it can be treated as small perturbation in $3d$ transition metal oxides (e.g., in Cu: $Z = 29$ and $\lambda \approx 0.01\,\mathrm{eV}$ [22]), the spin-orbit interaction is found to play a major role in $5d$ transition metal oxides (e.g., in Ir: $Z = 77$ and $\lambda \approx 0.5\,\mathrm{eV}$ [23]).

In the presence of a sizeable cubic crystal field the spin-orbit interaction in the t_{2g} and e_g manifold can be treated separately, because the orbital angular momentum l becomes modified [24]. In the matrix representation of the orbital angular momentum operator, written in the basis of the t_{2g}/e_g and p states,[1]

$$l_x^d = \begin{array}{c} \begin{matrix} d_{yz} & d_{xz} & d_{xy} & d_{z^2} & d_{x^2-y^2} \end{matrix} \\ \left(\begin{array}{ccc|cc} 0 & 0 & 0 & -i\sqrt{3} & -i \\ 0 & 0 & i & 0 & 0 \\ 0 & -i & 0 & 0 & 0 \\ \hline i\sqrt{3} & 0 & 0 & 0 & 0 \\ i & 0 & 0 & 0 & 0 \end{array}\right) \end{array} \quad \Leftrightarrow \quad l_x^p = \begin{array}{c} \begin{matrix} p_x & p_y & p_z \end{matrix} \\ \begin{pmatrix} 0 & 0 & 0 \\ 0 & 0 & -i \\ 0 & i & 0 \end{pmatrix} \end{array} \tag{2.6}$$

the matrix elements in the e_g states are found to be zero. Therefore, the angular momentum l becomes fully quenched in the e_g manifold and no first-order spin-orbit interaction is found in this state. In contrast, the matrix elements in the t_{2g} states are nonzero and can be mapped onto the atomic p states. This relation is called T-P-equivalence

$$\mathbf{l}(t_{2g}) = -\mathbf{l}(p) \tag{2.7}$$

and can be interpreted as a partial quenching of the angular momentum from $l = 2$ to $l_{\mathrm{eff}} = 1$ in the t_{2g} manifold, if the cubic crystal field splitting is sufficiently large to neglect the off-diagonal elements that connect the t_{2g} and e_g states.

Within the LS coupling scheme, the spin-orbit interaction between the effective orbital momentum $l_{\mathrm{eff}} = 1$ of an electron in a t_{2g} state and its spin $s = 1/2$ results in three Kramers doublets with effective total angular momenta $J_{\mathrm{eff}} = 1/2$ ($m_{J_{\mathrm{eff}}} = \pm 1/2$) and $J_{\mathrm{eff}} = 3/2$ ($m_J = \pm 1/2, \pm 3/2$) as shown in Fig. 2.2. In an alternative approach, the formation of the J_{eff} states can be interpreted as result of a crystal field splitting of the $J = 5/2$ states formed in the d manifold within the JJ-coupling scheme.

The resulting electronic states $|J_{\mathrm{eff}}, m_{J_{\mathrm{eff}}}\rangle$ are given by:

$$\begin{aligned}
\left|\frac{1}{2}, \pm\frac{1}{2}\right\rangle &= \frac{1}{\sqrt{3}}\left(|d_{yz}, \mp\tfrac{1}{2}\rangle \pm i\,|d_{xz}, \mp\tfrac{1}{2}\rangle \pm |d_{xy}, \pm\tfrac{1}{2}\rangle\right) \\
\left|\frac{3}{2}, \pm\frac{1}{2}\right\rangle &= \frac{1}{\sqrt{6}}\left(\pm|d_{yz}, \mp\tfrac{1}{2}\rangle + i\,|d_{xz}, \mp\tfrac{1}{2}\rangle - 2\,|d_{xy}, \pm\tfrac{1}{2}\rangle\right) \\
\left|\frac{3}{2}, \pm\frac{3}{2}\right\rangle &= \frac{1}{\sqrt{2}}\left(\pm|d_{yz}, \pm\tfrac{1}{2}\rangle + i\,|d_{xz}, \pm\tfrac{1}{2}\rangle\right)
\end{aligned} \tag{2.8}$$

Of these states the $J_{\mathrm{eff}} = 3/2$ quartet is fully occupied by four electrons. The lowest energy

[1] While only the l_x component is shown as an example, analogous relations hold for the l_y and l_z components of the orbital angular momentum.

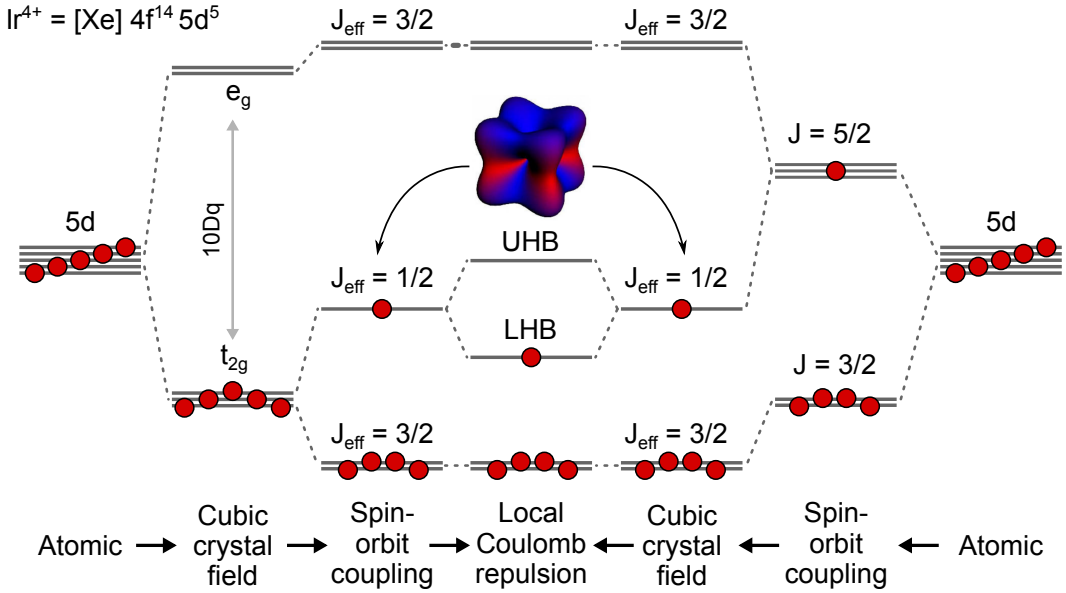

Figure 2.2: Energetic splitting of the atomic d levels in the presence of an octahedral crystal field, strong spin-orbit coupling and strong on-site Coulomb interactions. From the left the crystal field is introduced before the spin-orbit coupling, vice versa from the right. The resulting charge density profile of the $J_{\text{eff}} = 1/2$ state exhibits cubic symmetry and a complex spin texture encoded in the color gradient *Charge density profile adapted with permission from Ref. [8]. Copyright © (2009) by the American Physical Society. All rights reserved.*

level is a half-filled isospin $J_{\text{eff}} = 1/2$ Kramers doublet, which is a coherent superposition of different orbital and spin states with an inherent quantum phase. As shown in Fig. 2.2 the charge density profile of an electron (or hole) in the $J_{\text{eff}} = 1/2$ state exhibits a cubic symmetry and a complex spin texture (represented by the color gradient). This peculiar nature of the $J_{\text{eff}} = 1/2$ state has important consequences for the symmetry of intersite interactions [8] and a potential unconventional superconducting pairing mechanism [11, 12]. However, noncubic distortions will result in a deviation from this idealized scenario and a sizeable noncubic crystal field will restore a situation, where the orbitals are essentially real t_{2g} orbitals [8, 25].

In the band theory of non- or weakly interacting electrons in a periodic lattice of atoms, the distinction between metals and insulators is based on the filling of the electronic bands. In contrast to insulators, where the chemical potential lies within a band gap and all bands are either filled or empty, metals are characterized by a band that is only partially filled up to the chemical potential [26–28]. While the band theory successfully describes a large variety of insulators, simple metals and semiconductors, many transition metal oxides with partially filled d electron bands are poorly conducting or even insulating at variance with band theory [29]. The reason for the localization of the expectedly itinerant electrons is the on-site Coulomb interaction between electrons, which can be neglected in s or p electron systems, but becomes sizeable in materials with spatially confined $3d$ orbitals [30].

N. F. Mott undertook the first attempts to theoretically describe the *Mott-insulating* state as consequence of electron-electron correlations by considering a lattice model with a

single electronic orbital on each site [31–33]. While a single metallic band would form in the absence of electron-electron interactions due to the orbital overlap of neighboring sites, according to Mott the large Coulomb repulsion experienced by two electrons on the same site splits the band into a lower and upper band, thus rendering the system insulating.

Hubbard developed a prototypical theoretical description of correlation effects based on a simplified lattice model considering a single band with two possible spin states per electron [34–36]:

$$H_{\text{Hubbard}} = -t \sum_{\langle i,j\rangle,\sigma} \left(c^{\dagger}_{i,\sigma} c_{j,\sigma} + c^{\dagger}_{j,\sigma} c_{i,\sigma} \right) + U \sum_{i} n_{i,\uparrow} n_{i,\downarrow} \tag{2.9}$$

Here, the first term describes the kinetic energy of the electrons due to nearest-neighbor hopping processes as in a tight-binding Hamiltonian, where t is the transfer integral

$$t = \int d\mathbf{r}\ \varphi^{*}_{i,\sigma}(\mathbf{r})\ \frac{\nabla^2}{2m}\ \varphi_{j,\sigma}(\mathbf{r}), \tag{2.10}$$

$c^{\dagger}_{i,\sigma}$ ($c_{i,\sigma}$) is the creation (annihilation) operator of an electron at site i and in spin state σ and the summation $\langle i,j\rangle$ runs over nearest-neighbor sites only. In a non-interacting system the single-electron band width W is directly proportional to the transfer integral t. The second term describes the competing electron-electron interaction, where U is the local Coulomb repulsion between two electrons on site i

$$U = \int d\mathbf{r}\, d\mathbf{r}'\, \varphi^{*}_{i,\sigma}(\mathbf{r})\, \varphi_{i,\sigma}(\mathbf{r})\, \frac{e^2}{|\mathbf{r}-\mathbf{r}'|}\, \varphi^{*}_{i,-\sigma}(\mathbf{r}')\, \varphi_{i,-\sigma}(\mathbf{r}') \tag{2.11}$$

and $n_{i,\sigma} = c^{\dagger}_{i,\sigma} c_{i,\sigma}$ is the number operator. A pictorial representation of the Hubbard model is given in Fig. 2.3 (a), where electrons on a two-dimensional square lattice are represented as spin up or down. While hopping to an adjacent site releases the energy $-t$, the Coulomb repulsion U has to be overcome if the adjacent site is already occupied by an electron (with opposite spin) and, depending on the ratio U/t of the competing energy scales, the resulting system will be rendered metallic or insulating. If the number of electrons per site deviates from integer filling by δ, some electrons may hop to an adjacent site without the energy loss due to Coulomb repulsion. Therefore, it is intuitive that the metal-insulator transition (MIT) can be either driven by the value U/t in the band width-controlled MIT or by the number of electrons in the band filling-controlled MIT. The latter is widely recognized as one of the most important aspects in the Mott MIT since the discovery of high-temperature superconductivity in the metallic states of p-doped Mott insulators [1].

Although the interplay and competition between kinetic energy and the Coulomb term can be intuitively understood in this oversimplified picture, to date a rigorous theoretical solution of this many-body problem remains elusive despite intensive efforts. As a starting point, it is possible to approach the Mott transition from the purely localized, i.e., atomic limit or from a purely delocalized, i.e., band-theoretical limit. As mentioned above, Hubbard presented an exact solution of his model for the atomic limit, in which the electronic density

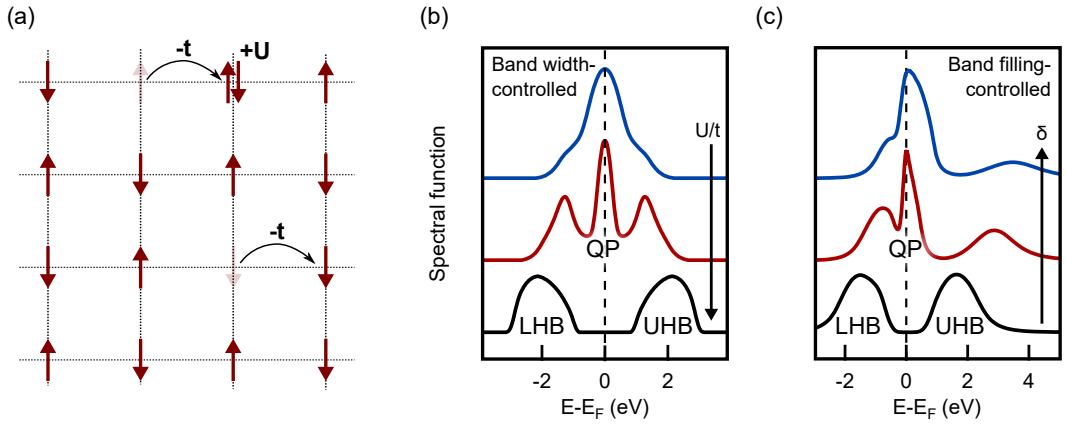

Figure 2.3: (a) Pictorial representation of the Hubbard model on a two-dimensional square lattice. While a nearest-neighbor hopping process releases the kinetic energy $-t$, the electron-electron Coulomb repulsion U has to be overcome if the adjacent site is already occupied. Depending on the ratio U/t and the average band filling the system may therefore become metallic or insulating. (b) and (c) Dynamical mean-field theory calculations of the the spectral function across the band width- and band filling-controlled metal-insulator transition. *Data in (b) adapted with permission from Ref. [18]. Copyright © (1996) by the American Physical Society. All rights reserved. Data in (c) from R. Bulla [37].*

of states splits into two energy levels above and below the chemical potential. Upon inclusion of a finite hopping term t ($U \gg t$) these energy levels gain a finite width and are termed upper and lower Hubbard bands (UHB and LHB).

In contrast, Brinkman and Rice undertook the attempt to describe the metallic phase near the Mott transition, where spin or charge fluctuations may become critically enhanced, by approaching it from the non-interacting limit [38]. Starting from Fermi-liquid theory, in which the ground state and its low-energy excitations are described by an adiabatic switching on of the electron-electron interactions, the Fermi surface volume has to be conserved when the Mott transition is approached according to the Luttinger theorem [39, 40]. In this framework a continuous divergence (or: renormalization) of the effective single-quasiparticle mass lies at the core of the metal-insulator transition and hence mass enhancement is a typical property of metals near the Mott transition. In the Fermi-liquid description the coherent part of the spectral function, i.e., the quasiparticle, therefore becomes narrower until it vanishes. However, the incoherent part, i.e., the LHB and UHB are not described successfully.

A successful unifying description of the coherent and incoherent properties was achieved by the dynamical mean-field theory (DMFT), which is also called the infinite-dimensional approach as it exactly describes the problem in $d = \infty$ dimensions [18]. As the coordination number of an atom diverges with d, spatial fluctuations are ignored within DMFT, whereas the dynamical fluctuations are treated correctly. As shown in Fig. 2.3 (b) and (c) the DMFT-calculated spectral function captures the renormalization of the quasiparticle peak at the chemical potential as well as the formation of the incoherent lower and upper Hubbard bands across the band width- and band filling-controlled Mott transitions.

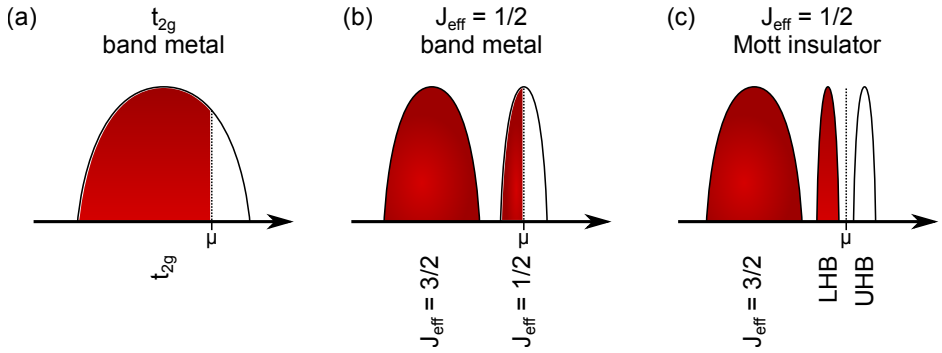

Figure 2.4: Schematic representation of the low-energy electronic structure of a $5d^5$ system upon consideration of different energy scales. (a) If SOC is not considered, the width of the t_{2g} bands (in presence of a cubic crystal field) is much larger than the local Coulomb repulsion U, resulting in a metallic system. (b) With inclusion of SOC the t_{2g} manifold is split into narrow $J_{\text{eff}} = 1/2$ and $J_{\text{eff}} = 3/2$ bands. (c) Even a small U may induce a Mott transition for the upper $J_{\text{eff}} = 1/2$ states.

The Hubbard model in Eq. 2.9 successfully explains the formation of an insulating state as consequence of electronic correlations in systems that are expected to host a metallic ground state in band theory. For a correct quantitative description of realistic materials, however, various complexities need to be included that go beyond this model. One particular simplification in the Hubbard model is the consideration of electrons in a single orbital. Although orbital degeneracy becomes important in d electron systems, the single-band model is often employed as a good starting point for the theoretical description of materials, where strong anisotropic crystal fields lift this degeneracy. For example, the layered perovskite lattice structure of the high-T_C cuprates results in fully occupied t_{2g} and d_{z^2} bands and an isolated, half-filled $d_{x^2-y^2}$ band. Furthermore, the strong hybridization between the e_g and adjacent oxygen p states in many heavy $3d$ transition metal oxides is neglected in the original Hubbard model and was first introduced by Zaanen, Sawatzky and Allen [41]. According to their model, the character of the charge gap is determined by the energy difference between the oxygen p and the transition metal d levels $|\epsilon_d - \epsilon_p|$ relative to the $d-d$ on-site Coulomb repulsion U_{dd}. If $|\epsilon_d - \epsilon_p| > U_{dd}$, the original Hubbard model is retained, the charge gap is determined by U_{dd} and the system is called *Mott-Hubbard* insulator. If in contrast, $|\epsilon_d - \epsilon_p| < U_{dd}$ the character of the lowest-lying charge excitations is determined by a charge transfer from the ligand to the transition metal site and the system is called *charge-transfer* insulator.

As elaborated above, the lowest energy state of a tetravalent iridium ion with strong spin-orbit coupling in a cubic crystal field is a half-filled $J_{\text{eff}} = 1/2$ state and, naively, metallic behavior would be expected in a crystal according to band theory. In general, the importance of electronic correlations in the $4d$ and $5d$ transition metal oxides is smaller than in their $3d$ counterparts because the spatial extent of the radial part of the wave function increases, resulting in a smaller on-site Coulomb repulsion between two electrons as seen from Eq. 2.11. Since the extended radial charge distribution furthermore enhances the orbital hybridization with the adjacent oxygen states, also the band width is enhanced

and a weakly correlated electronic behavior is expected. The inclusion of SOC reduces the effective band width by splitting the t_{2g} manifold into a fully occupied $J_{\text{eff}} = 3/2$ and a half-filled, narrow $J_{\text{eff}} = 1/2$ state as shown in Fig. 2.4 (a) and (b). Therefore, the energy balance of the system is readjusted in favor of electronic correlations, making it susceptible to a Mott-type metal-insulator transition (cf. Fig. 2.4 (c)), which may be triggered by small perturbations of the on-site Coulomb repulsion U and/or the hopping term t.

The experimental observation of an insulating state in bulk Sr_2IrO_4, that has been interpreted as spin-orbit-induced Mott state, has put the perovskite-type iridates in the focus of research interest in the last decade [7]. In this thesis, the structural, electronic and magnetic properties of epitaxially grown thin films of the three-dimensional perovskite material $SrIrO_3$ are investigated. In the following, the structural properties of the perovskite structure and its derivatives in general, as well as the electronic, magnetic and structural properties of the perovskite-related strontium iridates in particular are introduced.

2.2 The perovskite structure and its hetto- and polytypes

The perovskite structure is one of the most commonly found crystal structures of ternary metal oxides with the general formula ABO_3. The ideal cubic perovskite structure (space group $Pm\overline{3}m$) consists of an A cation located at the corners of the cubic unit cell and a B cation at the body-centered position, which is sixfold-coordinated by an octahedron of oxygen ligands positioned at the face centers of the unit cell (cf. Fig. 2.5 (a)). However, the majority of perovskites exhibits distortions from the ideal structure, which have been the subject of intense research efforts in crystallography and can be subsumed in three categories: cation displacements within the BO_6 octahedra, distortions of the octahedra, or tiltings of the octahedra [42]. The former two are typically driven by electronic instabilities, e.g., ferroelectric displacements or Jahn-Teller distortions [42]. The latter (and most common) distortion mechanism results from a too small A cation size to maintain the cubic BO_6 corner-shared network [42], which can be compensated by tilting, because the first coordination sphere of the B cation is virtually unchanged, while the A-O bond distance is drastically altered [43]. As a rule of thumb the susceptibility to octahedral rotations can be predicted by the Goldschmidt tolerance factor [44]

$$t_G = \frac{1}{\sqrt{2}} \cdot \frac{R_A + R_O}{R_B + R_O}, \tag{2.12}$$

which treats the lattice as a close-packed array of hard spheres with the (ionic) radii R_i [45]. The ideal cubic perovskite lattice is realized for a tolerance factor close to unity, whereas distortions to tetragonal, orthorhombic and monoclinic symmetries are expected for lower values of t_G [43]. Although the tolerance factor can be helpful in predicting whether a tilting distortion is expected at all, it makes no statement about the type of the resulting tilt system in the crystal, i.e., the direction and magnitude of the rotations of neighboring octahedra in the crystal.

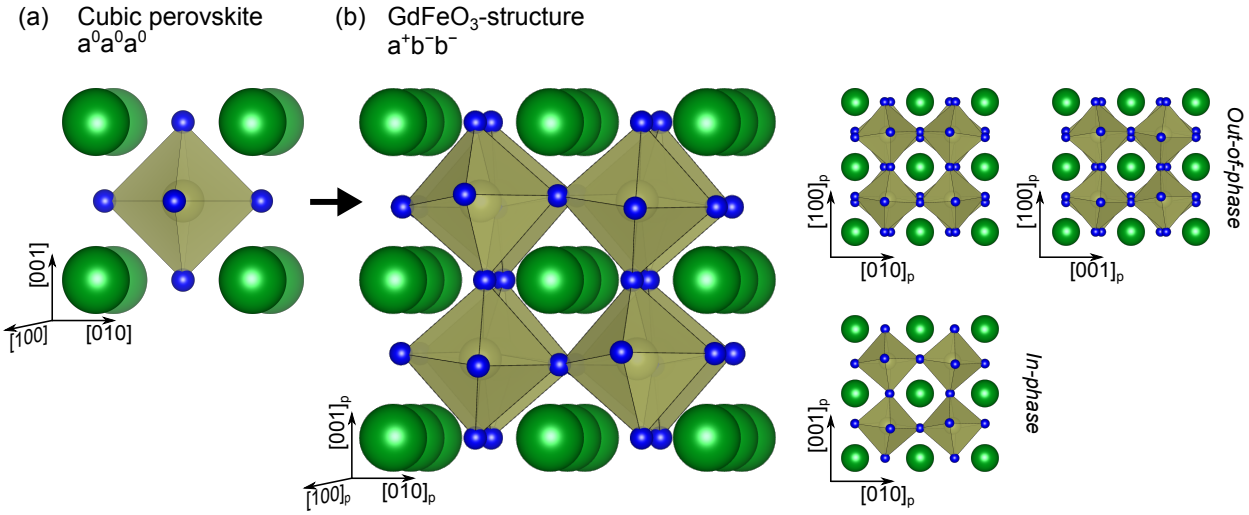

Figure 2.5: (a) Ideal cubic perovskite structure. (b) Distorted $GdFeO_3$ structure with $a^+b^-b^-$ tilting system. Projections along the three pseudo-cubic axes emphasize the in-phase rotations along the $[100]_p$ and out-of-phase rotations along the $[010]_p$ and $[001]_p$ directions.

Starting from the ideal cubic perovskite structure ("aristotype") Glazer developed a general classification to describe all 23 octahedral tilting systems[2] ("hettotypes") in terms of component tilts of rigid octahedra about each of the three pseudo-cubic, i.e., Cartesian axes [47, 48]. Since the octahedra are connected by a corner-linked network, the rotation of one octahedron about one of these axes unequivocally determines the rotations (about the same axis) of all octahedra within the plane perpendicular to this axis. In contrast, successive octahedra *along* this axis can be rotated in either the same or the opposite sense. In any direction the repeat period consists of no more than two octahedra. In Glazer's notation the tilting is denoted by a set of three letters with a superscript, which refer to the tetrad axes in the order $[100]_p$, $[010]_p$, $[001]_p$: $a^\#b^\#c^\#$. The superscript takes the value 0, + or − to indicate no tilt about an axis or tilts of successive octahedra in the same (in-phase) or opposite sense (out-of-phase). Repeating letters denote the equality of the tilting angle and the combination of equal tilts about two (or three) tetrad axes is equivalent to one tilt about one of the diad axes, e.g., $[110]_p$ (or triad axes, e.g., $[111]_p$). In nature, the most abundant tilting distortion is the $GdFeO_3$-type perovskite shown in Fig. 2.5 (b), since its orthorhombic $a^+b^-b^-$ tilt system results in the lowest total energy [43].[3]

If the A cation is too large and the Goldschmidt factor $t_G > 1$, crystal structures of hexagonal symmetry hosting face-sharing octahedra are favored over the cubic perovskite structure and its derivatives. As shown in Fig. 2.6 a number of different hexagonal polytypes (or: polymorphs) of the perovskite structure with a mix of corner- and face-sharing octahedra are known. Upon application of high temperature and/or pressure the polytypes may transform into each other following a sequence (denoted by arrows), since the A-O

[2] A subsequent group theoretical analysis dismissed eight of the originally proposed 23 tilt systems due to symmetry arguments [46].

[3] In this thesis, lattice planes and vectors with a subscript p refer to the *pseudo-cubic* unit cell, while lattice planes and vectors without subscript refer to the actual, enlarged unit cell.

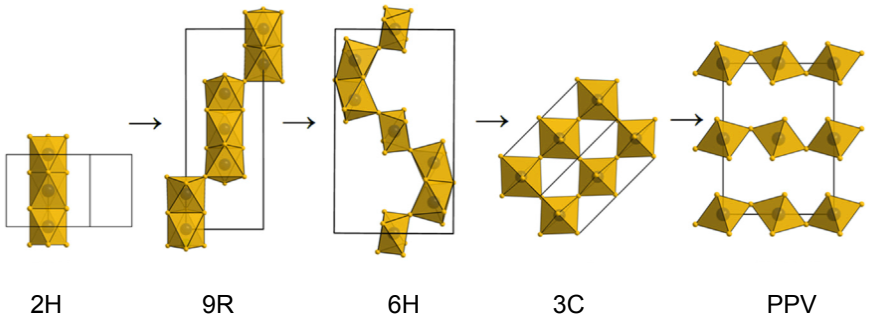

Figure 2.6: Structure of the perovskite polymorphs and the post-perovskite (PPV). In the 2H structure all BO_3 layers are hexagonal close packed. In the 9R structure the packing sequence is *chhchhchh* (c = cubic, h = hexagonal). In the 6H structure the packing sequence is *cchcch*. In the 3C, i.e., perovskite structure, the BO_3 layers are cubic close packed. *Figure adapted with permission from Ref. [49]. Copyright © (2016) by Elsevier. All rights reserved.*

bond is compressible [49–54].

A number of perovskite-related lattice structures are known for ternary oxides with a stoichiometry other than ABO_3 [55, 56], of which the homologous Ruddlesden-Popper series $A_{n+1}B_nO_{3n+1}$ = $([ABO_3]_n, BO)$ is the most prominent [15, 57]. As shown in Fig. 2.7 the idealized Ruddlesden-Popper compounds consist of layers comprised of n ABO_3 perovskite blocks with corner-shared BO_6 octahedra, which are intercalated by an AO layer and laterally shifted against each other by half a face diagonal, such that the two adjacent AO layers form a rock salt-like structure. The n = 1 end member A_2BO_4 is also known as the K_2NiF_4 crystal structure and has been subject of intensive research, mainly because the isostructural La_2CuO_4 is the parent material of the high-temperature cuprate superconductors $La_{2-x}Sr_xCuO_4$ [3, 10]. In the n = ∞ limit the Ruddlesden-Popper phase merges into the three-dimensional perovskite structure. In real materials the Ruddlesden-Popper compounds exhibit distortions from the idealized structure in form of rotations and/or tetragonal distortions of the octahedra.

2.3 Structural, electronic and magnetic properties of the employed materials

2.3.1 The Ruddlesden-Popper family $Sr_{n+1}Ir_nO_{3n+1}$

The Ruddlesden-Popper compounds $Sr_{n+1}Ir_nO_{3n+1}$ form a homologous series that exhibits a striking variety of electronic and magnetic properties, which are strongly coupled to the lattice degrees of freedom as a result of the strong spin-orbit coupling. In the following, the most relevant structural, magnetic and electronic properties of the known members of the Ruddlesden-Popper family are summarized.

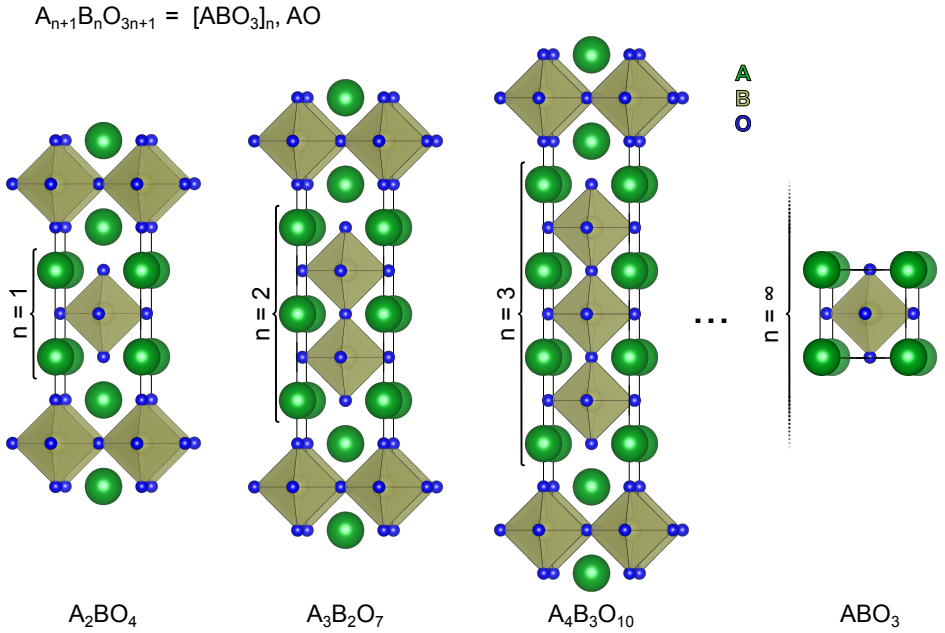

Figure 2.7: Idealized Ruddlesden-Popper structure consisting of layers comprising n ABO_3 perovskite blocks intercalated by an AO layer and laterally shifted against each other by half a face diagonal.

Bulk properties of Sr_2IrO_4 (n = 1)

Sr_2IrO_4 is the quasi-two-dimensional n = 1 end member of the $Sr_{n+1}Ir_nO_{3n+1}$ Ruddlesden-Popper series and adopts a distorted K_2NiF_4 lattice structure. The space group symmetry is reduced from $I4/mmm$ to $I4_1/acd$ by a staggered cooperative octahedral rotation of $\approx 12\,^\circ$ about the c-axis and a tetragonal out-of-plane elongation of the IrO_6 octahedra by 4%. The resulting unit cell is rotated by 45° and – with respect to the idealized structure – enlarged by $\sqrt{2} \times \sqrt{2} \times 2$ ($a = 5.4994\,\text{Å}$, $c = 25.7841\,\text{Å}$) [58–60].

As elaborated in Sec. 2.1, 5d transition metal oxides are naively expected to host a metallic ground state due to their wide bands and relatively small Coulomb interactions. In contrast, Sr_2IrO_4 is a magnetic insulator, which exhibits weak ferromagnetism below $T_N = 240\,\text{K}$ [16,61]. Its ground state can be described by localized $J_{\text{eff}} = 1/2$ moments with an inherent quantum phase as evidenced by intra-atomic interference effects in resonant x-ray scattering experiments [9]. Accordingly, the Mott instability in Sr_2IrO_4 is induced by a narrowing of the 5d band width by the strong relativistic spin-orbit coupling [7]. The weak ferromagnetism exhibits a large anisotropy with the easy axis in the basal plane and originates from an in-plane canted G-type antiferromagnetic order with magnetic moments that are rigidly locked to the IrO_6 octahedra and thereby induce a nonzero net magnetic moment, when aligned by a critical external magnetic field of $H_C \geq 0.2\,\text{T}$ (cf. Fig. 2.8 (a)) [9,62–65]. The strong coupling between magnetic and structural degrees of freedom as consequence of the strong spin-orbit interaction further manifests itself in a pronounced magnetoelastic effect in Sr_2IrO_4 [66,67].

The magnetic exchange interactions in the layered iridates can be described by an effec-

tive low-energy Hamiltonian in the strong SOC limit, which incorporates the effects of a tetragonal distortion of the crystal field and rotations of the IrO_6 octahedra [8]:

$$H_{ij} = J_{ij}\,\mathbf{S_i}\cdot\mathbf{S_j} + \Gamma_{ij}\,S_i^z\,S_j^z + \mathbf{D_{ij}}\cdot[\mathbf{S_i}\times\mathbf{S_j}] \tag{2.13}$$

The $J_{\text{eff}} = 1/2$ pseudospins (denoted by $\mathbf{S_i}$) are coupled via an isotropic Heisenberg exchange J_{ij}, a symmetric anisotropic exchange Γ_{ij} including pseudo-dipolar terms due to Hund's exchange and an asymmetric Dzyaloshinsky-Moriya interaction $\mathbf{D_{ij}}$ [68–70]. Depending on the magnitude of the tetragonal distortion the resulting ground state reproduces the basal-plane canted antiferromagnetic order observed in experiment, with an exact locking of the pseudospins to the octahedral rotations in the cubic limit. As shown in the phase diagram in Fig. 2.8 (c), a spin-flop transition to a collinear Néel ordering along the c-axis is found above a threshold tetragonal distortion.

Sr_2IrO_4 has attracted much attention due to its structural, electronic and magnetic similarities to La_2CuO_4, the Mott-insulating parent material of a class of layered high-temperature superconducting cuprates, which also adopts the K_2NiF_4 structure and hosts a two-dimensional square lattice of antiferromagnetically coupled $S = 1/2$ magnetic moments [71]. In particular, strikingly similar magnon dispersions are found despite the fundamentally different $S = 1/2$ and $J_{\text{eff}} = 1/2$ magnetism in La_2CuO_4 and Sr_2IrO_4 [72–74]. Based on a mapping of the effective Hamiltonian to the $J_{\text{eff}} = 1/2$ space, superconductivity in Sr_2IrO_4 has been predicted theoretically. Due to the opposite sign of the next-nearest-neighbor hopping term in the resulting Hamiltonian the doping phase diagram is expected to be the particle-hole conjugate of the cuprates and hence high-T_C is predicted in electron- rather than hole-doped Sr_2IrO_4 [11]. However, the nature of the paring mechanism in a potential superconducting state in Sr_2IrO_4 remains controversial, with predictions of an odd-parity triplet $p_x + ip_y$ pairing mechanism [75] or $s^*_{\pm}$-wave superconductivity [76] on the hole-doped side, and d-wave superconductivity on the electron-doped side [12, 76].

Experimentally, electron-doped Sr_2IrO_4 is found to reproduce some of the phenomenology exhibited by cuprate superconductors upon transition from the enigmatic pseudogap phase into the superconducting phase [3, 77]. In particular, the observation of Fermi arcs, i.e., disconnected segments of zero-energy states at high temperatures [13] and the opening of a d-wave gap at low temperatures [14] in potassium surface-doped Sr_2IrO_4 is reminiscent of the behavior of cuprates in the vicinity to the superconducting dome [3]. However, to date all attempts to reproduce these findings in chemically doped bulk samples have failed and experimental evidence for superconductivity remains elusive [78–86].

Bulk properties of $Sr_3Ir_2O_7$ (n = 2)

$Sr_3Ir_2O_7$ is the n = 2 member of the strontium iridate Ruddlesden-Popper series and hence the bilayer analogue of Sr_2IrO_4. Its space group symmetry is reduced from $I4/mmm$ to $Bbcb$ by octahedral rotations of $\approx 12°$ about the c-axis [89] and a tetragonal out-of-plane distortion of the IrO_6 octahedra by 2.3% [90]. While the octahedral rotations within each bilayer are out-of-phase, some controversy remains about the correlation of octahedral rotations in adjacent bilayer blocks [90–92].

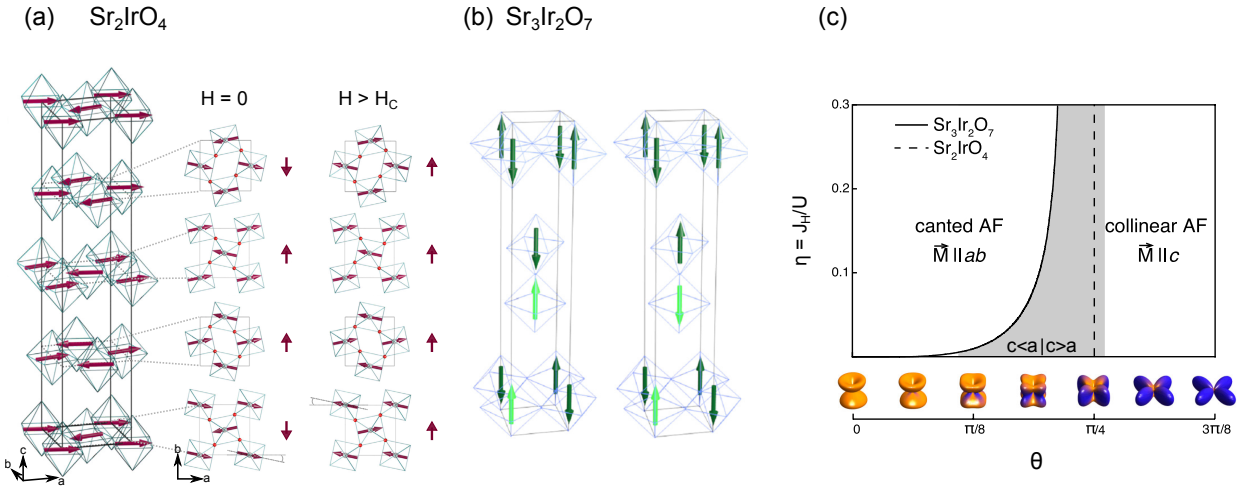

Figure 2.8: (a) Sr_2IrO_4 hosts a basal-plane G-type antiferromagnetic order with canted magnetic moments. The weak ferromagnetic moment results from the rigid locking of the magnetic moments to the rotated IrO_6 octahedra. (b) $Sr_3Ir_2O_7$ hosts a c-axis collinear G-type antiferromagnetic order. (c) Ground state phase diagram of the Hamiltonian in Eq. 2.13 as function of the tetragonal distortion parameter[a] θ and the ratio of Hund's exchange and local Coulomb repulsion $\eta = J_H/U$. The solid (dashed) line marks a spin-flop transition from basal-plane to collinear antiferromagnetic order in $Sr_3Ir_2O_7$ (Sr_2IrO_4). *Figures (a) and (b) adapted with permission from Ref. [65] and Ref. [87], respectively. Copyright © (2013) and (2012) by IOP Publishing. Figure (c) adapted with permission from Ref. [88]. Copyright © (2012) by the American Physical Society. All rights reserved.*

[a]The tetragonal distortion parameter θ is introduced in Ref. [8] as $\tan(2\theta) = 2\sqrt{2}\lambda/(\lambda - 2\Delta)$, where λ is the spin-orbit coupling and Δ the crystal field splitting in the single ion Hamiltonian $H_0 = \lambda \mathbf{l}\cdot\mathbf{s} + \Delta l_z^2$.

$Sr_3Ir_2O_7$ is a narrow-gap insulator in proximity to a metal-insulator transition, that can be described in terms of localized $J_{\text{eff}} = 1/2$ states [16, 90]. Its complex magnetic behavior with three distinct magnetic transitions at 280 K, 230 K and 50 K [90, 91, 93–95] has been attributed to the onset of an incommensurate (280 K) and a commensurate (230 K) collinear G-type antiferromagnetic order (cf. Fig. 2.8 (b)) [87, 91]. At low temperatures the magnetic properties are strongly influenced by oxygen vacancies [96]. In analogy to Sr_2IrO_4, the exchange interactions between the $J_{\text{eff}} = 1/2$ pseudospins can be described by the effective Hamiltonian in Eq. 2.13 [88]. However, the three-dimensional shape of the spin-orbit-entangled wave function (cf. Fig. 2.2) promotes strong interlayer coupling within the bilayer and, as a result, the phase boundary for the spin-flop transition is shifted with respect to the monolayer system Sr_2IrO_4 as shown in Fig. 2.8 (c). Hence, the same microscopic parameters lead to in-plane antiferromagnetism for single-layer Sr_2IrO_4 and collinear antiferromagnetism for bilayer $Sr_3Ir_2O_7$ [88]. In stark contrast to cuprates, where the $S = 1/2$ magnetic moment is carried by a planar e_g orbital, the magnetic states in iridates are therefore strongly affected by changes of the dimensionality due to the peculiar nature of the $J_{\text{eff}} = 1/2$ state.

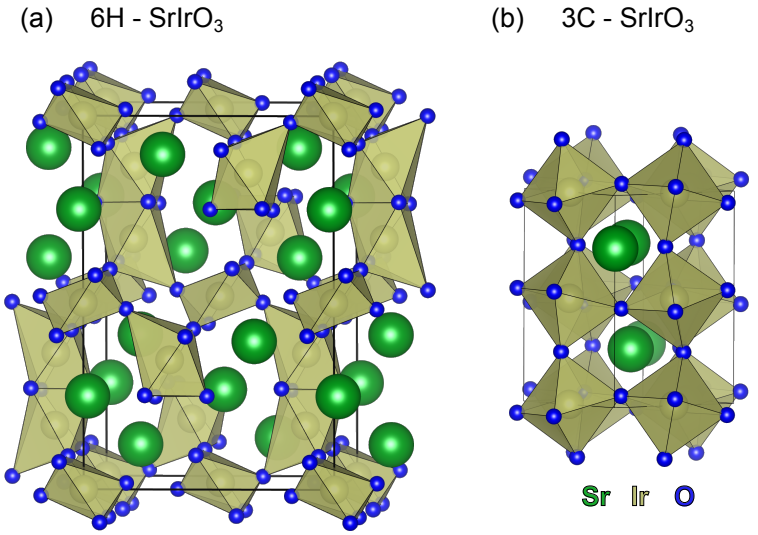

Figure 2.9: Lattice model of the (a) atmospheric pressure (6H) [17] and (b) high-pressure (3C) [99, 100] polytypes of $SrIrO_3$. The high-pressure form adopts a $GdFeO_3$-like perovskite structure with an orthorhombic unit cell, which is enlarged by $\sqrt{2} \times \sqrt{2} \times 2$ with respect to the pseudo-cubic unit cell.

Bulk properties of $SrIrO_3$ ($n = \infty$)

$SrIrO_3$ is the three-dimensional $n = \infty$ end member of the $Sr_{n+1}Ir_nO_{3n+1}$ Ruddlesden-Popper series. Although the Goldschmidt tolerance factor $t_G = 0.992$ predicts a stable (pseudo-)cubic ambient lattice structure, the atmospheric pressure form of $SrIrO_3$ adopts a monoclinic distortion of the hexagonal 6H-$BaTiO_3$ structure [17, 97] (Fig. 2.9 (a)). Accordingly, the crystal structure of $SrIrO_3$ is insufficiently described by the simple ionic average size model underlying the Goldschmidt model, most likely owing to the high covalency of the Ir-O bonds [49]. 6H-$SrIrO_3$ is metallic and believed to be near a quantum critical point since it exhibits non-Fermi-liquid behavior at low temperatures [98].

An orthorhombic $GdFeO_3$-type perovskite polymorph, 3C-$SrIrO_3$ (cf. Fig. 2.9 (b)), can be stabilized by application of high pressure ($p > 8.8\,\mathrm{GPa}$) and high temperature ($T > 1000\,^\circ\mathrm{C}$) [17,99]. Polycrystalline, i.e., strain-free, metastable 3C-$SrIrO_3$ has been shown to be metallic and exhibits an almost temperature-independent magnetic susceptibility, characteristic for Pauli paramagnetism of the conduction electrons (with an upturn at low temperatures due to paramagnetic impurities) [99, 101]. While the synthesis of macroscopic single crystals is not technically feasible due to the required high pressure, the 3C crystal structure can be stabilized by epitaxial strain during thin-film synthesis.

In general, $SrIrO_3$ is believed to be in the vicinity of a metal-insulator transition as its electronic transport properties are susceptible to external perturbations. In particular, $SrIrO_3$ thin films are found to exhibit non-Fermi liquid behavior $\rho \propto T^\epsilon$ with different values of $\epsilon \neq 2$ depending on the applied compressive strain by choice of the substrate material [102, 103]. However, the transport properties of $SrIrO_3$ are highly sensitive to disorder (off-stoichiometry, crystal defects,...) and dominated by weak localization and variable-range hopping in the thin-film limit [102,104,105]. The presence of a Drude-like metallic response, i.e., the absence of an optical gap in optical absorption spectra despite the observation of insulating transport behavior further evidences the importance of disorder and places these metal-insulator transitions in the class of Anderson localization [102, 106–108]. It has been argued, that the interplay between electronic correlations and disorder in $SrIrO_3$ may

give rise to an intermediate state between the Landau-Fermi-liquid state and the Anderson-insulating state [109, 110].

From the theoretical point of view $SrIrO_3$ has attracted attention as potential candidate for a ternary transition metal oxide with topologically nontrivial band structure. A line of symmetry-protected Dirac nodes in the $J_{\text{eff}} = 1/2$ band near the Fermi level has been predicted [111] and the engineering of topological phases at interfaces or in superlattices may change the system into a topological crystalline metal with nontrivial surface zero modes protected by the chiral and mirror-reflection symmetry of the orthorhombic crystal structure [111–113].

2.3.2 $SrTiO_3$

At room temperature $SrTiO_3$ adopts the ideal cubic perovskite structure ($a^0a^0a^0$, space group $Pm\overline{3}m$) with the lattice parameter $a = 3.905\,\text{Å}$. The cubic point group symmetry is broken by an antiferrodistortive transition at $T = 105\,\text{K}$, which is associated with the condensation of a soft-phonon mode and results in a $a^0a^0c^-$ tilting system [47, 114, 115]. $SrTiO_3$ is a band insulator with a wide band gap of $E_{\text{gap}} \approx 3.2\,\text{eV}$ separating the occupied O $2p$ valence band and the unoccupied Ti $3d$ states [116, 117]. Electrons can be easily doped into the Ti $3d$ states by creation of oxygen vacancies ($SrTiO_{3-\delta}$) [118–121] or through chemical substitution with niobium ($SrTi_{1-x}Nb_xO_3$) [122].

While $SrTiO_3$ by itself exhibits a variety of intriguing physical phenomena, such as quantum paraelectricity [123], superconductivity [124] and/or ferromagnetism [125], it is also a widely used substrate material for epitaxial growth of transition metal oxides, because atomically flat (001) surfaces can be easily prepared. Along the ⟨100⟩ crystallographic directions $SrTiO_3$ can be considered as alternating sequence of electrically neutral SrO and TiO_2 layers. After hydroxylation in water, the topmost SrO layer of mixed-terminated $SrTiO_3$ can be selectively etched in a buffered HF solution. As a result a well-defined, uniform TiO_2-terminated surface is obtained after a final heating step under oxygen atmosphere [126, 127].

2.3.3 Artificial ($[SrIrO_3]_m$,$[SrTiO_3]_k$) superlattices

A truly systematic investigation of the effect of dimensionality in the bulk Ruddlesden-Popper iridates $Sr_{n+1}Ir_nO_{3n+1}$ is impeded by their instability for $n > 2$. As an alternative approach, their layered structure can be mimicked by substitution of the intercalated SrO layers with $SrTiO_3$ monolayers in artificial ($[SrIrO_3]_m$,$SrTiO_3$) superlattice structures ($k = 1$). Indeed, such superlattices also exhibit a metal-insulator transition and a concurrent magnetic transition as a function of m, i.e., dimensionality [128].

In contrast to the Ruddlesden-Popper iridates, no spin-flop transition as function of dimensionality is observed, as all superlattices with $m < 4$ exhibit a weak in-plane ferromagnetic moment attributed to a canted antiferromagnetic order reminiscent of – yet subtly different to – bulk Sr_2IrO_4. As shown in Fig. 2.10, along the c-axis the superlattices exhibit a ferromagnetic ordering of the weak in-plane magnetic moments produced by canting [128], at variance with Sr_2IrO_4, where they cancel each other antiferromagnetically (below a crit-

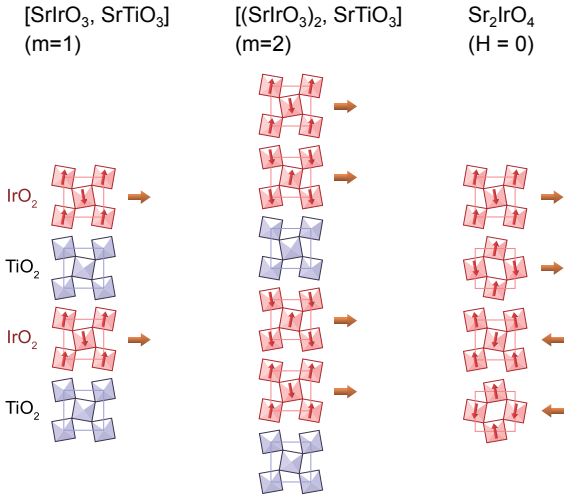

Figure 2.10: Layer-resolved in-plane magnetic structure of $([SrIrO_3]_m,SrTiO_3)$ superlattices with m = 1 and m = 2 and bulk Sr_2IrO_4. The superlattices host an ferromagnetic out-of-plane order of the canted net moments in contrast to the antiferromagnetic order in Sr_2IrO_4. *Figure adapted with permission from Ref. [128]. Copyright © (2015) by the American Physical Society. All rights reserved.*

ical field H_C, cf. Fig. 2.8 (a)). Accordingly, the magnetic exchange coupling between adjacent $SrIrO_3$ layers is mediated by the $SrTiO_3$ layers via Ir-O-Ti bonds and is not negligible [129]. By insertion of more than one blocking layer of $SrTiO_3$ in $(SrIrO_3,[SrTiO_3]_k)$ superlattices (m = 1) [130], the interlayer coupling via vertical electron hopping can be suppressed, thereby significantly modifying the magnetic ordering temperature and resistivity. Therefore, neither the Ruddlesden-Popper iridates nor their superlattice analogues should be regarded as truly two-dimensional due to the residual coupling between adjacent iridium layers.

2.4 Role of dimensionality in the layered strontium iridates

The electronic and magnetic properties of the layered strontium iridates $Sr_{n+1}Ir_nO_{3n+1}$ exhibit a stunning variety as function of n. While the quasi-two-dimensional end member Sr_2IrO_4 (n = 1) exhibits a wide-gap Mott-insulating state, the bilayer system $Sr_3Ir_2O_7$ (n = 2) is a narrow-gap insulator and the three-dimensional end member (3C-)$SrIrO_3$ (n = ∞) is metallic (cf. Fig. 2.11). Accordingly, the variations in the lattice degrees of

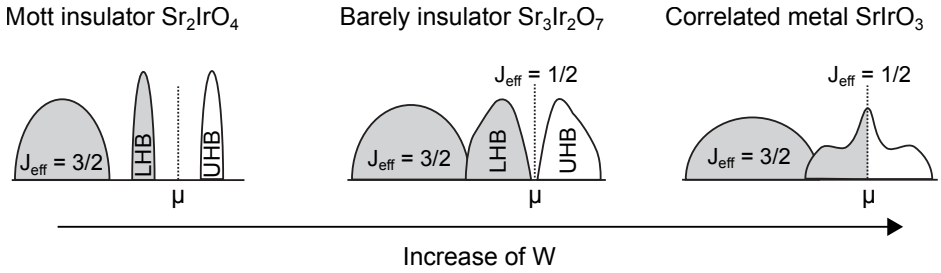

Figure 2.11: Schematic band diagrams of the strontium iridate Ruddlesden-Popper series $Sr_{n+1}Ir_nO_{3n+1}$. With reduced dimensionality the kinetic energy (i.e., band width W) changes because hopping along z becomes increasingly suppressed. *Figure adapted with permission from Ref. [16]. Copyright © (2008) by the American Physical Society. All rights reserved.*

freedom within the homologous series $Sr_{n+1}Ir_nO_{3n+1}$ trigger a Mott metal-insulator transition by tipping the balance between the hopping term t and the local Coulomb repulsion U [16]. Similarly, artificial ($[SrIrO_3]_m$,$SrTiO_3$) superlattices exhibit a metal-insulator transition as function of the $SrIrO_3$ thickness m.

The most obvious structural change within the layered-perovskite family is the number of nearest-neighbor iridium atoms per iridium site, which changes from 4 (n = 1) to 5 (n = 2) to 6 (n = ∞). In a first approximation the band width W is proportional to the number of nearest-neighbor hopping channels and hence the average coordination of an iridium ion [16]. Although sizeable coupling across the intercalated SrO or $SrTiO_3$ blocks has been shown to have an effect on the electronic properties, the narrowing of the band width W as function of decreasing dimensionality therefore plays a dominant role in the observed Mott transitions [131, 132]. Additionally, the magnitude of the on-site Coulomb repulsion U undergoes a significant change as function of dimensionality, due to an enhancement of screening at higher iridium coordination [132]. Accordingly, both U and W play an active role in the dimensionality-induced Mott transition in the layered iridate compounds.

Since the nearest-neighbor hopping between iridium sites is mediated by the interjacent oxygen ligand, the hopping amplitude furthermore depends upon the bonding geometry, i.e., the Ir-O-Ir distances and bonding angles. Therefore, the manipulation of the lattice spacing and/or octahedral rotations via external perturbations such as epitaxial strain or pressure offers a playground to tune the electronic and magnetic properties in these materials [133,134]. In this thesis, $SrIrO_3$ thin-film synthesis by pulsed laser deposition was established to investigate the cooperative effect of structural degrees of freedom (strain, octahedral rotations), dimensionality and magnetic ordering.

Chapter 3

Thin-film growth and characterization techniques

The intriguing physical properties of solid materials are governed by the microscopic arrangement of atoms and their interactions. Most prominently, crystalline solids have served as playground for researchers because the periodic arrangement of their constituents results in a plethora of fascinating phenomena including metallicity, magnetic order or superconductivity. While the growth and investigation of macroscopic crystals has significantly advanced the understanding of the emergent effects in solids, the fabrication of crystalline epitaxial thin films offers several advantages. From the perspective of fundamental research, these comprise the possibility to tune the physical properties via application of epitaxial strain by choice of the substrate material and the possibility to impose an otherwise metastable crystal structure onto a material through epitaxial stabilization. Furthermore, the symmetry breaking at the interface between substrate and film may bring forward completely new physical phenomena which do not exist in a bulk crystal. From the perspective of applied research, thin films are a prerequisite for switchable device applications since they offer the opportunity to manipulate the physical properties by an electric field via a gate dielectric.

In this thesis, pulsed laser deposition (PLD) is used to epitaxially grow the material $SrIrO_3$ on $SrTiO_3$ single crystal substrates. Since the crystalline quality of the film is crucially dependent on the growth conditions, one key challenge is to find the optimum growth parameters. For this purpose, several techniques are used to characterize the structural properties of the thin films, among them high- and low-energy electron diffraction, atomic force microscopy, x-ray diffraction and transmission electron microscopy. Following the successful synthesis of phase-pure thin films with high crystalline long-range order, photoelectron spectroscopy and x-ray absorption spectroscopy serve as tools to investigate the interplay between electronic correlations, structural degrees of freedom and dimensionality.

In this chapter the basic principles and theoretical background of the thin-film growth and the employed characterization methods are introduced.

3.1 Pulsed Laser Deposition

Pulsed laser deposition (PLD) became popular with the advent of cuprate high-T_C superconductors due to its convenience for the film growth of multicomponent materials and has been developed into a versatile and wide-spread technique within the last decades. The basic principle of PLD is illustrated in Fig. 3.1. A high-intensity nanosecond KrF excimer

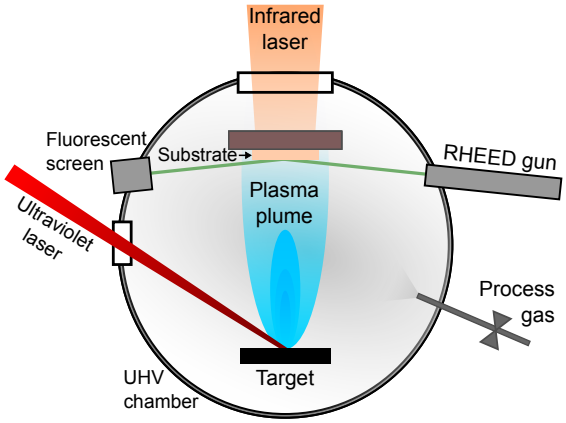

Figure 3.1: Schematic sketch of the pulsed laser deposition setup. An ultraviolet laser is used to ablate the target material, resulting in plasma plume propagation towards and film deposition on the heated substrate. Reflection high-energy electron diffraction (RHEED) is used to monitor the growth process.

laser pulse ($\lambda = 248\,\mathrm{nm}$) is focused onto the single- or polycrystalline target material with the desired stoichiometry, resulting in evaporation, plasma formation and propagation, and eventually deposition on a vis-à-vis mounted, heated substrate.

A theoretical model describing the interaction of the laser irradiation with the target material in three steps was developed by Singh and Narayan [135]. In the first step, the absorption of the laser beam leads to substantial heating and evaporation of essentially unionized target material. The details of this process heavily depend on the laser parameters (energy density, wavelength, pulse duration, shape) and material properties (reflectivity, absorption, heat capacity, density, thermal conductivity,...). In the second step, the laser increasingly ionizes the evaporated material and heats the resulting plasma to temperatures of 7 000 - 20 000 K. The initially confined plasma isothermally expands into the vacuum while being constantly augmented with further particles from the target. The highly anisotropic expansion is preferentially normal to the surface and results in an elongated shape of the plasma plume. In the third step, the plasma adiabatically expands into the vacuum after the termination of the pulse. Since neither energy nor particles are injected into the plasma the temperature drops significantly as the thermal energy is converted into kinetic energy. In this regime, scattering with the background gas can significantly influence the growth kinetics, resulting in an atomic mass-dependent deceleration and angular distribution, and potentially in an off-stoichiometry of the deposited film. Furthermore, the chemical composition of the plasma may be influenced upon propagation through the background gas, e.g., by oxidation of certain species when using an oxygen atmosphere.

After deposition the energy required for diffusion and nucleation into a crystalline lattice is in part provided by the thermal energy of the substrate, which is heated to a temperature between 300 and 1200 K by a high-power infrared laser directed at the backside of the sample holder. However, in contrast to other epitaxy techniques like molecular beam epitaxy (MBE) and depending on the type and pressure of the background gas, the ablated particles impinge upon the substrate with a rather high kinetic energy of 10-100 eV. Therefore the kinetics of the arriving species has to be taken into account and the assumption of (near-)thermodynamic equilibrium, which lies at the core of the traditional classifica-

tion of growth modes[4], is not strictly valid [136, 137]. The most common kinetical growth modes encountered during PLD are step-flow, layer-by-layer and island growth. In step-flow mode all deposited adatoms diffuse to existing unit cell steps on the surface and no nucleation of two-dimensional islands occurs. In contrast, the layer-by-layer growth mode results from crystallization of 2D nuclei, which grow in size and coalesce until a complete layer is terminated. Multi-level or island-growth evolves if premature nucleation occurs on the top of islands due to low adatom mobility. In reality, transitions between the three idealized growth modes may be encountered depending on the growth conditions [137]. Two-dimensional layer-by-layer growth is a prerequisite for the investigation of atomically flat films with a predefined homogeneous thickness, since real-time growth rate control, i.e., the termination of the growth after a predefined number of atomic layers is not possible in the step-flow regime. In this thesis time-resolved reflection high-energy electron diffraction (RHEED) is employed to monitor the growth process.

3.2 Structural characterization

In general, the optimum growth conditions for high-quality epitaxial thin films are not predictable *a priori* and have to be determined iteratively. Therefore, the effects of a certain set of growth parameters are investigated by a number of complementary structural characterization methods, which can be roughly categorized in real-space and reciprocal-space probes. The former include (scanning) imaging techniques like (scanning) transmission electron microscopy (STEM/ TEM) and atomic force microscopy (AFM). The latter probe the periodic bulk or surface lattice by diffraction of x-rays or electrons and include low-energy electron diffraction (LEED), reflection high-energy electron diffraction (RHEED), selected-area electron diffraction (SAED) in transmission and x-ray diffraction (XRD).

3.2.1 Electron Surface Diffraction

Electrons with non-relativistic kinetic energy E can be viewed as de Broglie waves with wavelength

$$\lambda = \frac{h}{\sqrt{2m_e E}}, \tag{3.1}$$

where h is Planck's constant and m_e the free electron mass. In electron diffraction experiments electrons are accelerated onto a sample at a specific kinetic energy, where they interact with the atomic nuclei and electrons via the Coulomb force. In the kinematic scattering approximation, electrons experience single elastic scattering processes and interfere

[4]The layer-by-layer (Franck-van der Merwe), island (Volmer-Weber) and layer-plus-island (Stranski-Krastanov) growth modes have thermodynamic counterparts in three different forms of adsorption isotherms [136].

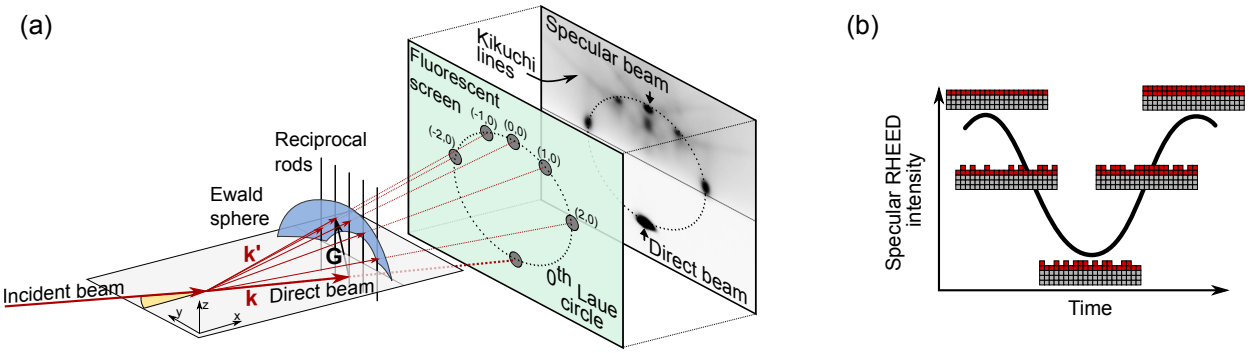

Figure 3.2: (a) Schematic depiction of the reflection high-energy electron diffraction (RHEED) process and exemplary experimental pattern. Due to the high surface sensitivity of the diffracted electrons, the three-dimensional reciprocal lattice transforms into reciprocal rods elongated in the direction of the surface normal. (b) Schematic representation of the specular RHEED intensity oscillations as function of time, i.e., coverage.

constructively if the Laue condition is fulfilled:

$$\Delta\mathbf{k} = \mathbf{k} - \mathbf{k}' = \mathbf{G} \tag{3.2}$$

Here, $\mathbf{k}$ and $\mathbf{k}'$ denote the initial and final wave vector of the electron and $\mathbf{G}$ is a reciprocal lattice vector. A geometrical visualization is given by the Ewald construction, where the head of the $\mathbf{k}$-vector terminates at a reciprocal lattice point and a sphere with radius $|\mathbf{k}| = |\mathbf{k}'| = 2\pi/\lambda$ is drawn around its origin. By construction, the Laue condition is fulfilled by every wave vector $\mathbf{k}'$, that is centered at the same origin as $\mathbf{k}$ and terminates at a intersection between reciprocal lattice and Ewald sphere. If the penetration depth of the impinging electrons is on the order of a few atomic layers only diffraction from a two-dimensional surface lattice needs to be considered. In this case the three-dimensional reciprocal lattice transforms into reciprocal rods which are elongated along the surface normal. Due to the strong interaction with matter and the high sensitivity to surface contaminations electron diffraction experiments are usually performed under (ultra) high vacuum (UHV) conditions.

Reflection High-Energy Electron Diffraction

In reflection high-energy electron diffraction (RHEED) experiments [138] electrons with a kinetic energy of $\approx 30\,\mathrm{keV}$ ($\lambda \approx 7\,\mathrm{pm}$) strike the sample surface in almost grazing incidence ($1° - 3°$) and are thereafter detected by a fluorescent screen as schematically depicted in Fig. 3.2 (a). Due to its grazing-incidence geometry RHEED is a highly surface-sensitive technique despite the high kinetic energy of the electrons. Therefore, the Laue condition for constructive interference is fulfilled at intersections between reciprocal rods and the Ewald sphere, resulting in diffraction spots on concentric Laue circles. An exemplary diffraction pattern showing the 0^{th} Laue circle of the (001)-surface of a $SrTiO_3$ crystal is given in Fig. 3.2 (a).

In general, the sharpness of the diffraction spots is a measure for the surface quality since imperfections (defects, roughness, ...) reduce the long-range order and cause a broadening

of the Laue spots, resulting in a streaky pattern normal to the surface. A further attribute of high surface quality is the observation of Kikuchi lines, which originate from a second-order process beyond the kinematic scattering approximation involving a forward-directional inelastic scattering from plasmons and/or phonons and a subsequent diffraction off bulk lattice planes [139–141]. Furthermore, the presence of islands on the sample surface is indicated by RHEED patterns with symmetries different from the Laue circle, as the high-energy electrons can penetrate the islands and interfere with their three-dimensional lattice structure. The resulting transmission interference pattern is distinctly different from that of the two-dimensional surface lattice and is easily distinguished by changing the azimuthal angle of incidence [138].

The rather large electron mean free path due to the high kinetic energy and the grazing incidence geometry allow for the performance of RHEED during pulsed laser deposition in a background pressure of up to $\approx 2 \cdot 10^{-1}$ mbar, if a differential pumping system is employed to protect the electron emitting filament [142]. The diffraction pattern can be monitored live using a charge coupled device (CCD) camera to film the fluorescent screen, thereby yielding information about the film coverage in real time [138,143]. Due to the high surface sensitivity of RHEED, the intensity of diffracted electrons is reduced by the presence of surface steps, which act as diffuse scatterers in the empirical step density model [144–146]. In contrast to step-flow growth, the average step density changes upon nucleation and coalescence of two-dimensional islands in the layer-by-layer growth mode as depicted in Fig. 3.2 (b). Therefore, the observation of periodic intensity oscillations of the specular RHEED spot signals the desired two-dimensional layer-by-layer growth, where one oscillation period equates to the deposition of one monolayer, and allows for the controlled termination of the film deposition after a predefined number of layers [142, 147].

Low-Energy Electron Diffraction

In low-energy electron diffraction (LEED) experiments electrons are accelerated to 10-300 eV and strike the sample surface perpendicularly as depicted in Fig. 3.3. The electrons are backscattered and form a diffraction pattern on a fluorescent screen, which directly reflects the two-dimensional reciprocal lattice. Due to the low kinetic energy a large background of inelastically scattered electrons has to be suppressed by an electric potential applied to concentric grids in front of the screen. LEED is a highly surface sensitive technique and very susceptible to surface contaminations and/or imperfections, which are reflected in a damped or broadened interference pattern. Furthermore, LEED is routinely employed to detect structural surface reconstructions due to an altered surface symmetry.

3.2.2 X-ray Diffraction

Unlike electrons, which are charged particles and strongly couple to matter via the Coulomb interaction, the interaction between x-rays and matter is rather weak and dominated by coupling to the spatial distribution of the valence electrons. Since the typical x-ray penetration length therefore extends over several micrometers, x-ray diffraction (XRD) probes the three-dimensional bulk lattice structure rather than the surface of a sample. In comparison to

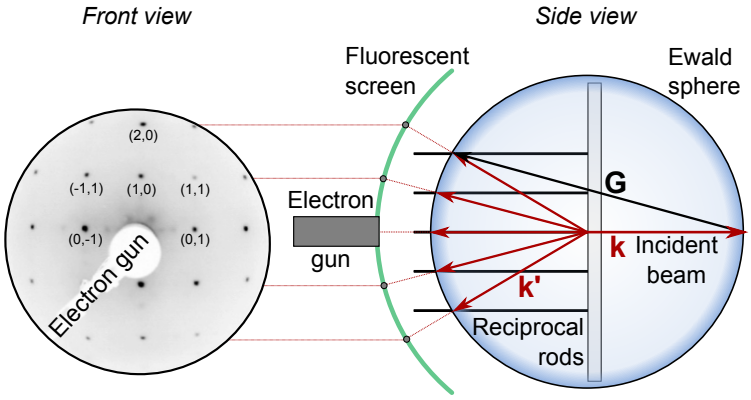

Figure 3.3: Schematic depiction of the low-energy electron diffraction (LEED) process and exemplary experimental pattern.

electron diffraction, the Laue condition (Eq. 3.2) for constructive interference is hence only satisfied in rare cases since the Ewald sphere has to intersect a reciprocal lattice point rather than a rod. The basic measurement geometry employed for the x-ray diffraction experiments in this thesis is shown in Fig. 3.4 (a). By variation of the angles ω and 2θ, the wave vectors $\mathbf{k}$ and $\mathbf{k}'$ of the incident and outgoing (measured) photons are rotated, thereby continuously moving the momentum transfer $\Delta\mathbf{k}$ through the reciprocal lattice in the plane spanned by $\mathbf{k}$ and $\mathbf{k}'$. Depending on the objective of the measurement, different modes are employed to probe different sections of the reciprocal space.

In this thesis, Cu K_α radiation with wavelength $\lambda = 1.54\,\text{Å}$ from a copper x-ray tube is employed. Despite monochromatization by a Ge (022) channel-cut monochromator weak Cu K_β satellite lines may appear in the diffraction patterns. Furthermore, the $SrTiO_3$ substrates used for pulsed laser deposition of $SrIrO_3$ exhibit a vicinal angle of $0.7° - 1.3°$ between surface and high-symmetry (001) lattice plane, which needs to be considered as offset during the adjustment of measurements.

Determination of the out-of-plane lattice constant in $\theta - 2\theta$ geometry

The $\theta - 2\theta$ measurement mode is the most commonly used geometry for the structural analysis of crystalline thin films with the objective to determine the out-of-plane lattice constant. For this purpose, the angles ω and 2θ are varied in a fixed 1:2 ratio ($\omega = \theta$) such that the transferred momentum $|\Delta\mathbf{k}| = q_z = 4\pi \sin\theta/\lambda$ is sampled along the surface normal (cf. Fig. 3.4 (b)). In this geometry, the Laue condition is satisfied if $q_z = n \cdot 2\pi/d_{hkl}$, where d_{hkl} is the out-of-plane lattice constant and $n \in \mathbb{N}$, resulting in the well-known Bragg condition

$$2d_{hkl} \sin\theta = n\lambda. \tag{3.3}$$

For epitaxial thin films with a defined thickness (and an out-of-plane lattice spacing different from the substrate) the number of coherent scattering centers N is finite. In analogy to optical interference patterns from multiple slits, the finite thickness results in periodic intensity fringes (or: Laue oscillations) on either side of the diffraction peak, which

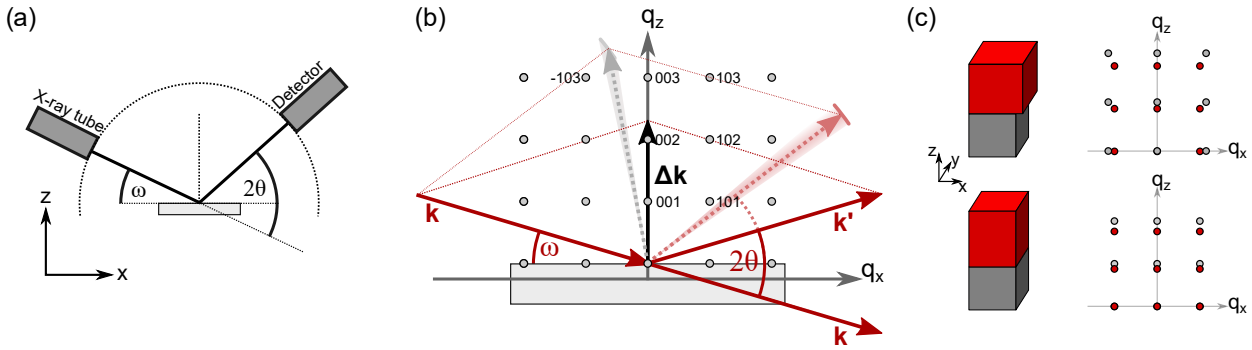

Figure 3.4: (a) Basic measurement geometry of an x-ray diffraction experiment. The incident photons from an x-ray source impinge upon the sample under an angle ω, while the outgoing photons are measured under an angle 2θ. The exact measurement geometry is determined by the objective of the measurement. (b) In the $\theta - 2\theta$ geometry ($\omega = \theta$, dark red) the out-of-plane lattice constant is measured because the transferred momentum $\Delta\mathbf{k}$ (black) is sampled along the surface normal. By changing ω and 2θ independently ($\omega \neq \theta$, dashed arrows) a two-dimensional cut of the reciprocal space can be mapped as indicated by the finite shaded width of the dashed arrows. (c) Reciprocal space mapping is frequently used to determine the epitaxial strain between a thin film and a substrate, since the ratio of in- and out-of-plane lattice constants is reflected in the reciprocal lattice points away from the surface normal.

are described by

$$I_N(q_z) \propto \frac{\sin^2\left(\frac{1}{2} N\, d_{hkl}\,(q_z - Q)\right)}{\sin^2\left(\frac{1}{2}\, d_{hkl}\,(q_z - Q)\right)}, \tag{3.4}$$

where d_{hkl} is the lattice parameter, $d = N \cdot d_{hkl}$ is the film thickness and $Q = n \cdot 2\pi/d_{hkl}$ is the reciprocal lattice vector of the diffraction peak. In experiment, the Laue fringes can be exploited as complementary method to determine the film thickness.

Reciprocal Space Mapping

If the angles ω and 2θ are varied in a ratio different from the $\theta - 2\theta$ geometry, the transferred momentum $\Delta\mathbf{k}$ picks up an in-plane component as shown in Fig. 3.4 (b). This allows for the investigation of reciprocal lattice points away from the surface normal. Since, typically, a two-dimensional area around a reciprocal lattice point is scanned, this technique is called reciprocal space mapping (RSM). In thin-film epitaxy studies, RSM is frequently employed to investigate the epitaxial relationship between substrate and film, since the ratio of in- and out-of-plane lattice constants is (inversely) reflected in the respective reciprocal lattice points away from the surface normal. As exemplarily depicted in Fig. 3.4 (c) for two cubic materials with different lattice constant, epitaxial strain results in an equal in-plane and elongated/contracted out-of-plane lattice constant. Therefore, the reciprocal lattice points adopt the same q_x position.

Powder X-Ray Diffraction

In contrast to the above-described diffraction techniques, which work best with single crystals or crystalline thin films, powder diffraction is employed to characterize the structure of polycrystalline or powder materials, in which the microcrystallites adopt a well-ordered crystal structure but are oriented randomly. For this purpose, the powder sample is carefully flattened and then measured in the $\theta - 2\theta$ geometry. As the momentum transfer is varied, for every possible set of crystallographic planes a small percentage of the randomly oriented microcrystallites will be aligned such that the Laue condition is satisfied. Therefore, a characteristic pattern hosting all possible diffraction peaks is measured allowing for the determination of the crystal structure(s) within the sample.

3.2.3 Atomic Force Microscopy

Atomic force microscopy (AFM) is a real-space scanning probe technique which provides information about the surface morphology. In this thesis a commercial Bruker Dimension Icon AFM was employed to investigate the $SrTiO_3$ substrates prior to film growth to guarantee an atomically flat TiO_2-terminated surface and to investigate the resulting $SrIrO_3$ thin-film surface morphology. During imaging a sharp silicon tip at the end of a cantilever is laterally scanned across the sample surface at a distance of $\approx 200\,\mathrm{nm}$ and interacts with the microscopic force field of the sample. Depending on the application AFM can be operated in a number of measurement modes. Here, the tapping (or: dynamic contact) imaging mode is employed, where the cantilever is driven to oscillate near its resonance frequency by a small piezo element with constant driving amplitude and frequency. As the tip approaches the sample the oscillation amplitude is modulated by interaction forces acting on the tip (dipole-dipole interactions, van der Waals forces, ...) and used as feedback to adjust the height of the cantilever, thereby creating a point-to-point height profile. In addition, the phase shift between cantilever oscillation and driving signal provides information about the dissipated energy, i.e., the adhesion properties and hence to some extent the surface material. While the lateral resolution of the used AFM is on the order of 20 nm, the height resolution is sufficient to map single unit cell steps of 4 Å.

3.2.4 Transmission Electron Microscopy

According to the Abbe diffraction limit the minimum resolvable distance using light with wavelength λ is given by

$$d = \frac{\lambda}{2n \sin\theta}, \tag{3.5}$$

where n is the refractive index and θ the half angular aperture [148]. For visible light the Abbe limit ($\lambda = 400 - 700\,\mathrm{nm}$, $d \approx 200 - 350\,\mathrm{nm}$) therefore exceeds interatomic distances by four orders of magnitude. One way to push the spatial resolution to the atomic limit is to exploit the extremely small de Broglie wavelength of electrons with high kinetic energy ($\lambda = 1.97\,\mathrm{pm}$ at $E = 300\,\mathrm{kV}$) [149]. The invention of electron optical lens systems using

electromagnetic fields in the 1920's [150] initiated the design and development of the first electron microscopes, of which transmission electron microscopy (TEM) has evolved into the most versatile technique with subatomic spatial resolution. Today, a number of operating modes with a variety of contrast mechanisms are routinely performed, including conventional imaging, scanning TEM imaging (STEM), selected-area electron diffraction (SAED) or electron energy loss spectroscopy (EELS). In this thesis, high-resolution TEM (HRTEM) using phase contrast, STEM using high-angle annular dark field (HAADF) contrast and SAED were employed to study $SrIrO_3$ thin films and will be briefly introduced based on Ref. [151] in the following.

Generally, from top to bottom, a TEM is composed of an electron emission source, a series of electromagnetic lenses, electrostatic plates and apertures, a sample manipulator and an imaging device, which are operated in ultra high vacuum (UHV). Typically, the electrons are emitted from a heated tungsten or LaB_6 cathode via thermionic and/or field emission and then accelerated by a series of high-voltage electrostatic plates until they reach their final kinetic energy of 100-300 keV. Operation under UHV conditions is therefore necessary to avoid the generation of plasma sparks upon application of the high acceleration voltages, but also to increase the electron mean free path. After acceleration, the electron beam passes through a complex series of electromagnetic coils acting as focusing lenses, electrostatic plates used to deflect or laterally shift the beam and concentric apertures, which shut off parts of the beam. Since, in contrast to optical microscopes, rapid changes of the optical configurations are possible by modification of the applied currents and/or voltages, TEM has a high flexibility of operation as shown in Fig. 3.5. The condenser lens system initially focuses the accelerated electron beam to the desired size and location on the sample. By choice of the lens settings and apertures, the sample can be illuminated by a parallel beam with up to 1 mm diameter (TEM, SAED), a focused beam with subatomic diameter (STEM) or anything in between. After transmission through and interaction with the sample the electron beam passes the objective lens system, which forms the image, that is eventually expanded onto a phosphor screen by the projector lens.

The interaction between electron beam and sample is complex and comprises a manifold of processes. In the direction of the incoming beam backscattered electrons, Auger electrons, characteristic x-rays and cathodoluminescence are observed and routinely exploited as signal in scanning electron microscopy (SEM), thereby offering spatially resolved chemical information of the sample surface. In transmission, the outgoing electrons can be categorized in elastically and inelastically scattered, where inelastic scattering is due to the interaction between incoming electrons and the bound electrons in the material. The characteristic energy loss due to the excitation of plasmons, phonons or core electrons into unoccupied states is exploited in EELS to obtain information about the chemical composition or the atomic valence states in the sample. The elastic scattering processes include incoherent Rutherford scattering from the screened charge of the atomic nuclei and coherent Bragg scattering from the periodic arrangement of atoms. The former is observed at high scattering angles, depends on the atomic number Z and is exploited in HAADF-STEM. The latter is observed at small scattering angles and exploited in bright-field, annular dark-field and phase-contrast TEM, where an aperture is inserted in the back focal plane of the objective

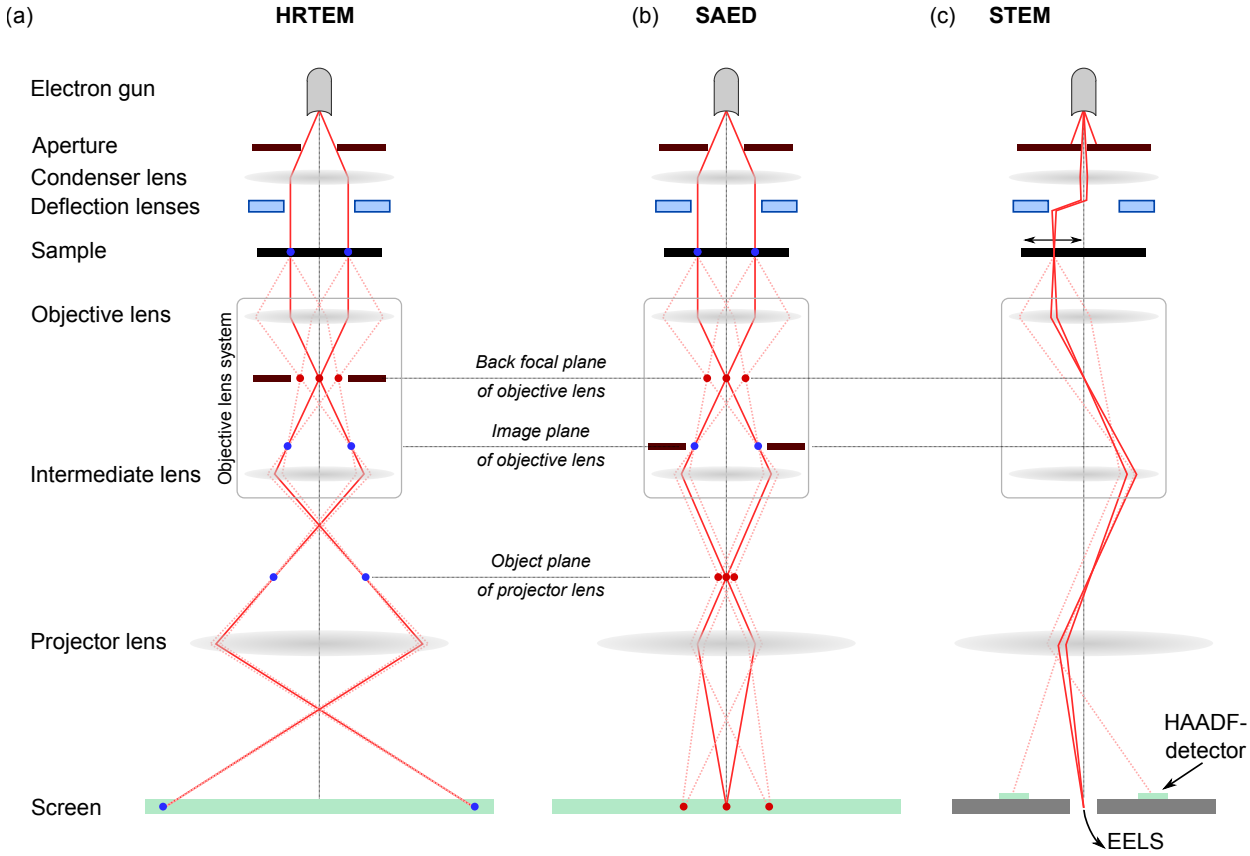

Figure 3.5: Schematic views of the different measurement modes of transmission electron microscopy. (a) High-resolution transmission electron microscopy (HRTEM). (b) Selected-area electron diffraction (SAED). Here, the focal length of the intermediate lens is adjusted such that its back focal plane and hence the diffraction pattern is projected onto the screen. (c) Scanning transmission electron microscopy (STEM). The primary beam is focused to a subatomic diameter and scanned across the sample, where the electrons are scattered. The gathered information highly depends on the detection angle away from the optical axis (high angle: high-angle annular dark field (HAADF)). *Figure adapted from WikiMedia Commons [152] under the Creative Commons BY-SA 4.0 license.*

lens to only transmit the specular, a single or all diffracted beam(s) for imaging, respectively (cf. Fig. 3.5 (a)). In this thesis, high-resolution TEM measurements using phase contrast were performed to investigate the microscopic structure of $SrIrO_3$ films.

High-Resolution Transmission Electron Microscopy

High-resolution transmission electron microscopy (HRTEM) is a specialized imaging mode of TEM which allows for the investigation of crystalline samples with atomic resolution. For this purpose the sample is illuminated with a parallel electron beam which can be described as plane wave

$$\Psi_i(\mathbf{r}) = \Psi_0 \, e^{ik_z z}. \tag{3.6}$$

As the electron beam propagates through the sample the amplitude and phase of the wave is modulated by interaction with the periodic potential of the crystal. The outgoing beam is described by

$$\Psi_o(\mathbf{r}) = \Psi_i(\mathbf{r}) \cdot a(\mathbf{r})\, e^{i\phi(\mathbf{r})}, \tag{3.7}$$

where $a(\mathbf{r})$ and $\Phi(\mathbf{r})$ are the local amplitude modulation and phase shift. If the sample thickness is significantly smaller than the electron mean free path, it can be approximated as phase object, which exclusively causes a spatial modulation of the phase upon transmission ($a(\mathbf{r}) = 1$). However, in an ideal electron optical lens system the phase information is completely lost as the experimentally measured quantity is the intensity $I(\mathbf{r}) \propto |\Psi_o(\mathbf{r})|^2$. In reality, the phase contrast observed in the image plane of the microscope in HRTEM imaging is due to the interference of the electron beam with itself, resulting from an additional relative phase shift between the paraxial and off-axial beams caused by optical aberrations. The interplay of the contributing aberrations, (spherical, chromatic, ...) is described by the phase contrast transfer function (PCTF), which can be experimentally manipulated in TEM by changing the defocus. Since the phase contrast is highly influenced by the aberrations and defocus, the interpretation of of HRTEM images is not always intuitive and may require numeric simulations.

Selected-Area Electron Diffraction

In the case of a crystalline sample, electrons are Bragg scattered into discrete locations in the back focal plane of the objective lens as shown in Fig. 3.5 (a) and (b). By tuning the intermediate lens of the objective lens system such that the back focal plane rather than the image plane is projected, a diffraction pattern can be generated on the screen. Depending on the sample's long-range order a single or a superposition of several diffraction patterns will be observed. In selected-area electron diffraction (SAED), an aperture is located in the image plane of the objective lens as shown in Fig. 3.5 (b) to selectively measure the diffraction pattern from a small area of the specimen. In contrast to x-ray diffraction, SAED is therefore a suitable tool to identify the local crystal structure, lattice (mis)matching or the orientation of microcrystallites in polycrystalline materials with a spatial resolution of $\approx 1\,\mu$m.

High-Angle Annular Dark Field Scanning Transmission Electron Microscopy

In scanning transmission electron microscopy (STEM) a focused electron beam is scanned over the sample [153]. For this purpose magnetic deflection coils are employed such that the sample is always illuminated with the beam normal to the surface. The versatility of STEM exceeds that of conventional TEM as the output of a variety of detectors can be used to form an image. Typical detectors include a bright-field detector that measures the transmitted beam (low-angle scattering) and an (high-angle) annular dark field (HAADF) detector surrounding the transmitted beam to intercept scattered electrons. Furthermore, complementary analysis techniques such as energy dispersive x-ray (EDX) spectroscopy, electron

energy loss spectroscopy (EELS) or cathodoluminescence microscopy can be employed to gain insight into the chemical composition of the sample.

Whereas the low-angle scattering of the electron beam is mostly caused by Coulomb interactions with the electron cloud, the higher scattering angles are predominated by incoherent Rutherford scattering off the screened charges of the nuclei. Therefore, the high-angle annular dark field (HAADF) contrast is directly related to the atomic number Z (Z-contrast), as the Rutherford scattering cross section reads

$$\frac{d\sigma}{d\Omega} = \left(\frac{Z\,\alpha\,\hbar\,c}{4E_{\mathrm{kin}}\sin^2\frac{\theta}{2}} \right)^2, \tag{3.8}$$

where α is the fine structure constant, $\hbar$ Planck's constant, c the speed of light, E_{kin} the electron kinetic energy and θ the scattering angle. In real materials the scattering cross section becomes modified because the Coulomb potential of the bare nucleus is screened by the atomic electron cloud [154], such that

$$\frac{d\sigma}{d\Omega} \propto Z^n \quad \text{with} \quad n \approx 1.7. \tag{3.9}$$

While this material contrast simplifies the interpretation of HAADF-STEM images in comparison to conventional TEM, the quantitative analysis in the presence of atomic species with different atomic numbers may require extensive numerical simulations [155].

Sample preparation

Sample preparation for TEM can be a complex procedure, since the thickness of high-quality specimens should not exceed the electron mean free path in the material, which may only be on the order of several tens of nanometers. For the investigation of heterostructures a cross-sectional lamella is cut from the sample perpendicularly to the surface using a focused ion beam (FIB). Since the sample surface may severely suffer from ion bombardment, it is passivated by a protective amorphous platinum layer using electron and ion beam induced deposition from an organometallic precursor [156,157]. Subsequently, a lamella with a typical length of several micrometers and thickness of about a hundred nanometers is sputtered free with gallium ions. After transfer to a sample holder, the lamella is further thinned to its final thickness below 100 nm by low energy ion milling to prevent excessive amorphization of the lamella surface. Due to its microscopic dimensions a single TEM lamella is therefore not *a priori* representative of the macroscopic sample.

3.3 Photoelectron Spectroscopy

Photoelectron spectroscopy (PES) is one of the most widely used and versatile analytical techniques in solid state physics, surface and material science. Its basic principle relies on the measurement of the kinetic energy of electrons which are emitted from a material via the photoelectric effect, which was discovered by Hertz in 1887 [158] and explained by Einstein

in 1905 by introducing the concept of photons [159]. Starting in the 1950's Siegbahn developed the first high-resolution photoelectron spectrometer to measure the binding energies of strongly bound core states using x-rays [160]. The technique earned the name electron spectroscopy for chemical analysis (ESCA) as its inherent element specificity can be exploited to determine the stoichiometric composition as well as the chemical environment of an elemental species within a material. With the ongoing development of x-ray photoelectron spectroscopy (XPS) it was realized that the investigation of core-level spectra provides further insights about the electronic structure via a coupling to the valence states [161, 162]. In the 1970's angle-resolved photoelectron spectroscopy (ARPES) using ultraviolet light was developed to study the band dispersions of delocalized valence states in crystalline solids by measuring the photoelectron intensity as function of energy and angle, i.e., momentum [77]. To date, the design and development of novel photoelectron spectroscopy techniques is ongoing and comprises spin-resolved PES, the expansion into the hard x-ray regime, two-photon absorption, time-resolved PES and many other applications. In this chapter, the most relevant concepts of PES are introduced with focus on the applications within this thesis and based on several reviews and textbooks [77, 163, 164].

3.3.1 Instrumentation and basic principle

Upon illumination with light of energy $h\nu$ photoelectrons are emitted from a material into the half-space above the sample under investigation by the photoelectric effect. Photoelectron spectroscopy (PES) measures the resulting photocurrent as function of the kinetic energy and the angle under which the electrons are emitted with respect to the surface normal. Depending on the employed excitation energy PES is often distinguished into (vacuum) ultraviolet (VUV/UPS, $h\nu \approx 20 - 200\,\mathrm{eV}$) and x-ray photoelectron spectroscopy (XPS), the latter being further subdivided into soft x-ray (SX, $h\nu \approx 300 - 2000\,\mathrm{eV}$) and hard x-ray photoemission spectroscopy (HAXPES, $h\nu > 2500\,\mathrm{eV}$). To access the different energy regions a variety of light sources can be used, among them laboratory sources (gas discharge lamps, x-ray tubes, lasers) and large-scale facilities (synchrotrons, free-electron lasers). In this thesis, laboratory-based UPS and XPS were performed using the He I line from a Helium discharge lamp ($h\nu = 21.2\,\mathrm{eV}$) and the monochromatized Al K_α line ($h\nu = 1486.7\,\mathrm{eV}$) from an x-ray tube, respectively. Furthermore, soft x-ray synchrotron radiation was used for angle-resolved PES measurements, thereby exploiting the tunability of the photon energy and the high brilliance.

While a number of different methods have been developed for the analysis of the kinetic energy of charged particles, the hemispherical electron energy analyzer is predominantly used in photoemission spectroscopy. As shown in Fig. 3.6 (a) a hemispherical analyzer consists of two concentric electrodes with a certain voltage applied to selectively let pass electrons with a given pass energy E_{pass}. Electrostatic lenses are placed in front of the analyzer to collect and focus the photoelectrons onto the entrance slit and to decelerate the photoelectrons to the pass energy via a retardation field. After passing the analyzer on a hemispherical orbit the photoelectrons become amplified by electron multipliers. In the Würzburg laboratory a set of channeltrons acts as electron counter, whereas state-of-

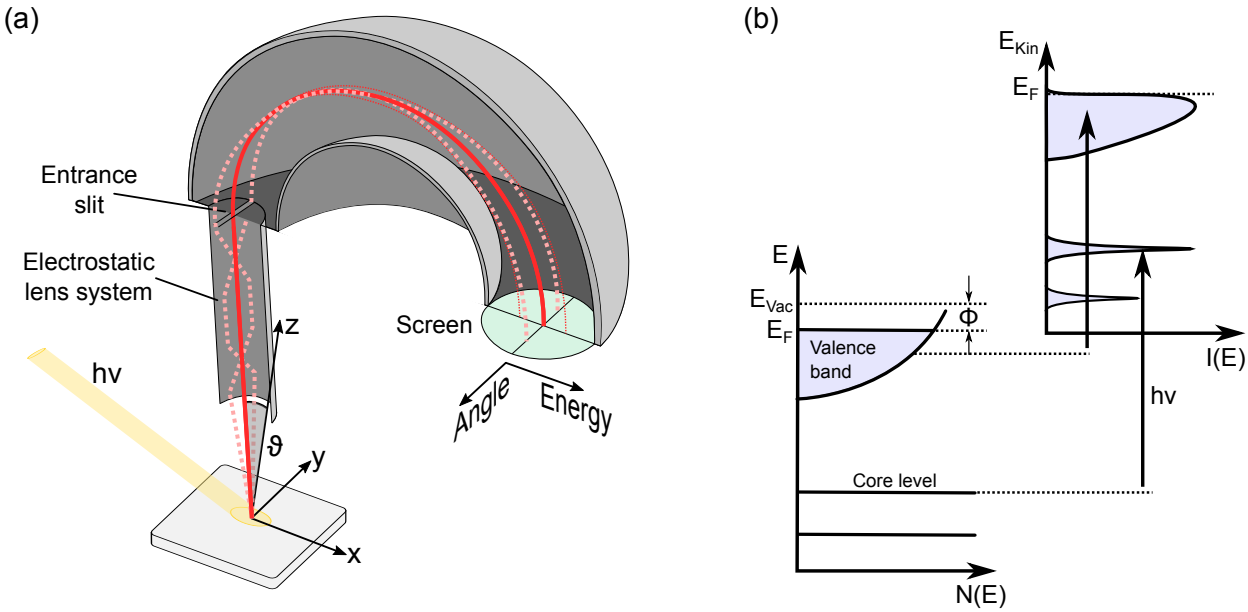

Figure 3.6: (a) Schematic view of the ARPES data acquisition using a hemispherical electron energy analyzer. After photoemission the electrons are collected, decelerated and focused onto the entrance slit by an electrostatic lens system. After a hemispherical trajectory the electrons impinge onto the screen, where a two-dimensional image as function of kinetic energy and emission angle is formed. (b) In a first approximation, the distribution of energies in the emitted photocurrent reflects the occupied density of states in a solid, where the Fermi energy E_F is generally used as energy reference.

the-art ARPES setups typically employ micro-channel plates (MCP) in combination with a fluorescent screen for two-dimensional electron detection, which is recorded by a charge-coupled device (CCD) camera. Thereby, a finite energy and angular range is covered at once and by tilting the sample with respect to the analyzer the half-space can be mapped. By measuring the kinetic energy and the photoemission angle (polar and azimuthal angles: θ, ϕ) the photoelectron wave vector $\mathbf{K}$ is completely determined by

$$|\mathbf{K}| = \frac{1}{\hbar}\sqrt{2mE_{\text{kin}}} \tag{3.10}$$

$$K_x = |\mathbf{K}|\sin\theta\cos\phi\ ,\ \ K_y = |\mathbf{K}|\sin\theta\sin\phi\ ,\ \ K_z = |\mathbf{K}|\cos\theta. \tag{3.11}$$

and can be related to the wave vector of the bound electron in the initial state under certain assumptions.

Furthermore, in a first approximation, the kinetic energy of the photoelectron in the vacuum is related to the binding energy E_{bin} in the initial state by

$$E_{\text{kin}} = h\nu - E_{\text{bin}} - \Phi, \tag{3.12}$$

where ν is the photon frequency and Φ the work function, which is a measure of the potential barrier at the surface preventing the valence electrons from escaping. Since the sample is typically in galvanic contact with the electron energy analyzer the Fermi levels of sample

and analyzer align such that Φ is actually determined by the work function of the analyzer. Under consideration of the instrumental resolution and intrinsic lifetime broadening, the distribution of kinetic energies in the emitted photocurrent reflects the occupied density of states in a solid as shown in Fig. 3.6 (b). In the simplest case, the core-level line shape can hence be described by a Voigt profile, i.e., a convolution of a Lorentzian (lifetime) and a Gaussian (experimental) resolution. In reality, more complex line shapes result from interactions between the core hole and the residual electrons as discussed in the following.

3.3.2 Theoretical background

In a rigorous theoretical description of the photoemission process the transition probability for an optical excitation between the N-electron ground state and an excited N-electron state including the photoelectron needs to be evaluated as a single coherent process involving the bulk, surface and vacuum [165]. In the *one-step model*, the photoelectron final state is described as time-inversed LEED state, which matches a free electron wave in vacuum to a high-lying Bloch wave in the crystal [166]. While the one-step model has been successfully applied to a number of material systems [167], its evaluation is cumbersome. Therefore, the photoemission process is often subdivided into three independent and sequential steps within the phenomenological *three-step model* [168], which successfully describes many observed spectral features:

1. Excitation of the photoelectron inside the solid

2. Propagation of the photoelectron to the surface

3. Emission of the electron into the vacuum

The probability to measure a photoelectron with kinetic energy E_{kin} using the excitation energy $h\nu$, i.e., the photoemission intensity (or: photocurrent) $I(E_{\mathrm{kin}}, h\nu)$ is proportional to the product of the probabilities of the three sequential steps:

$$I(E_{\mathrm{kin}}, h\nu) \propto P_1(E_{\mathrm{kin}}, h\nu) \cdot P_2(E_{\mathrm{kin}}, h\nu) \cdot P_3(E_{\mathrm{kin}}, h\nu) \tag{3.13}$$

The first step contains all information about the intrinsic electronic structure including many-body and matrix-element effects. In the second step the electrons may experience inelastic scattering due to plasmon, exciton or interband excitations, thereby creating an inelastic background signal in the PES spectrum. Since these inelastic processes are strong PES is a highly surface-sensitive technique. The final step describes the transmission probability through the potential step at the surface and leads to a modification of the photoelectron momentum conservation perpendicular to the sample surface. In the following, the theoretical background of the three sequential steps is illustrated with focus on the consequences on the experimental findings within this thesis, following Refs. [77] and [164].

Excitation of the photoelectron

In general, a formal description of the photoemission process involves the calculation of the transition rate $w_{i\to f}$ for an optical excitation between the initial N-electron ground state $|i\rangle$ and a final N-electron state $|f\rangle$. In first-order perturbation theory, the transition rate is given by Fermi's golden rule

$$w_{i\to f} = \frac{2\pi}{\hbar} \left|\langle f| H_{\text{int}} |i\rangle\right|^2 \cdot \delta\left(E_f - E_i - h\nu\right), \tag{3.14}$$

where E_f and E_i are the initial- and final-state energies of the N-particle system. In a semiclassical description, the interaction with the photon is introduced as perturbation by the canonical replacement $\mathbf{p} \to \mathbf{p} - e\mathbf{A}$ in the unperturbed Hamiltonian $H_0 = \frac{\mathbf{p}^2}{2m} + V(\mathbf{r})$, where $\mathbf{A} = \mathbf{A_0} \cdot \exp(i\mathbf{qr} - i\omega t)$ is the electromagnetic vector potential of the incident light:

$$H = \frac{1}{2m}\left(\mathbf{p} - e\mathbf{A}\right)^2 + V(\mathbf{r}) = H_0 - \frac{e}{m}\mathbf{A}\cdot\mathbf{p} - \frac{e}{2m}\left(-i\hbar\nabla\mathbf{A}\right) + \frac{e^2}{2m}\mathbf{A}^2 \tag{3.15}$$

$$\approx H_0 \; - \frac{e}{m}\mathbf{A_0}\,\mathbf{p}\cdot e^{-i\omega t} \tag{3.16}$$

In the second step, several approximations were made. The quadratic term is omitted ($\mathbf{A}^2 = 0$) since two-photon processes are negligible for weak light intensities. Furthermore, $\nabla\mathbf{A} = 0$, if specific surface effects (e.g., surface photoemission [169,170]) are neglected and, finally, the dipole approximation $\exp(i\mathbf{qr}) = 1 + i\mathbf{qr} + ... \approx 1$ holds if the photon wavelength exceeds the atomic dimensions, which is justified for light in the VUV or soft x-ray region. In second quantization, the perturbation operator is given by

$$H_{\text{int}} = -\frac{e}{m}\sum_{\mathbf{k},n}\langle\mathbf{k}|\,\mathbf{A_0}\,\mathbf{p}\,|n\rangle\, c_{\mathbf{k}}^{\dagger}c_n = \sum_{\mathbf{k},n} M_{\mathbf{k},n}c_{\mathbf{k}}^{\dagger}c_n, \tag{3.17}$$

where $c_{\mathbf{k}}^{\dagger}$ creates a photoelectron in a high-energy Bloch state with momentum $\mathbf{k}$ (and the omitted band index κ) and c_n annihilates an electron in any state n.

The final N-electron state comprises $(N-1)$ electrons in the solid and one photoelectron in a high-energy Bloch state (wave vector $\mathbf{k}$ and energy $E_{\mathbf{k}}$). In the *sudden approximation* the photoemission process is assumed to be instantaneous, thereby entirely decoupling the photoelectron from the remaining $(N-1)$ electron system, i.e., without considering any relaxation of the system. The final state therefore factorizes into a photoelectron in the state $|\mathbf{k}\rangle$ and an excited eigenstate of the $(N-1)$ electron system with energy E_s^{N-1}

$$|f\rangle = |N-1, s; \mathbf{k}\rangle \xrightarrow[\text{approximation}]{\text{sudden}} c_{\mathbf{k}}^{\dagger}\,|N-1, s\rangle = |\mathbf{k}\rangle\,|N-1, s\rangle\,, \tag{3.18}$$

where s denotes a set of quantum numbers uniquely describing the state and $c_{\mathbf{k}}^{\dagger}$ is the electron creation operator acting on the photoelectron subspace. Assuming a negligible

energy dependence of the single-particle matrix element the transition rate then becomes

$$w_{i\to f} = \frac{2\pi}{\hbar}|\sum_{\mathbf{k}',n} M_{\mathbf{k}',n} \langle N-1,s|\underbrace{c_{\mathbf{k}}c^{\dagger}_{\mathbf{k}'}}_{\delta_{\mathbf{k},\mathbf{k}'}} c_n |N,0\rangle|^2 \cdot \delta\left(E_{\mathbf{k}} + E_s^{N-1} - E_0^N - h\nu\right) \tag{3.19}$$

$$= \frac{2\pi}{\hbar}\sum_n |M_{\mathbf{k},n}|^2 \cdot |\langle N-1,s| c_n |N,0\rangle|^2 \cdot \delta\left(E_{\mathbf{k}} + E_s^{N-1} - E_0^N - h\nu\right) \tag{3.20}$$

and summation over all possible quantum numbers s yields the probability for photoexcitation

$$P_1(E_{\mathbf{k}}, h\nu) = \frac{2\pi}{\hbar}\sum_n |M_{\mathbf{k},n}|^2 A^{<}(E_{\mathbf{k}}, h\nu) \tag{3.21}$$

with the spectral function

$$A^{<}(E_{\mathbf{k}} - h\nu, h\nu) = \sum_s |\langle N-1,s| c_n |N,0\rangle|^2 \cdot \delta\left(E_{\mathbf{k}} + E_s^{N-1} - E_0^N - h\nu\right). \tag{3.22}$$

Therefore, photoemission spectroscopy measures the spectral function $A^{<}(E_{\mathbf{k}}, h\nu)$ weighted by the single-particle dipole matrix element $|M_{\mathbf{k},n}|^2$. The latter comprises the light polarization dependence of the observed spectra and the orbital and photon-energy dependence of the photoionization cross sections [171], which are shown in Fig. 3.7 (a) for the Ir $5d$, Ti $3d$ and O $2p$ orbitals investigated in this thesis [172].

Valence-band photoexcitation for non-interacting electron systems In a non-interacting electron system the initial state can be described as product of single-particle states, and annihilation of one electron results in a $(N-1)$ electron system in the s_0^{th} eigenstate $|N-1,s_0\rangle$ of the $(N-1)$-particle Hamiltonian

$$c_n |N,0\rangle = |N-1,s_0\rangle \text{ with } E_0^N = \epsilon_n + E^{N-1}, \tag{3.23}$$

where $\epsilon_n < 0$ is the one-electron energy of the n^{th} electron and the one-electron binding energy $E_{\mathrm{bin},n} = -\epsilon_n$ (Koopman's theorem). Therefore,

$$\langle N-1,s| c_n |N,0\rangle = \langle N-1,s|N-1,s_0\rangle = \delta_{s,s_0} \tag{3.24}$$

and in case of photoemission of a valence electron with wave vector $\mathbf{k_i}$, Eq. 3.21 becomes

$$P_1(E_{\mathbf{k_i}}, h\nu) = \frac{2\pi}{\hbar}\sum_n |M_{\mathbf{k_i},n}|^2 \cdot \delta\left(E_{\mathbf{k_i}} + E_{\mathrm{bin},n} - h\nu\right), \tag{3.25}$$

which is a direct measure of the density of states (DOS) of the electron system in its ground state weighted by the one-electron dipole matrix element.

Valence-band photoexcitation for strongly correlated electron systems For a strongly correlated electron system in which the short-range Coulomb interactions between the electrons are not negligible, the electron system is in general not in an eigenstate of the system after annihilation of an electron in state n and

$$|\langle N-1, s|\, c_n\, |N, 0\rangle\,|^2 \tag{3.26}$$

describes the probability that the electron removal leaves the $(N-1)$-electron system in the excited eigenstate s. Therefore, depending on the interactions in the system, the electron removal spectral function in Eq. 3.22 and hence the resulting photoemission spectrum may strongly deviate from the non-interacting case. In theory, many-body interactions are typically described in the Green's-function formalism, where all correlation effects are captured by the complex self energy $\Sigma(\mathbf{k}, \epsilon) = \Sigma'(\mathbf{k}, \epsilon) + i\Sigma''(\mathbf{k}, \epsilon)$:

$$G(\mathbf{k}, \epsilon) = \frac{1}{\epsilon - \epsilon^0_{\mathbf{k}} - \Sigma(\mathbf{k}, \epsilon)} \tag{3.27}$$

Taking into account the Dirac identity $(x + i\eta)^{-1} = P\left(\frac{1}{x}\right) - i\pi\delta(x)$, where η is a positive infinitesimal and P denotes the principal value, the identity

$$A^{<}(\mathbf{k}, \epsilon) = -\frac{1}{\pi}\mathrm{Im}\; G(\mathbf{k}, \epsilon - i\eta) \cdot f(\epsilon, T) \tag{3.28}$$

follows, where the Fermi-Dirac-distribution is introduced because PES exclusively probes the electron removal part of the spectral function. Therefore, PES can in principle capture all many-body interactions in a correlated electron system via determination of the complex self energy.

Core-level photoexcitation for strongly correlated electron systems Core-level photoemission spectroscopy is a powerful tool for the investigation of the electronic structure in solids. For example, its inherent element specificity yields information about the presence and local chemical environment of elemental species. Furthermore, static core-level shifts can shed light on local (or global) variations of the electrostatic potential at interfaces or due to a changing Madelung potential [173–175]. In strongly correlated electron systems core-level PES can be employed to gather information about the delocalized valence states, since the core hole in the photoemission final state couples to the valence electrons via the Coulomb interaction. For a theoretical description the N-electron system is divided into a N_c-core and a N_v-valence-electron subsystem ($N = N_c + N_v$) [176]. In the sudden approximation the initial and final state can hence be written as

$$|i\rangle \;= |0_{PE}\rangle\, |0_c\rangle\, |N_v^i\rangle \quad \text{and} \tag{3.29}$$

$$|f\rangle = |\mathbf{k}\rangle\, |c\rangle\, |N_v^f, s\rangle\,, \tag{3.30}$$

where $|N_v^i\rangle$ ($|N_v^f\rangle$), $|\mathbf{k}\rangle$ and $|c\rangle$ stand for the valence-electron subsystem in the initial (final) state without (in the presence of) the core hole, the photoelectron in a high-energy Bloch

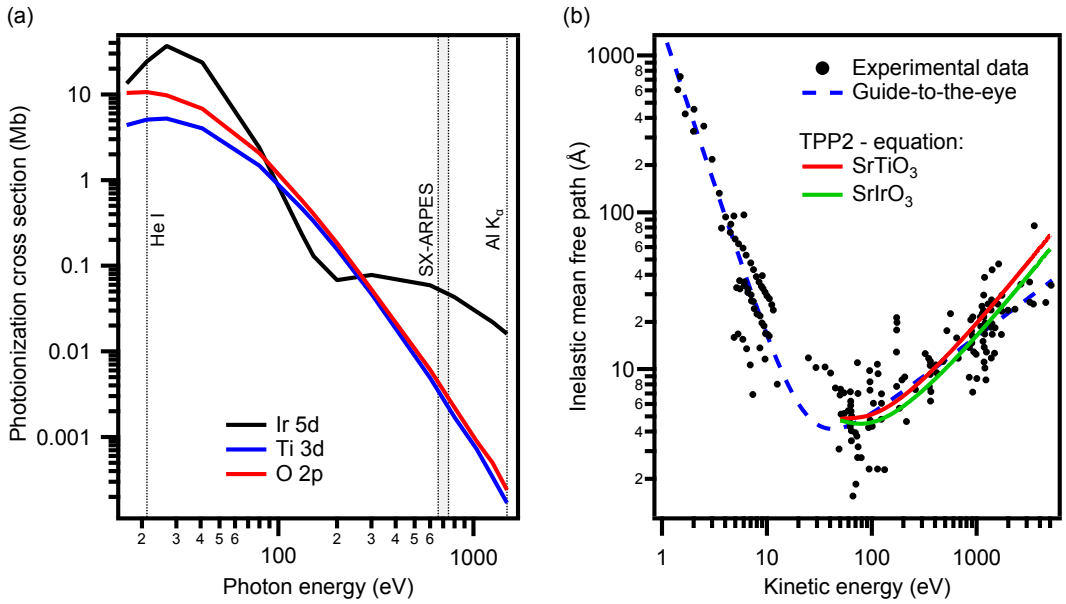

Figure 3.7: (a) Calculated photoionization cross sections of Ir 5*d*, Ti 3*d* and O 2*p* subshells as function of photon energy. Data taken from Ref. [172]. (b) Inelastic electron mean free path as function of kinetic energy. The experimental values are taken from Ref. [177] and the numerical values for $SrTiO_3$ and $SrIrO_3$ are calculated using the TPP2-equation in Eq. 3.35 [178].

state $|\mathbf{k}\rangle$ and the core hole, respectively. Then, Eq. 3.21 becomes:

$$P_1(E_\mathbf{k}, h\nu) = \frac{2\pi}{\hbar} \sum_c |M_{\mathbf{k},c}|^2 \sum_s |\langle N_v^f, s| \overbrace{\langle c| \langle \mathbf{k}| c_\mathbf{k}^\dagger c_c |0_{PE}\rangle |0_c\rangle}^{=1} |N_v^i\rangle|^2 \tag{3.31}$$

$$\cdot \delta\left(E_\mathbf{k} + E_{N_v,s}^f - E_{N_v}^i - \epsilon_c - h\nu\right) \tag{3.32}$$

$$\propto \underbrace{\sum_{c,s} |\langle N_v^f, s|N_v^i\rangle|^2 \cdot \delta\left(E_\mathbf{k} + E_{N_v,s}^f - E_{N_v}^i - \epsilon_c - h\nu\right)}_{\text{core-level spectral function}} \tag{3.33}$$

Here $M_{\mathbf{k},c}$, c_c and ϵ_c are the one-electron photoexcitation matrix element, the core-hole creation operator and the one-electron core-level energy, respectively, and $M_{\mathbf{k},c}$ is assumed energy-independent. Hence, different core-hole coupling mechanisms to the valence electrons can give rise to a multi-peak structure in core-level spectra, for example, atomic multiplets, charge-transfer satellites and well-screened final states. In order to correctly interpret the experimental photoemission spectra of strongly correlated electron systems different theoretical models taking into account the electron-electron interactions can be employed to calculate the ground and excited states with and without core hole. Often-used models include the Anderson impurity model, cluster models, the Hubbard model or dynamical mean-field theory (DMFT).

Propagation of the photoelectron to the surface

In the second step of the three-step model the excited photoelectron adopts a high-energy state in the solid and propagates through the material, where it is subject to inelastic scattering. The probability of retaining its original kinetic energy after propagating for a distance z is given by a Beer-Lambert law $e^{-z/\lambda_{\mathrm{IMFP}}}$, where λ_{IMFP} is the kinetic energy- and material-dependent photoelectron inelastic mean free path (IMFP). Therefore, the measured photoelectron signal from a depth z below the surface is

$$I(z) = I_0 \cdot e^{-z/\lambda_{\mathrm{eff}}} = I_0 \cdot e^{-z/\lambda_{\mathrm{IMFP}} \cos\theta}, \tag{3.34}$$

where θ is the photoemission angle with respect to the surface normal and I_0 is the number of excited electrons, which can be assumed spatially constant since the x-ray penetration depth exceeds the photoelectron IMFP by several orders of magnitude. By variation of the angle θ under which the photoemission spectrum is acquired the depth information of core-level PES can be tuned, hence allowing for the depth profiling of the chemical or electronic properties at heterointerfaces or surfaces [179]. The simple model in Eq. 3.34 breaks down if θ exceeds $\approx 60\,^\circ$ due to the increasing occurrence of elastic scattering events.

As shown for a selection of materials from Ref. [177] in Fig. 3.7 (b), for kinetic energies above $\approx$ 30 eV the IMFP is experimentally found to be similar for most materials and its energy dependence therefore often empirically described as *universal curve* [177]. A minimum IMFP of $\approx$ 5 Å is observed for kinetic energies of $\approx$ 20 eV and, accordingly, (angle-resolved) PES using ultraviolet light predominantly probes the surface rather than the bulk properties of the investigated material. Therefore, a possible way to investigate the bulk electronic structure is to use light in the soft or hard x-ray regime for ARPES experiments. Considerable efforts have been made to reliably calculate material-specific inelastic mean free paths to accurately describe the information depth of photoemission and related electron spectroscopy techniques. In this thesis, the TPP2 relation developed by Tanuma *et al.* is used to determine λ_{IMFP} [180]:

$$\lambda_{\mathrm{IMFP}} = \frac{E_{\mathrm{kin}}}{E_P^2 \left[\beta \ln(\gamma E_{\mathrm{kin}}) - \frac{C}{E_{\mathrm{kin}}} + \frac{D}{E_{\mathrm{kin}}^2}\right]} \tag{3.35}$$

The TPP2 relation yields the electron inelastic mean free path λ_{IMFP} in Å and requires several element-specific parameters as input: the free electron plasmon energy E_P and the empirical parameters β, γ, C, D which incorporate the density, gap energy, atomic weight and number of valence electrons per atom [180]. As shown in Fig. 3.7 (b) the IMFP of $SrIrO_3$ and $SrTiO_3$ are slightly different, mainly due to the different number of valence electrons as given by their d^0/d^5 electron configurations.

After experiencing one or more inelastic scattering events the photoelectrons may leave the sample with a reduced kinetic energy and superimpose the intrinsic photoelectron spectrum as a background signal, which needs to be subtracted for the successful evaluation of core-level line shapes with respect to many-body interactions. Mathematically, the measured spectrum can be described as a convolution of the intrinsic spectrum with a electron energy

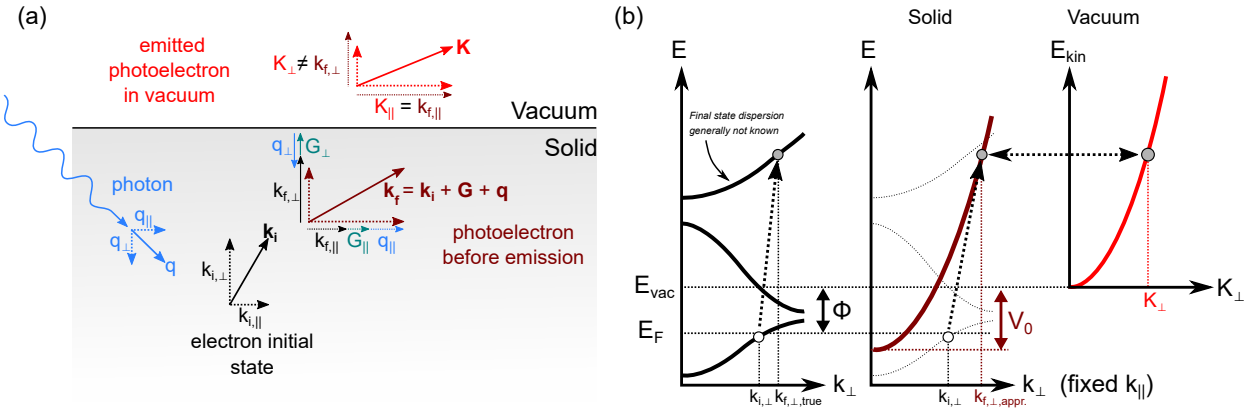

Figure 3.8: (a) Schematic representation of the momentum conservation at each step in the photoemission process. Within the solid, the photoexcited electron has the momentum $\mathbf{k_f} = \mathbf{k_i}+\mathbf{G}+\mathbf{q}$ ($\mathbf{k_i}$: momentum in the initial state, $\mathbf{G}$: reciprocal lattice vector, $\mathbf{q}$: photon momentum). Upon transmission into the vacuum, only the momentum parallel to the surface is conserved ($K_{||} = k_{f,||}$), since the translational symmetry is broken at the surface ($K_\perp \neq k_{f,\perp}$). (b) In the nearly-free-electron approximation, the unknown final-state dispersion is approximated as parabola with the bottom at an energy V_0 (= inner potential) beneath the vacuum level E_{vac}. Thereby, the measured quantity $K_\perp$ can be related to the initial state wave vector $k_{i,\perp}$.

loss spectrum, which may either be determined experimentally [181] (including all discrete structures due to excitations of phonons or plasmons) or approximated as steplike function [182]. The latter is called *Shirley background* and assumes a direct proportionality between the inelastic background signal at any energy E and the total intensity of the intrinsic spectrum at all higher kinetic energies:

$$I_{\mathrm{cor}}^{n+1}(E) = I_{\mathrm{exp}}(E) - I_{\mathrm{exp}}(E_1)\left(\frac{\int_E^{E_2} I_{\mathrm{cor}}^n(E')dE'}{\int_{E_1}^{E_2} I_{\mathrm{cor}}^n(E')dE'}\right) \tag{3.36}$$

Here, I_{exp} is the measured spectrum, I_{cor}^n the corrected spectrum after n iterations ($I_{\mathrm{cor}}^0 = I_{\mathrm{exp}}$) and E_1 (E_2) is the kinetic energy to (from) which the background is calculated ($E_1 < E_2$). In practice $n = 5$ iterations suffice to appropriately approximate the intrinsic spectrum for most applications.

Emission of the electron into the vacuum

In the final step of the photoemission process the electron is transmitted from the bulk into the vacuum and, as implicitly included in Eq. 3.12, the photoelectrons have to overcome the work function $\Phi = E_{\mathrm{vac}} - E_F$ to leave the sample. At the same time, the discontinuity of the electrostatic potential breaks the translational symmetry perpendicular to the surface and affects the photoelectron momentum conservation, thereby complicating the interpretation of angle-resolved PES measurements.

Experimentally, the photoelectron wave vector in vacuum $\mathbf{K}$ is obtained from ARPES

measurements via Eq. 3.11. Within the solid, the excited photoelectron has the momentum

$$\mathbf{k_f} = \mathbf{k_i} + \mathbf{G} + \mathbf{q}, \tag{3.37}$$

where $\mathbf{k_i}$ is the photoelectron momentum in the initial state, $\mathbf{G}$ is a reciprocal lattice vector and $\mathbf{q}$ is the incident photon momentum, which is often neglected in low-energy ARPES since it is much smaller than $\mathbf{k_i}$ or $\mathbf{k_f}$. Since the translational invariance is only broken perpendicular to the surface, momentum conservation holds for the electron momentum parallel to the surface:

$$k_{f,||} = K_{||} = \frac{\sqrt{2mE_{\text{kin}}}}{\hbar}\sin\theta \tag{3.38}$$

$$= k_{i,||} + G_{||} + q_{||} \tag{3.39}$$

In contrast, the determination of the perpendicular momentum is more complex as it changes upon transmission through the sample surface. Since the final state dispersion $E_f(k_{f,\perp})$ is not known in general, there is no direct relation between the final state momentum in the solid $k_{f,\perp}$ and the measured quantity $K_\perp$. The *free-electron final-state model* circumvents this problem by assuming a free-electron-like parabolic final state dispersion with its vertex at an energy V_0 below the vacuum level (cf. Fig. 3.8 (b)):

$$E_f(k_{f,\perp}) \equiv \frac{\hbar^2}{2m_e}k_{f,\perp}^2 - V_0 \tag{3.40}$$

Then one obtains

$$k_{f,\perp,\text{approx.}} = \sqrt{K_\perp^2 - \frac{2m_e}{\hbar^2}V_0} \quad \text{and hence} \tag{3.41}$$

$$k_{i,\perp,\text{approx.}} = \frac{1}{\hbar}\sqrt{2m_e\left(E_{\text{kin}}\cos^2\theta - V_0\right)} - q_\perp - G_\perp. \tag{3.42}$$

For a given kinetic energy ARPES therefore maps a spherical rather than a planar cut through the reciprocal space. By changing the incident photon energy the out-of-plane component of the initial wave vector is modified, thus allowing for the complete mapping of the three-dimensional reciprocal space. The energy V_0 is often referred to as *inner potential* since it can be interpreted as the depth of a potential well at the surface. It is a phenomenological parameter, which is typically adjusted to match the periodicity of the electronic dispersion in k_z- (i.e, $k_\perp$-)direction. The free electron final-state model works particularly well for PES using photon energies beyond the VUV range, since the effect of the crystal potential on the excited photoelectron becomes smaller with increasing kinetic energy.

3.4 X-ray Absorption Spectroscopy

X-ray absorption spectroscopy (XAS) measures the x-ray absorption cross section as function of the photon energy at and above the excitation threshold from a core level into the unoccupied states above the chemical potential. Depending on the energy of the excited electron, XAS is typically distinguished into the regimes of extended x-ray absorption fine structure (EXAFS, $200 - 1000\,\mathrm{eV}$ above threshold) and x-ray absorption near-edge structure (XANES, $0 - 100\,\mathrm{eV}$ above threshold). The former is employed to investigate the type, number and distance of neighboring atoms of a certain elemental species in a sample by analysis of interference patterns resulting from backscattering of high-energy excited photoelectrons [183]. The latter yields element-specific information about the unoccupied states and hence the chemical environment within a sample. In solid-state physics, the absorption threshold signal is often used to investigate the electronic and magnetic structures of the low-lying valence states near the chemical potential by comparison of the x-ray absorption signals of linearly or circularly polarized light. In the following, the basic principles of XAS are briefly introduced based on Ref. [184–188] and with focus on the applications within this thesis.

3.4.1 Instrumentation and basic principle

X-ray absorption spectroscopy became increasingly popular with the advent of synchrotron radiation sources which provide an intense, continuous spectrum of polarized light. Today, XAS is almost exclusively performed at specialized beamlines with insertion devices and x-ray optics dedicated to a certain spectral range, depending on the absorption threshold of interest. Typically, the sample is kept in a UHV-compatible liquid-He cryostat equipped with a strong electromagnet for the investigation of magnetic material properties.

The most obvious method to acquire the x-ray absorption spectrum of a material involves the measurement of the x-ray intensity before and after transmission through a sample as function of photon energy. However, this measurement mode imposes serious technological challenges, since the small attenuation length of light in the soft x-ray regime requires a sample thickness of only $\approx 100\,\mathrm{nm}$, which particularly complicates the investigation of epitaxial heterostructures. An alternative to the transmission mode is provided by measuring the various decay products of the core hole created in the absorption process, which is filled by an electron in a higher energy state after a life time on the order of $10^{-15}\,\mathrm{s}$. The two dominant decay processes involve the emission of a fluorescent photon or an Auger electron. The probability of a core hole being filled by a radiative or non-radiative process depends strongly on the core-hole shell and the atomic number Z.

In the Auger decay process, the filling of an inner core hole by an electron from a higher shell is accompanied by the emission of a third electron. The kinetic energy of an Auger electron and hence its inelastic mean free path (IMFP) is independent of the incident photon energy as it corresponds to the difference between the energy of the initial electronic transition and its ionization energy. Therefore, the number of emitted Auger electrons is proportional to the number of core holes created within a layer of thickness $\lambda_{\mathrm{IMFP}} \approx 20\,\mathrm{Å}$

below the surface [185] and hence a very surface-sensitive measure of the x-ray absorption cross section. Additionally, each Auger electron leaves behind another core hole and therefore – besides the emission of fluorescence photons – gives rise to a cascade of secondary Auger transitions, which can be collectively measured as drain current in the total electron yield (TEY) measurement mode. While the ease of detection and the large signal make TEY the most widely used method, the specific processes leading to the emission of electrons are involved and highly material-dependent. The probing depth of TEY is typically estimated to be slightly larger than that of Auger electron yield [185].

In the fluorescence decay process, a valence or shallow core electron fills the deep core hole and thereby emits photons with an energy corresponding to the energy difference. Since the created photon has a mean free path of the same order of magnitude as the incoming x-ray photons, fluorescence yield (FY) is not surface sensitive and probes a volume exceeding 100 nm below the surface [185]. However, FY is not an exact measure of the absorption cross section, since self-absorption effects can distort the spectra if the fluorescent photons are reabsorbed by the material upon propagation to the surface. Furthermore, the interpretation of FY spectra may be severely complicated by saturation effects depending on the concentration of the absorbing elemental species [189].

3.4.2 Theoretical background

Near-edge x-ray absorption is a first-order optical process, where a core electron is excited into a state just above the chemical potential, rather than into the high-energy continuum states. In first-order perturbation theory the transition rate between an initial $|i\rangle$ and final $|f\rangle$ N-electron state is given by Fermi's golden rule

$$w_{i\to f} = \frac{2\pi}{\hbar} \left|\langle f| H_{\text{int}} |i\rangle\right|^2 \cdot \delta\left(E_f - E_i - h\nu\right) \text{ (cf. Eq. 3.16).} \tag{3.43}$$

In a single-particle picture, in particular, when the influence of the core hole can be neglected, the matrix element transforms into a single-particle matrix element and, since the core level shows no dispersion, the δ-function in Eq. 3.43 describes the density of unoccupied states [190]. After expanding the initial and final state into spherical harmonics the matrix element can be decomposed into Clebsch-Gordon coefficients and a reduced matrix element, depending only on the angular momentum and principal quantum numbers of the initial and final states. These determine the strict dipole selection rules, which give XAS its symmetry-selective properties. Hence, if the interaction between the core hole and the excited electrons is negligible, the absorption cross section

$$\mu(h\nu) \propto \sum_f w_{i\to f} \tag{3.44}$$

is a measure of the symmetry-projected partial density of unoccupied states [190].

To a good approximation, this is the case for x-ray absorption at the O K-edge ($1s \to 2p$) since the intra-atomic Coulomb interaction between a hole in the $1s$ and an electron in the $2p$ orbital is negligibly small [184]. Hence, in transition metal oxides no multiplet-splitting or

charge-transfer excitations are observed in the O K-edge XAS and, typically, the absorption spectrum can be well reproduced by the oxygen $2p$-projected DOS calculated by density functional theory (DFT). Furthermore, O K edge XAS is a useful tool to quantify the metal-ligand covalency, since the electronic configuration of an O^{2-} ion in an ionic picture would be $1s^2 2s^2 2p^6$ and hence the absorption into the fully occupied $2p$ shell would be forbidden without hybridization with the neighboring cations.

In contrast, the interaction between a transition metal $2p$ core hole and the transition metal $3d$ valence electrons of transition metal oxides is significant and has to be taken into account for a correct description of the XAS line shape. Similar to optical interband excitations the final state of $L_{2,3}$-edge absorption in transition metal oxides is a tightly bound exciton, which cannot be described in the one-electron picture [188]. In this case, the N-electron initial ground state $|i\rangle = |2p^6 3d^n\rangle$ in Eq. 3.43 describes the valence band and the filled core shell for which spin-orbit coupling is not important. In contrast, the N-electron final state $|f\rangle = |2p^5 3d^{n+1}\rangle$ describes the exciton, which has nothing to do with the band structure, and the partially filled core shell, where spin-orbit coupling is important. In contrast to XPS, the atomic multiplet splitting dominates over the charge transfer effect, since the exciton is strongly localized to a single site (and partially to the surrounding oxygen cluster) [185].

Polarization dependence

The interaction of an electromagnetic wave with matter is not entirely determined by its frequency but can also crucially depend on the polarization of the electric field. For dipole transitions the absorption strength for a final state depends upon the symmetry of the initial state and the incident light polarization, which can either interact with the magnetic moments (circularly polarized light) or with the charge distribution (linearly polarized light) of the core and valence states. Therefore, the analysis of the differential x-ray absorption (or: dichroism) of light with opposite linear or circular polarization can yield valuable information about the orbital symmetries and magnetic properties of the system.

X-ray linear dichroism For systems with nonspherical charge distribution the x-ray absorption can depend on the relative orientation of the linear light polarization. While anisotropic charge distributions may also originate from anisotropic chemical bonding or magnetic ordering, the simplest form of x-ray linear dichroism (XLD) is due to a difference in the orbital occupancy, e.g., of the five d levels in transition metal oxides, which can be understood in the one-electron picture.

In general, the transition rate for an optical excitation is proportional to[5]

$$|\langle f|\,\mathbf{A_0}\cdot\mathbf{p}\,|i\rangle|^2 \propto |\langle f|\,\mathbf{A_0}\cdot e\,\mathbf{r}\,|i\rangle|^2 \ , \tag{3.45}$$

where $e\,\mathbf{r}$ is the electrical dipole operator. Accordingly, the transition rate is determined by the matrix element of the electrical dipole vector's component which lies parallel to the light

[5]Using the identity $\langle f|\,\mathbf{p}\,|i\rangle = -im\frac{E_f - E_i}{\hbar}\langle f|\,\mathbf{r}\,|i\rangle$.

	$s \rightarrow p_j$	$p_j \rightarrow d_j$
I_x	$\frac{h_x}{h}$	$\frac{1}{h}(\frac{1}{2}h_{xy} + \frac{1}{2}h_{xz} + \frac{1}{6}h_{z^2} + \frac{1}{2}h_{x^2-y^2})$
I_y	$\frac{h_y}{h}$	$\frac{1}{h}(\frac{1}{2}h_{xy} + \frac{1}{2}h_{yz} + \frac{1}{6}h_{z^2} + \frac{1}{2}h_{x^2-y^2})$
I_z	$\frac{h_z}{h}$	$\frac{1}{h}(\frac{1}{2}h_{xz} + \frac{1}{2}h_{yz} + \frac{2}{3}h_{z^2})$

Table 3.1: X-ray absorption intensity $I_{x,y,z}$ using linearly polarized light along the x-,y- or z-direction as function of the number of holes h_j in subshell j [191].

polarization vector $\mathbf{A_0}$. Therefore, depending on the symmetry of the involved subshells with respect to the linear polarization vector, the dipole excitations $s \rightarrow p_h$, $p_k \rightarrow d_l$,... ($\Delta l = \pm 1$) may or may not be allowed. Since an electron can only be excited into unoccupied states the absorption intensity is furthermore proportional to the number of holes h_j in the final state. The selections rules for the $s \rightarrow p_h$ and $p_k \rightarrow d_l$ transitions are summarized in Tab. 3.1.

Beyond that, magnetic ordering may in principle also lead to a linear dichroism although the dipole operator does not act on the spin space. However, $2p-3d$ electron correlations are needed to describe the magnetic linear dichroism, since the exchange interaction in the excitonic final state splits the multiplet terms depending on their spin configuration.

X-ray circular magnetic dichroism When using photons with a defined helicity, i.e., circular polarization, the x-ray absorption process becomes sensitive to spin degrees of freedom. The difference in absorption between the (anti-)parallel orientations of the net magnetic moment and the photon helicity is called x-ray magnetic circular dichroism (XMCD). The integrated magnetic dichroic signal is a measure of the magnetization, which may be induced by an external magnetic field in a para- or diamagnetic system or originate from remanent ferro- or ferrimagnetic order. XMCD is therefore commonly used to investigate the magnetic properties of systems with more than one magnetically active element to obtain the element-specific magnetization or systems with dilute magnetic moments, that cannot be investigated with a global probe.

Typically, XMCD is performed at the transition metal $L_{2,3}$-absorption edge ($2p \rightarrow 3d$), where significant changes of the white-line intensities are observed as function of sample magnetization and/or circular polarization. In the simple one-electron picture, the XMCD effect can be understood by a two-step model [192, 193]. In the first step, a photoelectron is excited by circularly polarized light and effectively spin-polarized by the Fano effect, since the core-level spin-orbit coupling allows a (partial) transfer of the circularly polarized photon's angular momentum to the spin of the electron [194, 195]. As the number of unoccupied states in a magnetic system is spin-dependent, in the second step, the minority- and majority-spin DOS acts as spin filter, resulting in a spin-dependent absorption cross section. Although this model splits the absorption process in an artificial way, a rigorous theoretical approach starting from the general expression for the x-ray absorption process in Eq. 3.43 similarly leads to sum rules that link the integrated XMCD spectra to the expectation val-

ues of the spin and angular momentum [196–198]. These sum rules are commonly adopted for the analysis of the microscopic magnetic structure, since the contributions of spin and angular momentum to the total magnetic moment can be disentangled by comparison of the integrated XMCD signals at the L_2- and L_3-edge.

Chapter 4

Synthesis of phase-pure epitaxial $SrIrO_3$ films – perils and pitfalls

Within the last decades the heavy $5d$ transition metal oxides moved into the focus of research after it was realized that the interplay between strong spin-orbit coupling and electronic correlations may promise an even richer electronic behavior than found in their $3d$ counterparts [8]. The observation of a metal-insulator transition in the Ruddlesden-Popper series $Sr_{n+1}Ir_nO_{3n+1}$ and the phenomenological similarity of Sr_2IrO_4 (n = 1) to the high-T_C superconductor parent material La_2CuO_4 have raised particular interest in the layered-perovskite strontium iridates. Due to the availability of macroscopic single crystals the electronic structures of the mono- and bilayer compounds Sr_2IrO_4 and $Sr_3Ir_2O_7$ have been thoroughly investigated. In contrast, the three-dimensional $SrIrO_3$ adopts a thermodynamically stable hexagonal lattice structure at ambient conditions, which can be transformed into the metastable perovskite phase only upon application of high pressure and temperature, thereby impeding single crystal growth. As an alternative approach, perovskite $SrIrO_3$ thin films can be stabilized epitaxially by effectively substituting the external pressure by epitaxial strain to the underlying substrate.

Pulsed laser deposition became popular due to its convenience for the growth of multicomponent materials and has been developed into a versatile and common epitaxy technique. During the course of this thesis, pulsed laser deposition of high-quality, phase-pure epitaxial $SrIrO_3$ films on TiO_2-terminated (001)-oriented $SrTiO_3$ was established to systematically investigate the evolution of the electronic structure as function of film thickness. The following chapter identifies the optimum growth conditions and potential pitfalls to be circumvented in the endeavor to obtain layer-by-layer growth of stoichiometric $SrIrO_3$. The resultant film structure is characterized with respect to distortions from the idealized perovskite structure, i.e., octahedral rotations and tetragonal elongation of the unit cell, and the chemical termination of the film surface.

4.1 Surface termination-dependent nucleation of $SrIrO_3$ on $SrTiO_3$ (001) substrates

For the heteroepitaxial growth of $SrIrO_3$ thin films (001)-oriented $SrTiO_3$ substrates were chemically treated and heated under oxygen atmosphere to obtain a homogenous chemical TiO_2 surface termination as described in Sec. 2.3.2. However, annealing under oxidizing

conditions and excessive temperature may lead to SrO surface segregation and nucleation at vicinal step edges and their neighboring strained regions [199–201]. In such cases, patches with self-organized SrO termination along substrate step edges may coexist with atomically flat TiO_2 terraces.

Figure 4.1 shows an amplitude-modulation atomic force microscopy (AFM) image of a $SrTiO_3$ substrate that displays patches of SrO termination at kinked step edges. An exemplary line profile across a patch (blue) reveals a step size of 3.9 Å, corresponding to one unit cell of $SrTiO_3$, between neighboring terraces and two intermediate steps of 2.7 Å and 1.2 Å. The uneven step size is caused by the chemical sensitivity of amplitude-modulation AFM, which also manifests itself in the clear phase-shift signal contrast of the SrO patch (inset) [202, 203]. After deposition of $SrIrO_3$ the film surface displays deep trenches with lateral dimensions similar to the SrO patches shown in Fig. 4.1 (b). Cross-sectional scanning transmission electron microscopy (STEM) (Fig. 4.1 (c)) evidences the formation of several layers of $SrIrO_3$ at the bottom of the trench but an absence of the like at the very substrate step edge (white arrow).

Similar findings have been reported for the heteroepitaxial growth of $SrRuO_3$ on mixed-terminated $SrTiO_3$ (001) surfaces and explained in terms of different adatom sticking coefficients and consequent termination-dependent nucleation [204, 205]. While the self-assembly of the chemical termination may therefore also offer opportunities for the fabrication of oxide nanostructures [204], the use of high-quality uniformly terminated $SrTiO_3$ substrates is imperative for the synthesis of homogenous epitaxial $SrIrO_3$ films.

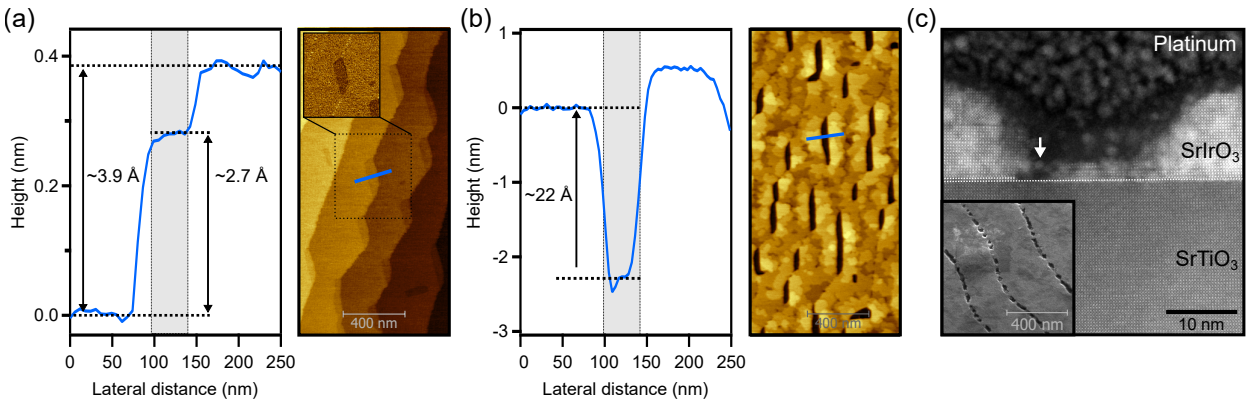

Figure 4.1: (a) AFM image of a $SrTiO_3$ substrate with mixed termination at step edges. Inset: Phase shift signal of a SrO patch. The line profile along the blue line shows a step size of one $SrTiO_3$ unit cell between neighboring terraces and two intermediate steps. (b) AFM image after deposition of a $SrIrO_3$ film displays deep trenches with lateral dimensions similar to the SrO patches. (c) STEM cross-sectional image of a trench. Inset: Scanning electron microscopy image of the film surface.

4.2 Iridium deficiency and Ruddlesden-Popper-like lattice defects

One of the key challenges of pulsed laser deposition of ternary oxides is to obtain the correct cation stoichiometry within the film. Even for nonvolatile compounds stoichiometric transfer of the different atomic species to the substrate is not trivially achieved and may critically depend upon their respective atomic masses and/or details of the ablation process such as laser fluency, repetition rate and scanned ablation area [206–210]. Another key challenge is to control the oxidation state of the transition metal cation, which crucially depends on the provided background gas (e.g., O_2, O_3, Ar, NO_2, ...) and the partial pressure thereof [211–213]. These two challenges may become intertwined if one or more constituent element forms a gaseous compound upon oxidation, e.g., leading to Ru-loss during the growth of $SrRuO_3$ [214–216]. Similarly, the noble character of iridium necessitates a rather high oxygen chemical potential for the growth of $SrIrO_3$, whereas excessively oxidizing conditions promote the formation of volatile IrO_3 [217, 218], potentially resulting in an iridium deficiency within the films.

4.2.1 Tuning the film stoichiometry

Figure 4.2 shows out-of-plane x-ray diffraction (XRD) patterns of PLD-grown thin films using a $SrIrO_3$ target in comparison to the theoretical diffraction peak positions of bulk $SrIrO_3$, $Sr_3Ir_2O_7$ and Sr_2IrO_4, i.e., the $n = \infty$, 2 and 1 members of the Ruddlesden-Popper family of layered perovskites $Sr_{n+1}Ir_nO_{3n+1}$ (cf. Sec. 2.3.1). The films were grown at (a) constant oxygen partial pressure p_{O_2} and variable temperature T as well as (b) constant T and variable p_{O_2}. At moderate temperatures ($T = 600\,°C$ and $700\,°C$) the orthorhombic (pseudo-cubic) 3C perovskite phase is epitaxially stabilized, rather than the thermodynamically stable monoclinic distortion of the hexagonal $BaTiO_3$ structure adopted by $SrIrO_3$ under ambient conditions [17, 219]. At elevated temperatures ($T \approx 800\,°C$) a crossover from the pseudo-cubic perovskite phase to $Sr_3Ir_2O_7$ is observed. At $T = 900\,°C$ the diffraction pattern is dominated by Sr_2IrO_4 diffraction peaks ((0,0,4), (0,0,8), (0,0,12) and (0,0,16)) and shows some residual $Sr_3Ir_2O_7$ signal at the (0,0,4) and (0,0,10) diffraction peaks. A similar trend is observed upon increasing the oxygen partial pressure, albeit not as pronounced as for increasing temperature. In a systematic investigation of the formation of different Ruddlesden-Popper iridates from a single $SrIrO_3$ target Nishio *et al.* found that the growth conditions resulting in different Ruddlesden-Popper phases can be mapped directly onto the temperature-oxygen partial pressure phase diagram expected from thermodynamic equilibrium despite the inherent non-equilibrium nature of PLD [220].

4.2.2 Ruddlesden-Popper-like lattice faults in $SrIrO_3$ and $Sr_3Ir_2O_7$ thin films

It is established that Ruddlesden-Popper-type iridates can be selectively fabricated by PLD from a $SrIrO_3$ target by adjusting the cation stoichiometry via control of the substrate tem-

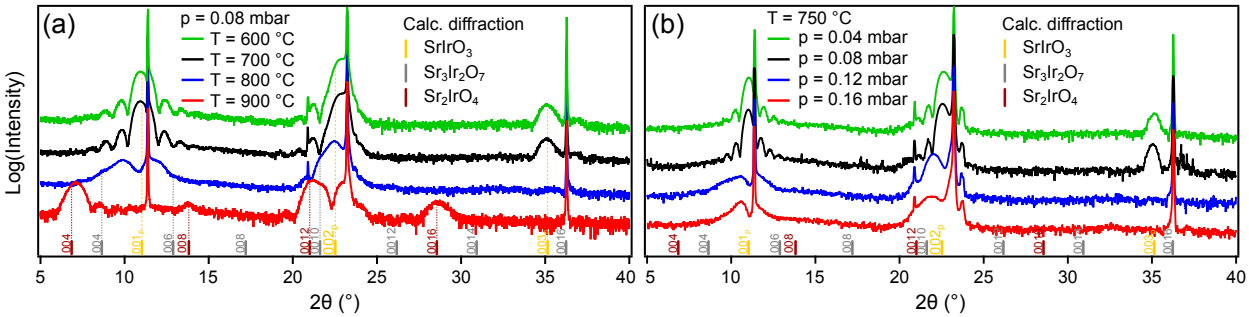

Figure 4.2: Out-of-plane XRD patterns of epitaxial films grown from a $SrIrO_3$ target in comparison to the theoretical diffraction peak positions of $SrIrO_3$, $Sr_3Ir_2O_7$ and Sr_2IrO_4. Upon increasing temperature and oxygen partial pressure the films become iridium-deficient.

perature and oxygen pressure [220]. Figure 4.3 (a) shows the XRD pattern of an exemplary strontium iridate film deposited onto a $SrTiO_3$ substrate held at $T = 820\,°C$. In addition to the substrate diffraction peaks (denoted by a subscript s), the film pattern exhibits an excellent agreement to the calculated diffraction spots of bulk $Sr_3Ir_2O_7$, which evidences the presence of a long-range ordered $Sr_3Ir_2O_7$ phase. Similarly, the selected-area electron diffraction (SAED) pattern in Fig. 4.3 (b) exhibits a superposition of a $Sr_3Ir_2O_7$ (highlighted red) and a cubic diffraction pattern from the $SrTiO_3$ substrate (highlighted blue), as seen by comparison to the theoretically expected patterns shown in Fig. 4.3 (c) and (d). A closer investigation of the film microstructure by HAADF-STEM imaging confirms the excellent match to the $Sr_3Ir_2O_7$ lattice structure in significant parts of the films (Fig. 4.3 (e)). As highlighted in the inset of Fig. 4.3 (e), the neighboring bilayers are laterally shifted with respect to each other such that the adjacent SrO layers adopt a rock salt-like structure. However, the similar thermodynamic stability of the neighboring Ruddlesden-Popper phases [220] is reflected in the abundance of Ruddlesden-Popper-like stacking faults in the form of isolated mono- or trilayers, that are embedded in a $Sr_3Ir_2O_7$ matrix as shown in Fig. 4.3 (f). Furthermore, regions are found with high disorder due to finite $SrIrO_3$-like blocks as exemplarily shown in Fig. 4.3 (g). Accordingly, achieving high crystalline quality and low defect density by PLD growth of Ruddlesden-Popper phases $Sr_{n+1}Ir_nO_{3n+1}$ using a $SrIrO_3$ target remains a challenge.

While on the one hand the volatility of IrO_3 can hence be exploited to selectively grow Ruddlesden-Popper iridates, on the other hand it poses a challenge for the growth of stoichiometric $SrIrO_3$. As shown in Fig. 4.4 (a) a slight cation off-stoichiometry may lead to the formation of highly ordered lattice defects in the form of SrO double layers, which lie in the $\{001\}_p$ lattice planes and span several tens of nanometers (black arrows). Upon closer inspection the lattice on both sides of the defect is found to be laterally shifted in Fig. 4.4 (b). While impossible to resolve by cross-sectional STEM along the $\langle 100\rangle_p$ directions, the SrO double layer most likely adopts a rock salt-like arrangement as found in the Ruddlesden-Popper structure, i.e., a translation of the lattice by half a face diagonal such that the Sr cations lie above the oxygen anions of the adjacent SrO layer. Indeed, the observed distance of 6.5 Å between neighboring Ir layers across the lattice fault corresponds to that observed in Sr_2IrO_4 and $Sr_3Ir_2O_7$ [64, 92]. Similar lattice faults have been reported for Sr-excess $SrTiO_3$

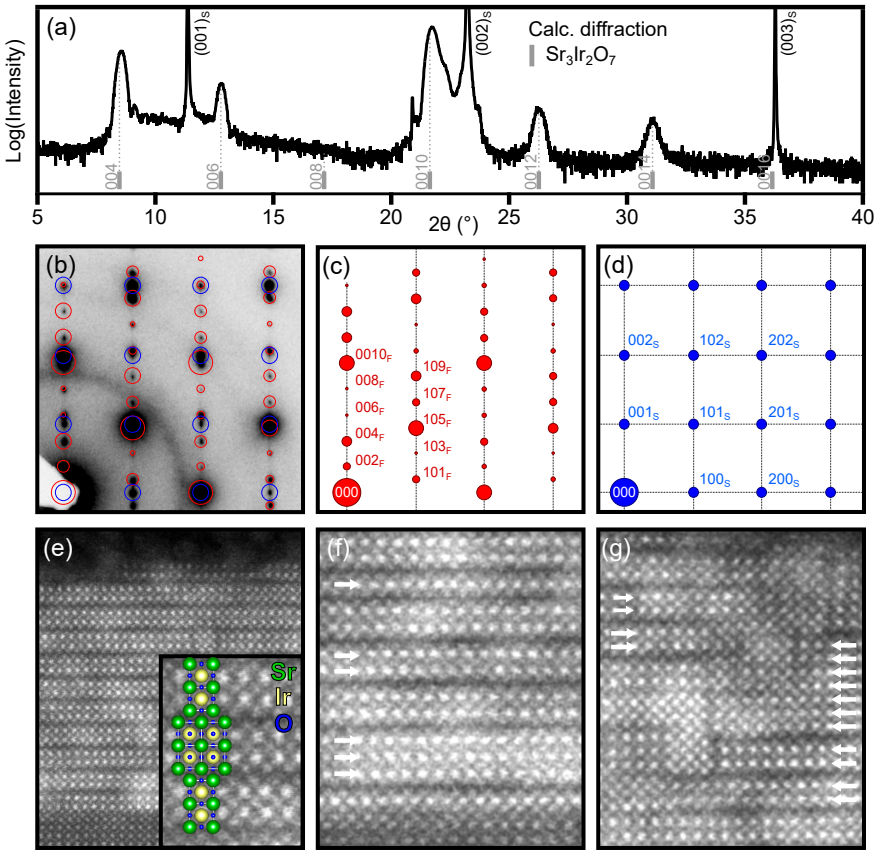

Figure 4.3: Structural characterization of a $Sr_3Ir_2O_7$ film grown from a $SrIrO_3$ target. (a) XRD pattern and theoretical diffraction positions of bulk $Sr_3Ir_2O_7$. (b) - (d) SAED pattern and theoretical diffraction pattern expected from bulk $Sr_3Ir_2O_7$ (red, film) and $SrTiO_3$ (blue, substrate).[a] (e) STEM image of the microstructure showing a coherent $Sr_3Ir_2O_7$ crystal structure. (f) Ruddlesden-Popper-like stacking faults showing a mono- and trilayer embedded in a $Sr_3Ir_2O_7$, i.e., bilayer matrix. (g) Region with high disorder due to $SrIrO_3$-like blocks of several unit cells thickness.

[a] Theoretical diffraction pattern calculated using the freeware JEMS (v. 4.64, www.jems-swiss.ch).

homoepitaxial thin films [221].

The corresponding XRD pattern exhibits no signs of other phases. However, the film inhomogeneity and poor long-range order due to lattice faults is reflected in the absence of Laue fringes as shown exemplarily for the $SrIrO_3$ $(001)_p$ diffraction peak in Fig. 4.4 (c). Indeed, the diffraction peak can be modeled (blue line) by assuming a normal distribution of $SrIrO_3$ blocks with thickness $d = i \cdot d_{hkl}$ which incoherently contribute to the diffraction signal

$$I(q_z) = \sum_{i=4}^{i=32} A_i \cdot I_i(q_z) \quad \text{(cf. Eq. 3.4)} \tag{4.1}$$

$$\text{where} \quad A_i = \frac{1}{\sqrt{2\pi}w} \exp\left[-\left(\frac{(i-i_0)\cdot d_{001}}{4w}\right)^2\right].$$

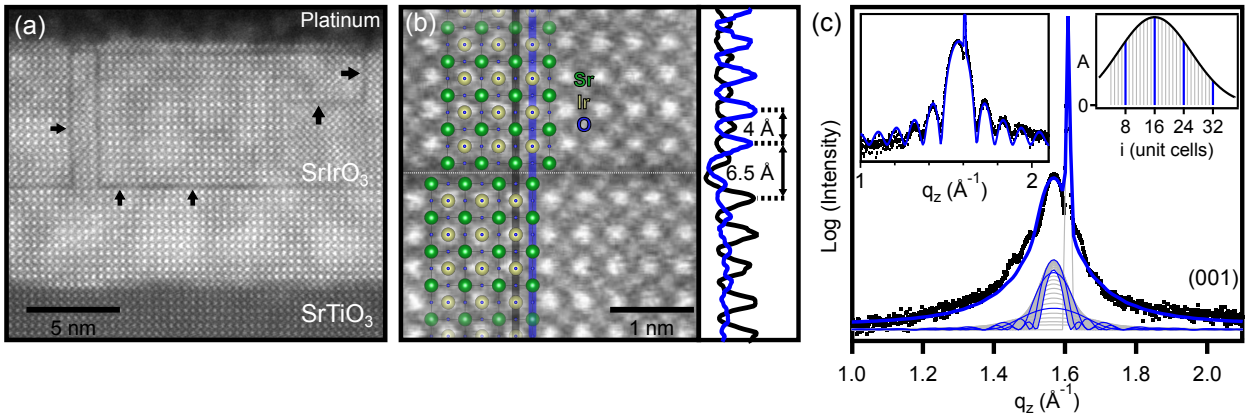

Figure 4.4: $SrIr_{1-\delta}O_3$ film with slight cation off-stoichiometry. (a) Cross-sectional HAADF-STEM image of the film. Highly-ordered lattice faults in form of SrO double-layers along the $\{001\}_p$ lattice planes are marked with black arrows. (b) A closeup of a SrO double layer reveals a lateral shift of the $SrIrO_3$ lattice above and below the lattice defect. Neighboring IrO_2 layers exhibit a distance of 6.5 Å across the lattice fault as seen in the line profiles (averaged over 15 lines equivalent to the blue and black line, respectively). (c) $(001)_p$ XRD diffraction peak. The absence of pronounced Laue fringes is caused by the poor long-range order due to the lattice defects and can be modeled by assuming a normal distribution (right inset) of $SrIrO_3$ blocks with thickness $d = i \cdot a$ contributing incoherently to the signal. In contrast, a stoichiometric $SrIrO_3$ film exhibits pronounced Laue fringes (left inset).

Here, $d_{hkl} = d_{001} = a$ is the lattice parameter, $w = 40\,\text{Å}$ and $i_0 = 16$ (full film: $i = 32$). In contrast, the inset shows the $(001)_p$ diffraction peak of a stoichiometric $SrIrO_3$ film with pronounced Laue fringes, signaling coherent growth throughout the entire film.

4.3 Thin-film growth mode – influence of the target composition

Two-dimensional layer-by-layer film growth is a prerequisite for the precise control of the film thickness and hence the systematic study of dimensionality-induced effects in ultrathin films. RHEED intensity oscillations are considered a footprint of layer-by-layer growth and a damping, i.e., only partial recovery of their amplitude can be interpreted as a general reduction of the surface order and/or a transition from pure layer-by-layer to multilevel growth [222, 223].

The initial $SrIrO_3$ film growth attempts in Würzburg were performed using a commercially purchased target from the supplier SurfaceNet (diameter: 1 inch = 2.54 cm; depth: 3 mm; prize: 4350 €). Despite extensive optimization of growth parameters, a quick decay of the RHEED intensity was consistently observed after only three to four oscillations (cf. Fig. 4.5 (a)). The presence of inhomogeneities, i.e., white grains imbedded in a matrix of black target material, triggered an x-ray powder diffraction analysis (Fig. 4.5 (b)), which revealed its true chemical composition to be a mixture of $Sr(OH)_2$ and IrO_2. For this reason,

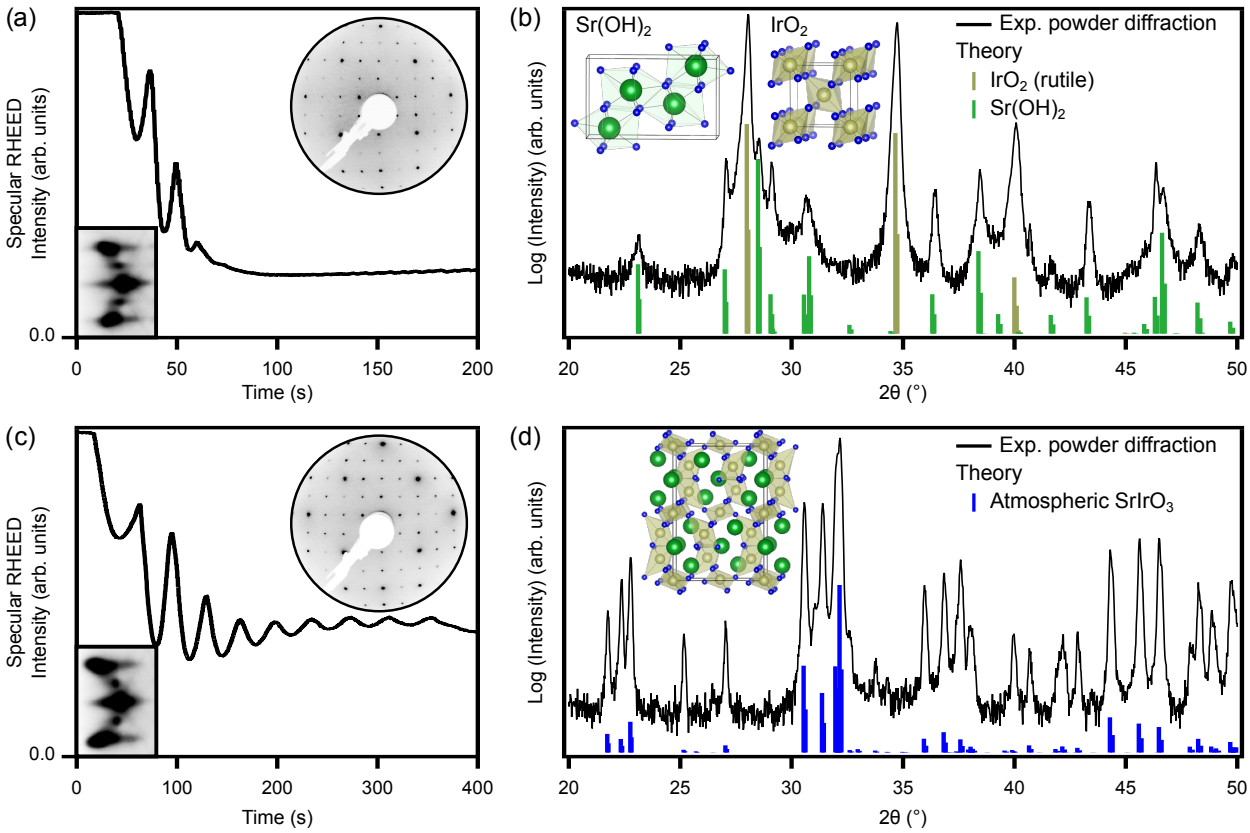

Figure 4.5: (a) Typical RHEED intensity evolution during PLD from the commercially purchased target. Inset: RHEED and LEED images of the film. (b) X-ray powder diffraction reveals the target composition to be a mixture of $Sr(OH)_2$ and IrO_2 instead of $SrIrO_3$. (c) Typical RHEED intensity evolution during PLD from the retreated target shows persistent intensity oscillations indicating prolonged layer-by-layer growth. Inset: RHEED and LEED images of the as-grown film. (d) The retreated target exhibits the low-pressure 6H-$SrIrO_3$ phase in x-ray powder diffraction.

a part of the target material was thoroughly ground, heated and pressed into a new pellet,[6] thereby creating a small target (diameter: 1/2 inch = 1.27 cm) composed of the atmospheric pressure form of $SrIrO_3$ (Fig. 4.5 (d)). Intriguingly, persistent layer-by-layer growth could be readily achieved using the chemically treated target as seen in Fig. 4.5 (c). Therefore, the target microstructure, i.e., its homogeneity and chemical composition are found to be crucial for the desired layer-by-layer growth.

During laser ablation the $SrIrO_3$ target surface stoichiometry and morphology is known to change by formation of Ir-enriched conical structures [224, 225], which align along the incoming laser direction. Therefore, after film growth the target surface has to be refurbished by manually removing the top layer with abrasive paper to ensure the reproducibility of growth results. As the typical target surface area used for ablation during the growth of one film equates to $3 \times 5\,\mathrm{mm}^2$ in Würzburg, a target with diameter of 1/2 inch only

[6] Retreatment of target material and powder diffraction measurements in Fig. 4.5 were performed by Dr. Yingkai Huang, Van der Waals-Zeeman Instituut, University of Amsterdam, The Netherlands.

Material	$SrCO_3$	IrO_2	CO_2	$SrIrO_3$
Molar mass (g/mol)	147.63	224.22	44.01	327.84
Space group	$Pmcn$ [226]	$P4_2/mnm$ [227]	—	$C2/c$ [17]
a (Å)	5.1075 [226]	4.5051 [227]	—	5.6040 [17]
b (Å)	8.4138 [226]	4.5051 [227]	—	9.6180 [17]
c (Å)	6.0269 [226]	3.1586 [227]	—	14.1740 [17]

Table 4.1: Molar mass, space group and lattice spacings of the constituent materials for the $SrIrO_3$ target manufacture.

allows for the growth of four consecutive films before having to expose the target to ambient conditions. While being very time consuming this also enhances the risk of target degradation through formation of $Sr(OH)_2$ due to atmospheric humidity and hence jeopardizes the desired layer-by-layer growth. Therefore, a process was established to manufacture high-quality, mechanically stable and homogeneous $SrIrO_3$ targets with a diameter exceeding 2.5 cm with the goal of enabling the growth of up to 20 consecutive films.

4.3.1 $SrIrO_3$ target manufacture

The atmospheric pressure form of $SrIrO_3$ can be prepared by the equimolar reaction

$$SrCO_3 + IrO_2 \rightarrow SrIrO_3 + CO_2 \quad [17]. \tag{4.2}$$

A reproducible and complete solid-state reaction is achieved by following an operational procedure depicted in Fig. 4.6. (a) Using an analytical balance the starting materials $SrCO_3$ (white powder) and IrO_2 (black powder) are mixed in the correct mass ratio $m_{SrCO_3} : m_{IrO_2} = 1 : 1.519$ (cf. Tab. 4.1) and (b) thoroughly ground using an agate pestle and mortar to (c) receive a homogeneous, fine gray powder. (d) The mixture is filled into a Al_2O_3 crucible and heated in a quartz tube within a tube furnace at $T = 885\,°C$ in 30 l/h pure oxygen flow for 12 hours. Temperatures exceeding 900 °C result in up to 2% mass loss and precipitation of black residue at the inner tube walls outside the furnace in the direction of the oxygen flow due to formation of volatile IrO_3 [217] and subsequent IrO_2 condensation in the cooler area of the tube. (e) After a slow cooldown to room temperature the crucible contains a brittle black disk that is (f) reground into (g) a fine black powder. (h) The resulting powder is checked for glittering white micro-crystallites with a typical size of 20 µm with the bare eye and an optical microscope (Fig. 4.7 (a)). Additionally, as shown in Fig. 4.7 (b), x-ray powder diffraction of a powder sample may be performed to verify the solid state reaction, albeit not sufficiently sensitive to detect small traces of residual starting material. At all times exposure to ambient conditions and hence humidity should be reduced to a minimum due to the hygroscopy of $SrIrO_3$, which is evidenced by an increase of the powder

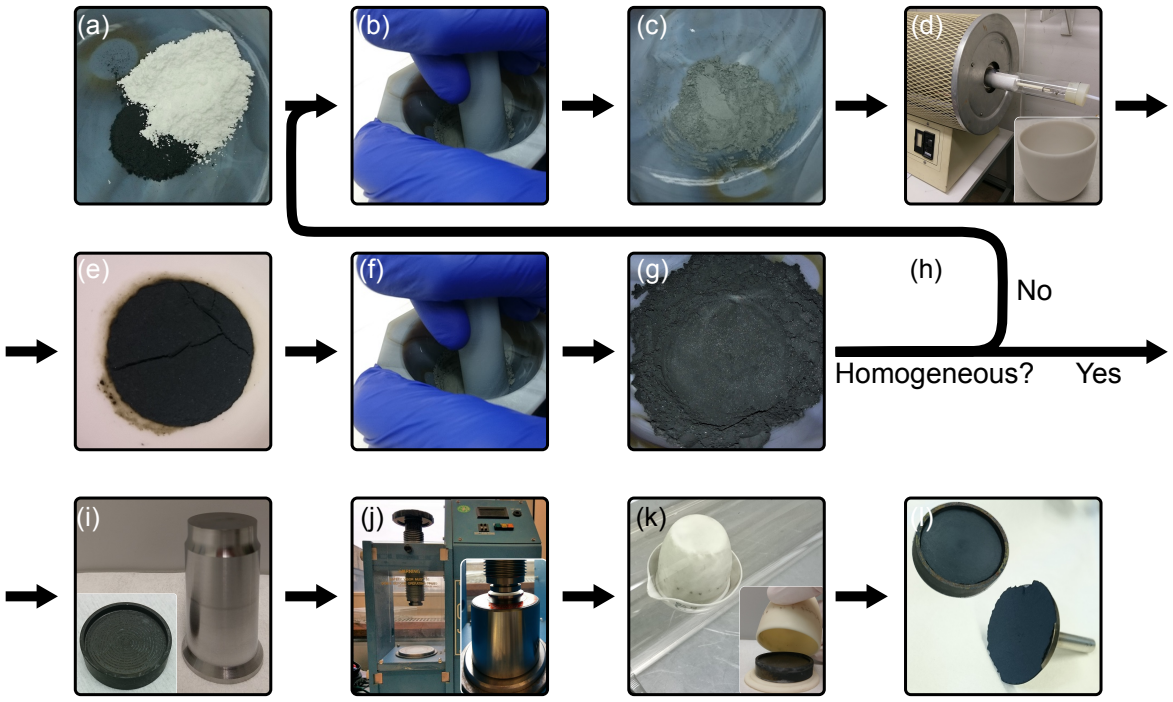

Figure 4.6: Flow chart depicting the target manufacture process. For details see text.

mass by 0.1 % within only 15 min storage in air, as opposed to storage in a dry nitrogen atmosphere. In case the powder inhomogeneity is assessed unacceptable, steps (b) - (g) are repeated thoroughly. (i) Else, the powder is pressed into a pellet using a hardened-steel dry-pressing die and (j) a pressing machine with $20 - 30$ t load. (k) The resulting pellet is sintered within an Al_2O_3 crucible in the tube furnace at $T = 885\,^{\circ}C$ in 30 l/h pure oxygen flow for 12 hours to further increase its density and stability. (l) The resulting target may be attached to a standard target stamp by using carbon tape.

As polycrystalline $SrIrO_3$ is a brittle material large pellets produced in the traditional pressing die design shown in Fig. 4.7 (c), (i) & (ii) may be mechanically unstable and hence pose a risk of dropping into the PLD chamber. Furthermore, a thin target is desirable due to the high prize of ultra-pure IrO_2. For these reasons a special hardened steel pressing die (DIN 9861, FORM C, 275.3.3175.071.2540.006, Jugard+Künstner GmbH, Germany) is used to press the pellet into a manufactured steel shell (Fig. 4.7 (c), (iii) & (iv)) for increased mechanical stability. However, due to the different thermal expansion coefficients of steel and the target material, and a possible shrinking of the target (increase of the $SrIrO_3$ density) during the final sintering step, the pellet does not adhere to the shell after cooldown. Hence, further optimization of the pressing process is necessary in the future. Nonetheless, the manufactured targets were mechanically stable despite a diameter of ≈ 27 mm and a thickness of only ≈ 1.5 mm, allowing for the consecutive growth of up to 25 $SrIrO_3$ films in a coherent layer-by-layer growth mode.

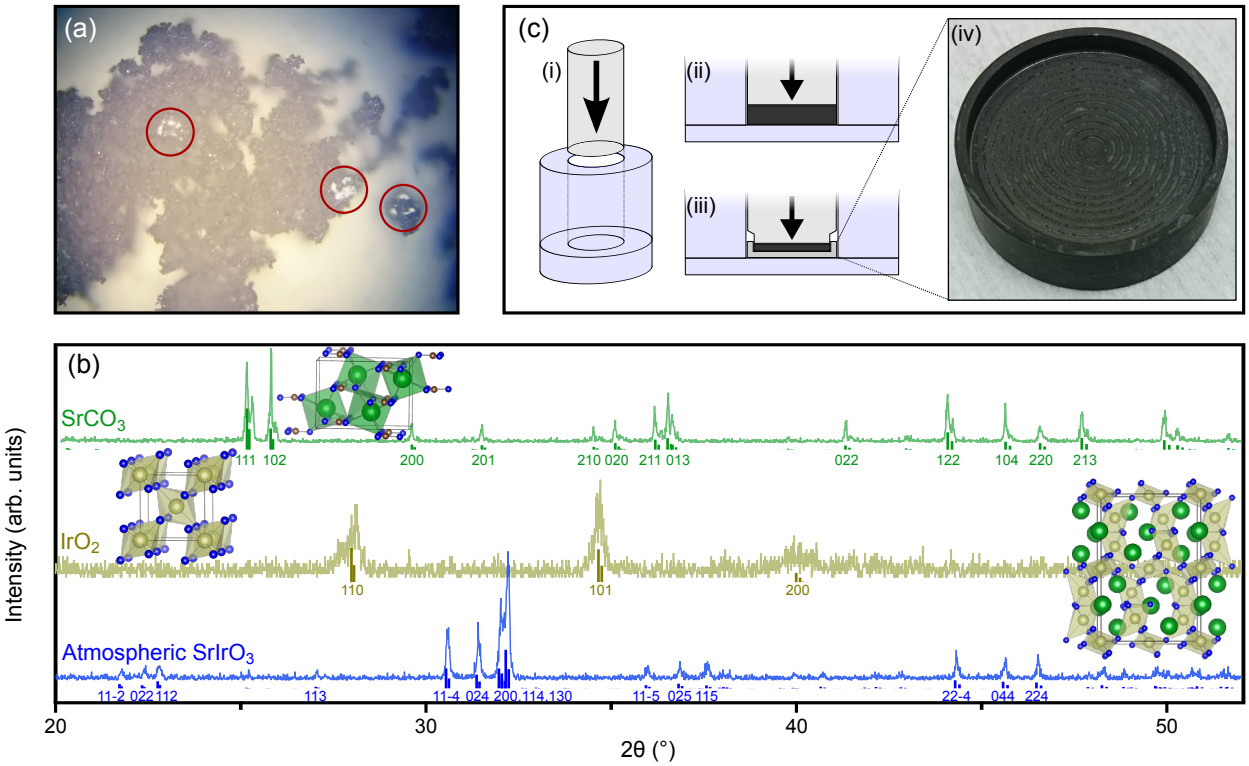

Figure 4.7: (a) Photograph of $SrIrO_3$ powder after one heating step taken through an optical microscope. Micro-crystallites with size of $\approx 20\,\mu m$ are highlighted in red. (b) X-ray powder diffraction patterns of the starting and final materials of the solid state reaction $SrCO_3 + IrO_2 \rightarrow SrIrO_3 + CO_2$. (c) (i) Schematic design of the dry pressing die. (ii) Conventional pressing of a polycrystalline pellet. (iii) Pressing of a pellet into a steel shell for greater stability. (iv) Steel shell with striation for increased adhesion.

4.4 Surface-termination conversion during the initial growth of $SrIrO_3$

Figure 4.8 (a) shows the intensity of the specular RHEED signal during the growth of two equally thick $SrIrO_3$ films on TiO_2-terminated $SrTiO_3$. The use of different laser fluencies results in different growth rates ($\approx 50\%$ variation) despite the comparable substrate temperatures ($700 - 720\,°C$) and oxygen partial pressures ($0.05 - 0.08\,mbar$). Interestingly, the RHEED intensity oscillation period T_n of the n^{th} oscillation does not remain constant throughout the deposition process, as shown in Fig. 4.8 (b) for a selection of films grown at similar conditions. After a significantly prolonged first period a minimal T_n is observed for the second ($n = 2$, blue) or third ($n \approx 3$, black) period, followed by a gradual increase of T_n. The latter effect, i.e., a reduction of the deposition rate, is well-known and caused by the increasing reflectance of the target surface due to changes in the target surface morphology [224, 225, 228]. The prolonged first oscillation period bears a striking resemblance to the initial growth of $SrRuO_3$ on TiO_2-terminated $SrTiO_3$, where it is due to a deviation from the expected preservation of the perovskite stacking order AO-BO_2 in $[001]_p$ direction, which would result in a RuO_2-terminated surface [229]. Specifically, the topmost RuO_2 layer

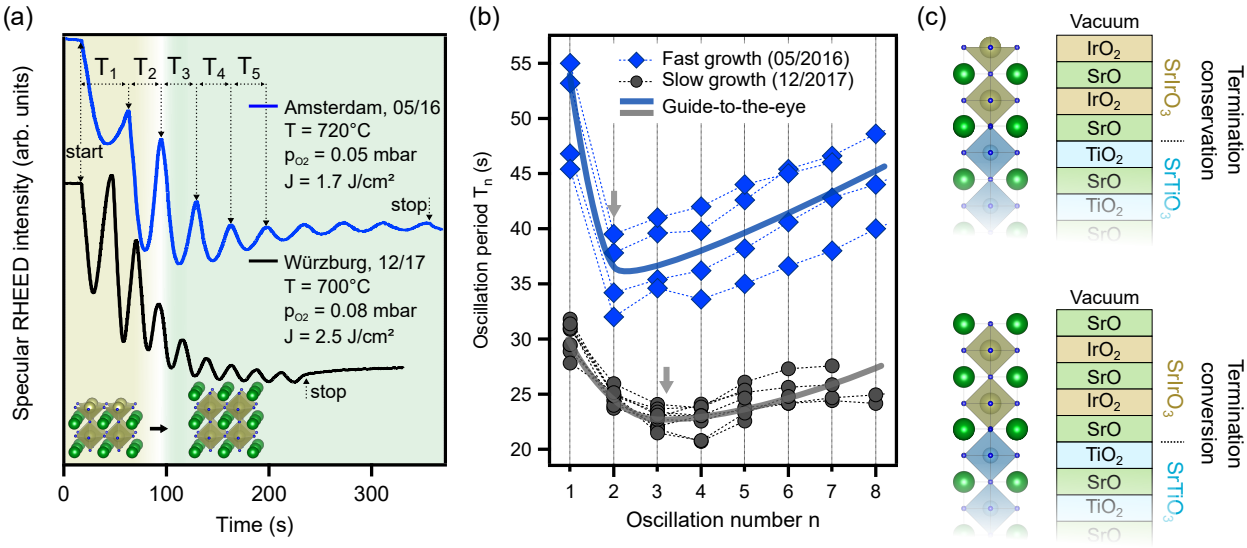

Figure 4.8: (a) Specular RHEED intensity oscillations of two exemplary $SrIrO_3$ films grown on TiO_2-terminated $SrTiO_3$. (b) Oscillation period T_n as function of the oscillation number n for a selection of films. (c) Structural model of a $SrIrO_3/SrTiO_3$ heterostructure with conventional termination conservation (top) and with a conversion to an A-site termination (bottom).

is unstable and forms volatile compounds (e.g., RuO_4 [216, 230]), which evaporate until the terminating layer is completely converted to SrO. As evidenced by a doubling of the first oscillation period, for $SrRuO_3$ the conversion from A- to B-site termination is completed within the first unit cell at 700 °C and distributed over several oscillation periods at lower temperatures [229].

It is proposed that a similar conversion from IrO_2 to SrO termination occurs during the growth of $SrIrO_3$ by over-oxidation of the terminating IrO_2 layer and subsequent evaporation of IrO_3. As shown in Fig. 4.8 (c), the conservation of the perovskite stacking order on a TiO_2-terminated $SrTiO_3$ substrate results in a IrO_2-terminated surface with an incomplete IrO_6 octahedron. The tendency of BO_2-terminated perovskite transition metal oxides to adsorb excess oxygen ions at the apical site is well-documented [231]. It is proposed that the adsorption of an apical oxygen ion leads to the decomposition of the IrO_6 octahedron into gaseous molecular IrO_3 and the remaining SrO-terminated surface. Rather than a doubling of the first oscillation period as in the case of $SrRuO_3$, a prolongation of the first oscillation is observed experimentally during the growth of $SrIrO_3$. However, the minimal oscillation period consistently appears after a similar absolute time span (≈ 100 s) and independent of the growth rate, signaling that the IrO_3 formation and evaporation rate is only sensitive to the thermodynamic conditions to a good approximation.

Since the characteristic signature of the RHEED intensity oscillations, albeit consistent, is only a weak indication for a termination conversion, a 4 uc thin $SrIrO_3$ film was deliberately grown and covered with a protective layer of amorphous carbon to facilitate the direct imaging of the surface by high-angle annular dark field (HAADF)-STEM. Figure 4.9 (a) shows an overview STEM image along the $[010]_p$ lattice direction of the thin $SrIrO_3$ film, which at the first glance appears to be terminated by an IrO_2 layer. Indeed, the iridium

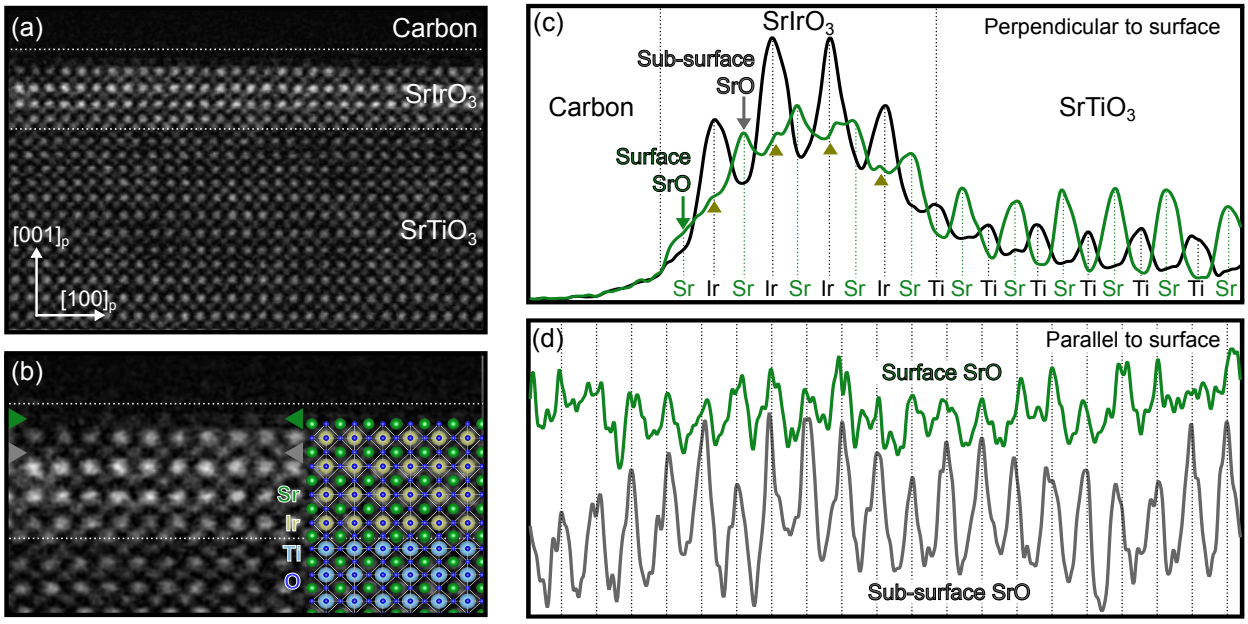

Figure 4.9: (a) HAADF-STEM image of a 4 uc thick $SrIrO_3$ film on $SrTiO_3$, capped with a protective layer of amorphous carbon. (b) Closeup of the $SrIrO_3$ film superimposed with a structural model. A faint SrO layer is discerned at the surface (green arrows). (c) $[001]_p$ line profiles of the IrO_2/TiO_2 (black) and SrO layers (green) (each averaged over 20 layers). In contrast to the IrO_2 profile, the SrO profile exhibits a shoulder at the film surface despite its much smaller Z-contrast. (d) $[100]_p$ line profiles of the surface and subsurface SrO layer (denoted by green and gray arrows in (a), respectively). The surface SrO profile exhibits a clear periodicity, which is in-phase with the subsurface SrO, albeit less intense.

columns (atomic number $Z = 77$) are most pronounced due to the Rutherford-like dependence of the scattering cross section in HAADF-imaging ($\propto Z^n$ with $n \approx 1.7$ [154]), followed by strontium ($Z = 38$) and titanium ($Z = 22$), while carbon and oxygen atoms are not detected. However, a signal is discerned above the topmost IrO_2 layer (cf. Fig. 4.9 (b)), as highlighted by averaged line profiles of the IrO_2/TiO_2 and SrO layers perpendicular to the surface (along $[001]_p$) in Fig. 4.9 (c). The strong scattering from the heavy iridium atoms results in a broadened iridium signal, which overshadows the other atomic species. Nonetheless, the topmost atomic layer apparently stems from a SrO rather than a IrO_2 layer, as is suggested from the comparison of the SrO and IrO_2 line profiles, with the last shoulder towards the surface seen for the former. For clarity, two horizontal line profiles of the subsurface (gray) and surface (green) SrO layer (cf. Fig. 4.9 (b), triangles) along the $[100]_p$ lattice direction are shown in Fig. 4.9 (d). Despite the weak intensity of the surface layer both signals clearly exhibit an in-phase periodicity that substantiates the conjecture of a SrO termination. Whether the weak signal strength of the terminating layer is exclusively caused by the broken translational symmetry at the surface or also due to an only partial, inhomogeneous SrO coverage of the sample remains an open question. Further investigations with atomic-resolution scanning probe techniques (e.g., scanning transmission or atomic force microscopy) may shed light on this in the future.

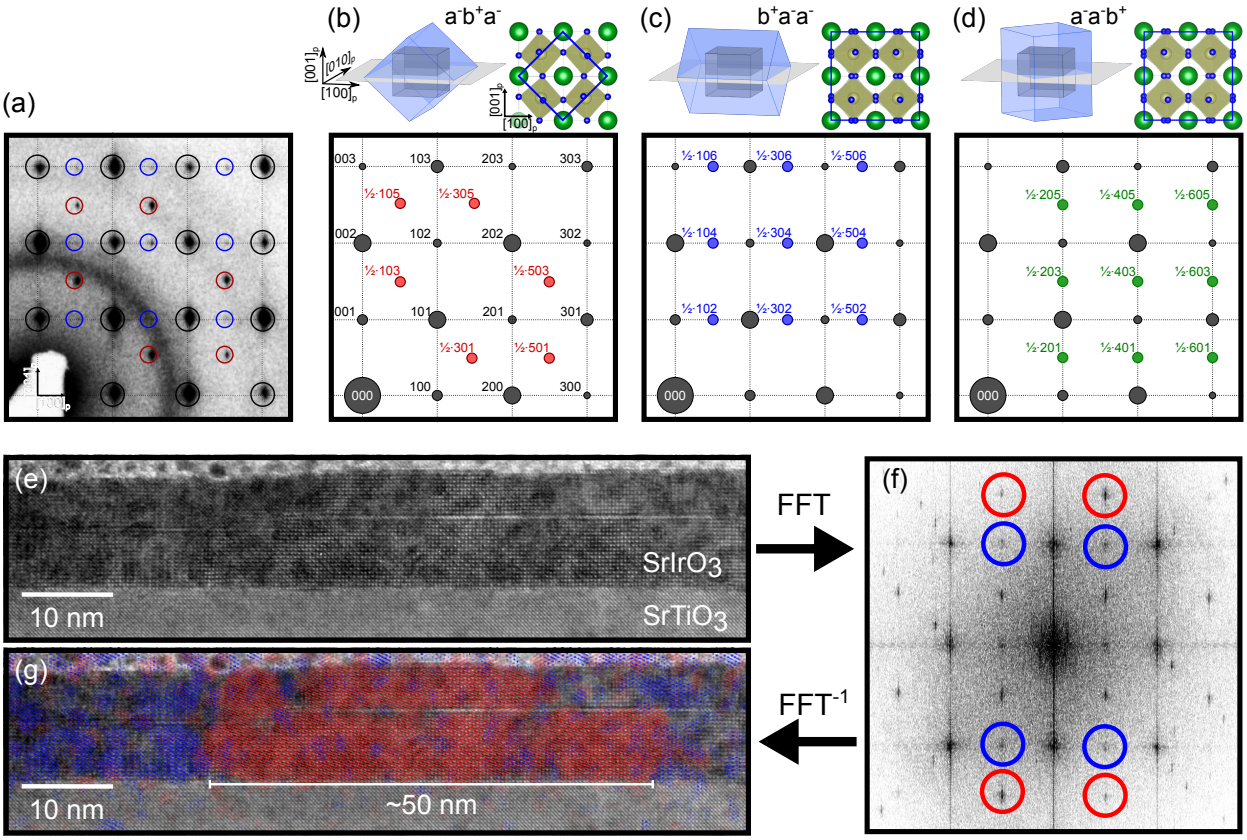

Figure 4.10: (a) SAED pattern of a $SrIrO_3$ film grown on $SrTiO_3$. In addition to strong $(h, 0, l)$ diffraction peaks from the pseudo-cubic perovskite lattice (black), half integer reflections due to octahedral rotations (blue, red) are seen. (b) - (d) Theoretical diffraction patterns for all three theoretically possible orientations of the orthorhombic unit cell (light blue) with respect to the pseudo-cubic unit cell (dark gray) and the film-substrate interface (light gray). Pattern (d) is not found experimentally. (e) HRTEM image of a $SrIrO_3$ film grown on $SrTiO_3$. (f) FFT of the HRTEM image. (g) Composite image of the HRTEM image and the inverse fast Fourier transform (FFT^{-1}) of the Fourier components belonging to the $a^-b^+a^-$ (red) and $b^+a^-a^-$ (blue) domain. The octahedral rotations are spatially confined to the $SrIrO_3$ film and have an estimated domain size of 50 nm.

4.5 Octahedral rotations and domain structure

Bulk $SrIrO_3$ exhibits a collective rotational pattern of the IrO_6 octahedra, which can be described by $a^-a^-b^+$ in Glazer notation and increases the unit cell by $\sqrt{2} \times \sqrt{2} \times 2$ with respect to the pseudo-cubic unit cell [17]. Figure 4.10 (a) shows one quadrant of the zeroth-order Laue zone (Miller index $k = 0$) SAED pattern of a $SrIrO_3$ film grown on $SrTiO_3$. The diffraction pattern is dominated by strong $(h, 0, l)$ peaks (black circles, $h, l \in \mathbb{Z}$) arising from the pseudo-cubic lattice symmetry of $SrIrO_3$ (and the $SrTiO_3$ substrate). Upon closer inspection extra reflections can be discerned at half-integer reciprocal-lattice sites (red, blue), which arise from the enlarged unit cell due to octahedral rotations.

Diffraction rules for reflections arising from only in- (+) or antiphase (−) tiltings were

Antiphase tilt	produces reflections	In-phase tilt	produces reflections
a^-	$\frac{1}{2}(ooo)$ with $k \neq l$	a^+	$\frac{1}{2}(eoo)$ with $k \neq l$
b^-	$\frac{1}{2}(ooo)$ with $h \neq l$	b^+	$\frac{1}{2}(oeo)$ with $h \neq l$
c^-	$\frac{1}{2}(ooo)$ with $h \neq k$	c^+	$\frac{1}{2}(ooe)$ with $h \neq k$
Mixed tilt	produces concert reflections		
a^+	$\frac{1}{2}(oee)$ with $\frac{1}{2}(h00)$ absent		
b^+	$\frac{1}{2}(eoe)$ with $\frac{1}{2}(0k0)$ absent		
c^+	$\frac{1}{2}(eeo)$ with $\frac{1}{2}(00l)$ absent		

Table 4.2: Top: Diffraction rules for antiphase (−) and in-phase (+) tilt systems [48]. Bottom: Diffraction rules for concert reflections in mixed-tilt systems [232]. Notation: $o \mathrel{\widehat{=}}$ odd, $e \mathrel{\widehat{=}}$ even

first proposed by Glazer [48] and have been extended to concert reflections caused by the combination of in- and antiphase tiltings in mixed tilt systems by Woodward & Reaney [232] (cf. Tab. 4.2). Based on these general rules, diffraction patterns for incident electrons along the $[010]_p$ direction can be deduced for all three possible orientations of the orthorhombic unit cell of $SrIrO_3$ (blue) with respect to the pseudo-cubic perovskite unit cell (dark gray) and the film-substrate interface (light gray) shown in Fig. 4.10 (b) - (d):

- $a^-b^+a^-$: reflections for $\frac{1}{2}(\text{odd}, 0, \text{odd})$ with $h \neq l$.
- $b^+a^-a^-$: reflections for $\frac{1}{2}(\text{odd}, 0, \text{even})$ with $\frac{1}{2}(h, 0, 0)$ absent.
- $a^-a^-b^+$: reflections for $\frac{1}{2}(\text{even}, 0, \text{odd})$ with $\frac{1}{2}(0, 0, l)$ absent.

Only two ($a^-b^+a^-$ and $b^+a^-a^-$) of three theoretically possible orientations are found experimentally (highlighted red and blue in Fig. 4.10 (a)) and accordingly form domains oriented at an angle of 90°. This finding is in line with molecular beam epitaxy (MBE)-grown $SrIrO_3$ films on LSAT substrates [233]. Figure 4.10 (e) and (f) show a high-resolution transmission electron microscopy (HRTEM) image of a $SrIrO_3$ film and its fast Fourier transform (FFT). A selective inverse FFT of only the Fourier components belonging to the $a^-b^+a^-$ (red) and $b^+a^-a^-$ (blue) domains yields the approximate spatial distribution of these domains. As seen in the composite image in Fig. 4.10 (g) the octahedral rotations are spatially confined to the $SrIrO_3$ films and have an estimated domain size of 50 nm.

Figure 4.11 shows the (a) low-energy electron diffraction (LEED) and (b) reflection high-energy electron diffraction (RHEED) patterns obtained from a $SrIrO_3$ film grown on $SrTiO_3$. In both patterns a 2×2 periodicity is observed (highlighted blue). LEED and RHEED are highly surface sensitive and accordingly probe the 2×2 surface projection of the three-dimensional $2\times\sqrt{2}\times\sqrt{2}$ ($\sqrt{2}\times2\times\sqrt{2}$) unit cell due to $b^+a^-a^-$ ($a^-b^+a^-$) octahedral rotations as depicted in Fig. 4.11 (c). In other words, the combination of octahedral rotations about

all three orthogonal axes leads to four inequivalent Ir lattice sites in the topmost $SrIrO_3$ layer shown in Fig. 4.11 (d).

The observation of half-integer reflections in SAED, LEED and RHEED patterns unequivocally evidences the presence of octahedral rotations, that resemble the $b^+a^-a^-$ pattern reported for bulk $SrIrO_3$ [17]. However, strictly speaking, a comprehensive quantitative analysis of the intensity of the reflections (i.e., the structure factor) from a single domain would be necessary to prove the equal magnitude of rotations about the x- (y-) and the z-axis that is implied by the $a^-b^+a^-$ ($b^+a^-a^-$) notation. Moreover, in contrast to the polycrystalline bulk form, the orthogonal x-/y- and z-axes are not equivalent due to the influence of the substrate in the present thin-film geometry. Therefore, some ambiguity remains whether the correct description of the lattice structure of the two domains is $a^-b^+a^-/b^+a^-a^-$ or rather $a^-b^+c^-/a^+b^-c^-$.

4.6 Epitaxial strain and tetragonal distortion of the film structure

Figure 4.12 (a) shows an XRD reciprocal space map (RSM) of the $(103)_p$ Bragg reflex of a $SrIrO_3$ film grown on $SrTiO_3$. Due to the large depth information of XRD the diffraction signal from the semi-infinite $SrTiO_3$ substrate is very sharp and several orders of magnitudes more intense than the film signal, which exhibits pronounced Laue fringes along $k_\perp$ due to its finite thickness of 16 unit cells as emphasized by a line profile (red) in Fig. 4.12 (b). In contrast, along $k_\parallel$ the diffraction peak (Fig. 4.12 (c)) is similarly narrow for film and substrate, indicating a comparable lateral long-range order. Furthermore, the coincident diffraction peak maxima in $k_\parallel$ evidence the coherent heteroepitaxial strain imposed upon the $SrIrO_3$ film by the $SrTiO_3$ substrate. Figure 4.12 (d) shows the SAED pattern of the $(202)_p$ and neighboring diffraction peaks. In accordance with XRD, the $(202)_p$ film Bragg

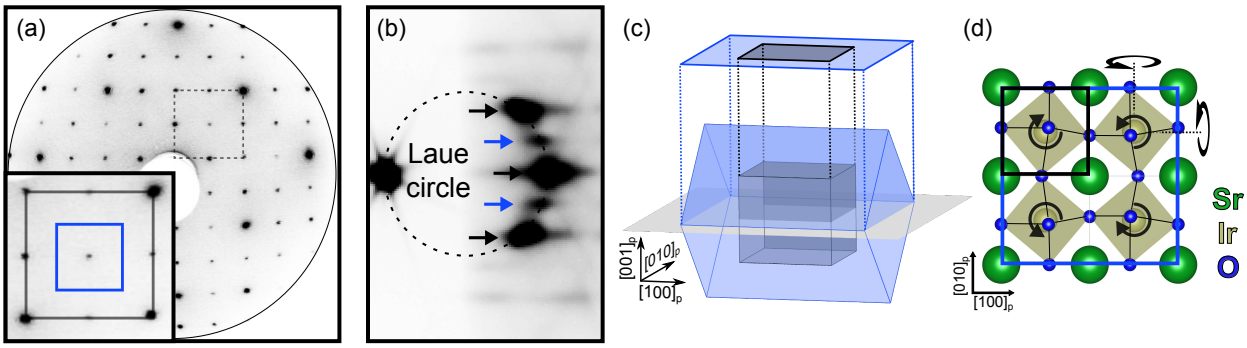

Figure 4.11: (a) LEED (E_{kin} = 100 eV) and (b) RHEED (E_{kin} = 30 keV) patterns of a $SrIrO_3$ film grown on $SrTiO_3$ exhibit a 2×2 periodicity (highlighted blue). (c) Due to the high surface sensitivity of LEED and RHEED the 2×2 surface-projection of the $2 \times \sqrt{2} \times \sqrt{2}$ real-space unit cell is probed. (d) Surface view of the topmost $SrIrO_3$ layer. The combination of octahedral rotations about all three axes leads to four inequivalent lattice sites.

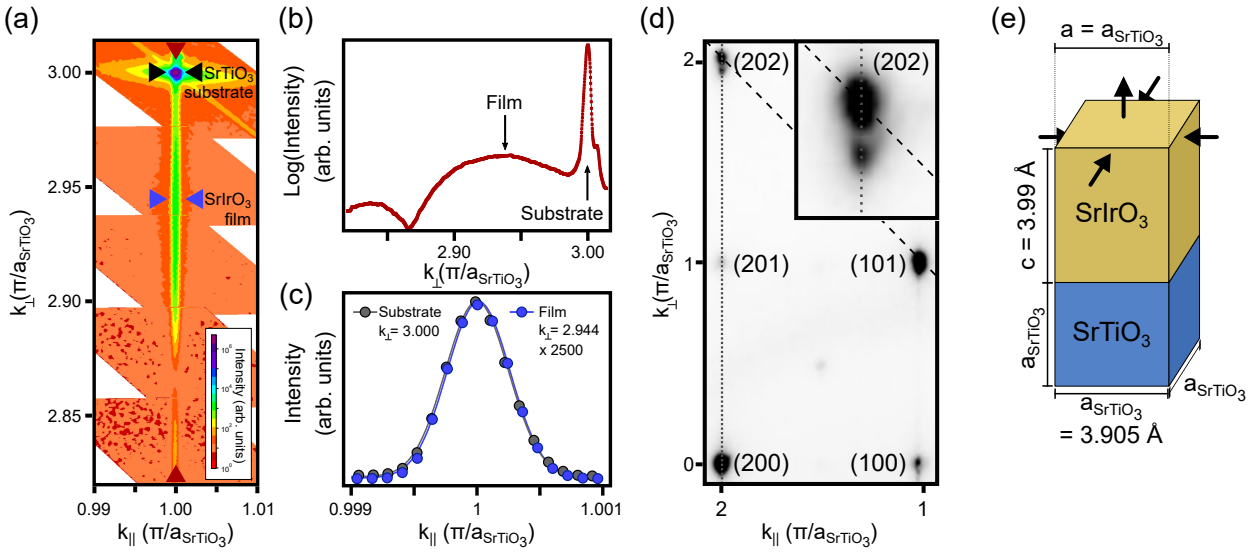

Figure 4.12: (a) RSM of the $(103)_p$ Bragg diffraction peak of a $SrIrO_3$ film on $SrTiO_3$. The pronounced (103) substrate peak is accompanied by a broad film diffraction peak. The film is found to be coherently strained to the substrate. Arrows indicate the line profiles along $k_\perp$ and $k_\parallel$. (b) Pronounced Laue fringes are observed due to the finite film thickness of 16 unit cells. (c) Substrate and film diffraction peaks both lie at $k_\parallel = \pi/a_{SrTiO_3}$ and have a similar peak width. (d) SAED pattern of the (202) and neighboring diffraction peaks similarly evidences the coherent strain to the substrate. (e) The $SrIrO_3$ out-of-plane lattice constant c is found to be elongated by $\approx 2\%$ with respect to the in-plane lattice constant $a = a_{SrTiO_3}$.

peak lies at the same $k_\parallel$-value as the substrate peak. As a pseudo-cubic film lattice structure would result in a Bragg peak on the $[101]_p$ diagonal through the (000) spot (dashed line, cf. also Fig. 3.4 (c)), the $SrIrO_3$ pseudo-cubic unit cell is hence found to be tetragonally distorted as depicted in Fig. 4.12 (e). The out-of-plane lattice constant $c = 3.99$ Å is found to be elongated by $\approx 2\%$ with respect to the in-plane lattice constant $a = a_{SrTiO_3} = 3.905$ Å.

The combined effect of tetragonal strain to the $SrTiO_3$ substrate and collective octahedral rotations on the real-space lattice structure is depicted in Fig. 4.13 (a). The pseudo-cubic cation sublattice exhibits a tetragonal elongation along the c-axis (black). The enlarged unit cell due to octahedral rotations (blue) is correspondingly distorted along the c-axis as depicted in Fig. 4.13 (b), which results in a rhombic distortion of two faces of the unit cell ($\alpha \neq \beta$).

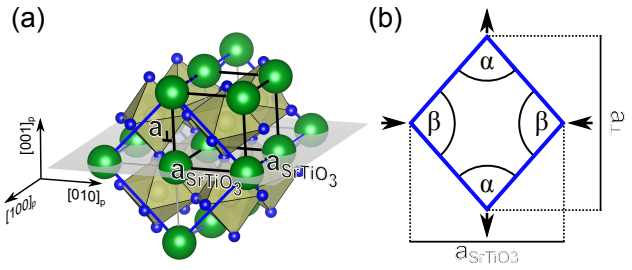

Figure 4.13: (a) Real-space lattice structure of a $SrIrO_3$ film strained to a $SrTiO_3$ substrate including octahedral rotations. Black: pseudo-tetragonal perovskite unit cell due to strain. Blue: Actual, enlarged unit cell due to octahedral rotations. (b) The combination of epitaxial strain and octahedral rotations results in a monoclinic unit cell.

4.7 Summary

The thermodynamical instability of the $SrIrO_3$ perovskite phase impedes the growth of macroscopic single crystals and therefore necessitates an alternative synthesis route as precondition for the investigation of its electronic structure. In this thesis, thin-film epitaxy of $SrIrO_3$ by pulsed laser deposition was employed to stabilize the perovskite lattice via epitaxial strain to the underlying substrate. The basic working principle of pulsed laser deposition comprises the evaporation of a target material with the desired stoichiometry by a focused high-intensity laser, plasma propagation through a process gas and, eventually, deposition and nucleation on a heated substrate. The challenges and pitfalls to be circumvented in the endeavor to obtain persistent layer-by-layer growth of stoichiometric, phase-pure and high-quality $SrIrO_3$ are elaborated in this chapter.

Prior to the growth process, the $SrTiO_3$ substrate is chemically and thermally treated to obtain a single TiO_2-termination of the (001)-oriented substrate. The coexistence of residual patches of SrO-termination is found to be detrimental for the film homogeneity since the reduced nucleation rate on SrO results in the formation of deep trenches. Therefore, the use of high-quality single-terminated $SrTiO_3$ is imperative for the synthesis of homogeneous $SrIrO_3$ films.

Two key challenges of pulsed laser deposition of ternary transition metal oxides are the stoichiometric transfer of the different atomic species from the target to the substrate and the control of the oxidative state of the transition metal cation. In the case of $SrIrO_3$, these challenges become intertwined because excessive substrate temperature and, to a lesser extent, partial pressure of the oxygen process gas result in the formation of over-oxidized, volatile IrO_3 and hence off-stoichiometry. In the extreme case, up to 50% iridium deficiency results in the formation of poorly ordered Sr_2IrO_4 or $Sr_3Ir_2O_7$ films, whereas less iridium loss results in $SrIr_{1\text{-}\delta}O_3$ films with embedded Ruddlesden-Popper-like lattice faults. The optimum growth results for phase-pure $SrIrO_3$ were obtained using a substrate temperature $T = 700\,^{\circ}\mathrm{C}$, an oxygen partial pressure $p_{O_2} = 0.08\,\mathrm{mbar}$, a laser intensity of $J = 75\,\mathrm{mJ}$ per pulse and a laser repetition rate $f = 1.5\,\mathrm{Hz}$, although the latter two were not found to profoundly influence the growth apart from the overall growth rate.

Of several possible growth modes, only layer-by-layer growth allows for the live-monitoring of the film thickness, which is a prerequisite for the controlled deposition of a predefined number of atomic layers. The homogeneity and chemical purity of the target material was found to be imperative to achieve persistent layer-by-layer growth. Since commercially available targets did not meet the qualitative requirements for this purpose, a manufacture process for high-quality, phase-pure $SrIrO_3$ target pellets with lateral dimensions allowing for the consecutive growth of up to 25 samples was established. At variance with the expected conservation of the AO-BO_2-AO-BO_2-...stacking order along the $[001]_p$ direction, $SrIrO_3$ is found to undergo a termination conversion during the initial growth on TiO_2-terminated $SrTiO_3$. Since the terminating IrO_2 layer is thermodynamically unstable and prone to volatilization via IrO_3 formation, the resulting film exhibits a SrO termination.

Polycrystalline 3C-$SrIrO_3$ is known to adopt the distorted $GdFeO_3$-type perovskite structure hosting an $a^+b^-b^-$ pattern of octahedral rotations, which breaks the cubic symmetry.

Heteroepitaxial $SrIrO_3$ films on $SrTiO_3$ are found to host two of three theoretically possible orientations of the orthorhombic $GdFeO_3$-structure ($a^-b^+a^-$ and $b^+a^-a^-$), which form orthogonally aligned domains with an estimated size of 50 nm. The $SrIrO_3$ films are coherently strained to the $SrTiO_3$ substrate, resulting in an elongated c-axis ($c/a \approx 1.02$).

In summary, persistent layer-by-layer growth of high-quality, stoichiometric $SrIrO_3$ thin films adopting a coherently strained $GdFeO_3$-type perovskite structure was achieved, thereby laying the groundwork for a successful investigation of the electronic structure of perovskite $SrIrO_3$ as function of film thickness.

Chapter 5

The electronic structure of $SrIrO_3$

The valence-band electronic structure of crystalline materials is the fundamental characteristic that determines most of their physical and chemical properties. Angle-resolved photoemission spectroscopy (ARPES) is a suitable tool to study the electronic structure with energy and momentum resolution because of the conservation of energy and momentum upon photoexcitation of an electron from its initial state to a final state in the continuum of unoccupied states.

Although conventional ARPES is traditionally performed using vacuum ultraviolet (VUV) light due to the ready availability of laboratory-based light sources and monochromators, its low excitation energy brings about several disadvantages. On the one hand, the assumption of a free-electron-like final-state dispersion, typically adopted to recover the perpendicular momentum of the initial state, is questionable since the modulation of the crystal potential is not *a priori* negligible in the VUV range. On the other hand, the minute photoelectron inelastic mean free path λ_{IMFP} makes VUV-ARPES extremely surface sensitive and limits the experimental resolution of the perpendicular momentum due to the intrinsic broadening $\Delta k_\perp = \lambda_{\mathrm{IMFP}}^{-1}$. To some extent these problems can be circumvented by expanding the photon energy range to the soft x-ray (SX) regime, because, firstly, the photoelectrons are excited into energetically higher, truly free-electron-like final states and, secondly, the increase of λ_{IMFP} following the universal curve results in a larger bulk sensitivity and a sharpening of the intrinsic resolution of $k_\perp$. Therefore, due to the tunability of the photon energy at synchrotron light sources soft x-ray ARPES can probe the three-dimensional bulk electronic structure of materials.

After the successful establishment of a synthesis route for epitaxial thin films of perovskite $SrIrO_3$, as elaborated in the previous chapter, the three-dimensional band structure of a metallic $SrIrO_3$ film was investigated by SX-ARPES. In the following chapter, the combined effects of spin-orbit coupling, on-site Coulomb repulsion, epitaxial strain and octahedral rotations on the electronic structure is discussed by comparison of the energy- and momentum-resolved photoemission data to *ab initio* density functional theory calculations (DFT+U).

5.1 Band structure determination by soft x-ray angle-resolved photoemission spectroscopy – experiment vs. theory

In order to investigate the bulk electronic structure of $SrIrO_3$ in the three-dimensional limit SX-ARPES measurements were performed at the ADRESS beam line of the Swiss Light Source (SLS) synchrotron, Paul Scherrer Institute, Switzerland [234, 235]. The $SrIrO_3$ thin films were heteroepitaxially grown on TiO_2-terminated $SrTiO_3$ in Würzburg using a polycrystalline target consisting of 6H-$SrIrO_3$ in the atmospheric-pressure form[7] (cf. Sec. 4.3). All measurements in this chapter were performed on a 9 unit cells thick film grown on TiO_2-terminated $SrTiO_3$. Galvanic contact with the spectrometer was ensured by shorting the film and the grounded sample carrier with silver paint applied to the side faces of the sample. The samples were transferred to the synchrotron in a UHV vessel at a pressure below $1 \cdot 10^{-8}$ mbar to avoid surface contaminations and/or sample degradation. The measurements were performed at a temperature of 20 K using circularly polarized light. The photoelectron analyzer was operated with a pass energy of 120 eV resulting in an overall energy resolution of 100 meV.

The measured band structure is compared to density functional theory (DFT+U) calculations by Dr. Domenico Di Sante[8]. The calculations were performed using the VASP *ab initio* package [236] within the projector-augmented-plane-wave (PAW) method [237, 238], using the generalized gradient approximation as parametrized by the Perdew-Burke-Ernzerhof GGA functional [239]. Spin-orbit coupling was self-consistently included [240] and the Coulomb repulsion U and exchange interaction J of Ir 5d orbitals were treated within the rotationally invariant DFT+U scheme of Liechtenstein, Anisimov, and Zaanen [241].

Epitaxial strain and short-range Coulomb repulsion

Figure 5.1 (a) shows the theoretical Fermi surface topology of an ideal cubic (lattice constant $a = 3.943$ Å) and a tetragonally distorted (in-plane $a = a_{SrTiO_3} = 3.905$ Å and out-of-plane lattice constant $c = 3.990$ Å, cf. Sec. 4.6) $SrIrO_3$ perovskite structure obtained from DFT(+U) calculations without ($U = 0$ eV, $J = 0$ eV) and with ($U = 3.4$ eV, $J = 0.4$ eV) on-site Coulomb repulsion U and exchange coupling J. The introduction of a sizeable U and J strongly alters the Fermi surface topology by removing the $J_{\text{eff}} = 3/2$ (blue) and Ir 5d e_g (gray) pockets at the A and Γ points, respectively, while leaving the $J_{\text{eff}} = 1/2$ Luttinger volume (red) relatively unchanged for both settings. The tetragonal out-of-plane elongation of the unit cell due to epitaxial strain to the $SrTiO_3$ substrate causes a tubular distortion of the Fermi surface.

Figure 5.1 (b) shows the energy-resolved band structure of the tetragonal setting with and without on-site Coulomb repulsion U and exchange coupling J along the high-symmetry lines Γ-X-M-Γ and Z-R-A-Z in comparison to the experimental E vs. k dispersions of a 9 unit

[7] Target preparation performed by Dr. Yingkai Huang, Van der Waals-Zeeman Instituut, University of Amsterdam, The Netherlands.

[8] Institut für Theoretische Physik und Astrophysik, Universität Würzburg

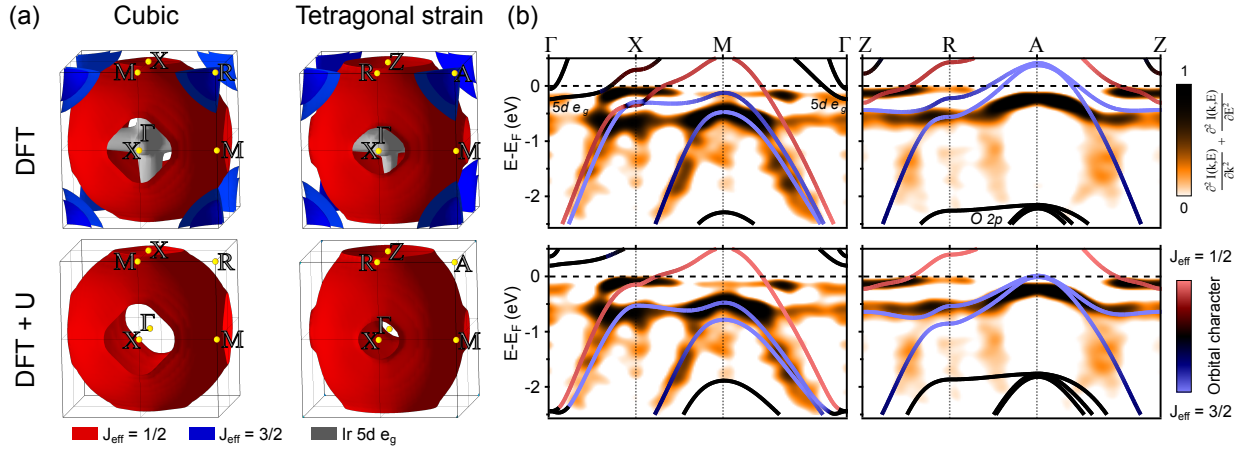

Figure 5.1: (a) Fermi surface topology of an ideal cubic and a tetragonally distorted $SrIrO_3$ perovskite structure obtained from DFT+U calculations with and without on-site Coulomb repulsion U and exchange coupling J. (b) E vs. k dispersion along the high-symmetry lines Γ-X-M-Γ and Z-R-A-Z measured by SX-ARPES and compared to DFT+U calculations. The band structure was calculated for the tetragonal setting with $U = 0\,\text{eV}$, $J = 0\,\text{eV}$ (top) and $U = 3.4\,\text{eV}$, $J = 0.4\,\text{eV}$ (bottom) and projected onto a $J_{\text{eff}} = (1/2,\, 3/2)$ basis (red/blue color code).

cell thick metallic $SrIrO_3$ film grown on $SrTiO_3$ measured by SX-ARPES ($h\nu = 745\,\text{eV}$ and $h\nu = 660\,\text{eV}$, respectively). The resulting bands are projected onto a $J_{\text{eff}} = (1/2,\, 3/2)$ basis [8] as encoded in the red-blue color gradient. Although the DFT calculations already capture some of the low-energy spectral features, the predicted Ir $5d\,e_g$ electron pocket around Γ and the Ir $J_{\text{eff}} = 3/2$ hole pocket around the A point are not observed in experiment. This discrepancy can be reduced by including short range Coulomb repulsion U. However, rather than looking for the lowest-energy solution within DFT+U, which would be a magnetic insulator at variance with experiment, magnetism is discarded. In this framework, U mainly acts to shift orbitals with different occupations relative to each other and is chosen to match the position of the ARPES bands, thereby pushing the bands either above or below the chemical potential. The e_g electrons are being predominantly transferred into the $J_{\text{eff}} = 3/2$ band, resulting in a Fermi topology composed of a single $J_{\text{eff}} = 1/2$ band. It does not come as a surprise that the resulting values of U (3.4 eV) and J (0.4 eV) are significantly larger than *ab initio* estimates using the constraint random phase approximation (cRPA) [131, 132]. A more accurate treatment of the many-body processes based on dynamical mean-field theory (DMFT) would most likely account for the experimental features with smaller values of the interaction.

SX-ARPES vs. DFT+U – similarities and discrepancies

Figure 5.2 (a) depicts the measured photoelectron intensity in the $[001]_p$ direction (sample normal) for photon energies between $h\nu = 575\,\text{eV}$ and 900 eV. The data set has been converted to reciprocal lattice vectors using Eq. 3.42 with the inner potential $V_0 = 10\,\text{eV}$ in correspondence to Ref. [242]. The dotted white lines denote the tetragonal Brillouin zone

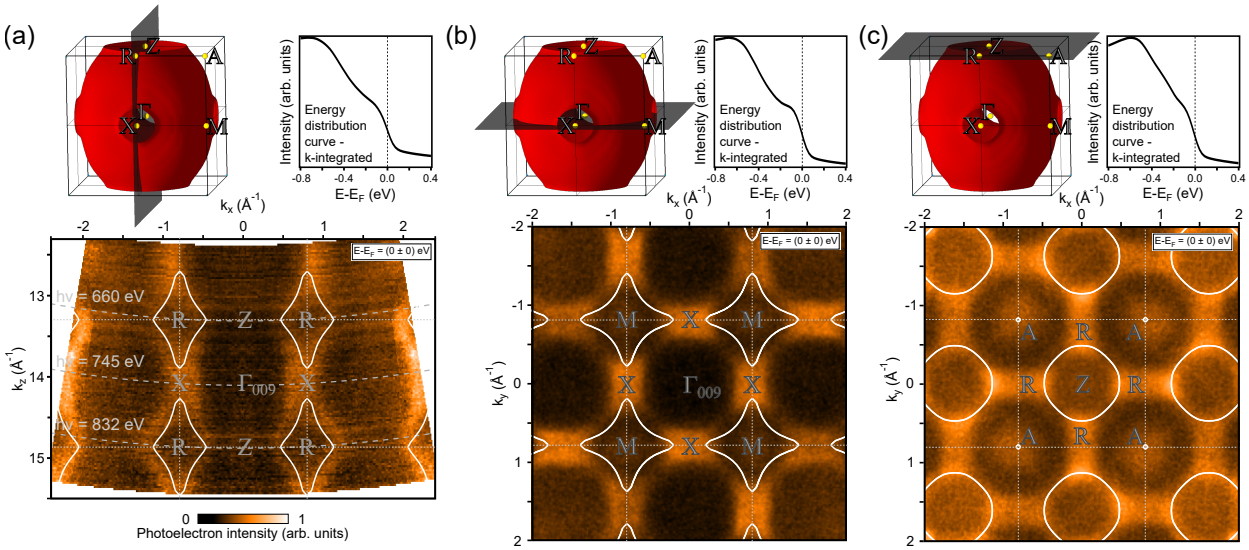

Figure 5.2: Experimental Fermi surface cuts. Solid white lines depict the DFT+U Fermi surface, dotted white lines the tetragonal Brillouin zone boundaries. The energy-distribution curves (EDCs) are each integrated over one two-dimensional cut through one Brillouin zone and exhibit a pronounced Fermi cutoff. (a) k_z- (photon energy)-scan in the Γ-X-R-Z-Γ plane. Exemplary constant-photon-energy cuts are depicted by dashed gray lines. The data set was converted using an inner potential $V_0 = 10\,\mathrm{eV}$. (b) Γ-X-M-Γ plane ($h\nu = 745\,\mathrm{eV}$). (c) Z-R-A-Z plane ($h\nu = 660\,\mathrm{eV}$).

boundaries, the dashed gray lines depict three constant-photon energy lines intersecting with the high-symmetry points and the solid white lines depict the DFT+U Fermi surface calculated for the tetragonally distorted unit cell. The overall good agreement between theoretical and experimental Fermi surface and the significantly lower photoelectron intensity at the Z point as compared to the X point evidence the tubular distortion of the Fermi surface, that results from the out-of-plane elongation of the perovskite unit cell (cf. Fig. 5.1 (a)). In contrast, Yamasaki *et al.* do not observe this tubular distortion in a SX-ARPES study of significantly thicker (60 unit cells) $SrIrO_3$ films grown on $SrTiO_3$ [242]. Although the authors claim to measure coherently strained films, the lattice structure may be partially relaxed in the topmost area of the film, i.e., within the limited depth information of SX-ARPES, hence giving rise to a cubic electronic structure.

Figure 5.2 (b) and (c) show the experimental Fermi surface cuts Γ-X-M-Γ and Z-R-A-Z, which intersect the Brillouin zone center ($h\nu = 745\,\mathrm{eV}$, $k_z = 18\,\pi/c$ where $c = 3.990\,\mathrm{Å}$) and boundary ($h\nu = 660\,\mathrm{eV}$, $k_z = 17\,\pi/c$), respectively. Both Fermi surface cuts exhibit a fourfold rotational symmetry, which reflects the Brillouin zone of the tetragonally strained perovskite unit cell without octahedral rotations (dashed gray lines). Furthermore, the DFT+U Fermi surface (white) captures the main features in the photoelectron distribution, i.e., the absence of spectral weight at the Γ, M and Z points and the small spectral weight at the A point. However, a closer inspection reveals subtle differences to the experimental data. In particular, the high spectral weight found at the X and R points is not expected from the calculations, whereas spectral weight is missing in the Γ-M and Z-A path, respectively.

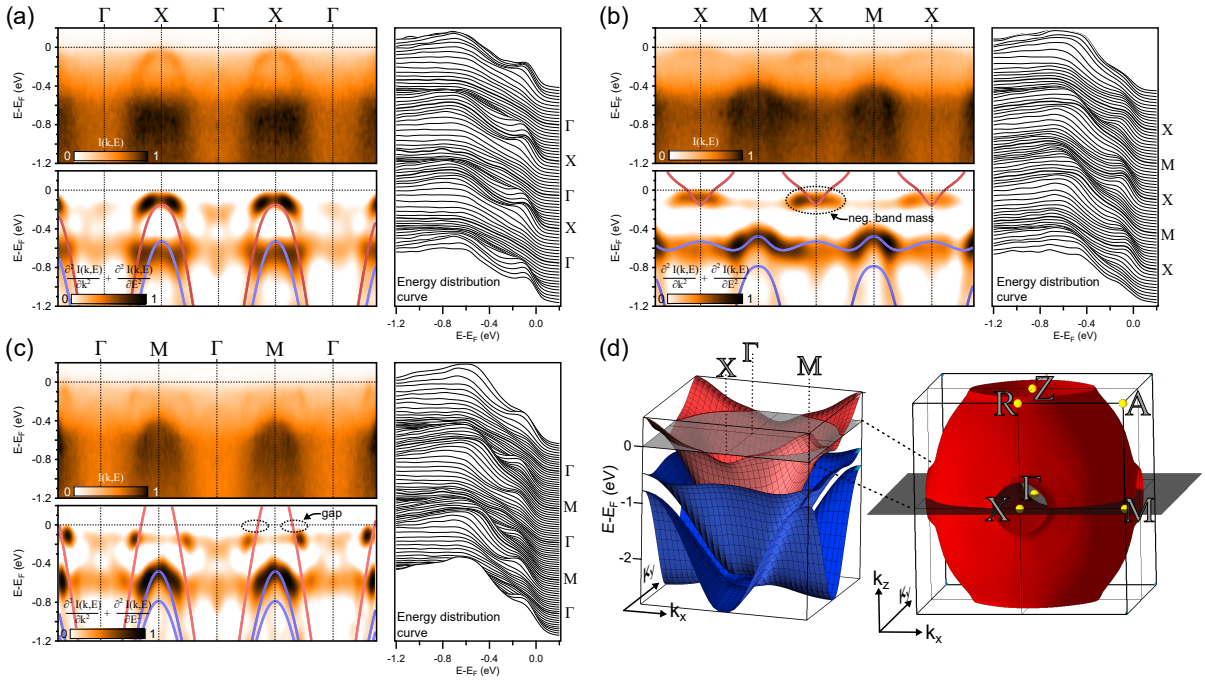

Figure 5.3: Photoelectron intensity, second derivative curve thereof with superimposed DFT+U bands and energy distribution curves along the three high-symmetry directions (a) Γ-X-Γ, (b) X-M-X and (c) Γ-M-Γ. (d) DFT+U Fermi surface in the three-dimensional Brillouin zone and energy-resolved band structure in the Γ-X-M-Γ plane ($k_z = 0$).

For a more detailed discussion, the photoelectron intensity along six high-symmetry lines in the Brillouin zone is shown as a function of energy in Figs. 5.3 and Fig. 5.4, side-by-side with the second derivative along k and E and energy distribution curves (EDCs). In agreement with the Fermi surface cuts in Fig. 5.2, the experimental band dispersion is generally well-reproduced by the DFT+U band structure, but subtle discrepancies are found (highlighted by black circles) – most obviously at the X and R points. Figures 5.3 (a) and (b) depict the spectral weight at the X point. While the band dispersion along the Γ-X-Γ direction is in principle described correctly by theory (despite a slightly underestimated band maximum), in stark contrast to DFT+U, a negative band mass is found experimentally along the M-X-M direction. Similarly, the band dispersion at the R point is well-reproduced along the Z-R-Z direction in Fig. 5.4 (a), whereas a clearly visible shadow band with negative band mass is observed along the A-R-A direction at variance with DFT+U in Fig. 5.4 (b). Beyond that, the $J_{\mathrm{eff}} = 1/2$ band does not fully intersect the chemical potential in the Γ-M-Γ (Fig. 5.3 (c)) and Z-A-Z directions (Fig. 5.4 (c)) although predicted by DFT+U.

In general, all energy distribution curves are found to exhibit residual spectral weight between the expected band crossings at the chemical potential, which may be easily interpreted as stemming from phonon-assisted nondirect transitions during the photoemission process [243–245], surface contaminations or poor long-range order of the surface. However, these explanations fail to explain the appearance of shadow bands as observed at the R point or the inverted band mass at the X point. In the following, these discrepancies are

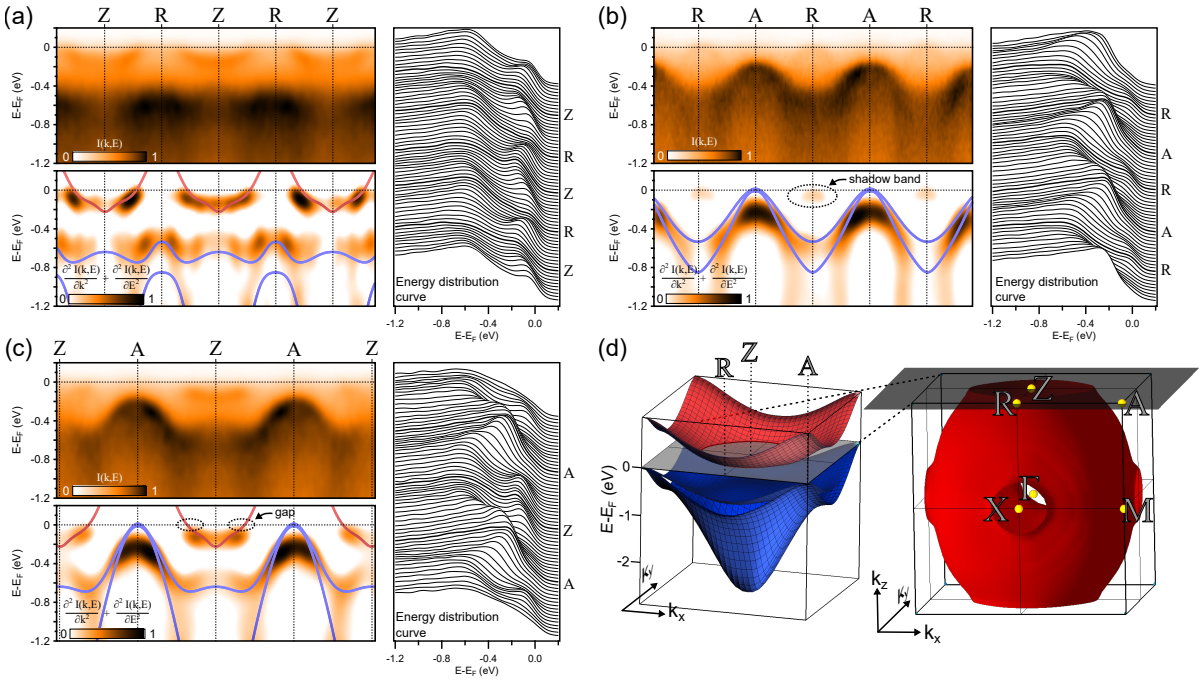

Figure 5.4: Photoelectron intensity, second derivative curve thereof with superimposed DFT+U bands and energy distribution curves along the three high-symmetry directions (a) Z-R-Z, (b) R-A-R and (c) Z-A-Z. (d) DFT+U Fermi surface in the three-dimensional Brillouin zone and energy-resolved band structure in the Z-R-A-Z plane ($k_z = \pi/c$).

explained by the presence of octahedral rotations and the concurrent backfolding of bands.

5.2 Footprints of octahedral rotations in photoemission spectroscopy

Previous ARPES studies of $SrIrO_3$ using ultraviolet light have reported narrow bands as a result of backfolding due to octahedral rotations, which introduce a periodic perturbation of the crystal potential that enlarges the real-space unit cell by $2 \times \sqrt{2} \times \sqrt{2}$ [233]. Figure 5.5 depicts the real-space lattice structure of a $SrIrO_3$ film including the effect of epitaxial strain to the substrate and collective octahedral rotations, and the corresponding original (black) and reduced (blue) Brillouin zones in reciprocal space. As discussed in Sec. 4.5 two orthogonally aligned domains with a typical lateral size of the order of 50 nm are found in $SrIrO_3$ films grown on $SrTiO_3$. Since the soft x-ray beam diameter used for SX-ARPES exceeds 50 nm by several orders of magnitude [234, 235] the resulting photoemission spectra inevitably comprise the superimposed signal from those two types of domains.

The effect of the weak symmetry breaking due to octahedral rotations can be taken into account in DFT+U calculations by unfolding the reduced Brillouin zone back into the original Brillouin zone [246]. The proper spectral weight distribution is thereby approximated

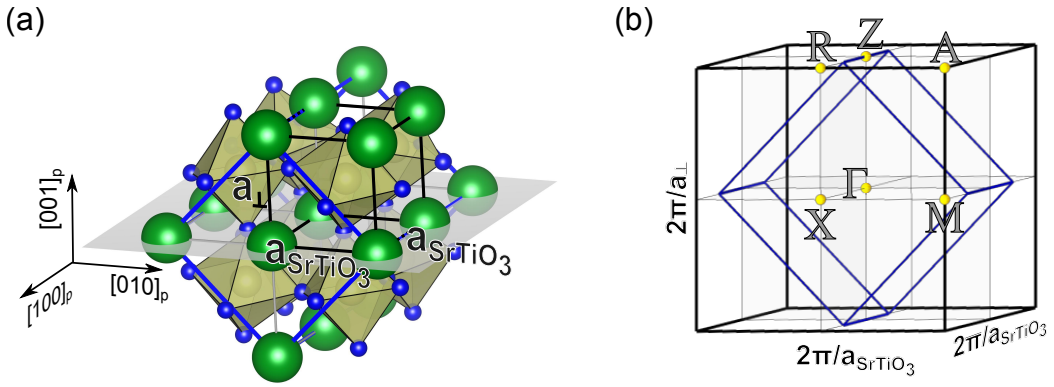

Figure 5.5: (a) Real-space lattice structure of a $SrIrO_3$ film strained to a $SrTiO_3$ substrate including octahedral rotations. Black: pseudo-tetragonal perovskite unit cell due to strain. Blue: Actual, enlarged unit cell due to octahedral rotations. (b) The combination of epitaxial strain and octahedral rotations results in a monoclinic unit cell.

by

$$A_{kn,kn}(\omega) = \sum_{KN} |\langle kn \,|\, KN\rangle|^2 \; A_{KN,KN}(\omega) \tag{5.1}$$

where $A_{kn,kn}(\omega)$ and $A_{KN,KN}(\omega)$ are the spectral functions of the retarded one-particle Green functions in the eigenorbital basis $|kn\rangle$ and $|KN\rangle$ of the original and enlarged unit cell, respectively, and $|\langle kn \,|\, KN\rangle|^2$ is used as a measure of the spectral weight. Figure 5.6 and 5.7 depict the unfolded DFT+U band structure along six high-symmetry lines for both orthogonal domains. It is shown in comparison to the second derivative of the photoelectron intensity signal and the DFT+U band structure obtained for the tetragonal setting (cf. Figs. 5.3 and 5.4). The calculated spectral weight $|\langle kn \,|\, KN\rangle|^2$ is decoded in the marker size for each band N and point K in reciprocal space. For the sake of clarity, the relevant two-dimensional cuts through reciprocal space are projected out in Fig. 5.6 (d) and 5.7 (d), thereby considering the higher-order reduced Brillouin zones (blue) with respect to the original Brillouin zone (black). The on-site Coulomb repulsion U and exchange coupling J were left unchanged with respect to the above-shown calculations.

Figure 5.6 (a) shows the unfolded band structure along the high-symmetry line Γ-X-Γ. As the real-space unit cell volume quadruples upon introduction of octahedral rotations the number of bands increases by the same factor. At the boundaries of the reduced Brillouin zone (blue vertical lines) – depending on the domain orientation – the $J_{\text{eff}} = 1/2$ band is folded back. However, the perturbational character of the octahedral rotations is reflected in the significantly weaker spectral weight of the backfolded band at the Γ point, in agreement with experiment. Along the X-M-X direction (Fig. 5.6 (b)) the intense band at the X point is slightly shifted towards the chemical potential and exhibits a negative band mass as observed in SX-ARPES. Furthermore, the octahedral rotations open a gap between the Γ and M points and hence impede an intersection of the $J_{\text{eff}} = 1/2$ with the Fermi level. The predicted Fermi level crossing at the M point is not visible in Fig. 5.3 (c) due to its small

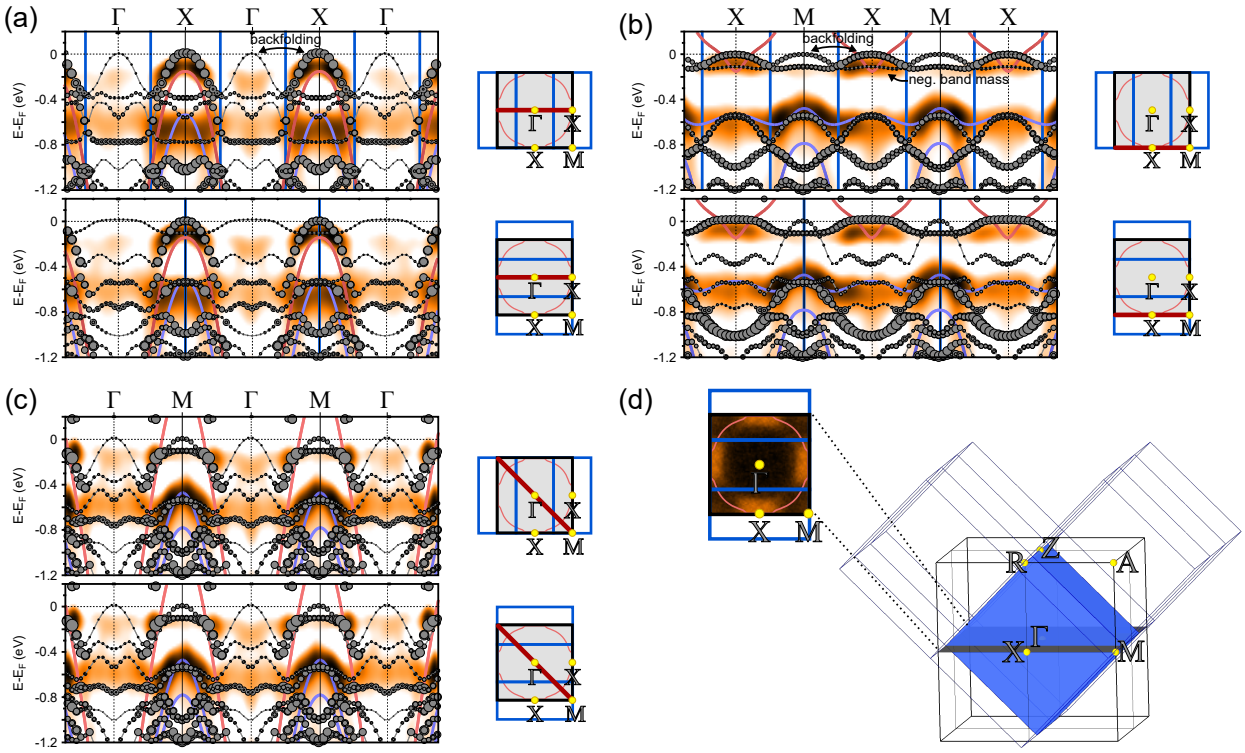

Figure 5.6: (a) - (c) DFT+U band structure including octahedral rotations and epitaxial strain to the substrate, unfolded into the original tetragonal unit cell. Two domain orientations are depicted for each high-symmetry line. The approximated spectral weight $|\langle kn \,|\, KN\rangle|^2$ is decoded in the marker size for each band N and point K in reciprocal space. (d) Three-dimensional Brillouin zone scheme for the original (black) and reduced (blue) Brillouin zone. The relevant higher Brillouin zones and a two-dimensional projection of the Γ-X-M-Γ plane is shown superimposed with the experimental Fermi surface cut and the calculated Fermi surface without octahedral rotations (red).

spectral weight. Note that the Γ-M-Γ direction is equivalent for both domain orientations, but not a high-symmetry line with respect to the reduced Brillouin zone.

Figures 5.7 (a) and (b) show the backfolded $J_{\text{eff}} = 1/2$ band in the Z-R-Z and R-A-R direction. Evidently, the experimentally observed shadow band at the R point is explained by the intrinsic symmetry breaking due to octahedral rotations. Interestingly, in the reduced Brillouin zone scheme the R-A-R and Γ-X-Γ high-symmetry lines are equivalent for one domain orientation (top). Indeed, the bare band structures in Fig. 5.6 (a) and Fig. 5.7 (b) are identical, whereas the calculated unfolded spectral weight at the R point is significantly stronger than at Γ and – in contrast to Γ – indeed, only the R point exhibits a clear shadow band in experiment (cf. Fig. 5.4 (b)). Analogous to the Γ-M-Γ direction, the $J_{\text{eff}} = 1/2$ band between Z and A point forms a gap and does not intersect the chemical potential, hence accounting for the suppressed photoelectron intensity in the Fermi surface.

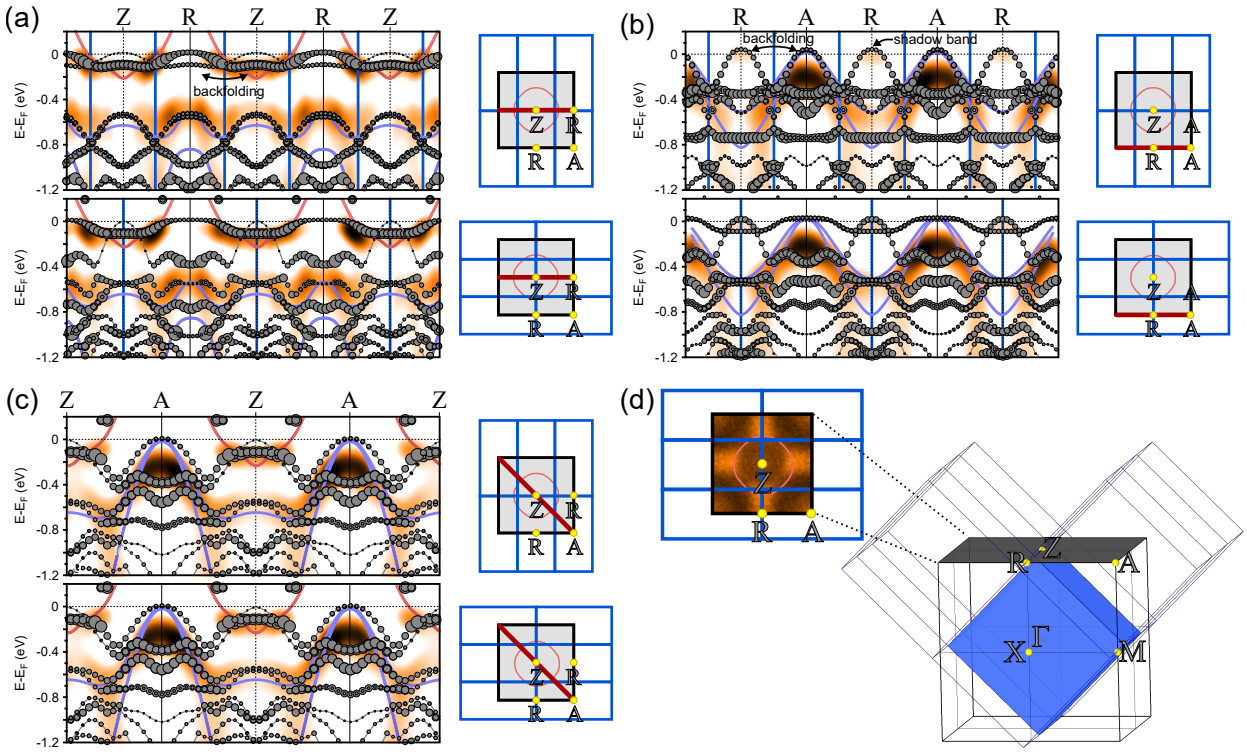

Figure 5.7: (a) – (c) DFT+U band structure including octahedral rotations and epitaxial strain to the substrate, unfolded into the original tetragonal unit cell. Two domain orientations are depicted for each high-symmetry line. The approximated spectral weight $|\langle kn \,|\, KN \rangle|^2$ is decoded in the marker size for each band N and point K in reciprocal space. (d) Three-dimensional Brillouin zone scheme for the original (black) and reduced (blue) Brillouin zone. The relevant higher Brillouin zones and a two-dimensional projection of the Z-R-A-Z plane is shown superimposed with the experimental Fermi surface cut and the calculated Fermi surface without octahedral rotations (red).

5.3 Summary

The electronic band structure of a 9 unit cells thick $SrIrO_3$ film is measured by SX-ARPES and analyzed in comparison to *ab initio* DFT+U calculations. $SrIrO_3$ exhibits a metallic ground state with coherent quasiparticle peaks and a well-defined Fermi surface. The main features of the band structure are well reproduced by DFT+U upon incorporation of an on-site Coulomb repulsion $U = 3.4\,\text{eV}$ and exchange coupling $J = 0.4\,\text{eV}$. Whereas bare DFT yields a Fermi surface with electronic states of $J_{\text{eff}} = 1/2$, $J_{\text{eff}} = 3/2$ and e_g orbital character, the introduction of a U shifts the e_g and $J_{\text{eff}} = 3/2$ states above and below the chemical potential, respectively, and results in a single-band Fermi surface of $J_{\text{eff}} = 1/2$ orbital character. As evidenced by Fermi-surface mapping along the k_z-direction, the tetragonal out-of-plane distortion of the $SrIrO_3$ perovskite lattice due to epitaxial strain to the $SrTiO_3$ substrate results in a tubular distortion of the Fermi surface in agreement with DFT+U. The remaining subtle discrepancies between experimental and theoretical band structure are explained by the weak symmetry breaking due to octahedral rotations within the film, which introduce a perturbation of the crystal potential and a backfolding of electronic bands.

In contrast to previous ARPES reports using ultraviolet light [233, 247], the overall symmetry of the electronic band structure is dictated by the pseudo-cubic perovskite symmetry and the octahedral rotations only act as perturbation. Whether this difference between photoemission spectroscopy using ultraviolet light and soft x-rays is due to their inherently different depth information or matrix elements remains an open question. On the one hand, due to its high surface sensitivity VUV-ARPES may exhibit a stronger footprint of octahedral rotations, since their magnitude may, in principle, be enhanced at the very surface as a result of the broken translational symmetry. On the other hand, the Ir-O-Ir bonding geometry may be reflected strongest in the finite O $2p$ component admixed to the $J_{\text{eff}} = 1/2$ electronic band via Ir $5d-$O $2p$ hybridization. The Ir $5d$ photoionization cross section exceeds that of O $2p$ states by an order of magnitude for soft x-rays, while they are almost equal for ultraviolet He I light (cf. Fig. 3.7 (a)). Therefore, octahedral rotations may be reflected differently in soft x-ray and ultraviolet photoemission spectroscopy. A thorough analysis of the orbital character of the backfolded DFT+U band structure may shed light on this question in the future.

Chapter 6

$SrIrO_3$ in the two-dimensional limit – electronic and structural degrees of freedom

The strontium iridate Ruddlesden-Popper compounds $Sr_{n+1}Ir_nO_{3n+1}$ = ($[SrIrO_3]_n$,SrO) essentially consist of n $SrIrO_3$ perovskite layers, which are intercalated by SrO layers and laterally shifted against each other such that no Ir-O-Ir bonds persist between neighboring $[SrIrO_3]_n$ blocks. As one veers away from the quasi-two-dimensional limit (Sr_2IrO_4, n = 1) the Mott-insulating state starts to break down as evidenced by the narrow-gap bilayer system $Sr_3Ir_2O_7$ with a collinear antiferromagnetic order [16,88] and the three-dimensional (n = ∞) semi-metallic $SrIrO_3$ [99]. However, the thermodynamic instability of bulk $Sr_{n+1}Ir_nO_{3n+1}$ for n > 2 impedes a systematic investigation of the dimensionality-induced metal-insulator transition (MIT) on single crystals.

In an attempt to mimic the layered Ruddlesden-Popper structure, a concurrent metal-insulator and magnetic transition has been observed in artificially tailored ($[SrIrO_3]_m$,$SrTiO_3$) superlattices, where the intercalated SrO layers are substituted with $SrTiO_3$ monolayers [128]. The different magnetic order of the iridium moments found in the superlattice analogues reflects the persisting non-negligible coupling between neighboring layers across the SrO and $SrTiO_3$ blocking layers. Moreover, both magnetism and resistivity have been shown to be affected by pronounced interlayer coupling in ($SrIrO_3$,$[SrTiO]_k$) superlattices [130]. Accordingly, neither the Ruddlesden-Popper iridates nor the artificial superlattice structures can be considered as truly two-dimensional.

Ultrathin epitaxial films represent a better-defined approach to the two-dimensional limit due to the inherent absence of interlayer coupling. In the following, a continuous crossover into the two-dimensional regime is induced by a progressive reduction of the film thickness. The electronic and structural properties of ultrathin $SrIrO_3$ films are investigated as function of dimensionality and discussed with respect to the electronic structure of bulk-like $SrIrO_3$ investigated in the previous chapter.

6.1 Dimensional crossover in ultrathin $SrIrO_3$

For the systematic study of dimensionality-induced effects in ultrathin heteroepitaxial films, the live-monitoring of reflection high-energy electron diffraction (RHEED) intensity oscillations is a prerequisite as it allows for monolayer-precise growth of a predefined film thickness

m by interrupting the deposition of material upon the observation of the m^{th} intensity maximum. Figure 6.1 (a) shows the specular RHEED intensity oscillations recorded during the growth of a series of $SrIrO_3$ films with thicknesses $m = 1$, 2, 3 and 4 unit cells (uc). In the following, the electronic and structural properties will be discussed as function of film thickness.

6.1.1 Dimensionality-induced metal-insulator transition

Figure 6.1 (b) shows the angle-integrated photoemission spectra (He I, $h\nu = 21.2\,\text{eV}$) of the films from Fig. 6.1 (a) and a bare Nb:$SrTiO_3$ substrate. As expected for the three-dimensional limit and consistent with Chap. 5, thick films ($m \geq 4$) exhibit a metallic density of states (DOS) with a pronounced Fermi-Dirac cutoff at the chemical potential. Intriguingly, at $m = 3$ the Fermi cutoff disappears and upon further reduction of the film thickness a distinct charge gap opens. Hence, the films undergo a metal-insulator transition as a function of dimensionality in analogy to the Ruddlesden-Popper iridates. In a complementary (magneto-)transport study of comparable samples, Groenendijk *et al.* similarly observe a thickness-dependent metal-insulator transition between 4 and 3 unit cells, as evidenced by a sharp increase of the sheet resistivity ρ and the onset of activated transport behavior ($d\rho/dT < 0$) in Fig. 6.1 (c) [248]. At the threshold thickness the sheet resistance is furthermore found to cross the value $h/e^2 = 25\,\text{k}\Omega$, which corresponds to the limit $k_F l_e \approx 1$ (k_F: Fermi wave vector, l_e: mean free path) and marks the transition from weak to strong localization [249].

In a first attempt to model the dimensionality-dependent changes in the electronic structure of $SrIrO_3$ films, magnetic DFT+U calculations were performed for supercells comprising m $SrIrO_3$ layers on 4 $SrTiO_3$ layers (denoted $m//4$) as shown in Fig. 6.2 (a), which are sep-

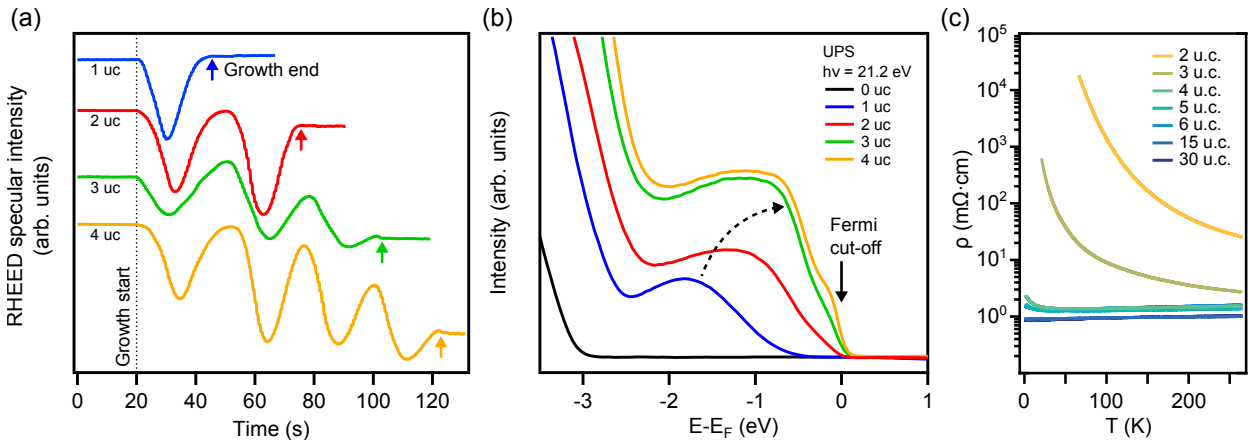

Figure 6.1: (a) Specular RHEED intensity oscillations of a series of $SrIrO_3$ films with thicknesses 1, 2, 3 and 4 unit cells (uc). (b) Room-temperature ultraviolet photoemission spectroscopy (UPS) of $SrIrO_3$ with thickness 1, 2, 3 and 4 uc and bare Nb:$SrTiO_3$ (0 uc) exhibits the opening of a charge gap between 3 and 4 uc. (c) Resistivity ρ vs. temperature T of $SrIrO_3$ films of different thickness. *Figure (c) adapted with permission from Ref. [248].*

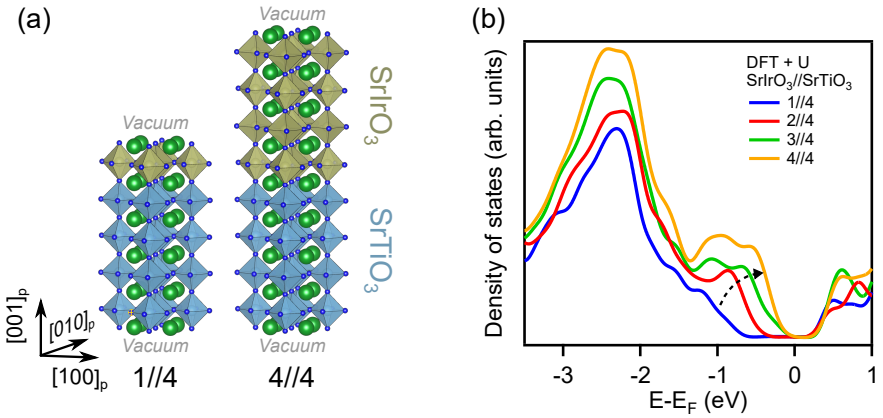

Figure 6.2: (a) Exemplary supercells of m SrO-terminated $SrIrO_3$ layers on 4 $SrTiO_3$ layers (m//4) used for magnetic DFT+U calculations. The unit cell size in the $(001)_p$ plane is enlarged by $\sqrt{2} \times \sqrt{2}$ with respect to the $SrTiO_3$ unit cell to allow for octahedral rotations about the $[001]_p$ direction. (b) Corresponding k-integrated DOS from DFT+U calculations. While the charge gap becomes smaller for increasing m, in the presence of magnetic ordering no MIT is observed.

arated by 2.8 nm of vacuum.[9] In the $(001)_p$ plane the unit cell is enlarged by $\sqrt{2} \times \sqrt{2}$ with respect to the $SrTiO_3$ unit cell to allow for octahedral rotations about the $[001]_p$ direction. The experimentally found $b^+a^-a^-$ rotational pattern in thick $SrIrO_3$ films (cf. Sec. 4.5) cannot be modeled in this geometry as the required 2×2 enlargement in the plane would exceed the computational capabilities due to the significantly higher number of atomic degrees of freedom. As seen in Fig. 6.2, in agreement with experiment the magnetic DFT+U calculations exhibit a decreasing charge gap in the k-integrated DOS as m is increased. However, in the presence of magnetic ordering the increasing film thickness alone does not trigger a transition from insulating to metallic in the calculations.

6.1.2 Oxygen octahedral rotations in the thin-film limit – a structural phase transition

Thick $SrIrO_3$ films exhibit a complex pattern of IrO_6 octahedral rotations with two domains described by $b^+a^-a^-/a^-b^+a^-$ in Glazer notation as shown in Sec. 4.5 [47]. The bulk crystal structure results in a 2×2 surface periodicity as observed by low-energy electron diffraction (LEED) and RHEED (cf. Fig. 4.11). Surprisingly, at the threshold thickness of the MIT ($m = 3$ uc) a structural transition to a $\sqrt{2} \times \sqrt{2}$ surface periodicity is observed as shown in Fig. 6.3, which persists for all insulating films.

Figure 6.4 (a) depicts a structural model of the topmost layer of a thick $SrIrO_3$ film with octahedral rotations about all three orthogonal axes. The peculiar $b^+a^-a^-$ pattern results in four inequivalent iridium sites, i.e., a 2×2 surface periodicity. However, the heteroepitaxial $SrIrO_3$ film forms a corner-shared oxygen octahedral network with the $SrTiO_3$ substrate as depicted in Fig. 6.4 (b). Since $SrTiO_3$ adopts a cubic perovskite structure without octahedral rotations at room temperature, rotations about the in-plane directions are suppressed in

[9] All DFT+U calculations in this chapter were performed by Dr. Domenico Di Sante.

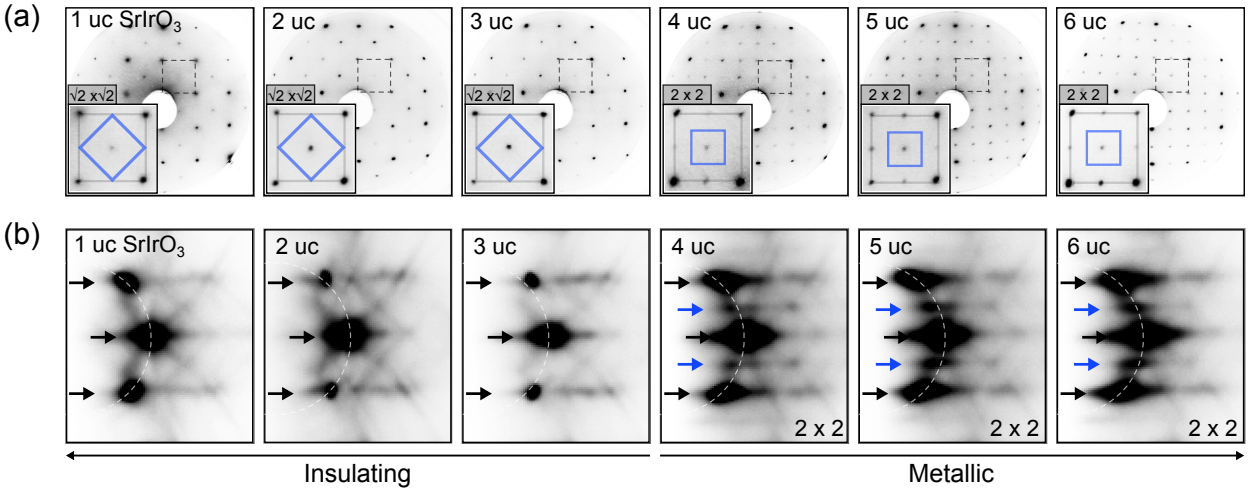

Figure 6.3: (a) Room-temperature LEED and (b) RHEED patterns of $SrIrO_3$ films with thicknesses $m = 1 - 6$ uc. While a 2×2 periodicity, corresponding to the $b^+a^-a^-$ bulk rotational pattern (cf. Fig. 4.11), is observed in the three-dimensional limit ($m \geq 4$) , a $\sqrt{2} \times \sqrt{2}$ periodicity is found for all insulating films ($m \leq 3$).

atomically thin films, whereas rotations about the surface normal may prevail. The topmost layer of a thin $SrIrO_3$ film with rotations about the c-axis only is shown in Fig. 6.4 (c). Similar to the basal plane of bulk Sr_2IrO_4 and $Sr_3Ir_2O_7$, it hosts two inequivalent iridium sites, resulting in a $\sqrt{2} \times \sqrt{2}$ surface periodicity. Therefore, the octahedral connectivity between the $SrTiO_3$ substrate and the thin $SrIrO_3$ film imposes strong constraints upon the film lattice structure, which modify the film symmetry.

Whether or not the amplitude $|\gamma|$ of the octahedral rotations is similar in all layers and film thicknesses $m \leq 3$ uc remains experimentally unsolved. Furthermore, it is not clear whether the structural transition at $m = 4$ uc causes the entire $SrIrO_3$ film to adopt a $b^+a^-a^-$ rotational pattern, thereby imposing octahedral rotations upon the interface region of the $SrTiO_3$ substrate, or if, alternatively, the octahedral tilt about the in-plane directions smoothly fades out towards the interface. One possible technique to target these questions is annular bright-field (ABF) imaging in aberration-corrected scanning transmission electron microscopy [250–252]. Alternatively, the oxygen anion positions in the lattice may be detected by negative spherical aberration coefficient imaging (NCSI) in high-resolution transmission electron microscopy (HRTEM) [253, 254]. From a theoretical point of view, the structural relaxation of the supercells in the DFT+U calculations shown in Fig. 6.4 (d) results in similar rotation angles for all $SrIrO_3$ thicknesses. Furthermore, TiO_6 octahedral rotations of roughly 5° are induced in the substrate. However, the predictive power of DFT structure relaxations is generally limited and, per definition, the supercell at hand does not include octahedral rotations about the a- and b-axis, since it merely comprises a $\sqrt{2} \times \sqrt{2}$ unit cell in the plane.

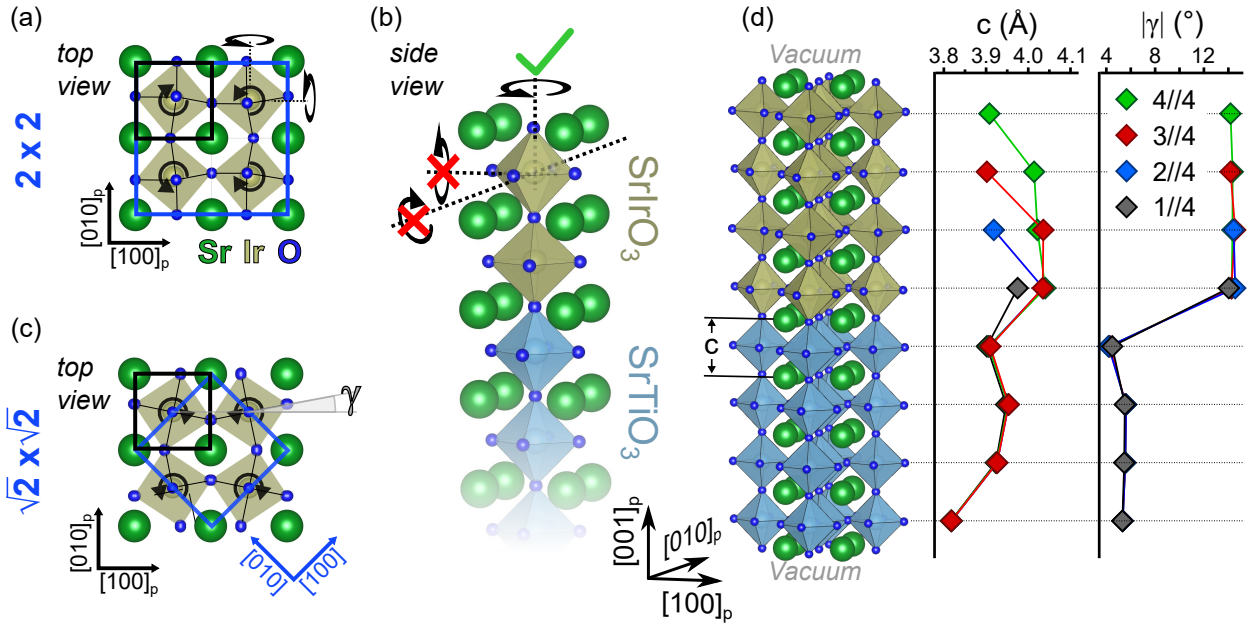

Figure 6.4: (a) Structural model of the topmost layer of a thick ($m \geq 4$) $SrIrO_3$ film with octahedral rotations about all three orthogonal axes ($b^+a^-a^-$), resulting in *four* inequivalent Ir sites, i.e., a 2×2 surface unit cell. (b) The oxygen octahedral network between $SrIrO_3$ and $SrTiO_3$ impedes octahedral rotations about the a- and b-axes in thin films. (c) Structural model of the topmost layer of a thin ($m \leq 3$) $SrIrO_3$ film with octahedral rotations about only the c-axis, resulting in *two* inequivalent Ir sites, i.e., a $\sqrt{2} \times \sqrt{2}$ surface unit cell. (d) DFT structural relaxation results for $m//4$ $SrIrO_3//SrTiO_3$ supercells (cf. Fig. 6.2). The layer-resolved amplitude of in-plane octahedral rotations $|\gamma|$ in $SrIrO_3$ is constant for all layers and $SrIrO_3$ thicknesses. Interestingly, an in-plane octahedral rotation of $|\gamma| \approx 5°$ is induced in the $SrTiO_3$ substrate.

6.1.3 Momentum-resolved electronic structure of ultrathin $SrIrO_3$ films – experiment vs. theory

In order to further elucidate the physical origin of the MIT, the electronic structure of ultrathin $SrIrO_3$ films was investigated by SX-ARPES. Measurements were performed for one film at the very boundary of the phase transition ($m = 3$ uc) and one film in the two-dimensional limit ($m = 1$ uc). The experimental conditions are equal to those described in Sec. 5.1, e.g., a sample temperature of $T = 25$ K, except for Nb-doped $SrTiO_3$ being used as substrate to ensure a sufficient conductivity to compensate for the photocurrent and hence prevent charging of the samples.

Band structure determination at the brink of the phase transition

Figure 6.5 and 6.6 show the photoelectron band maps of a $m = 3$ uc $SrIrO_3$ film along the pseudo-cubic high-symmetry directions Γ-X-Γ, X-M-X, Γ-M-Γ ($h\nu = 745$ eV) and Z-R-Z, R-A-R, Z-A-Z ($h\nu = 660$ eV), respectively. The photoelectron intensity and second derivative maps are superimposed with the DFT+U bands for strained bulk $SrIrO_3$ without octahedral rotations (cf. Sec. 5.1). Consistent with the k-integrated, highly surface-sensitive

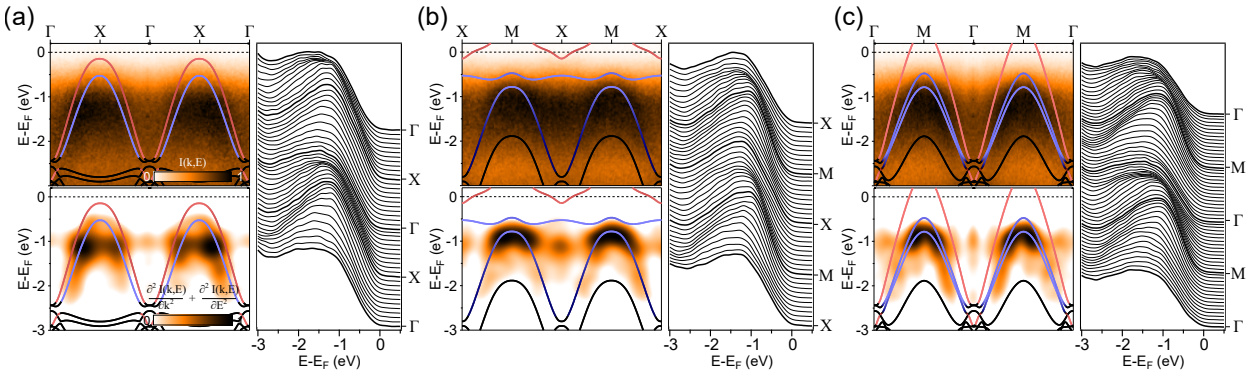

Figure 6.5: SX-ARPES band maps of a $m = 3$ uc $SrIrO_3$ film along the three pseudo-cubic high-symmetry directions (a) Γ-X-Γ, (b) X-M-X and (c) Γ-M-Γ ($h\nu = 745$ eV). The photoelectron intensity (top) and second derivative maps (bottom) are superimposed with the $J_{\text{eff}} = 1/2$ (red), $J_{\text{eff}} = 3/2$ (blue) and O $2p$ (black) DFT+U bands for bulk $SrIrO_3$ (strained, no octahedral rotations). Right panels: Energy distribution curves (EDCs).

ultraviolet photoemission spectroscopy (UPS) measurements in Fig. 6.1 (b), no spectral weight is observed at the chemical potential in SX-ARPES despite its inherently higher information depth. The bulk of the film is thus found to be insulating, in agreement with transport experiments [248].

The rather broad spectral feature between −0.5 eV and −2 eV, seen in all band maps, displays dispersion, which bears a striking similarity to that of the $J_{\text{eff}} = 3/2$ bands in DFT+U calculations for bulk $SrIrO_3$. In the EDCs the dispersive feature seems to be superimposed by a constant non-dispersive spectral feature positioned at ≈ -1.5 eV. Specifically, despite the absence of a $J_{\text{eff}} = 3/2$ band, significant spectral weight is observed at −1 eV at the Γ point in Fig. 6.5 (a) and (c). It is tempting to interpret this as incoherent spectral weight from a $J_{\text{eff}} = 1/2$ lower Hubbard band (LHB) that is superimposed with the dispersing $J_{\text{eff}} = 3/2$ bands. However, as discussed in Sec. 5.2 the effect of IrO_6 octahedral rotations must be taken into account and may similarly explain the observed spectral weight.

Band structure determination in the two-dimensional atomic limit

Figure 6.7 (a) depicts the real-space model of a monolayer of $SrIrO_3$. Due to octahedral rotations its unit cell is enlarged by $\sqrt{2} \times \sqrt{2}$ (blue) with respect to the pseudo-cubic perovskite structure (black) as evidenced by surface electron diffraction. In the following, the SX-ARPES band maps of a $SrIrO_3$ monolayer are compared to DFT+U band structure calculations of a 1//4 supercell (cf. Fig. 6.2 (a)). For this purpose, the band structure is unfolded into the pseudo-cubic, i.e., 1×1 Brillouin zone by employing the procedure described in Sec. 5.2, if not stated otherwise. The corresponding 1×1 and $\sqrt{2} \times \sqrt{2}$ Brillouin zones with the respective high-symmetry points are depicted in Fig. 6.7 (b).

Figure 6.8 shows the band maps of a $SrIrO_3$ monolayer ($m = 1$ uc) along the pseudo-cubic high-symmetry directions Γ-X-Γ and M-X-M ($h\nu = 745$ eV). The photoelectron intensity and second derivative maps are superimposed with the magnetic DFT+U band structure calculation of a 1//4 supercell, where the marker size denotes the spectral weight obtained

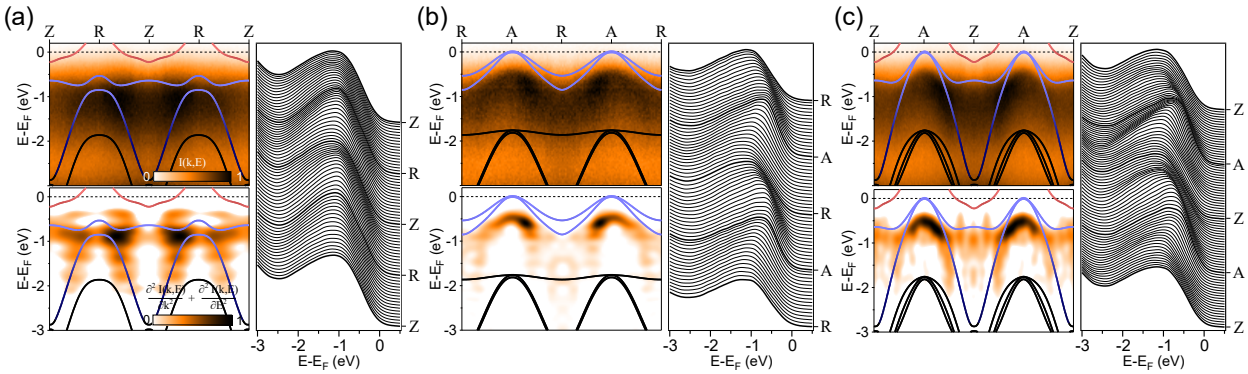

Figure 6.6: SX-ARPES band maps of a $m = 3$ uc $SrIrO_3$ film along the three pseudo-cubic high-symmetry directions (a) Z-R-Z, (b) R-A-R and (c) Z-A-Z ($h\nu = 660$ eV). The photoelectron intensity (top) and second derivative maps (bottom) are superimposed with the $J_{\text{eff}} = 1/2$ (red), $J_{\text{eff}} = 3/2$ (blue) and O $2p$ (black) DFT+U bands for bulk $SrIrO_3$ (strained, no octahedral rotations). Right panels: Energy distribution curves (EDCs).

from the unfolding procedure. Justified by the ambiguity of the position of the chemical potential in insulating compounds, the energy scale of the DFT+U band structure is offset by 0.5 eV for a better comparison to the experimental data. The broad spectral feature in Fig. 6.8 at ≈ -1.5 eV exhibits a weak but discernible dispersion, as seen, e.g., by comparing the energy distribution curves of the high-symmetry points Γ, M and X. In excellent agreement with each other the experimental and theoretical data exhibit a global valence band maximum at the M point and a second maximum at the X point.

Figure 6.9 (a) and (b) show the band structure of the SrO-terminated $SrIrO_3$ monolayer (i.e., 1//4 supercell) and bulk Sr_2IrO_4, respectively, along the pseudo-cubic Γ-X-M-Γ direction. For both cases the band structure of the magnetic DFT+U ground state is unfolded into the pseudo-cubic unit cell. Intriguingly, the electronic structure of the two-dimensional $SrIrO_3$ thin film and the quasi-two-dimensional layered bulk material Sr_2IrO_4 is found to be strikingly similar. With respect to Sr_2IrO_4 as potential parent material for exotic superconductivity, this similarity opens an interesting experimental avenue towards charge carrier

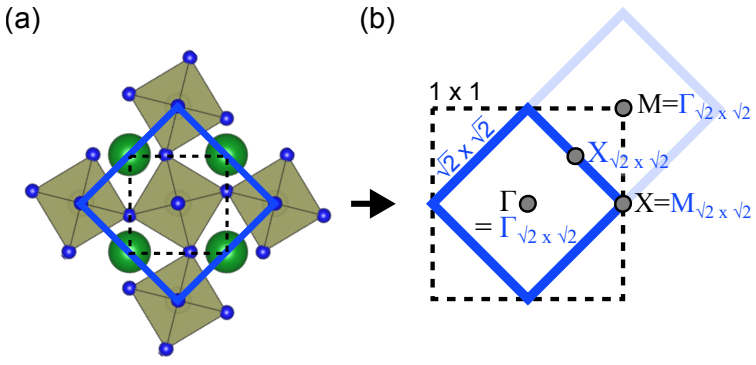

Figure 6.7: (a) Top view of a monolayer of $SrIrO_3$ showing the enlarged $\sqrt{2} \times \sqrt{2}$ (blue) unit cell with respect to the pseudo-cubic unit cell (black). (b) 1×1 (black) and reduced $\sqrt{2} \times \sqrt{2}$ (blue) Brillouin zone in reciprocal space with all corresponding high-symmetry points.

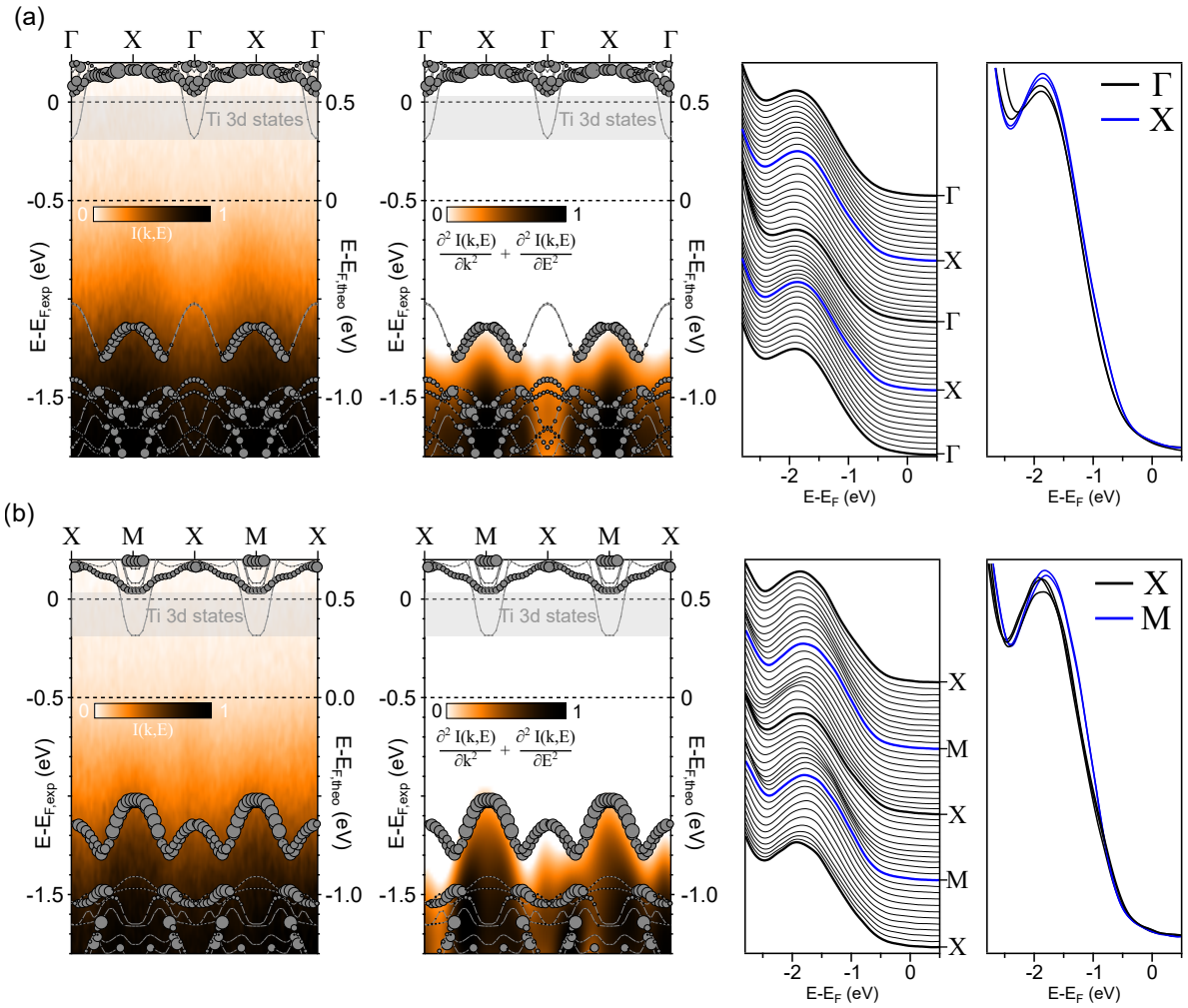

Figure 6.8: SX-ARPES band maps of a $SrIrO_3$ film with thickness $m = 1$ uc along the high-symmetry directions (a) Γ-X-Γ and (b) X-M-X ($h\nu = 745$ eV). The photoelectron intensity (left panels) and second derivative maps (middle panels) are superimposed with magnetic DFT+U bands obtained for a 1//4 supercell including in-plane octahedral rotations as shown in Fig. 6.2. The marker size reflects the spectral weight obtained by unfolding the band structure into the pseudo-cubic unit cell as described in Sec. 5.2.

doping of monolayer $SrIrO_3$ without the introduction of disorder, e.g., via electrostatic field or ionic liquid gating.

In the two-dimensional limit the surface structure becomes critical for the electronic band structure because of the divergent surface-to-bulk ratio. As discussed in Sec. 4.4, heteroepitaxially grown $SrIrO_3$ films on TiO_2-terminated $SrTiO_3$ are found to exhibit a terminating SrO surface layer contrary to the expected conservation of the perovskite stacking order in $[001]_p$ direction. Figure 6.10 compares the calculated DFT+U band structure of two 1//4 supercells with a SrO- and an IrO_2-terminated monolayer of $SrIrO_3$, respectively. Note, that the band structure in Fig. 6.10 is calculated for the $\sqrt{2} \times \sqrt{2}$ enlarged unit cell (highlighted in blue in the top view) and *not* unfolded into the pseudo-cubic Brillouin zone of the 1×1 unit cell (dashed black line) as in Fig. 6.9. Here, the sizes of the blue squares and red circles

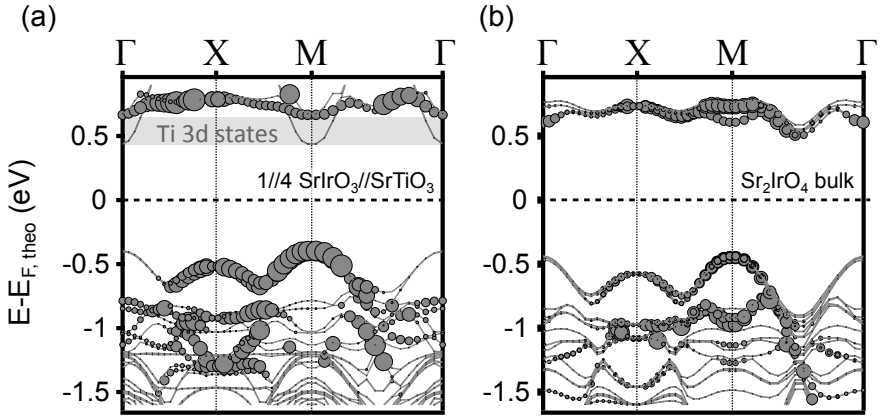

Figure 6.9: (a) Magnetic DFT+U band structure calculation of a 1//4 supercell (cf. Fig. 6.2). The marker size denotes the spectral weight obtained by unfolding the band structure. (b) Magnetic DFT+U band structure calculation of bulk Sr_2IrO_4. A striking similarity to the band structure of a $SrIrO_3$ monolayer (1//4) is found.

denote the Ir 5d e_g and t_{2g} orbital character, respectively, as obtained from a projection onto the basis of the total angular momentum L.

The valence and conduction bands of the IrO_2-terminated monolayer in Fig. 6.10 exhibit a strong mixing of e_g and t_{2g} states, whereas the SrO-termination results in a distinct separation thereof. Strictly speaking, the distinction between a t_{2g} and e_g manifold only holds in an octahedral crystal field with the point group symmetry O_h, which predominantly originates from the negative point charges of the nearest-neighbor oxygen ligands in perovskite oxides. Hence, the observed orbital mixing occurs as consequence of the broken local octahedral symmetry due to the absence of an apical oxygen at the IrO_2-terminated surface. In particular, the similarity between the electronic structure of $SrIrO_3$ in the monolayer limit and bulk Sr_2IrO_4 [7, 131] exclusively holds for SrO-terminated $SrIrO_3$. Hence, the observed self-organized conversion to a SrO termination is imperative for the close analogy between bulk Sr_2IrO_4 and monolayer $SrIrO_3$, since the quasi-two-dimensional network of fully closed IrO_6 octahedra constitutes their characteristic common structural feature.

The dimensionality-induced MITs observed in Ruddlesden-Popper iridate crystals [8, 65, 88, 91, 255] and ($[SrIrO_3]_m$,$SrTiO_3$) superlattices [128] are accompanied by a magnetic transition. Figure 6.9 (a) shows the k-integrated density of states (DOS) from magnetic and paramagnetic (i.e., nonmagnetic) DFT+U calculations of the supercell with SrO-termination. Interestingly, only the magnetic DFT+U ground state is insulating, whereas the paramagnetic solution exhibits a metallic DOS even in the two-dimensional limit. The magnetic ground state is characterized by antiferromagnetically aligned in-plane magnetic moments (cf. inset), which are rigidly locked to the octahedral rotations due to a Dzyaloshinsky-Moriya-type interaction [8, 70] and thereby result in a weak ferromagnetic component ($\approx 0.03\,\mu_B$/Ir) similar to bulk Sr_2IrO_4 [9, 62, 65]. Furthermore, Groenendijk *et al.* observed significantly enhanced spin fluctuations in the semimetallic state near the threshold thickness of the MIT in magnetoconductance measurements of samples identical to ours [248]. These findings indicate that the observed gap opening may be compatible with a transition from a nonmagnetic

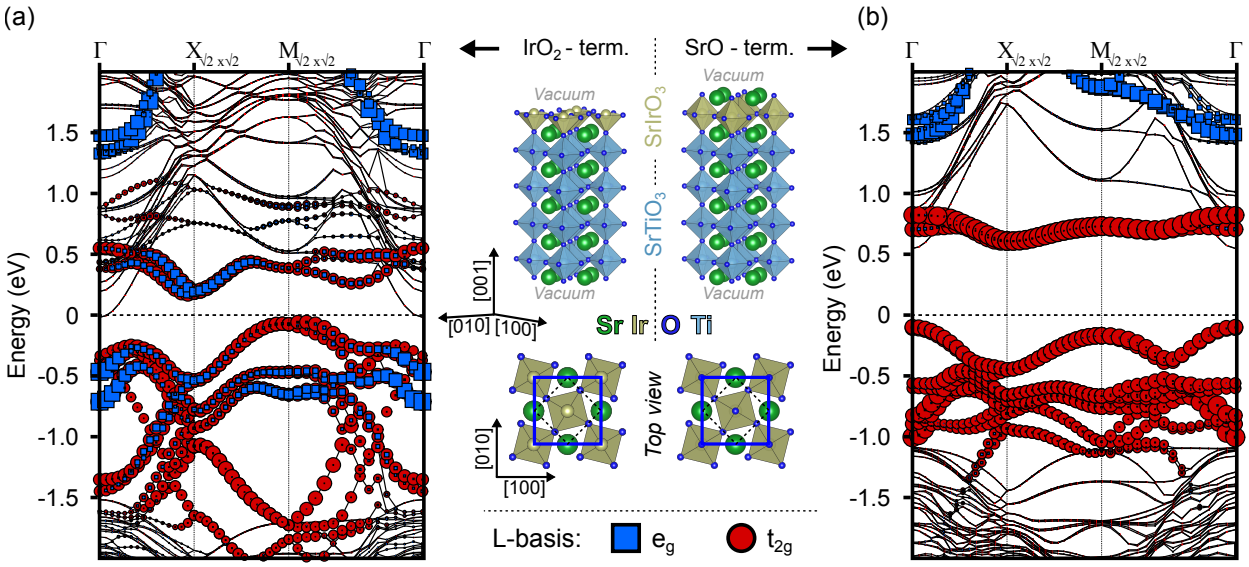

Figure 6.10: DFT+U band structure calculations of two supercells comprising four unit cells of $SrTiO_3$ and a monolayer of $SrIrO_3$ with different termination. The band structure is calculated for the $\sqrt{2} \times \sqrt{2}$ enlarged unit cell (blue in top view) and *not* backfolded into the pseudo-cubic Brillouin zone of the 1×1 unit cell (dashed black in top view). The blue and red marker sizes indicate the e_g and t_{2g} orbital character, respectively. (a) IrO_2-termination: Since the local O_h symmetry of the octahedral crystal field is broken, e_g and t_{2g} states mix for the valence and conduction bands. (b) SrO-termination: The bands have pure t_{2g}/e_g character. The band structure is highly reminiscent of the bulk band structure of Sr_2IrO_4

to a magnetic ground state in $SrIrO_3$ thin films as function of dimensionality. Whether or not this translates into a long range ordering at finite temperatures at the critical thickness and whether an order parameter persists in the two-dimensional limit ($m = 1\,\mathrm{uc}$) are currently debated open questions [130].

6.1.4 Discussion

Due to the sizeable spin-orbit coupling and – at the same time – local Coulomb repulsion the electronic structure of bulk-like $SrIrO_3$ is well-described by a single half-filled metallic

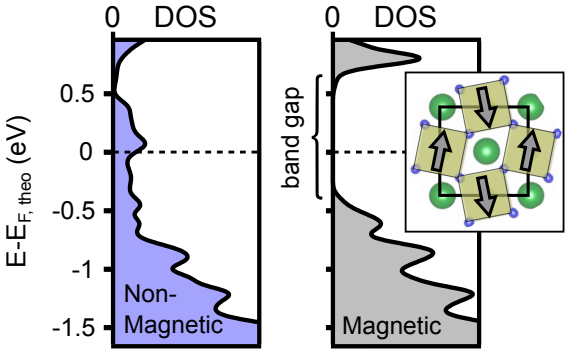

Figure 6.11: Density of states obtained from magnetic and nonmagnetic (i.e., paramagnetic) DFT+U calculations of a SrO-terminated $1//4$ supercell. Only the magnetic DOS exhibits a band gap, whereas the paramagnetic solution remains metallic even in the two-dimensional limit. Inset: Canted G-type antiferromagnetic order of the magnetic solution.

band with effective total angular momentum $J_{\text{eff}} = 1/2$ and fully occupied $J_{\text{eff}} = 3/2$ bands below the chemical potential. The correlated metallic ground state in $SrIrO_3$ is highly susceptible to small external perturbations that modify the delicate balance between the different physical interactions at play, i.e., the hopping term t (= band width), the Coulomb interaction U, spin-orbit coupling and magnetic interactions. Here, the film thickness is employed as experimental tuning parameter that triggers a metal-insulator transition at a threshold thickness of 3 unit cells.

Upon reduction of the film thickness the average coordination of each iridium site changes from 6 in the three-dimensional to 4 in the two-dimensional limit. As the number of possible hopping channels for conduction electrons decreases concurrently, the hopping integral t is reduced [16, 132]. At the same time, the decreasing coordination of the iridium atoms also reduces the screening of the bare on-site Coulomb repulsion U [132]. Both effects therefore cooperatively enhance the coupling strength U/t and push the system towards many-body Mott localization.

Additionally, the octahedral network with the underlying $SrTiO_3$ substrate increasingly influences the lattice structure of $SrIrO_3$ as the film thickness is reduced. Whereas bulk $SrIrO_3$ hosts collective rotations of the IrO_6 octahedra about all three orthogonal axes, only rotations about the surface normal prevail in the thin-film limit. It is noteworthy, that the insulating Ruddlesden-Popper compounds Sr_2IrO_4 and $Sr_3Ir_2O_7$ also only exhibit in-plane rotations of the IrO_6 octahedra. Since the electron hopping is mediated by the oxygen ligands, changes of the Ir-O-Ir bonding geometry will modify the band width and hence play a role in the metal-insulator-transition. This tendency is reflected in the (albeit small) resistivity drop of $SrIrO_3$ thin films at $T = 105\,\text{K}$ [225], where the cubic $SrTiO_3$ substrate undergoes an antiferrodistortive structural transition involving $a^0a^0c^-$ rotations of the TiO_6 octahedra [47,256], which can induce or amplify in-plane tiltings in the film. As the dropping resistivity implies the enhancement or opening of hopping channels upon introduction of in-plane rotations, the structural transition upon reduction of the film thickness is also expected to result in a decreased hopping term t, which pushes the system towards the insulating phase. Although the charge gap of thin $SrIrO_3$ films was not found to exhibit any changes as function of temperature, a more detailed analysis of the structural and electronic properties of ultrathin $SrIrO_3$ films near the antiferrodistortive transition temperature of $SrTiO_3$ may help in disentangling the effects of iridium coordination and structural changes.

6.2 Disentangling band-bending, Madelung-potential and final-state effects in core-level photoemission spectroscopy

Down to the present day the vast majority of electronic devices rests upon the use of semiconductors as functional materials. The key functionality in such devices usually originates from the physics of the heterointerface rather than that of the bulk constituents [257]. One of the cornerstone mechanisms in semiconductor heterostructures is the interfacial alignment

of bands, which may result in a spatially varying potential and concurrent charge transfer across the interface [258]. Photoemission spectroscopy is a frequently used technique to determine band discontinuities, Schottky-barrier heights and band bending at the interface of semiconductor heterojunctions, as the spatially varying electrostatic potential near the interface bends all bands and energy levels by the same amount [173, 174].

In recent years, transition metal oxides have been studied intensely as potential alternative to semiconductors [259, 260]. Similar to semiconductors, the interfacial band alignment may lead to a varying potential across the interface even in the absence of an interfacial polar discontinuity [258]. The associated charge transfer across the interface can be seen as intrinsic doping effect, which may lead to novel phenomena not present in neither of the bulk constituents [261–267]. For example, an unexpectedly large charge transfer was observed at the nonpolar $SrIrO_3/SrMnO_3$ heterointerface, resulting in emergent ferromagnetism [268, 269]. In addition, the interfacial band alignment is also relevant for other potential applications, such as the incorporation of atomically thin $SrIrO_3$ in a core-shell design as an attractive candidate for water electrolysis via an oxygen evolution reaction with enhanced activity and stability [270, 271].

Here, two series of $SrIrO_3$ films with varying thickness $m = 1 - 5$ uc were analyzed by means of core-level x-ray photoelectron spectroscopy (XPS) using monochromatized Al K_α radiation from an x-ray tube. The two series were grown on Nb-doped $SrTiO_3$ substrates with 0.5 wt. % and 0.05 wt. % Nb-doping concentration denoted $Nb_{0.5\%}$:$SrTiO_3$ and $Nb_{0.05\%}$:$SrTiO_3$, respectively. The film thickness-dependent spectra are compared to a $SrTiO_3$ ($m = 0$ uc) and $SrIrO_3$ ($m = 20$ uc) reference sample, the former being a $Nb_{0.5\%}$:$SrTiO_3$ substrate that was exposed to all pre-growth preparations (growth temperature and oxygen pressure) without actual deposition of $SrIrO_3$. For all samples, photoemission spectra were obtained at room temperature under normal emission, with some additional measurements under an emission angle of 50° off normal emission for enhanced surface sensitivity. For the $Nb_{0.5\%}$:$SrTiO_3$ samples, galvanic contact with the spectrometer was ensured by shorting the substrate and film with the grounded sample carrier by applying silver paint to the side faces of the sample. In contrast, the samples grown on the

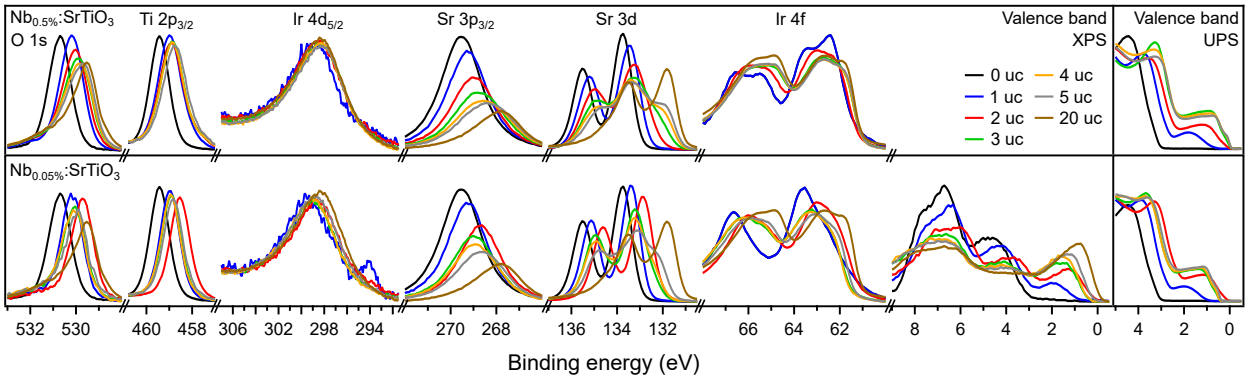

Figure 6.12: Overview of all measured core-level and valence-band spectra of $SrIrO_3$ films with thicknesses 1-5 uc grown on $Nb_{0.5\%}$:$SrTiO_3$ (top) and $Nb_{0.05\%}$:$SrTiO_3$ (bottom). All spectra except the Ir $5d_{5/2}$ core level (factor x2) share the same energy scale.

less conductive $Nb_{0.05\%}$:$SrTiO_3$ substrates exhibit a variable but static energy shift due to charging as a result of insufficient grounding. Therefore, the absolute binding energy shifts cannot be interpreted meaningfully in these cases.

An overview of all measured core-level spectra is given in Fig. 6.12. The measured core-level spectra are O 1s, Ti 2p, Ir 4d, Sr 3p, Sr 3d and Ir 4f. Additionally, the valence-band spectra were measured by UPS for both and XPS for only one series. In the following, the absolute and relative energy shifts as function of film thickness are discussed.

6.2.1 Schottky barrier formation at the $SrIrO_3$/$SrTiO_3$ interface

The band alignment between Nb:$SrTiO_3$ and complex oxides or elemental metals has been widely studied. Whereas the combination with some oxides (e.g., $LaAlO_3$, γ-Al_2O_3,...) may result in the formation of an interfacial potential trough hosting a two-dimensional electron system [261, 272–275], the combination with other oxides (e.g., $SrRuO_3$ [276]) or elemental metals (e.g., Au, Pt, Cu ... [277–280]) results in a Schottky-type upwards band bending, leading to rectifying behavior across the junction. Similarly, a recent study reported a rectifying Schottky barrier at the $SrIrO_3$/$SrTiO_3$ heterointerface as deduced from current-voltage, capacitance-voltage and internal photoemission measurements [281]. In the following, the energetic height and spatial shape of the Schottky barrier at the $SrIrO_3$/$SrTiO_3$ interface is investigated as function of the $SrIrO_3$ thickness and the Nb-dopant concentration in $SrTiO_3$.

Figure 6.13 (a) shows the Ti $2p_{3/2}$ core-level spectra of bare $Nb_{0.5\%}$:$SrTiO_3$ (0 uc) and of $Nb_{0.5\%}$:$SrTiO_3$ overgrown with 1, 2, 3, 4 and 5 uc of $SrIrO_3$. As sketched in Fig. 6.13 (b), the valence and conduction bands in the bare Nb:$SrTiO_3$ substrate can be considered as spatially constant to a good approximation due to the lack of a chemically shifted Ti^{3+} shoulder at the low-energy side of the Ti 2p spectrum in Fig. 6.13 (a), which would indicate the presence of significant amounts of oxygen vacancies acting as electron donors and at the same time giving rise to band bending owing to their effectively positive 2+ charge state [274, 282–285]. Interestingly, upon deposition of only a monolayer of $SrIrO_3$ an energy shift towards lower binding energy is observed, that can be explained by a Schottky-type band bending as sketched in Fig. 6.13 (c). The spectral contributions from each $SrTiO_3$ layer trace the electrostatic potential, which is characterized by its barrier height ΔE_{bb} and spatial extension into the substrate d. Following the Beer-Lambert law the contribution from each layer is damped by an exponential factor $\exp(-z/\lambda_{\mathrm{IMFP}})$, where z is the distance to the interface and λ_{IMFP} the inelastic mean free path (IMFP) of the photoelectrons. Therefore, depending on the length scale of the spatial variation d the effective energy shift of the Ti $2p_{3/2}$ peak is expected to be accompanied by a larger ($d \lesssim \lambda_{\mathrm{IMFP}}$) or smaller ($d > \lambda_{\mathrm{IMFP}}$) asymmetric broadening of its line shape for a given ΔE_{bb}.

Figure 6.14 (a) compares the shifted and normalized Ti $2p_{3/2}$ spectra of bare $Nb_{0.5\%}$:$SrTiO_3$ and two $SrIrO_3$/Nb:$SrTiO_3$ heterojunctions with the same film thickness (5 uc) but a different Nb-concentration (0.5% and 0.05%). The Ti $2p_{3/2}$ peak width is found to significantly depend upon the Nb-doping level. In particular, the peak width of the $SrIrO_3$/$Nb_{0.5\%}$:$SrTiO_3$ heterojunction (black) is found to be significantly larger than that of bare $Nb_{0.5\%}$:$SrTiO_3$ (red), whereas that of $SrIrO_3$/$Nb_{0.05\%}$:$SrTiO_3$ (blue) is almost similar to bare $Nb_{0.5\%}$:$SrTiO_3$,

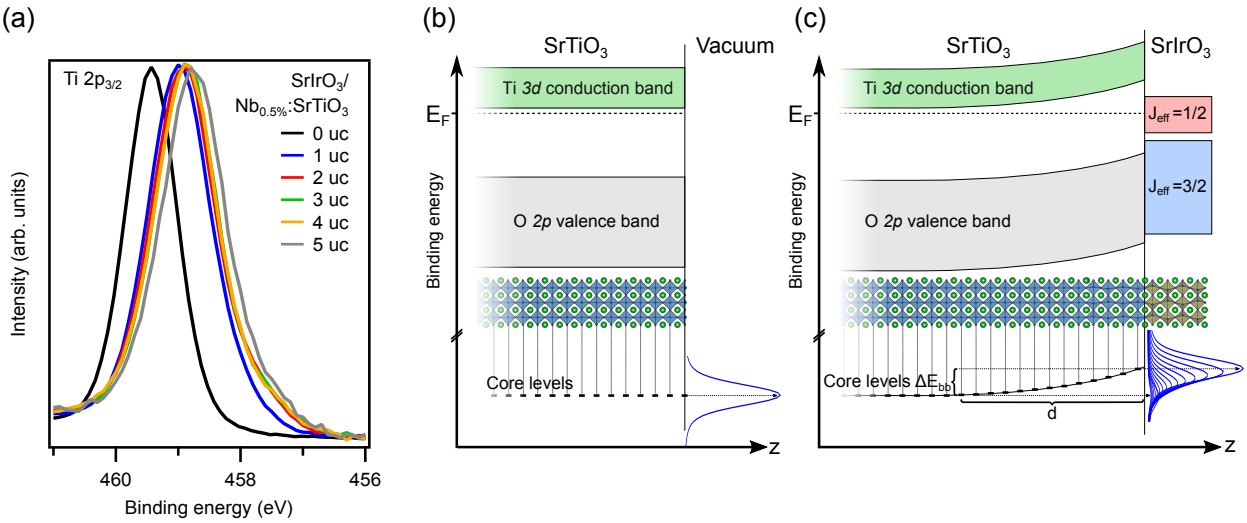

Figure 6.13: (a) Ti $2p_{3/2}$ core-level spectra of $Nb_{0.5\%}$:$SrTiO_3$ overgrown with 0, 1, 2, 3, 4 and 5 uc of $SrIrO_3$. A pronounced energy shift towards lower binding energy is observed. (b) A $SrTiO_3$ crystal can be considered as reference without electrostatic potential gradient at the surface, hence exhibiting core-level spectra without asymmetric broadening. (c) Formation of a Schottky-type band bending towards the chemical potential results in an energy shift and an asymmetric broadening of the substrate core levels, as the exponentially damped contributions from deeper layers trace the electrostatic potential.

except for a slight broadening of the peak footing. As summarized in Fig. 6.14 (b) this trend holds for all $SrIrO_3$ thicknesses.

As discussed above, such a variation may result from a different spatial extension d of the Schottky barrier. Experimentally, the effective IMFP and hence the depth information can be varied as

$$\lambda_{\mathrm{IMFP,\,eff}} = \lambda_{\mathrm{IMFP}} \cdot \cos\theta \tag{6.1}$$

by changing the angle θ under which the photoemission spectrum is acquired with respect to the surface normal. The respective Ti $2p_{3/2}$ spectra for $\theta = 0°$ and 50° off normal emission (NE) are shown in Fig. 6.14 (c). In contrast to that of $SrIrO_3$/$Nb_{0.05\%}$:$SrTiO_3$ (blue), the $SrIrO_3$/$Nb_{0.5\%}$:$SrTiO_3$ (gray) spectrum shows a distinct change as function of θ. Accordingly, for the higher Nb-doping concentration the spatial extension d is significantly smaller. This finding is in accordance with a study of the Schottky barrier profile at Pt/Nb_x:$SrTiO_3$ heterojunctions (x = 0.5, 0.05 & 0.01 wt.%) [279].

While the spatial extension d of the Schottky barrier is primarily reflected in the width of the Ti $2p$ line shape, its energetic height ΔE_{bb} essentially determines the Ti $2p$ peak position. Figure 6.14 (d) shows the Ti $2p_{3/2}$ peak positions of all samples under investigation. Since the peak positions of the $SrIrO_3$/$Nb_{0.05\%}$:$SrTiO_3$ samples (blue) are contorted by an energy shift of unknown magnitude due to electrostatic charging, a quantitative analysis of the Nb-doping concentration dependence of ΔE_{bb} is not possible. However, the 2 uc $SrIrO_3$/$Nb_{0.05\%}$:$SrTiO_3$ sample is found to lie at a significantly *lower* binding energy com-

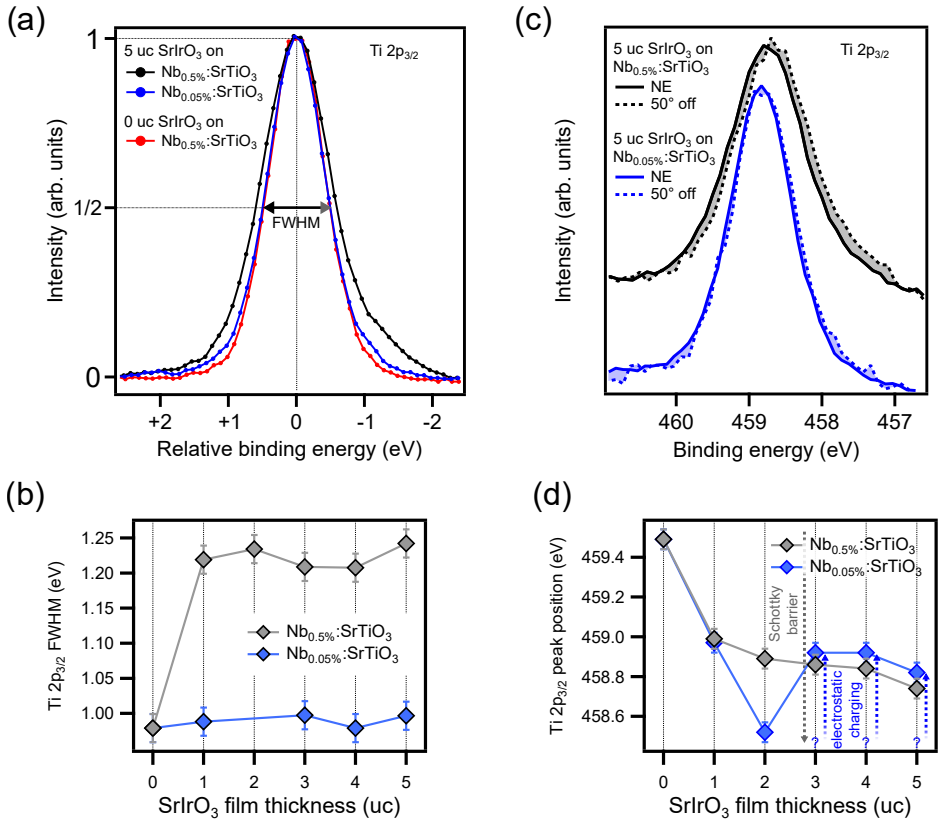

Figure 6.14: (a) Ti $2p_{3/2}$ core-level spectra of $Nb_{0.5\%}$:$SrTiO_3$ and $Nb_{0.05\%}$:$SrTiO_3$ overgrown with 5 uc of $SrIrO_3$ and a bare $Nb_{0.5\%}$:$SrTiO_3$ substrate. The spectra are shifted to the same peak position, background-subtracted and normalized to the peak maximum. The peak widths (FWHM) of the overgrown substrates significantly depend on the Nb-doping level. (b) Ti $2p_{3/2}$ peak widths as function of $SrIrO_3$ film thickness. (c) Ti $2p_{3/2}$ core-level spectra of $Nb_{0.5\%}$:$SrTiO_3$ and $Nb_{0.05\%}$:$SrTiO_3$ overgrown with 5 uc of $SrIrO_3$, acquired under normal and 50° off normal emission. (d) Ti $2p_{3/2}$ peak position as function of $SrIrO_3$ film thickness. The non-monotonous trend for $Nb_{0.05\%}$:$SrTiO_3$ is due to electrostatic charging, which counteracts the energy shift due to the formation of a Schottky barrier.

pared to $SrIrO_3$/$Nb_{0.5\%}$:$SrTiO_3$. Therefore, qualitatively, a lower Nb-doping concentration leads to a *larger* Schottky barrier height ΔE_{bb}. This finding is in agreement with a comparative internal photoemission spectroscopy study of $SrRuO_3$/Nb:$SrTiO_3$ junctions with 0.01 wt.% and 0.5 wt.% Nb-concentrations [276]. It is further confirmed by UPS valence-band spectra of a $SrIrO_3$ monolayer deposited on $Nb_{0.5\%}$:$SrTiO_3$ and $Nb_{0.05\%}$:$SrTiO_3$. As shown in Fig. 6.15 (a), the $SrTiO_3$ valence band onset is shifted towards the chemical potential by 0.62 eV and 0.75 eV, respectively, while the Ir 5*d* states in the band gap of $SrTiO_3$ are at equal binding energy.

For a more quantitative analysis of d and ΔE_{bb}, a simple model is adopted. The photoelectron line shape of a substrate core level $I_{\mathrm{substrate}}(E_{\mathrm{bin}})$ is assumed to result from a superposition of exponentially damped and energy-shifted spectra from all layers in the

substrate

$$I_{\text{substrate}}\left(E_{\text{bin}}\right) \propto \sum_{i=0}^{\infty} e^{-ia/\lambda_{\text{SrTiO}_3}(E_{\text{kin}})\cos(\theta)} \cdot I_{\text{SrTiO}_3}\left(E_{\text{bin}} - \Delta E_{bb,i}\right), \tag{6.2}$$

where the exponential term describes the damping of the signal from the i^{th} $SrTiO_3$ layer, $a = 3.905\,\text{Å}$ is the lattice parameter, λ_{IMFP} is the photoelectron IMFP from the TPP2 equation [178], I_{SrTiO_3} is the reference spectrum acquired from the bare $SrTiO_3$ substrate and $\Delta E_{bb,i}$ is the energy shift due to the Schottky-type barrier, parametrized by a parabolic approximation:

$$\Delta E_{bb,i}\left(z = i \cdot a\right) = \begin{cases} \Delta E_{bb}\left(\frac{z}{d} - 1\right)^2 & \text{for } 0 < z < d \\ 0 & \text{else.} \end{cases} \tag{6.3}$$

As exemplarily shown in Fig. 6.15 (b) the Ti $2p$ spectrum of the 5 uc $SrIrO_3/Nb_{0.5\%}$:$SrTiO_3$ sample is well-reproduced by a Schottky barrier height of $\Delta E_{bb} = 1.07\,\text{eV}$ and a spatial extension of $d = 69\,\text{Å}$. A small discrepancy between the model and the experimental data can be discerned at the low-energy side of the spectrum, which is reminiscent of a chemically shifted contribution from a small amount of Ti cations in the 3+ oxidation state [179]. However, the Schottky-type upwards band bending contradicts this interpretation [275, 286]. Instead, the rather simplified parabolic approximation of the potential distribution in Eq. 6.3 most likely accounts for the small discrepancy and a more accurate quantitative model incorporating the strong electric field dependence of the electrical permittivity of Nb:$SrTiO_3$ might further improve the fit results [279, 287, 288]. The Ti $2p$ spectrum of the 5 uc $SrIrO_3/Nb_{0.05\%}$:$SrTiO_3$ sample is equally well-reproduced by a Schottky barrier height of $\Delta E_{bb} = 0.75\,\text{eV}$ and a spatial extension of $d = 148\,\text{Å}$. However, as qualitatively discussed above, the obtained value for ΔE_{bb} is not physically meaningful due to the superimposed electrostatic charging effect. The fit results as function of film thickness for $SrIrO_3/Nb_{0.5\%}$:$SrTiO_3$ are summarized in Fig. 6.15 (c).

In a combined current-voltage, capacitance-voltage and internal photoemission study a barrier height of $\approx 1.44\,\text{eV}$ was recently reported for $SrIrO_3$/Nb:$SrTiO_3$ with 0.01 wt.% Nb-concentration and a $SrIrO_3$ thickness of 21 nm [281]. As shown in Fig. 6.15 (c), the Ti $2p$ fit analysis yields a systematical increase of $|\Delta E_{bb}|$ and d as function of $SrIrO_3$ thickness. Hence, given the differences in Nb-doping concentration and $SrIrO_3$ thickness, the Schottky barrier height from Ref. [281] is found to be of a comparable order of magnitude.

Finally, Fig. 6.15 (d) shows the absolute Ti $2p$ photoelectron intensity per time, normalized to the secondary electron background between 570 and 750 eV binding energy to approximately account for variations in the x-ray photon flux. An excellent agreement is found between the experimental intensity and the theoretically expected exponential damping due to the increasing number n of $SrIrO_3$ layers

$$I_{\text{Ti }2p,\text{ total}} \propto \exp\left(-\frac{n \cdot a}{\lambda_{\text{IMFP, SrIrO}_3}\left(E_{\text{kin, Ti }2p}\right)}\right), \tag{6.4}$$

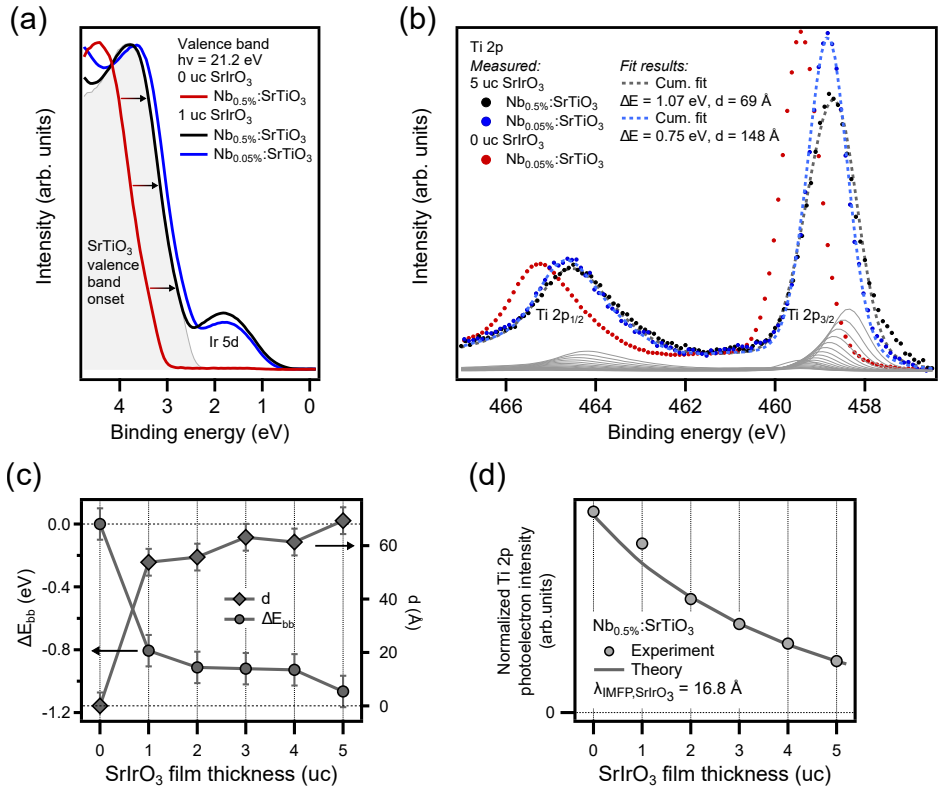

Figure 6.15: (a) UPS valence-band spectra of $Nb_{0.5\%}$:$SrTiO_3$ and $Nb_{0.05\%}$:$SrTiO_3$ overgrown with 1 uc of $SrIrO_3$ and a bare $Nb_{0.5\%}$:$SrTiO_3$ substrate. The $SrTiO_3$ band onset is found to be shifted towards the chemical potential for the overgrown samples. (b) Exemplary fit results for the Ti 2*p* peak assuming a parabolic Schottky barrier within the $SrTiO_3$ substrate. (c) Fit results for the barrier height ΔE_{bb} and spatial extension d of the parabolic Schottky model for $SrIrO_3$:$Nb_{0.5\%}$:$SrTiO_3$ heterostructures as function of $SrIrO_3$ thickness. (d) The normalized Ti 2*p* photoelectron intensity as function of $SrIrO_3$ thickness agrees with the exponential-damping model using the IMFP from the TPP2-equation [178].

where $\lambda_{\mathrm{IMFP,\,SrIrO_3}} = 16.8$ Å is the photoelectron IMFP calculated using the TPP2 equation [178] for $SrIrO_3$ at the kinetic energy of Ti 2*p* photoelectrons. The correctness of the TPP2 equation is thereby confirmed for $SrIrO_3$.

In summary, the observed changes in the Ti 2*p* substrate core-level spectra as function of $SrIrO_3$ thickness are qualitatively and quantitatively explained by the formation of a Schottky barrier within the substrate. In accordance with other reports of $SrTiO_3$-based heterojunctions the spatial distribution d of the Schottky barrier strongly depends upon the Nb-dopant concentration of the $SrTiO_3$ substrate, most likely due to screening by the doped charge carriers. The Schottky barrier forms after deposition of only one monolayer of $SrIrO_3$ and gradually increases as function of film thickness. The quantitative fit accuracy for the Ti 2*p* core-level spectra within a Schottky model may benefit significantly from a systematic variation of the depth information via the photoemission angle θ and/or the photon energy $h\nu$ during data acquisition. Furthermore, a more sophisticated quantitative model beyond the parabolic approximation used in this study might yield more detailed information about the physical origin of the band bending.

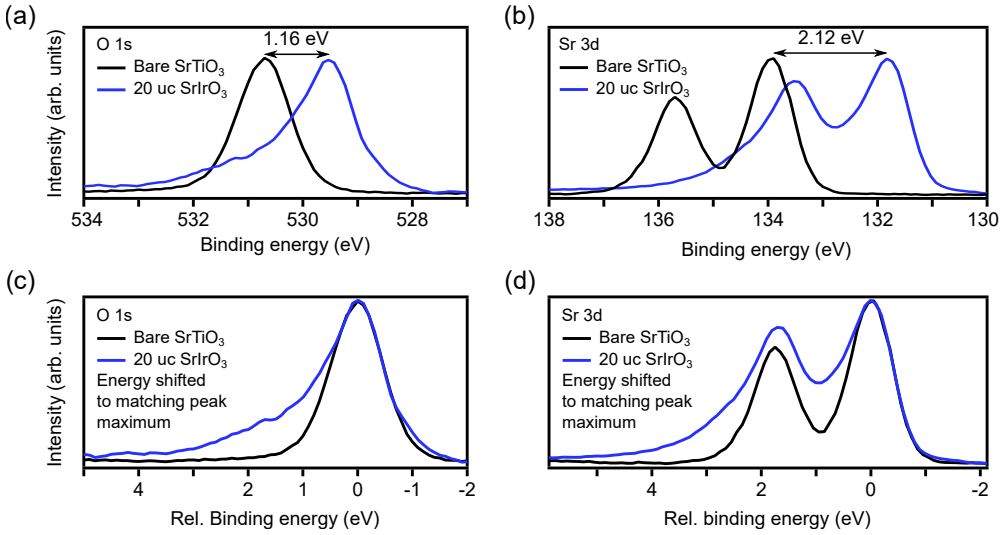

Figure 6.16: (a) O 1*s* (b) and Sr 3*d* core-level spectra of bulk $SrTiO_3$ and $SrIrO_3$ (a 20 uc thick film). The material-dependent energy shifts of the core levels are significantly different for strontium and oxygen. (c), (d) The core-level spectra of $SrIrO_3$ exhibit a significant asymmetric broadening in contrast to those of $SrTiO_3$.

6.2.2 Footprint of octahedral rotations in strontium and oxygen core-level spectra – Madelung potential vs. band alignment

The intrinsic elemental sensitivity of XPS allows for the separate investigation of electronic effects in the $SrTiO_3$ substrate and the $SrIrO_3$ film by analysis of the characteristic titanium and iridium core-level spectra, respectively. In contrast, the strontium and oxygen core-level spectra are composed of a substrate and a film contribution. As seen in Fig. 6.12, the Sr 3*d*, Sr 3*p* and O 1*s* spectra exhibit pronounced changes as function of $SrIrO_3$ film thickness, which seem to result from a varying binding energy offset between substrate and film contributions. The relative positions of core levels in XPS spectra has long been utilized for the determination of band offsets and band bending in semiconductor heterojunctions, based on the assumption that the binding energies of all core levels similarly trace the spatially varying electrostatic potential at a heterointerface [173, 174]. At first glance, the strong relative core-level shifts in the substrate and film XPS spectra may therefore be interpreted as a result of a changing band alignment (and bending) at the $SrIrO_3/SrTiO_3$ interface.

As a starting point for the analysis of the film-thickness-dependent spectral changes, Fig. 6.16 depicts the O 1*s* and Sr 3*d* core-level spectra of bare $SrTiO_3$ and a thick $SrIrO_3$ film (20 uc). While both core-level spectra of $SrIrO_3$ (blue) lie at smaller binding energies than those of $SrTiO_3$ (black), the energy differences of the Sr 3*d* and O 1*s* levels are not the same but amount to 2.12 eV and only 1.16 eV, respectively. Accordingly, the relative energy differences between strontium and oxygen sites $E_{\mathrm{bin}}(\mathrm{O}\ 1s) - E_{\mathrm{bin}}(\mathrm{Sr}\ 3d)$ in $SrTiO_3$ and $SrIrO_3$ deviate by almost 1 eV as summarized in Tab. 6.1. Therefore, the observed spectral changes cannot be (exclusively) attributed to changes of the interfacial band alignment (and bending), since the observation of site-dependent, local changes of the electrostatic potential

	$SrTiO_3$	$SrIrO_3$
E_{bin}(O 1s)	530.69 eV	529.53 eV
E_{bin}(Sr 3d)	133.93 eV	131.81 eV
E_{bin}(O 1s) − E_{bin}(Sr 3d)	396.76 eV	397.72 eV
	+0.96 eV	

Table 6.1: Absolute and relative binding energies of O 1s and Sr 3d core levels in $SrTiO_3$ and $SrIrO_3$

contradicts the fundamental assumption of an (only) globally varying potential [173].

The band structures of most semiconductors originate from the predominantly covalent bonding between their atomic constituents. In contrast, transition metal oxides exhibit a strong ionic character, which gives rise to a strongly varying site-dependent electrostatic (or: Madelung) potential. The Madelung potential for a single site in a crystal is made up of the Coulomb potentials of all other ions in the lattice and is therefore strongly susceptible to variations of the periodic arrangement thereof. Since $SrTiO_3$ adopts the ideal cubic and $SrIrO_3$ a distorted perovskite structure of the $GdFeO_3$-type their Madelung potentials differ and may give rise to the above-described differences in the core-level binding energies of $SrTiO_3$ and $SrIrO_3$. Moreover, owing to the large spatial extent of the 5d orbitals covalency effects are known to play a bigger role in 5d transition metal oxides like iridates than in their 4d or 3d counterparts (e.g., $SrTiO_3$). The resulting effective deviations from the formal ionic charges due to covalency may further influence the Madelung potentials and the corresponding binding energy shifts. To pursue these ideas further, the Madelung potentials for the strontium and oxygen sites in $SrTiO_3$ and $SrIrO_3$ are investigated quantitatively in the following.

Madelung potentials in bulk $SrTiO_3$ and $SrIrO_3$ − crystal structure and covalency effect

The Madelung potentials of the ideal cubic perovskite structure of bulk $SrTiO_3$ and those of the $GdFeO_3$-type distorted perovskite structure reported for polycrystalline $SrIrO_3$[10] are calculated numerically using Ewald's method [289], as described in detail in the Appendix, assuming the formal ionic charges Sr^{2+}, Ir^{4+}, Ti^{4+} and O^{2-}. As summarized in Tab. 6.2, the cubic (space group $Pm\bar{3}m$) and the orthorhombic perovskite structure (space group $Pnma$) host three and four inequivalent lattice sites, respectively. Indeed, the Madelung potentials Φ_i of the ionic sites are significantly renormalized as a result of the distortions of the lattice structure and the different bonding lengths. In particular, the energetic difference between strontium and oxygen sites $\Delta\Phi_{\text{O-Sr}} = \Phi_{\text{Sr}} - \Phi_{\text{O}}$ in $SrTiO_3$ is $\approx 1\,\text{eV}$ and $\approx 0.5\,\text{eV}$

[10]Note, that the originally reported lattice structure by Zhao *et al.* [99] was erroneous as pointed out by Puggioni *et al.* [100]. The corrected lattice structure was used for the Madelung potential calculations.

smaller than for the two inequivalent oxygen sites O(1) and O(2) of $SrIrO_3$, respectively. Accordingly, the observed discrepancy in Fig. 6.16 can be naturally explained by the different site-dependent electrostatic potentials in bulk $SrIrO_3$ and $SrTiO_3$ as a result of their different lattice structure.

Effect of covalency on the Madelung potentials Aside from differences in the lattice structure, the site-dependent Madelung potentials are influenced by deviations from the purely ionic picture due to covalent contributions to the interatomic bonds [175]. Covalency effects are expected and have been experimentally shown to be significant in iridates due to the rather large extent of the $5d$ orbitals [25, 290]. In Madelung potential calculations the covalency effect can be easily modeled by reducing the formal valency of the B cation, while correspondingly increasing the valency of the O anions to guarantee charge neutrality [175]:

$$\mathrm{Sr}^{2+}\mathrm{Ir}^{4+}\mathrm{O}_3^{2-} \rightarrow \mathrm{Sr}^{2+}\mathrm{Ir}^{(4-\delta)+}\mathrm{O}_3^{(2-\delta/3)-} \tag{6.5}$$

The resulting site-dependent Madelung potentials of the bulk form of $SrIrO_3$ [99, 100] as function of δ are shown in Fig. 6.17. As expected, the oxygen and iridium Madelung potentials are affected most strongly by the increasing covalency of the Ir-O bonds, whereas the strontium site is hardly affected. Specifically, the energetic difference between strontium and oxygen sites $\Delta\Phi_{\text{O-Sr}}$ becomes smaller as δ increases, since the absolute charge numbers in the lattice decrease. Therefore, in this simple model increasing covalency in bulk $SrIrO_3$ reduces the difference between $\Delta\Phi_{\text{O-Sr}}$ of $SrIrO_3$ and $SrTiO_3$.

In summary, the orthorhombic lattice structure of bulk $SrIrO_3$ reported by Zhao *et al.* [99] and Puggioni *et al.* [100] can thus naturally explain the experimentally observed binding energy differences. However, the reported structure only emerges under high temperature (1000 °C) and high pressure (5 GPa) and is quenched to ambient pressure as a metastable phase [17]. This is a fundamentally different synthesis route than the thin-film heteroepitaxy used in this study, where the perovskite structure is stabilized by epitaxial strain to

Cubic $SrTiO_3$		Orthorhombic $SrIrO_3$	
Φ_{Sr}	−19.86 V	Φ_{Sr}	−20.85 V
Φ_{Ti}	−45.64 V	Φ_{Ir}	−43.77 V
Φ_{O}	+23.81 V	$\Phi_{\text{O(1)}}$	+23.79 V
		$\Phi_{\text{O(2)}}$	+23.32 V
$\Delta\Phi_{\text{O-Sr}} = \Phi_{\text{O}} - \Phi_{\text{Sr}}$	43.67 V	$\Delta\Phi_{\text{O-Sr}} = \Phi_{\text{O(1)}} - \Phi_{\text{Sr}}$	44.64 V
		$\Delta\Phi_{\text{O-Sr}} = \Phi_{\text{O(2)}} - \Phi_{\text{Sr}}$	44.17 V

Table 6.2: Site-dependent Madelung potentials of bulk cubic $SrTiO_3$ and bulk orthorhombic $SrIrO_3$

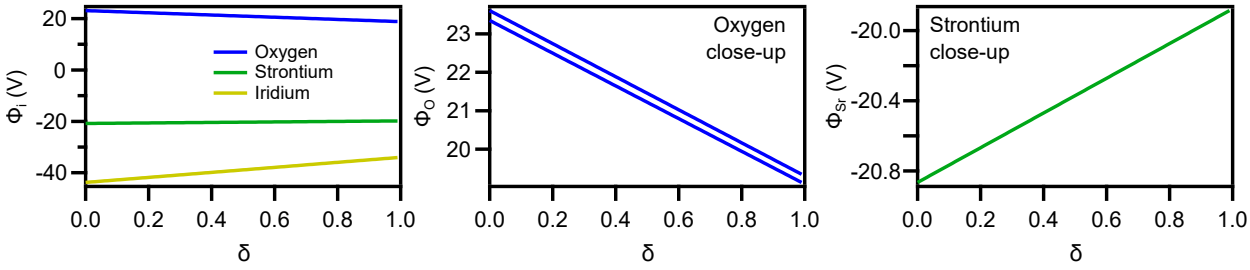

Figure 6.17: Site-dependent Madelung potentials Φ_i of bulk orthorhombic $SrIrO_3$ with formal ionic charges Sr^{2+}, $Ir^{4-\delta}$ and $O^{(\delta/3)-2}$, i.e., with increasing covalent character of the Ir-O bonds. The limit $\delta = 0$ corresponds to the values in Tab. 6.2.

the $SrTiO_3$ substrate. Here, the $SrIrO_3$ film adopts the in-plane lattice parameters of the substrate and, as shown in Sec. 6.1.2, the cubic $SrTiO_3$ imposes constraints upon the IrO_6 octahedral rotations. The resulting lattice structure may therefore differ significantly from the metastable ambient pressure form of $SrIrO_3$ and consequently the actual Madelung potentials in the film may differ from those in Tab. 6.2. For this reason, a structural model incorporating the constraints from the substrate is developed in the following.

Structural model of octahedral rotations in a strained perovskite

In an attempt to mimic the observed structural transition described in Sec. 6.1.2, a structural model of octahedral rotations in a strained perovskite is designed. Essentially, the model is based on the geometrical problem how to fit a rigid regular octahedron into a rectangular cuboid with two fixed edges, such that its vertices lie on the faces of said cuboid (cf. Fig. 6.18). Following the derivation of the model's mathematical description, it is employed to calculate more realistic values of the Madelung potentials in $SrIrO_3$ in a thin-film geometry.

The cation sublattice is assumed to be heteroepitaxially strained to the $SrTiO_3$ substrate, i.e., with the in-plane lattice parameters $a = b = 3.905\,\text{Å}$ and a variable out-of-plane lattice parameter c. The iridium cation acts as inversion center and is positioned at the origin of the coordinate system $\mathbf{v}_{Ir} = (0, 0, 0)$. It is surrounded by a regular IrO_6 octahedron with Ir-O bond length d (where $d > a/2$), described by three orthogonal vectors $\mathbf{v}_i$ ($\mathbf{v}_i \cdot \mathbf{v}_j = d^2 \cdot \delta_{i,j}$, where $\delta_{i,j}$ is the Kronecker delta). Since, in contrast to the A-O bond, the B-O bond is typically not compressible in ABO_3 perovskites [49], the octahedron is assumed rigid, i.e., d is fixed. The Ir-O bond length $d = 2.0219\,\text{Å}$ is adopted from the metastable room-temperature $SrIrO_3$ phase [99].

The oxygen anions lie on the faces of the unit cell, i.e., $v_{1,x} = a/2, v_{2,y} = a/2, v_{3,z} = c/2$. Hence, the position of the first oxygen ion can be parametrized by

$$\mathbf{v}_1 = \begin{pmatrix} a/2 \\ R\cos\varphi \\ R\sin\varphi \end{pmatrix}, \text{ where } R = \sqrt{d^2 - \left(\frac{a}{2}\right)^2}, \tag{6.6}$$

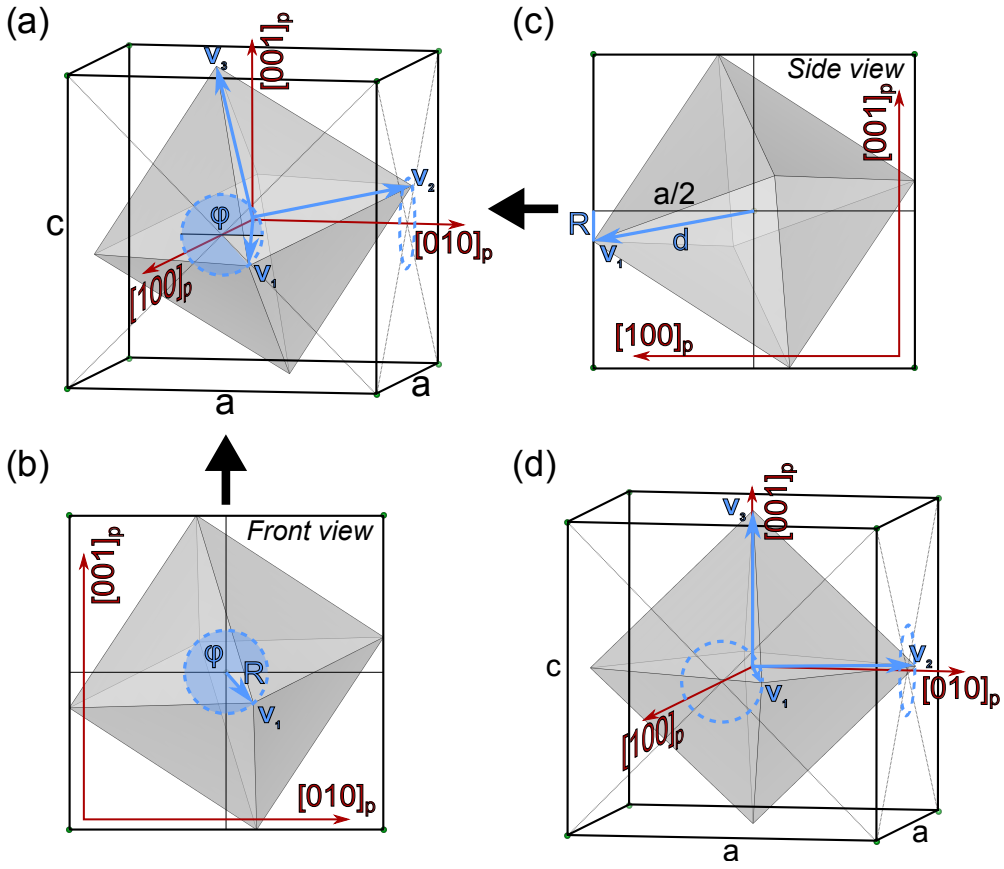

Figure 6.18: Model of the structural transition due to octahedral rotations in a strained perovskite. (a) Three-dimensional view of a tilted rigid IrO_6 octahedron in a strained cationic sublattice with in- and out-of-plane lattice parameters a and c. The tilt is parametrized by the angle φ. (b), (c) Front and side view of the structural model, defining φ, R and d. (d) Structural model without in-plane tilting of the octahedron, i.e., $\varphi = 0$.

where φ serves as parameter to continuously tune the octahedral rotations[11] as depicted in Fig. 6.18. The position of the second oxygen anion can be described by

$$\mathbf{v}_2 = \begin{pmatrix} v_{2,x} \\ a/2 \\ v_{2,z} \end{pmatrix}, \tag{6.7}$$

which fulfills the geometrical boundary conditions

$$\mathbf{v}_1 \cdot \mathbf{v}_2 = \frac{v_{2,x} \cdot a}{2} + \frac{aR}{2}\cos\varphi + v_{2,z} R \sin\varphi \stackrel{!}{=} 0 \quad \text{and} \quad R^2 \stackrel{!}{=} v_{2,x}^2 + v_{2,z}^2 \tag{6.8}$$

[11] Note, that in contrast to Glazer's notation [47], here, φ *does not* parametrize the rotation of the *whole* octahedron about any of the orthogonal axes.

if

$$v_{2,x} = \frac{-a^2 R\cos\varphi \mp 2R^2\sin^2\varphi\,\sqrt{a^2+4R^2}}{a^2+4R^2\sin^2\varphi} \tag{6.9}$$

$$\text{and} \quad v_{2,z} = \frac{-2aR^2\sin\varphi\cos\varphi \pm aR\sin\varphi\,\sqrt{a^2+4R^2}}{a^2+4R^2\sin^2\varphi}. \tag{6.10}$$

Finally, the position of the third, apical oxygen anion is given by the cross product

$$\mathbf{v}_3 = \begin{pmatrix} v_{3,x} \\ v_{3,y} \\ c/2 \end{pmatrix} = \frac{1}{d}\,\mathbf{v}_1 \times \mathbf{v}_2. \tag{6.11}$$

The resulting positions of the three oxygen sites of one octahedron as function of $\varphi \in [0°, 180°]$ are summarized in Fig. 6.19. As imposed by the geometrical boundary conditions the in-plane oxygen anions adopt positions which lie on a circle (Fig. 6.19 (a), black and blue). In contrast, the apical oxygen site (red) adopts the face center position for $\varphi = 0°$ (cf. Fig. 6.18 (d)) and moves on a club-like curve with a maximum distance from the face center at $\varphi \approx 90°$. The individual components of the vectors $\mathbf{v}_1$, $\mathbf{v}_2$ and $\mathbf{v}_3$ are shown as function of φ in Fig. 6.19 (b) - (d). Although the in-plane oxygen positions are described by an identical circle on the unit cell faces, the momentary positions are not identical for any $\varphi \neq 0°$ and $\neq 180°$. Furthermore, the model yields a variable c-axis with the extrema

$$v_{3,z} = c/2 = \frac{1}{d}\left(\frac{a^2}{4} - v_{1,y}v_{2,x}\right) \text{ (cf. Eq. 6.11)} \tag{6.12}$$

$$= \begin{cases} d \text{ for } \varphi = 0° \text{ and } \varphi = 180° \\ a - d \text{ for } \varphi = \cos^{-1}\left(\frac{\sqrt{a^2+4R^2}}{2R}\right). \end{cases} \tag{6.13}$$

If one particular octahedron in the perovskite structure is tilted, it will cause tilting in the neighboring octahedra, since the IrO_6 octahedra form a corner-shared network in the crystal. As described by Glazer [47] all possible resulting crystal structures can be described in a supercell consisting of $2 \times 2 \times 2$ octahedra and successive octahedra along a particular axis i are constrained to have opposite tilt about the orthogonal axes j and k. In other words, the vectors $\mathbf{v}_{i,100}$ spanning the next octahedron along the $[100]_p$ crystal direction are given by:

$$\mathbf{v}_{1,100} = \begin{pmatrix} 1 & 0 & 0 \\ 0 & -1 & 0 \\ 0 & 0 & -1 \end{pmatrix} \cdot \mathbf{v}_{1,000} \tag{6.14}$$

$$\mathbf{v}_{2,100} = \begin{pmatrix} v_{2,100,x} \\ a/2 \\ v_{2,100,z} \end{pmatrix} \text{ with } \mathbf{v}_{1,100} \cdot \mathbf{v}_{2,100} = 0 \text{ and } R^2 = v_{2,100,x}^2 + v_{2,100,z}^2 \tag{6.15}$$

$$\mathbf{v}_{3,100} = \mathbf{v}_{1,100} \times \mathbf{v}_{2,100}/d \tag{6.16}$$

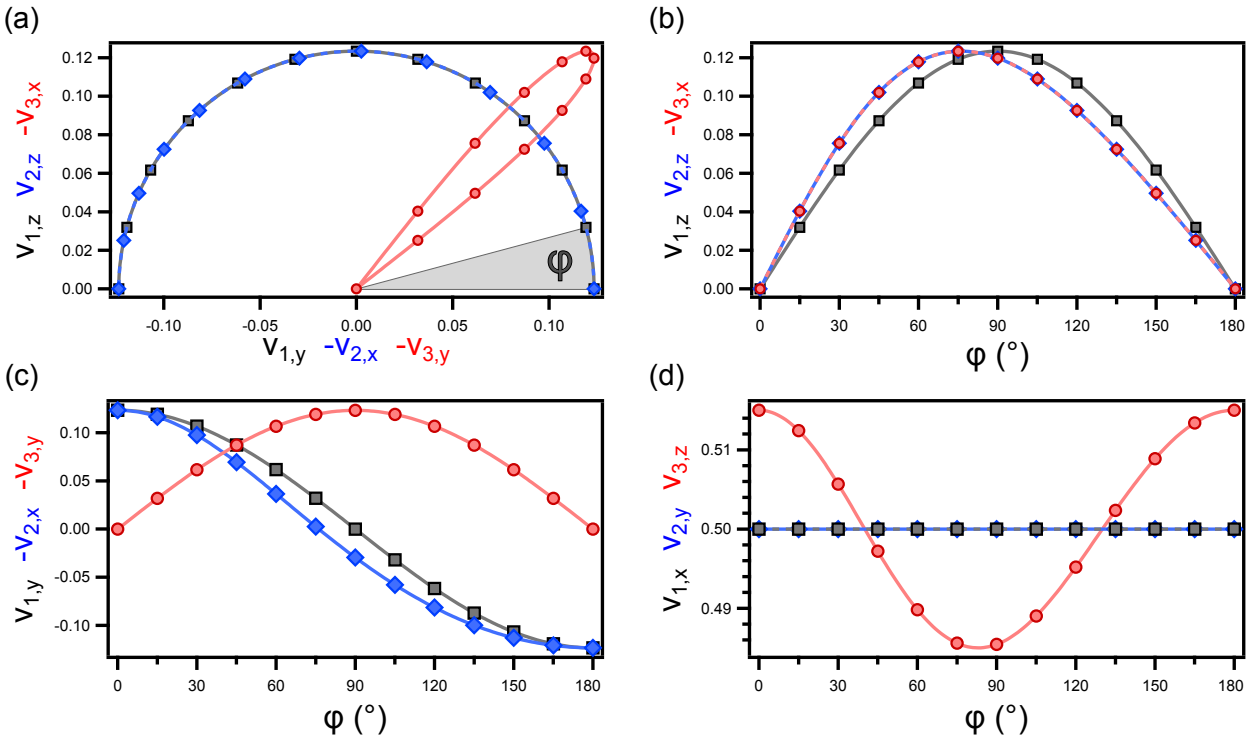

Figure 6.19: Components of the vectors $\mathbf{v}_1$, $\mathbf{v}_2$ and $\mathbf{v}_3$, spanning the IrO_6 octahedron as function of tilting, parametrized by φ. For definition of $\mathbf{v}_i$ and φ, see Fig. 6.18. The markers denote steps of $\Delta\varphi = 15°$. (a) Oxygen position on the three faces of the cationic unit cell in Fig. 6.18. (b) - (d) Vector components as function of φ.

The quadratic Eq. 6.15 has two solutions ($\pm$), which correspond to in- and out-of-phase rotations along this direction, as denoted in Glazer's notation by a superscript $a^{\pm}$. Using equivalent constraints and the correct sign for successive octahedra along the $[010]_p$ and $[001]_p$ directions, the whole $2 \times 2 \times 2$ supercell can be constructed. Figure 6.20 shows the resulting unit cell for the two cases $\varphi = 0°$ and $\varphi = 90°$ from a three-dimensional perspective and as projection onto the three orthogonal axes. Obviously, for $\varphi = 0°$ no octahedral rotations about the x- and y-axes persist, hence resulting in an $a^0a^0c^-$ structure in Glazer's notation (cf. Sec. 2.2). In this case, the $2 \times 2 \times 2$ unit cell is redundant as the crystal symmetry can be fully described by a $\sqrt{2} \times \sqrt{2} \times 2$ unit cell. As discussed in Sec. 6.1.2, this case corresponds to the octahedral pattern observed in thin $SrIrO_3$ films ($m \leq 3$ uc). In contrast, the oxygen octahedra exhibit rotations about all three orthogonal axes for $\varphi = 90°$. In particular, the octahedral rotations are found to rotate in-phase along the x- and out-of-phase along the y- and z-axes. Since the magnitude of these rotations is different, this case is described by $a^+b^-c^-$ in Glazer's notation and hence qualitatively corresponds to the experimentally observed lattice structure in thick ($m \geq 4$ uc) $SrIrO_3$ films (cf. Sec. 4.5).

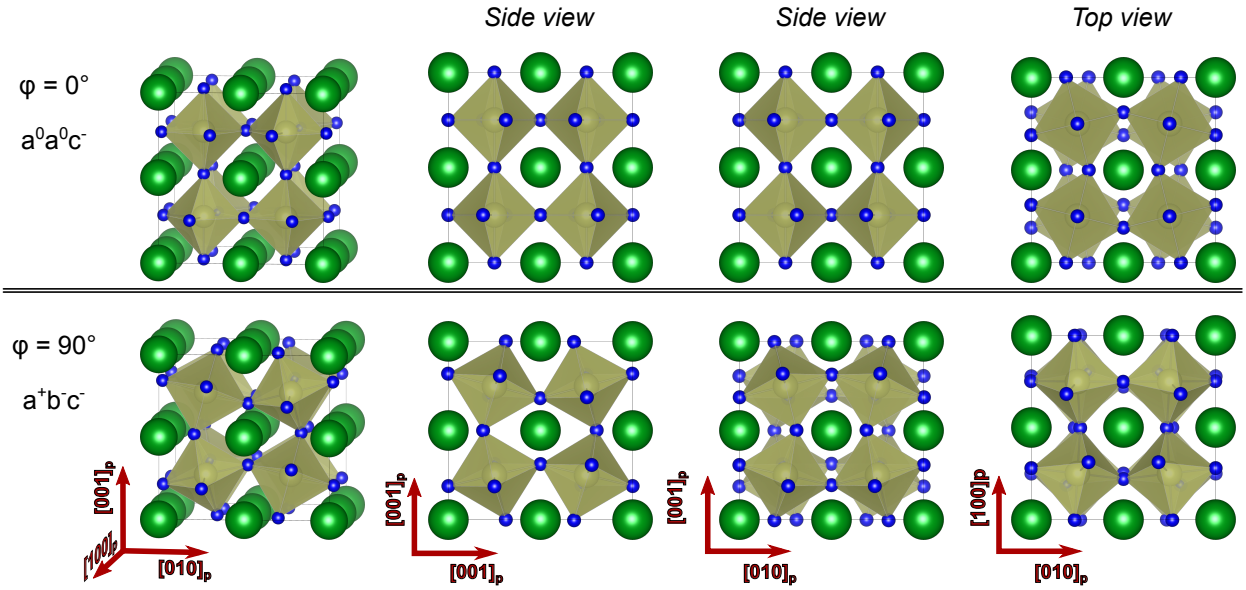

Figure 6.20: Structural model of the $2 \times 2 \times 2$ unit cell for two exemplary cases $\varphi = 0°$ and $\varphi = 90°$ corresponding to $a^0a^0c^-$ and $a^+b^-c^-$.

Madelung potential changes due to octahedral rotations

Figure 6.21 shows the site-dependent Madelung potentials calculated for the above-described structural model of strained $SrIrO_3$ as function of octahedral tilting (parametrized by φ). As shown in detail in Fig. 6.21 (b), the symmetry breaking due to the introduction of a finite tilting angle φ lifts the (partial) degeneracy of the site-dependent Madelung potentials. For $\varphi = 0°$ (and $\varphi = 180°$) a high-symmetry $a^0a^0c^-$ octahedral pattern is realized, where all iridium and strontium sites are equivalent and the oxygen sites can be discriminated into in-plane and apical oxygen sites with different Madelung potentials. Furthermore, at $\varphi \approx 105°$, an octahedral pattern described by $a^+a^-c^0$ is realized, i.e., rotations with equal magnitude about the x- and y-axes and no rotations about the z-axis. In this geometry, all iridium sites are equivalent, while there are two inequivalent strontium and three inequivalent oxygen sites. At intermediate φ values, a low-symmetry $a^+b^-c^-$ structure is realized, where all oxygen and strontium sites and every second iridium site are inequivalent, resulting in a complex distribution of the Madelung potentials. The bulk reference values from Tab. 6.2 are depicted as faint horizontal lines.

Figure 6.21 (c) depicts the average Madelung potentials of the three elemental species in $SrIrO_3$

$$\overline{\Phi}(\varphi) = \frac{1}{N} \sum_{i=0}^{N} \Phi_i(\varphi), \tag{6.17}$$

where N is the number of sites in the $2 \times 2 \times 2$ unit cell, which can be taken as an estimate for the observed peak binding energy in core-level photoemission spectroscopy. The average Madelung potential of the oxygen and strontium sites increases by $\approx 0.4\,\mathrm{eV}$ upon introduc-

tion of octahedral rotations about the a- and b-axes (increasing φ), whereas, in contrast, the average Madelung potential of the strontium sites decreases by $\approx 1.9\,\mathrm{eV}$. The (possibly asymmetric) broadening of the core-level spectra due to the distribution of the Madelung potentials is reflected by the standard deviation

$$\sigma_\Phi(\varphi) = \frac{1}{N}\sqrt{\sum_{i=0}^{N}\left[\Phi_i(\varphi) - \overline{\Phi}(\varphi)\right]^2}, \tag{6.18}$$

which is depicted as colored area around the mean value. In the high-symmetry $a^0a^0c^-$ lattice structure ($\varphi = 0°$) all strontium sites are equivalent and no broadening is expected. In contrast, the introduction of octahedral rotations lifts the degeneracy of strontium sites and is expected to introduce an asymmetric broadening. Indeed, the Sr $3d$ core-level spectrum of the $SrIrO_3$ reference in Fig. 6.16 (d) does exhibit a strong broadening, which is significantly more pronounced than, e.g., a typical Doniach-Ŝunjić-type broadening due to coupling between the core hole and the metallic conduction electrons [291]. The energy difference $\Delta\overline{\Phi}_{\text{O-Sr}} = \overline{\Phi}_{\text{O}} - \overline{\Phi}_{\text{Sr}}$ in Fig. 6.21 (d) shows an increasing trend as φ is increased. The calculated value of bulk cubic $SrTiO_3$ (cf. Tab. 6.2) is depicted as blue line and is found to be slightly smaller than that of the $a^0a^0c^-$ structure ($\varphi = 0°$). The experimentally found value in $SrIrO_3$ is 0.96 eV larger than that of $SrTiO_3$ (cf. Tab. 6.1) and corresponds to a value of $\varphi \approx 30°$.

In summary, the site-dependent Madelung potentials in a hypothetical infinite $SrIrO_3$ crystal with the in-plane lattice parameters of $SrTiO_3$ can change on the order of 0.5 - 2 eV as function of the tilting of the IrO_6 octahedra. Such a strong modification of the electrostatic potential within the crystal might have severe effects on the electronic structure. However, the calculation of the Madelung potential using Ewald's method is based on the assumption of an infinite crystal, whereas the investigated epitaxial $SrIrO_3$ films have a finite thickness. Accordingly the site-dependent Madelung potential within the thin films will differ from the calculated bulk value as the ions are subject to the electrostatic attraction from the ions in the adjacent $SrTiO_3$ and the symmetry-breaking at the interface to the vacuum has to be taken into account. While the analysis of the band bending in the substrate (cf. Sec. 6.2.1) may be likewise influenced by the film, its result will nonetheless essentially reflect the actual band bending. In contrast, the analysis of the interfacial band alignment and the band bending within the film is highly problematic for films with structural changes as function of the film thickness. To further pursue this question, in the following, the strontium and oxygen core-level spectra are decomposed into their substrate and film contributions in an attempt to disentangle the effects of film thickness and octahedral rotations.

Madelung potential in the thin-film limit − core level decomposition

For the analysis of the strontium and oxygen core-level spectra as function of film thickness a simple model is adopted by which they are interpreted as a linear superposition of the

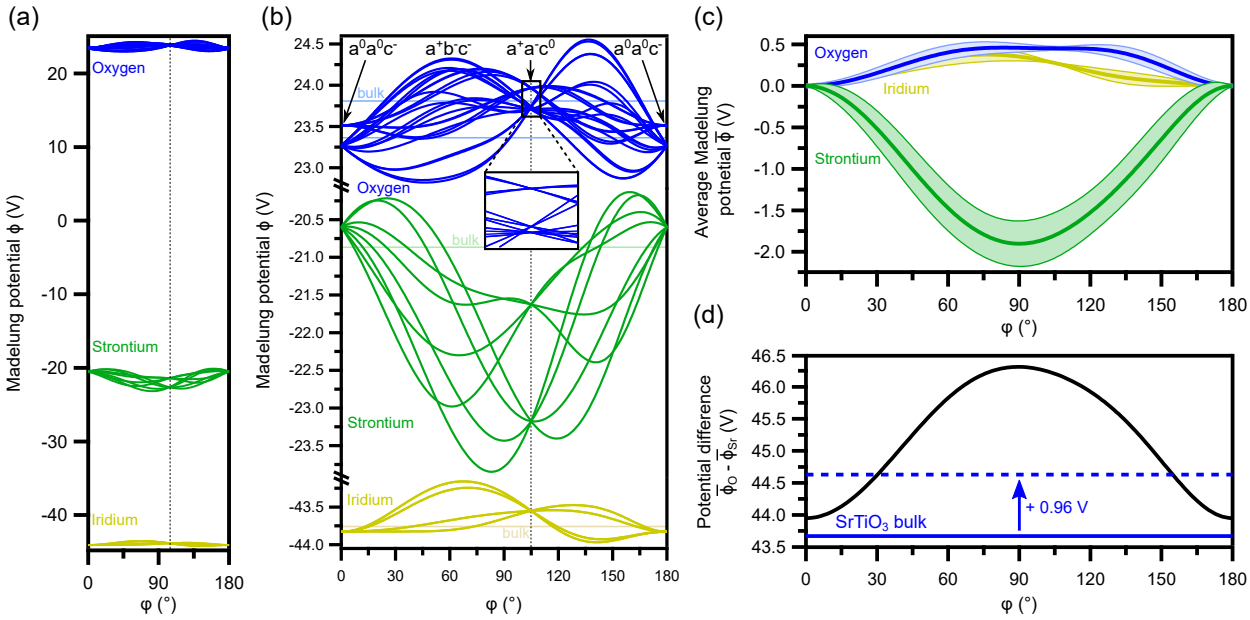

Figure 6.21: (a) Madelung potential Φ_i of all ion sites i in strained $SrIrO_3$ as function of octahedral tilting φ. (b) Closeup of the Madelung potentials of oxygen, strontium and iridium sites. A high-symmetry lattice structure is found for $\varphi = 0°$ ($a^0a^0c^-$) and $\varphi \approx 105°$ ($a^+a^-c^0$). (c) Mean Madelung potential deviation with respect to the $a^0a^0c^-$ pattern at $\varphi = 0°$ $\overline{\Phi}(\varphi) - \overline{\Phi}(\varphi = 0°)$ of oxygen, strontium and iridium. The colored areas reflect the standard deviation σ_Φ due to inequivalent ionic sites. (d) Difference of the mean Madelung potentials of oxygen and strontium sites ($\overline{\Phi}_O - \overline{\Phi}_{Sr}$) as function of φ. The potential difference changes by $\approx 2\,eV$ as the octahedral tilting is varied.

photoemission spectra from the $SrTiO_3$ substrate $I_{substrate}$ and the $SrIrO_3$ film I_{film}:

$$I\left(E_{bin}\right) = I_{film}\left(E_{bin}\right) + I_{substrate}\left(E_{bin}\right) \tag{6.19}$$

Under the assumption, that all substrate core levels trace the Schottky barrier similar to the Ti $2p$ core level in Sec. 6.2.1, the substrate contribution can be described as

$$I_{substrate}\left(E_{bin}\right) = I_0 \cdot e^{-na/\lambda_{SrIrO_3}(E_{kin})\cos\theta} \cdot \sum_{i=0}^{\infty} e^{-ia/\lambda_{SrTiO_3}(E_{kin})\cos\theta} \cdot I_{SrTiO_3}\left(E_{bin} - \Delta E_{bb,i}\right), \tag{6.20}$$

where n is the number of $SrIrO_3$ layers. For the $SrIrO_3/Nb_{0.5\%}$:$SrTiO_3$ samples $\Delta E_{bb,i}$ is given by Eq. 6.3 with the parameters ΔE_{bb} and d taken from the respective Ti $2p$ fits. In contrast, due to the negligible asymmetric broadening (cf. Fig. 6.14 (a)) and the complication due to electrostatic charging, $\Delta E_{bb,i} = \Delta E_{bb}$ is chosen as a constant fit parameter for the $SrIrO_3/Nb_{0.05\%}$:$SrTiO_3$ samples. I_{SrTiO_3} is a reference spectrum acquired from a bare $SrTiO_3$ substrate.

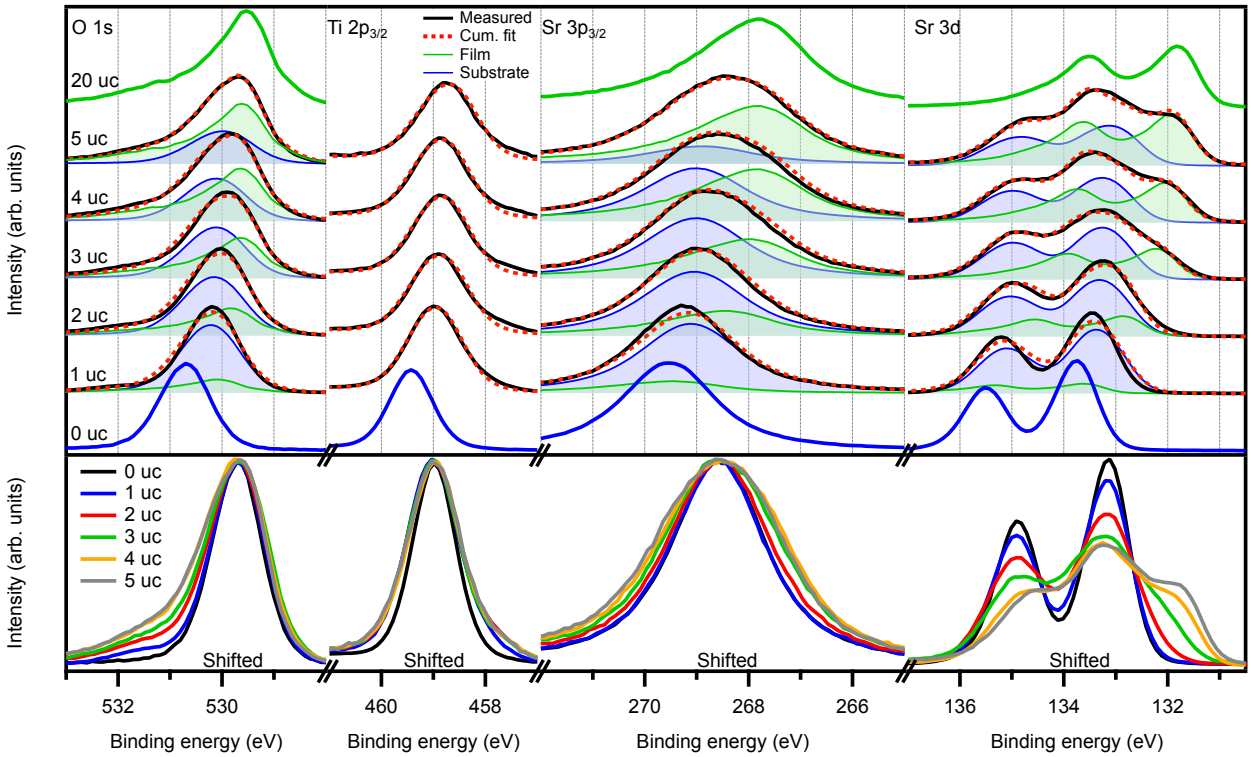

Figure 6.22: Decomposition of the O 1s, Sr 3$p_{3/2}$ and Sr 3d core-level spectra for $SrIrO_3$/$Nb_{0.5\%}$:$SrTiO_3$ heterostructures of different film thickness. The substrate contribution (thin blue) is modeled using the Schottky potential obtained from fitting the Ti 2p spectra using Eq. 6.2. The $SrTiO_3$ and $SrIrO_3$ bulk reference samples are shown in thick blue (0 uc) and thick green (20 uc). The lower section depicts the energy-shifted spectra. The O 1s, Ti 2$p_{3/2}$ and Sr 3$p_{3/2}$ spectra are normalized to their maximum intensity, the Sr 3d spectra are normalized to the same integrated intensity.

The film contribution is given by

$$I_{\text{film}}\left(E_{\text{bin}}\right) = I_0 \cdot \sum_{i=0}^{n} e^{-ia/\lambda_{SrIrO_3}(E_{\text{kin}})\cos\theta} \cdot I_{SrIrO_3}\left(E_{\text{bin}} - \Delta E_{SrIrO_3}\right) \ , \tag{6.21}$$

where I_{SrIrO_3} is a reference spectrum acquired from a $SrIrO_3$ film with a thickness of 20 uc and ΔE_{SrIrO_3} is a constant energy shift, i.e., the potential is assumed to be spatially constant within the film. I_0 is a fit parameter and taken to be equal in Eq. 6.20 and 6.21, as it depends upon the cation density per unit cell, the x-ray photon flux, the photoionization cross section and the photoelectron analyzer transmission, which are equal for any one given strontium or oxygen core level from the stoichiometric substrate and film. The photoelectron IMFP λ is calculated for each material and core level using the TPP2 equation [178], which was shown to yield reasonable results in Fig. 6.15 (d).

The model does not discriminate between the A, B or O ions in the ABO_3 perovskite lattice, since the spatial variations on the length scale of $a/2$ are assumed negligible with respect to the experimental resolution and fit accuracy. Furthermore, the model does not

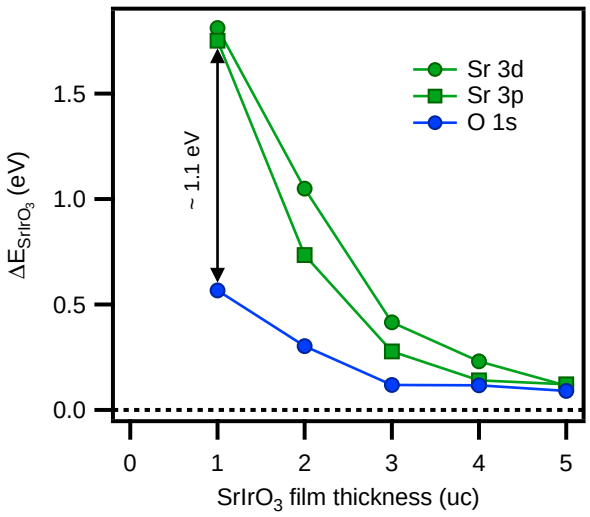

Figure 6.23: Binding energy shifts of the Sr 3*d*, Sr 3*p* and O 1*s* film core-level spectra with respect to the bulk reference spectra as obtained from the spectral decomposition. The energy shifts as function of film thickness reflect the changing Madelung potentials of strontium and oxygen sites.

take into account the termination conversion from B- to A-site termination described in Sec. 4.4, since strontium adopts the A-site in both the $SrIrO_3$ and $SrTiO_3$ lattice. At the very interface a discrimination between film and substrate is thus meaningless and from a strict microscopic point of view the naive model described in Eq. 6.19 breaks down as one approaches the monolayer limit.

Figure 6.22 shows the O 1*s*, Ti $2p_{3/2}$, Sr $3p_{3/2}$ and Sr 3*d* core-level spectra of bare $Nb{:}SrTiO_3$ and $SrIrO_3/Nb_{0.5\%}{:}SrTiO_3$ heterostructures with 1, 2, 3, 4, 5 and 20 uc of $SrIrO_3$. The upper panel depicts the as-measured spectra (black), superimposed with the cumulative fit result (red), as well as the substrate (blue) and film contributions (green) according to the above-described model. The lower panel depicts the same core levels, shifted and arbitrarily scaled to highlight the thickness-dependent changes in the spectral line shape. In general, the significant changes in the photoemission line shape of the core-level spectra are reproduced exceptionally well by the simple model. The resulting binding energy shifts ΔE_{SrIrO_3} of the film contributions of the Sr 3*d*, Sr 3*p* and O 1*s* core-level spectra with respect to the bulk reference spectra are shown as function of film thickness in Fig. 6.23. The excellent agreement between the independent Sr 3*p* and 3*d* decomposition evidences the fit quality. The different trends as function of film thickness are due to the different Madelung potentials of strontium and oxygen sites. In the bulk, the energy difference $E_{bin}(\text{O } 1s) - E_{bin}(\text{Sr } 3d)$ in $SrIrO_3$ exceeds that of $SrTiO_3$ by $\approx 1\,eV$ (cf. Tab. 6.1). In the monolayer, this deviation is compensated by the $\approx 1\,eV$ larger ΔE_{SrIrO_3} of the Sr 3*d* level. Hence, the difference between $SrIrO_3$ and $SrTiO_3$ fades out upon approaching the two-dimensional limit.

Figure 6.24 shows a detailed example of the fit results to confirm the validity of the adopted model. Fig. 6.24 (a) compares the Sr 3*d* core-level spectra of a 5 uc $SrIrO_3/Nb_{0.5\%}{:}SrTiO_3$ (black) and $SrIrO_3/Nb_{0.05\%}{:}SrTiO_3$ (gray) sample. The significant differences found in the Sr 3*d* line shape despite the equal $SrIrO_3$ thickness are captured in the fit model and hence primarily originate from a different Schottky barrier in the substrate, which is reflected in the line shapes of the substrate contributions (solid blue lines). The agreement between experiment and theory for the sample with 0.5 wt.% Nb-doping is satisfactory, but might

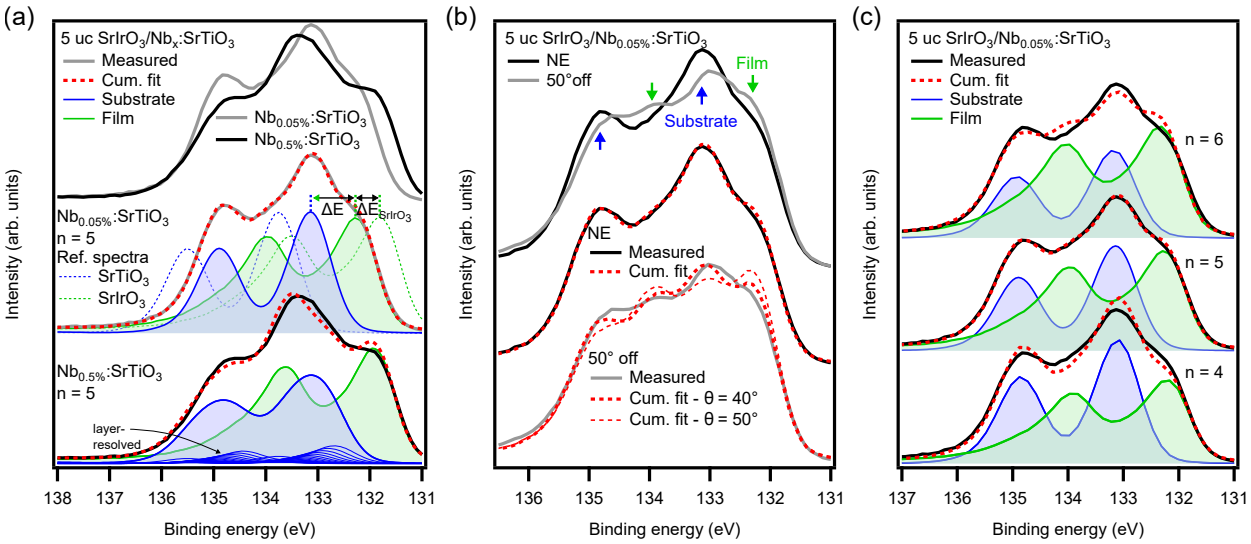

Figure 6.24: Sr 3*d* core-level spectra of 5 uc $SrIrO_3/Nb_x$:$SrTiO_3$ heterostructures. (a) Comparison of the as-measured Sr 3*d* core-level spectra and fit results of a 5 uc $SrIrO_3/Nb_{0.5\%}$:$SrTiO_3$ and $SrIrO_3/Nb_{0.05\%}$:$SrTiO_3$ sample. The measured discrepancies are captured in the fit model. (b) Photoemission angle-dependent measurements confirm the assignment of film and substrate contribution. (c) Comparison between experimental data and the model for different values of the film thickness n, where $n = 5$ is the experimental value from RHEED intensity oscillations.

increase by adapting the Schottky barrier parameters from those obtained from the Ti 2*p* spectrum.

The thus-far hand-waving attribution of film and substrate contribution is confirmed by the emission angle-dependent measurements shown in Fig. 6.24 (b), as the film contribution is clearly emphasized by the increased surface sensitivity at 50° off normal emission. Quantitatively, the model slightly deviates from the experimental data, as the best fit for the surface sensitive measurements is obtained for $\theta = 40°$ rather than $\theta = 50°$. However, this slight discrepancy may also result from the experimental uncertainty of θ, the rather large angular acceptance $\Delta\theta$ of the photoelectron analyzer lens in the used high-magnification mode or deviations from the inelastic mean free path model due to elastic scattering.

Finally, Fig. 6.24 (c) compares fit results by assuming a different n, rather than the experimental value $n = 5$ obtained from RHEED intensity oscillations during growth. The significant discrepancies between experimental and theoretical line shapes for $n = 4$ and $n = 6$ further accredit the validity of the model. In particular, the core-level line shape from all five involved $SrIrO_3$ layers is well-described by the asymmetrically broadened reference spectrum of the thick $SrIrO_3$ film shown in Fig. 6.16 (d).

Summary and conclusion

In summary, the strong deviations between the relative strontium and oxygen core-level binding energies in $SrIrO_3$ and $SrTiO_3$ are investigated with focus on the electrostatic Madelung potential. In comparison to the cubic perovskite $SrTiO_3$, the Madelung potential of the ionic sites becomes modified on the order of 1 eV by the presence of octahedral tiltings

in the $SrIrO_3$ bulk phase. Since the effect of octahedral tiltings is superimposed to the effect of the different lattice dimensions of bulk $SrIrO_3$ ($a/\sqrt{2} = 3.953\,\text{Å}$, $b/2 = 3.942\,\text{Å}$, $c/\sqrt{2} = 3.933\,\text{Å}$) and $SrTiO_3$ ($a = 3.905\,\text{Å}$), a more realistic structural model of $SrIrO_3$ films is introduced, which includes the constraints imposed upon the in-plane lattice parameter (via epitaxial strain) and the octahedral rotations (via the octahedral connectivity) by the substrate. Within this model the varying degree of octahedral tilting modifies the Madelung potential of the A site cation by $\approx -2\,\text{eV}$ and that of the B cation and O anion by $\approx 0.5\,\text{eV}$. Therefore, the structural transition to an $a^0a^0c^-$-order observed by LEED and RHEED at the threshold thickness of the metal-insulator transition is expected to alter the Madelung potential within the thin film.

In thin films the electrostatic potential is additionally influenced by the dimensionality, since the contribution of ions from the adjacent cubic $SrTiO_3$ substrate becomes increasingly dominant in thinner films due to the long range of the Coulomb potential. Accordingly, in the two-dimensional limit the potential is expected to converge against that of the substrate. Experimentally, the strontium and oxygen core-level binding energy in the bulk-like $SrIrO_3$ film deviates from the $SrTiO_3$ value by $\approx 2\,\text{eV}$ and $\approx 1\,\text{eV}$, respectively. In contrast, no multicomponent structure is visible in the thin-film limit, where the film and substrate contributions are almost congruent.

The effects of octahedral rotations and dimensionality act in the same direction and are intertwined due to the geometrical constraints imposed upon the thin film. At this stage, the leading factor cannot be determined unequivocally and Madelung potential calculations for the true thin-film geometry may help to disentangle the two contributions. In any case, the site-dependent electrostatic potential is found to be strongly modified as function of film thickness, which may have profound effects on the low-energy electronic structure. Therefore, it is imperative that any theoretical investigation considers a realistic model of the structural changes in the film, including the influence of the substrate.

6.2.3 Intrinsic and extrinsic effects in iridium core-level spectra

In general, an energetic shift of a core level of an element in a solid in photoemission spectroscopy, measured relative to the chemical potential μ, is given by [163, 175]

$$\Delta E = -\Delta\mu + K\Delta Q - \Delta\Phi + \Delta E_R \,, \tag{6.22}$$

where $\Delta\mu$ is a change in the chemical potential μ, ΔQ is the change in the number of valence electrons per atom, K is a constant, $\Delta\Phi$ is the change in the Madelung potential Φ (neglecting crystal field splitting) and ΔE_R is the change in the extra-atomic relaxation energy of the core-hole state. As elaborated above, the observed (relative) binding-energy shifts in the oxygen and strontium core-level spectra as function of film thickness are dominated by changes of the site-dependent Madelung potentials $\Delta\Phi$. While the iridium sites are subject to a comparable change of the average Madelung potential as the oxygen sites (cf. Fig. 6.21 (c)), additionally, the extra-atomic relaxation energy ΔE_R of an iridium core-hole state may change significantly upon the opening of a charge gap at the chemical potential due to the coupling to the Ir $5d$ electrons, which govern the low-energy physics of iridium

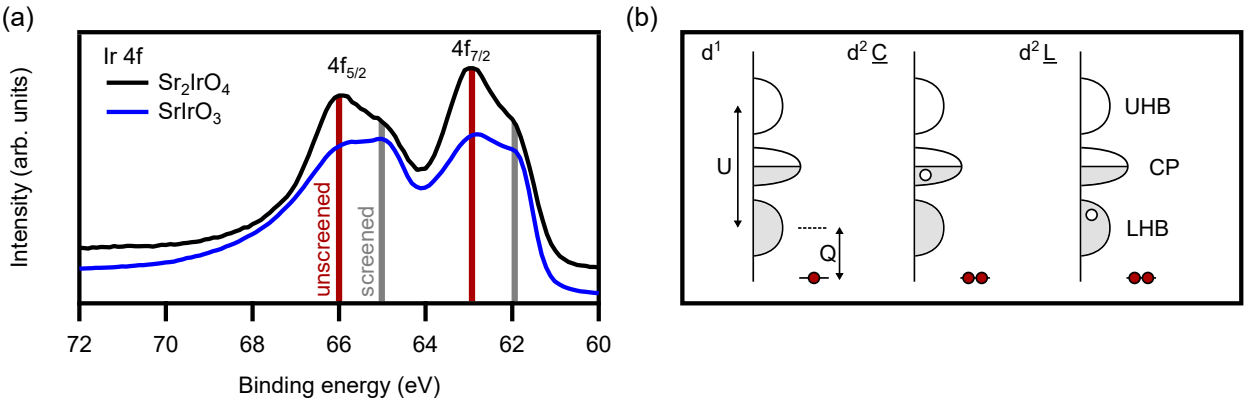

Figure 6.25: (a) Ir $4f$ core-level spectra of thick $SrIrO_3$ and Sr_2IrO_4. Both spectra exhibit a multicomponent peak structure due to a screened (gray) and unscreened (red) $4f$ doublet in the photoemission final state. (b) Schematic diagrams of the three major final-state valence-electron configurations in a Mott insulator d^1, $d^2\underline{C}$ and $d^2\underline{L}$, where d denotes the impurity level, C the coherent peak (CP) and L the lower Hubbard band (LHB) [297]. *Figure (b) adapted with permission from Ref. [297]. Copyright © (2004) by the American Physical Society. All rights reserved.*

oxides in general and $SrIrO_3$ in particular. Indeed, the Ir $4f$ core-level spectra of bulk $SrIrO_3$ and Sr_2IrO_4[12] shown in Fig. 6.25 (a) exhibit a multicomponent peak structure, which has been interpreted as a manifestation of core-hole screening by conduction electrons [292–296].

Intrinsic final-state effects in iridium core-level spectra

The origin of a similar peak structure found in the Ru $3d$ core-level spectra of the ruthenate family of $4d$ transition metal oxides has been subject of intensive debate. On the one hand, Kim *et al.* interpret the relative ratio of screened and unscreened contributions as measure for the strength of the effective correlations [297]. Using dynamical mean-field theory (DMFT) to calculate the core-level spectra of a single-band Hubbard model with a core-hole potential [297], they claim that the screened peak essentially originates from the screening of the core hole by quasiparticles on the Fermi surface [297]. Figure 6.25 (b) depicts the three major valence-electron configurations in the XPS final state, which include the impurity level at the core-hole site in the presence of the core hole [297] and three energy levels in the conduction band, i.e., the lower Hubbard band (LHB), the coherent peak (CP) and the upper Hubbard band (UHB) [297]. In this picture, the screened peaks in the metallic phase originate from the final-state configurations $d^2\underline{L}$ and $d^2\underline{C}$. In contrast, in the Mott-insulating phase the configuration $d^2\underline{C}$ is absent in ground and final state and $d^2\underline{L}$ is energetically located near the unscreened peak [297]. Based on this model, despite several shortcomings such as the neglect of the d orbital degeneracy and the role of the O $2p$ bands, the core-level multipeak structure can be qualitatively understood as manifestation of satellite structures expected in a Mott-Hubbard system [297].

On the other hand, van Veenendaal interprets the spectral line shape in the framework

[12] Sr_2IrO_4 film growth and XPS measurement performed by Dr. Ozan S. Kirilmaz.

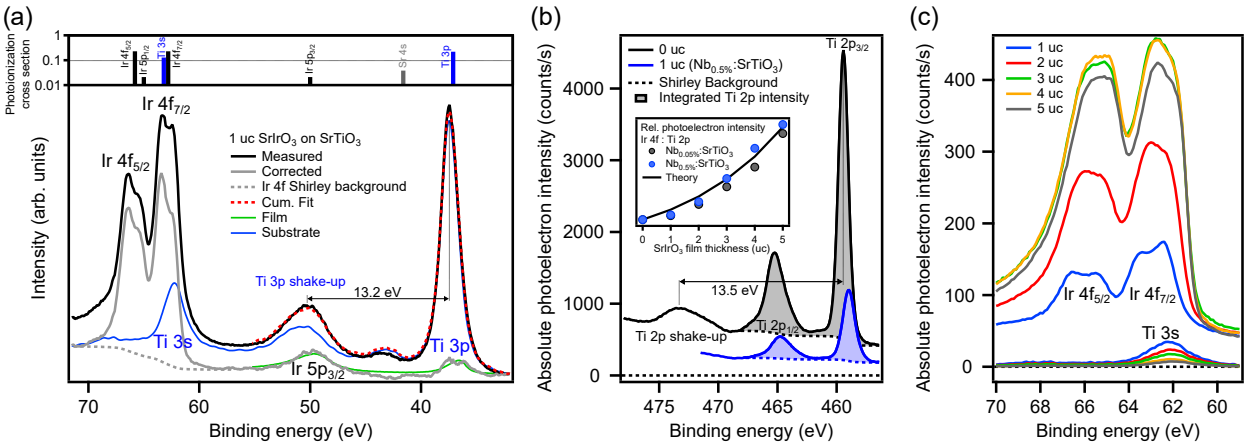

Figure 6.26: Ir $4f$ background correction. (a) In the monolayer limit the Ir $4f$ core level is superimposed by a significant Ti $3s$ contribution from the substrate. The lower-lying Ti $3p$ core level and its shakeup satellite can be exploited for a careful correction. The photoionization cross sections of all core levels in the upper panel are taken from Ref. [172]. (b) Alternatively, the Ti $2p$ core level can be used to determine the Ti $3s$ background. (c) Resulting Ti $3s$ contributions for $SrIrO_3$ thicknesses $1-5$ uc to the measured (uncorrected) Ir $4f$ spectra.

of the conventional Kotani model [292], i.e, as a result of the competition between local screening by electrons from oxygen ligands and nonlocal screening involving neighboring transition metal sites, independent of the presence of additional quasiparticle excitations at the Fermi level [298, 299]. Numerous experimental studies have investigated the Ru $3d$ core-level structure of perovskite [300–302] or pyrochlore [303] ruthenates, some favoring a certain model, others suggesting the equivalence of screening from coherent states in DMFT and nonlocal screening in multisite calculations [303].

In agreement with Ref. [297], Kawasaki *et al.* interpret the relative strength of the screened and unscreened component in the Ir $4f$ core-level spectra as measure for the effective correlations [296]. Consistent with Fig. 6.25 (a), the screened Ir $4f$ component of $SrIrO_3$ is found to be significantly stronger than in the Mott insulator Sr_2IrO_4. This trend continues to rutile IrO_2, a Fermi-liquid system with negligible electronic correlations, where the Ir $4f$ core level is completely dominated by the screened component [294]. The physical mechanism is rationalized by an increase of the Ir t_{2g} band width W and a concurrent decrease of the screened on-site Coulomb repulsion U due to a larger O $2p$ – Ir $5d$ hybridization, both driven by the increasing octahedral connectivity when going from two-dimensional Sr_2IrO_4 to three-dimensional corner-sharing $SrIrO_3$ to three-dimensional corner- and edge-sharing IrO_2.

Hence, the investigation of iridium core-level spectra may shed light on the physical nature of the thickness-dependent MIT observed in $SrIrO_3$ films and reveal similarities or differences between the insulating states found in monolayer $SrIrO_3$ and bulk Sr_2IrO_4. Of the theoretically available Ir $4s$, $4p$, $4d$, $4f$ and $5p$ core levels when using an Al K_α x-ray source, only the $4f$ and $4d$ photoionization cross sections are sufficiently large for routine measurements with acceptable signal-to-noise ratio. Of these, only the $4f$ core level has a sufficiently small intrinsic line width to resolve the narrow satellite features of interest.

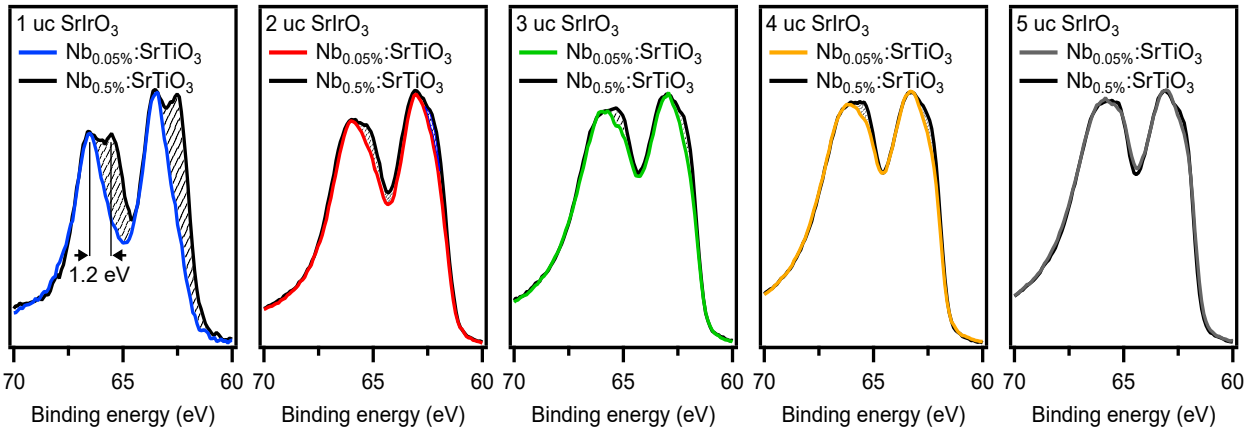

Figure 6.27: Background-corrected Ir $4f$ spectra as function of $SrIrO_3$ film thickness for two series of films grown on $Nb_{0.5\%}$:$SrTiO_3$ and $Nb_{0.05\%}$:$SrTiO_3$. In the two-dimensional limit the Ir $4f$ line shapes exhibit strong differences (highlighted by striped area).

However, a careful background correction becomes necessary as the $SrIrO_3$ film thickness approaches the two-dimensional limit, since the Ir $4f_{7/2}$ low-binding-energy shoulder is increasingly superimposed by the Ti $3s$ core-level spectrum from the $SrTiO_3$ substrate as shown in Fig. 6.26 (a). The neighboring Ti $3p$ core level and its shakeup satellite can be exploited to decompose the spectrum into a $SrTiO_3$ and $SrIrO_3$ contribution (cf. Eq. 6.19) and after subtraction of the substrate contribution and a subsequent Shirley background correction the intrinsic Ir $4f$ spectrum is obtained. Alternatively, the Ti $2p$ core level at higher binding energy can be used to determine the Ti $3s$ background after a careful normalization to the acquisition time (cf. Fig. 6.26 (b)) and incorporation of the binding energy shift due to the formation of the Schottky barrier (cf. Sec. 6.2.1). As seen in Fig. 6.26 (c) the thus-obtained Ti $3s$ background is significant in the monolayer limit and its subtraction hence imperative for a correct interpretation of the Ir $4f$ core-level spectra. Furthermore, the overlapping Ti $3s$ core level renders the investigation of the Ir $4f$ core level of samples overgrown with a protective $SrTiO_3$ capping virtually impossible.

Figure 6.27 shows the Ti $3s$ background-corrected Ir $4f$ spectra of two series of $SrIrO_3$ films grown on $Nb_{0.5\%}$:$SrTiO_3$ and $Nb_{0.05\%}$:$SrTiO_3$ (cf. Sec. 6.2.1 and 6.2.2). While the Ir $4f$ line shape in the thick films converges to that of the bulk limit shown in Fig. 6.25 (a), a pronounced change is observed between a thickness of 3 and 1 uc, i.e., as the charge gap opens. Interestingly, the 2 uc samples exhibit some differences at the low-energy side of the spectra, while the monolayer samples display a pronounced single- and double-peak structure for $Nb_{0.5\%}$:$SrTiO_3$ and $Nb_{0.05\%}$:$SrTiO_3$, respectively, the latter being reminiscent of a screened/unscreened doublet peak structure. Theoretically, the electronic screening within the $SrIrO_3$ monolayer may be influenced by the different Nb-doping and according charge carrier concentrations of the $SrTiO_3$ substrates shown in Fig. 6.27 even despite the formation of a Schottky barrier at the interface. However, as seen in Fig. 6.26 (a) a third monolayer sample grown on $Nb_{0.5\%}$:$SrTiO_3$ is found to exhibit a double-peak structure with a third, intermediate peak ratio. Therefore, the screening effect due to Nb-doping is discarded as explanation for the different Ir $4f$ line shape. As shown in the following, an unintentional

Spectrum No.	Δt (days)	Sample treatment prior to measurement
1	0	Storage in UHV
2	6	Storage in UHV
3	11	Storage in UHV
4	27	Storage in UHV + *ex situ* storage (10 hours)
5	31	20 min at 700 °C in $1 \cdot 10^{-1}$ mbar O_2 atmosphere
6	38	Storage in UHV
7	39	10 min at 350 °C in $1 \cdot 10^{-8}$ mbar O_2 atmosphere
8	54	Storage in UHV
9	76	Storage in UHV
10	77	20 min at 400 °C in $1 \cdot 10^{-8}$ mbar O_2 atmosphere
11	80	20 min at 700 °C in $1 \cdot 10^{-1}$ mbar O_2 atmosphere

Table 6.3: History of the $SrIrO_3$ monolayer sample used for the long-term study of extrinsic effects on the electronic structure.

substitution of oxygen by fluorine atoms is found to be responsible for this initially puzzling finding.

Unintentional charge carrier doping by fluorine substitution − absence of metallicity

In an effort to understand the origin of the puzzling versatility of the Ir $4f$ line shapes of different $SrIrO_3$ monolayer samples, it was found that the Ir $4f$ line shape changes upon prolonged storage under UHV conditions. Therefore, an unintentional contamination of the film surface was considered as extrinsic effect that results in spectral changes. For this reason a long-term study was conducted with one monolayer $SrIrO_3$ sample, in which various photoemission spectra were obtained after storage under UHV conditions and/or exposure to a certain oxygen partial pressure at elevated temperatures as summarized in Table 6.3. Figure 6.28 (a) shows all Ir $4f$ spectra obtained over the course of 80 days. Intriguingly, a continuous shift of spectral weight towards the lower binding energy feature (blue) is observed as the sample is stored (spectra 1-3) and exposure to ambient conditions further promotes this trend (spectrum 4). In stark contrast, exposure to an oxygen partial pressure of $p_{O_2} = 1 \cdot 10^{-1}$ mbar at $T = 700\,°C$ for 20 min counteracts this trend and causes an almost complete reversal, i.e., a shift of spectral weight to the high-binding-energy feature (green, spectrum 5). A renewed, continuous shift of spectral weight towards the low-energy feature is observed in the spectra 6-9 , culminating in spectrum 10, where a third feature at even lower binding energy (yellow) appears. A second exposure to an oxygen-rich atmosphere

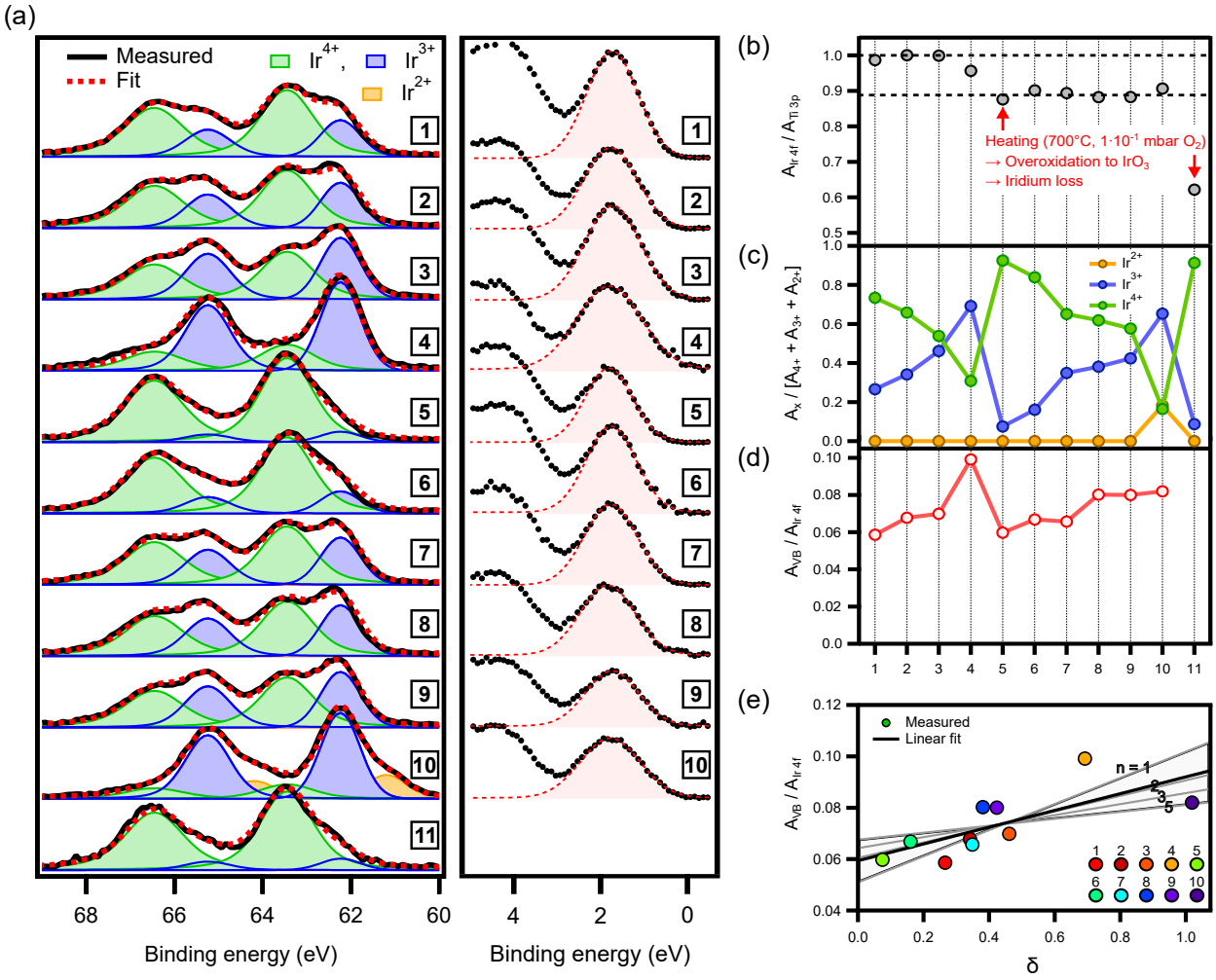

Figure 6.28: Long-term study of the effect of sample treatment as specified in Tab. 6.3 on the electronic structure of a $SrIrO_3$ monolayer sample. (a) Ir $4f$ core-level and valence-band spectra of the monolayer sample. The Ir $4f$ spectra are decomposed into three chemically shifted valence contributions as described in the text. The valence-band spectra are normalized to acquisition time and fit by a Gaussian (red). (b) Total Ir $4f$ spectral weight normalized to the neighboring Ti $3p$ spectral weight. Exposure to an oxygen-rich atmosphere at elevated temperatures leads to formation of volatile IrO_3 and iridium loss. (c) Spectral weight of the fitted Ir^{4+}, Ir^{3+} and Ir^{2+} contributions normalized to the total Ir $4f$ spectral weight. (d) Spectral weight of the valence-band spectra (Gaussian fit) normalized to the total Ir $4f$ spectral weight. (e) Spectral weight of the valence-band spectra vs. electron number from Ir $4f$ valence decomposition.

at elevated temperatures results in a reproducible second reversal of the spectral changes (spectrum 11).

These findings severely cast into doubt the (un)screened final state effect as origin of the multipeak structure observed in monolayer $SrIrO_3$. In contrast, the spectral changes are reminiscent of typical binding energy variations due to changes in the chemical environment or oxidation state, i.e., chemical shifts, which are commonly observed in transition metal oxides [163]. For example, the formation of oxygen vacancies in $SrTiO_3$ reduces the

neighboring titanium valence from Ti^{4+} to Ti^{3+} in $SrTiO_3$ [179, 274, 304, 305], while the incorporation of excess oxygen in $LaTiO_3$ overoxidizes the titanium valence from Ti^{3+} to Ti^{4+} [213]. In Eq. 6.22 the corresponding chemical binding energy shift is captured by the term $K\Delta Q$, i.e., a change in the number of valence electrons. Accordingly, the low- and high-energy features in the Ir $4f$ monolayer spectra are tentatively ascribed to iridium ions in the Ir^{3+} and Ir^{4+} valence state, respectively, the latter being the formal valence in stoichiometric $SrIrO_3$. From this point of view, the changes in the Ir $4f$ spectra are due to a steady reduction under UHV conditions ($Ir^{4+} \rightarrow Ir^{3+}$) and re-oxidation upon exposure to an oxygen-rich atmosphere at elevated temperatures ($Ir^{3+} \rightarrow Ir^{4+}$). Interestingly, as shown in Fig. 6.28 (b) the re-oxidation is accompanied by a decrease of the total Ir $4f$ spectral weight relative to that of the adjacent Ti $3p$ core level ($A_{\mathrm{Ir}\,4f}/A_{\mathrm{Ti}\,3p}$). Most likely, as discussed in Chap. 4, the oxidizing conditions result in the formation of volatile IrO_3, leading to an iridium deficiency, i.e., a reduction of the $SrIrO_3$ coverage.

For a more quantitative analysis, the Ir $4f$ core-level spectra are decomposed into three valence-state contributions Ir^{4+}, Ir^{3+} and Ir^{2+}. For this purpose each chemically shifted doublet is described by two Voigt profiles with a certain spin-orbit splitting Δ_{SO} and $4f_{5/2}$-to-$4f_{7/2}$ intensity ratio (equal for all doublets). While the Lorentz line width of each peak is different, the Gaussian line width is assumed equal for all peaks, as it reflects the experimental energy resolution. To obtain reliable fit results all Ir $4f$ spectra were fitted simultaneously, for each spectrum only allowing different relative intensities of the valence states. As seen in Fig. 6.28 (a) an excellent agreement between the measured and fit spectra is obtained. The relative spectral weight of the three valence states is summarized in Fig. 6.28 (c).

From a naive point of view a valence change from Ir^{4+} to Ir^{3+} implies a $5d^5$ to $5d^6$ band filling variation, i.e., from a half-filled to a completely filled $J_{\mathrm{eff}} = 1/2$ band. In the generic Mott scenario, this is expected to trigger a band filling-controlled Mott transition from a Mott insulator to a correlated metal and eventually to a band insulator [1]. In contrast, the valence-band spectra in Fig. 6.28 (a) do not exhibit any significant redistribution of spectral weight towards the chemical potential nor a sharp quasiparticle peak. However, the total Ir $5d$ spectral weight $A_{\mathrm{VB}}/A_{\mathrm{Ir}\,4f}$ observed in the band gap of $SrTiO_3$ (normalized to the total Ir $4f$ spectral weight to account for the observed iridium loss) changes with the iridium valency as shown in Fig. 6.28 (d).

In Fig. 6.28 (e) the total Ir $5d$ spectral weight is plotted against the average number of additional electrons per iridium site

$$\delta = \frac{A_{3+} + 2 \cdot A_{2+}}{A_{4+} + A_{3+} + A_{2+}} \tag{6.23}$$

as deduced from the Ir $4f$ core-level fits. Assuming an average band filling $5d^{n+\delta}$ the spectral weight can be described by

$$\frac{A_{\mathrm{VB}}}{A_{\mathrm{Ir\,4f}}} = k \cdot (n + \delta), \tag{6.24}$$

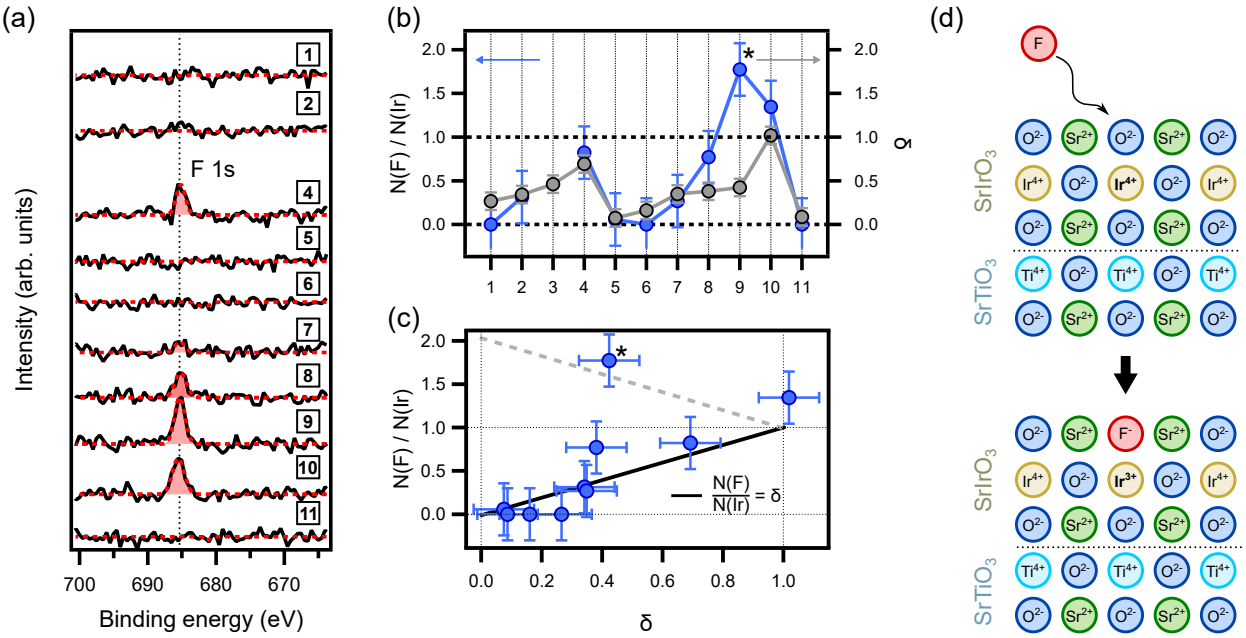

Figure 6.29: (a) F 1*s* core level with variable intensity indicates a fluorine contamination of the $SrIrO_3$ monolayer. (b) A clear correlation is found between fluorine content and the number of additional electrons per iridium site δ deduced from the Ir $4f$ valency. (c) A direct proportionality between the number of fluorine atoms per iridium and δ suggests the doping of exactly one electron per fluorine atom. (d) Proposed doping mechanism by substitution of an oxygen by a fluorine anion at the very surface.

where k is a fitting parameter that is determined by the ratio of the photoionization cross sections of $5d$ and $4f$ states and the analyzer transmission function. Since the data set exhibits a significant scattering due to inevitably large errors from the curve fitting procedure, a linear regression yields the value $n = 1.8$, at odds with the theoretically expected value $n = 5$ for stoichiometric $SrIrO_3$. However, as shown in Fig. 6.28 (e) (thin gray lines), the fit uncertainty yields a large margin of error that includes the expected value $n = 5$. A more accurate determination would require a more systematic study of the changes of the electronic structure. In particular, the determination of the Ir $5d$ spectral weight would benefit from a better signal-to-noise ratio and data acquisition under several photoemission angles to disentangle the $SrTiO_3$ and $SrIrO_3$ contributions of the valence-band spectra at higher binding energy. Nonetheless, the evident correlation between Ir $5d$ spectral weight and Ir $4f$ valency attests the existence of a doping mechanism for additional charge carriers, which, however, are localized and do not trigger a Mott transition. In the following, the nature of the doping mechanism at play is discussed.

For transition metal oxides numerous intentional doping mechanisms such as cation or anion substitution, alkali-metal deposition, electric-field gating or oxygen vacancy formation are established [306], the latter also being a common source of unintentional doping. For the present data set, actually a variable fluorine contamination that is easy to overlook is found in the XPS overview spectra (cf. Fig. 6.29 (a)). Possible sources of fluorine contamination in the UHV chamber in Würzburg are the introduction of residual fluorine via the HF-

Subshell	Photoionization cross section σ (kb)	E_{kin} (eV)
F 1s	19.00	800
Ir $4f_{5/2}$	64.44	1420
Ir $4f_{7/2}$	82.32	1420

Table 6.4: Photoionization cross sections for the F $1s$, Ir $4f_{5/2}$ and Ir $4f_{7/2}$ subshells taken from Ref. [308] and [309].

treated $SrTiO_3$ substrates or synthetic fluoropolymers (e.g., Teflon) used in movable UHV components such as sample transfer arms or wobble sticks. Under such conditions storage on the time scale of several days may result in sizeable contamination even at extremely low fluorine partial pressure, in particular with respect to the very high chemical reactivity of fluorine. For a quantitative estimation of the fluorine content, the number of fluorine atoms per iridium atom $N(F)/N(Ir)$ is estimated from the photoemission signal A_F/A_{Ir} by

$$\frac{N(\mathrm{F})}{N(\mathrm{Ir})} = \frac{T\left(E_{\mathrm{kin,Ir\,4f}}\right)}{T\left(E_{\mathrm{kin,F\,1s}}\right)} \cdot \frac{\frac{d\sigma}{d\Omega_{\mathrm{Ir\,4}f}}}{\frac{d\sigma}{d\Omega_{\mathrm{F\,1}s}}} \cdot \frac{A_{\mathrm{F}}}{A_{\mathrm{Ir}}}, \tag{6.25}$$

where

$$T\left(E_{\mathrm{kin}}\right) \propto E_{\mathrm{kin}}^{-1} \tag{6.26}$$

is the photoelectron analyzer transmission of the used Omicron EA 125 analyzer [307] as function of the kinetic energy E_{kin} of the photoelectrons and

$$\frac{d\sigma}{d\Omega_i} = \frac{\sigma_i}{4\pi}\left[1 - \frac{\beta_i}{2}\, P_2\left(\cos\theta\right)\right] \tag{6.27}$$

is the differential photoionization cross section as function of the subshell photoionization cross section σ_i, the asymmetry parameter β and the angle θ between the propagation vectors of the incoming photons and the outgoing photoelectrons. Here, the measurement geometry is chosen such that $\theta \approx 54.7°$, where the second-order Legendre polynomial

$$P_2\left(\cos\theta\right) \approx 0 \quad \text{and} \quad \frac{d\sigma}{d\Omega_i} \approx \frac{\sigma_i}{4\pi}. \tag{6.28}$$

The Ir $4f$ cross section is taken as the average of the cross sections of its spin-orbit-split subshells, weighted by their occupation numbers $(2j+1)$

$$\frac{d\sigma}{d\Omega_{\mathrm{Ir\,4}f}} = \frac{1}{14}\left(6 \cdot \frac{d\sigma}{d\Omega_{\mathrm{Ir\,4}f_{5/2}}} + 8 \cdot \frac{d\sigma}{d\Omega_{\mathrm{Ir\,4}f_{7/2}}}\right). \tag{6.29}$$

The respective literature values in Tab. 6.4 are taken from Ref. [308, 309].

Figure 6.29 (b) shows the resulting fluorine content per iridium ion. The error bars represent the rather large uncertainty due to the high noise level in the F 1*s* spectra, resulting from the small F 1*s* photoionization cross section and the short data acquisition time. Intriguingly, a significant amount of up to ≈ 1.5 fluorine atoms per iridium atom and a correlation between the fluorine content and the number of additional electrons δ (cf. Eq. 6.23) is found. Indeed, as shown in Fig. 6.29 (c), a direct proportionality between N(F)/N(Ir) and δ exists – if one data point (highlighted with an asterisk) is neglected – with every fluorine atom seeming to dope exactly one additional electron into the $SrIrO_3$ film. However, from a naive point of view, a surface contamination with fluorine, in particular the adsorption at an octahedral apex site on a (hypothetical) IrO_2-terminated $SrIrO_3$ film would result in an oxidation of the film ($Ir^{4+} \rightarrow Ir^{5+}$) [231] at odds with experiment. For this reason, a fluorine substitution of oxygen anions is proposed as explanation for the observed electron doping behavior. As shown in Fig. 6.29 (d) a substitution of an O^{2-} ion by a F^{1-} ion results in a formal reduction of the adjacent iridium ion, similar to the creation of a neutral oxygen vacancy [118, 119]. Indeed, anionic substitution of fluorine for oxygen is a well-known electron-doping mechanism of high-T_C cuprate superconductors [310–312].

Oxygen ions at the surface are stabilized by only five nearest-neighbor bonds rather than six in the bulk and may hence be more susceptible to fluorine substitution at ambient conditions. In this scenario, for a SrO-terminated $SrIrO_3$ monolayer, only one oxygen site per iridium site can be substituted by fluorine. Interestingly, the only deviation from the proportionality between fluorine content and δ is observed in spectrum 9, where the number of fluorine atoms is higher than that of iridium ($\frac{N(\mathrm{F})}{N(\mathrm{Ir})} > 1$). This strong accumulation of fluorine on the sample surface is due to the extraordinarily long storage in UHV (22 days) prior to the acquisition of spectrum 9. As seen in spectrum 10, after heating the sample to $T = 400\,^{\circ}\mathrm{C}$ in $p_{O_2} = 1 \cdot 10^{-8}\,\mathrm{mbar}$, N(F)/N(Ir) and δ become 1. Hence, it is proposed that rather than penetrating the deeper layers of the film, excess fluorine remains on top of a fully fluorinated SrF layer, acts as electron acceptor and counteracts the doping effect of fluorine substitution as implied by the gray dashed line in Fig. 6.29 (c). Upon heating in vacuum the excess fluorine evaporates, leaving behind a pristine SrF-terminated $SrIrO_3$ monolayer. This proposed strong confinement to the very first layer naturally explains the sensitivity of monolayer $SrIrO_3$ to spectral changes, whereas thicker films are affected less due to their higher bulk-to-surface ratio.

Despite significant doping of up to one electron per iridium site, no trace of a Mott transition, i.e., a redistribution of spectral weight at the chemical potential, is observed in Fig. 6.28 (a). However, upon closer inspection of the Ir 5*d* valence-band spectra 5 and 10, which correspond to the minimum and maximum of additional electrons per iridium site δ in Figure 6.30 (a), the low-energy shoulder is found to exhibit a small redistribution of spectral weight towards the chemical potential. Nonetheless, the persistence of the charge gap independent of the average band filling $5 + \delta$ becomes apparent in comparison to the reference spectrum of a thick, metallic $SrIrO_3$ film (red). The absence of a clear Fermi edge in the metallic spectrum is due to the limited energy resolution of the monochromatized Al K_α x-ray source and, hence, additional UPS valence-band spectra with higher energy resolution (cf. Fig. 6.1 (a)) might yield further information on the systematic changes of

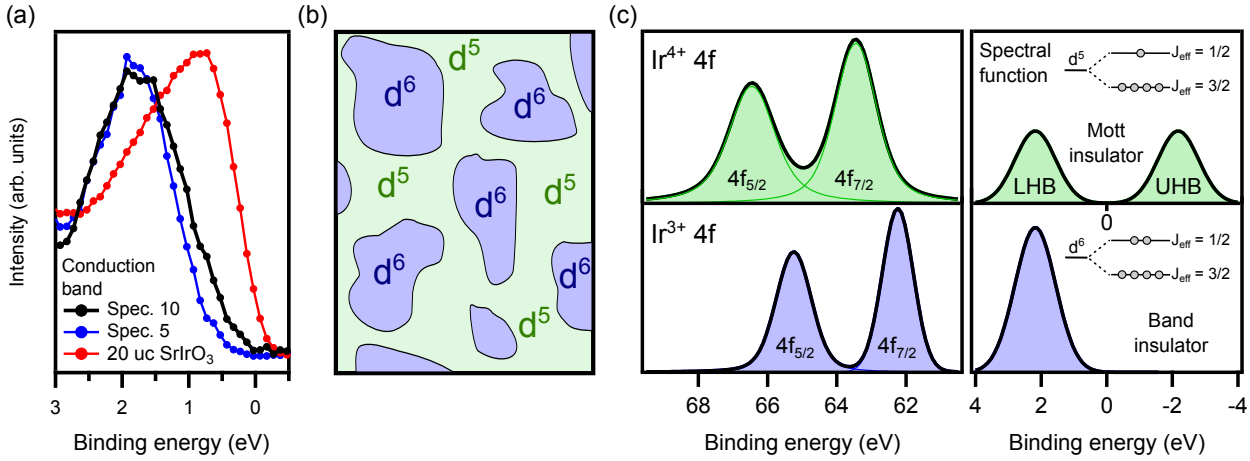

Figure 6.30: (a) Ir $5d$ valence-band spectra 5 and 10 from Fig. 6.28 (a) (minimum and maximum δ), in comparison to a reference spectrum of a thick, metallic $SrIrO_3$ film. While some spectral changes are observed, the charge gap persists independent of the average band filling. (b) One possible scenario explaining the absence of a band filling-induced MIT is the existence of two spatially separated electronic phases with a strong disproportionation of charges. (c) In this scenario the observed photoemission spectra are interpreted as linear superposition of laterally separated d^5 patches exhibiting a Mott-insulating spectral function near the chemical potential (occupied LHB and unoccupied UHB) and band-insulating d^6 patches.

the electronic structure of the low-energy spectral features.

One possible explanation for the absence of a band filling-induced MIT is the existence of two spatially separated electronic phases with a strong disproportionation of the electronic charge, similar to oxygen vacancy-doped $SrTiO_3$ surfaces [285]. The formation of such a domain structure may result from a nucleation process due to a reduced energetic barrier for fluorine substitution in the vicinity of a pre-existing fluorine site. In this scenario, the observed photoemission spectra consist of a superposition of the spectral function from laterally separated patches with $5d^5$ and $5d^6$ electronic configuration. Near the chemical potential, the Mott-insulating d^5 configuration exhibits an occupied LHB and an unoccupied UHB, whereas the band-insulating d^6 configuration only shows an occupied band below the Fermi level. The small changes in the shape of the valence-band spectra observed in Fig 6.30 (a) may originate from a (coincidentally) almost similar energy position of the LHB and the filled band.

Alternatively, the absence of metallicity in fluorine-doped monolayer $SrIrO_3$ may be explained in analogy to alkali metal-intercalated TiOCl, a prototypical low-dimensional Mott insulator with a $3d^1$ configuration, where the alkali-metal ion lowers the energy of its adjacent transition metal site due to its associated Coulomb potential [313]. The doped electrons from the alkali metal ions thus occupy sites with modified single-particle energies termed electrostatically induced alloy sites, resulting in doubly occupied impurity states, which do not hybridize with the singly occupied pristine transition metal states. In analogy, the effective positive charge of the fluorine impurity may trap its doped electron resulting in a local $5d^6$ configuration embedded in a $5d^5$ surrounding. However, in contrast to alkali metal-doped TiOCl, the concurrent transfer of spectral weight is not observed experimentally in

the $SrIrO_3$ case, possibly due to a degenerate energy position of the corresponding spectral features.

Summary

In summary, two distinctly different effects on the Ir $4f$ core-level spectra of $SrIrO_3$ films are identified and disentangled. The *intrinsic* Ir $4f$ line shape of stoichiometric $SrIrO_3$ films exhibits a strong variation as function of film thickness below the critical thickness for the MIT. In agreement with Ref. [293, 294, 296], the pronounced two-peak structure in the metallic regime is interpreted in terms of final-state effects during the photoemission process involving conduction-electron screening of the core hole. Upon approaching the two-dimensional limit the opening of a charge gap at the chemical potential is accompanied by a reduction and an almost entire extinction of the screened component in the monolayer limit. Taking the screened-to-unscreened peak ratio as measure for the effective strength of correlations in the iridates [296], this finding suggests a stronger prevalence of the on-site Coulomb interaction U over the hopping term t than in the quasi-two-dimensional bulk material Sr_2IrO_4, which exhibits a small screened component despite being in a Mott-insulating state.

The experimental observation of this core-level effect is complicated by an *extrinsic* chemical shift in the Ir $4f$ spectrum due to unintentional electron doping as a result of a fluorine contamination of the UHV chamber, which strongly depends upon the elapsed time between sample fabrication and data acquisition and the current state (cleanliness) of the UHV system. Since the fluorine substitution of oxygen is confined to the very surface, this effect becomes most evident in the monolayer limit and hence seemingly counteracts the observed intrinsic final-state effects. Hence, great care has to be exercised to investigate the properties of pristine $SrIrO_3$ thin films by avoiding any surface contaminations prior to data acquisition.

6.3 Absence of polar discontinuity-induced charge redistribution in $LaAlO_3/SrIrO_3/SrTiO_3$ heterostructures

Based on structural and electronic similarities to La_2CuO_4, which is a high-T_C cuprate parent material [3], it has been proposed that electron doping of Sr_2IrO_4 may potentially open an avenue towards unconventional superconductivity [11, 12]. Several experimental studies have spectroscopically reproduced the phenomenology found in cuprates, in particular the observation of Fermi arcs [13] and the formation of a d-wave gap [14] upon electron doping by alkali-metal deposition on the pristine Sr_2IrO_4 surface. One alternative route to electron doping, which avoids the introduction of disorder and/or impurity states by chemical substitution, is based on the exploitation of a polar discontinuity at an oxide heterointerface. The most prominent example is the $LaAlO_3/SrTiO_3$ heterostructure, where a metallic two-dimensional electron system (2DES) forms at the interface of the

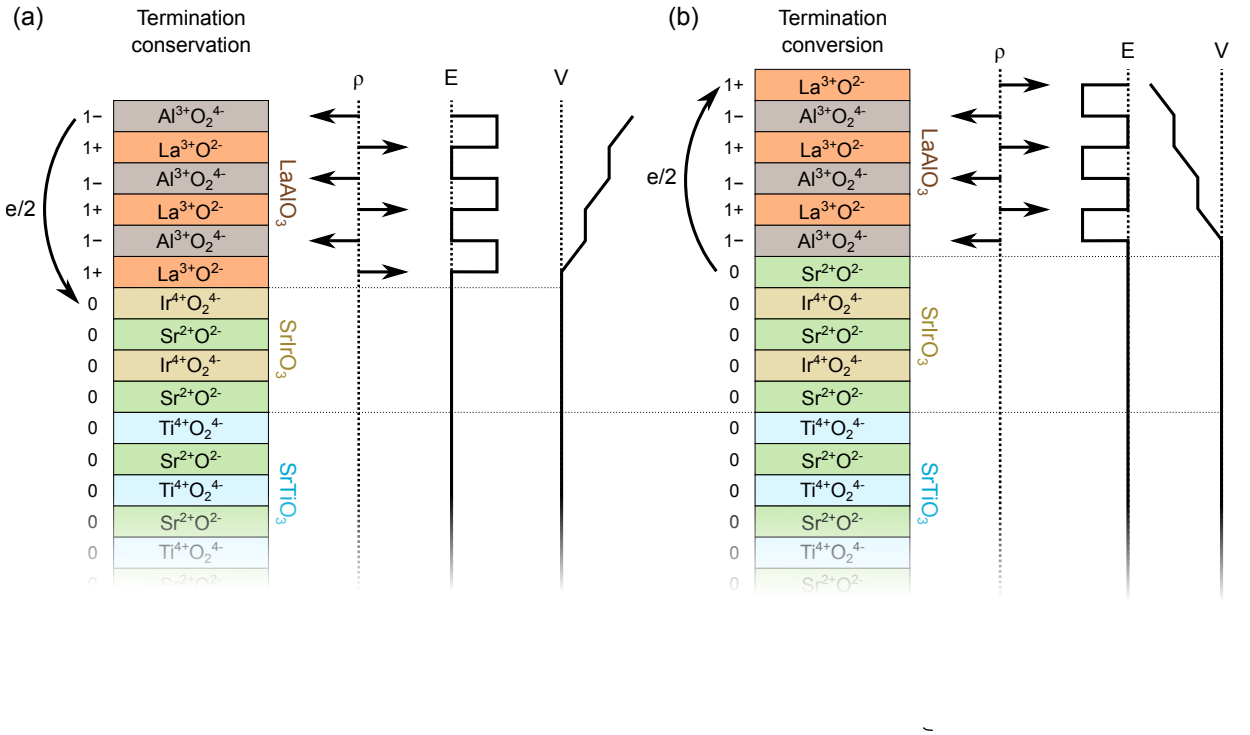

Figure 6.31: Model of the polar discontinuity at the $LaAlO_3/SrIrO_3/SrTiO_3$ interface [314]. The alternating net charges produce an electric field, which causes a diverging electric potential. In the electronic reconstruction model the electric potential is compensated by a charge transfer of half an electron per unit cell. (a) Conservation of the perovskite stacking order during growth results in a situation similar to the $LaAlO_3/SrTiO_3$ heterointerface. (b) A termination conversion results in a potential buildup with opposite sign and hence in a charge transfer in the opposite direction.

otherwise band-insulating constituent materials, if a critical thickness of four unit cells of $LaAlO_3$ is reached [179, 261, 315]. While numerous explanations including oxygen vacancies in $SrTiO_3$ [316, 317] or at the $LaAlO_3$ surface [318–320], cation off-stoichiometry [321] or interdiffusion [322], surface adsorbates [323] and antisite defects [324] have been put forward, it has been established that the polar discontinuity between the nonpolar $SrTiO_3$ and polar $LaAlO_3$ and the concomitant potential buildup as function of $LaAlO_3$ thickness acts as a generic mechanism that triggers an electron redistribution to the interface (cf. Fig. 6.31 (a)) [274, 314].

Since $SrIrO_3$ exhibits several structural and electronic similarities to bulk Sr_2IrO_4 in the monolayer limit, establishing a homogeneous electron doping mechanism promises the emergence of interesting physical phenomena. However, depending on the microscopic details of the heterointerface the potential buildup may differ dramatically from the prototypical $LaAlO_3/SrTiO_3$ system. As discussed in Sec. 4.4, the $SrIrO_3$ films undergo a conversion from B- to A-site termination during growth. Hence, when deposited on SrO-terminated $SrIrO_3$ the $LaAlO_3$ stacking order and thus polarity is inverse to that in $LaAlO_3/SrTiO_3$, resulting in a negative potential gradient as depicted in Fig. 6.31 (b) [314]. In the oversimplified electronic reconstruction model this would result in an electron transfer away from the

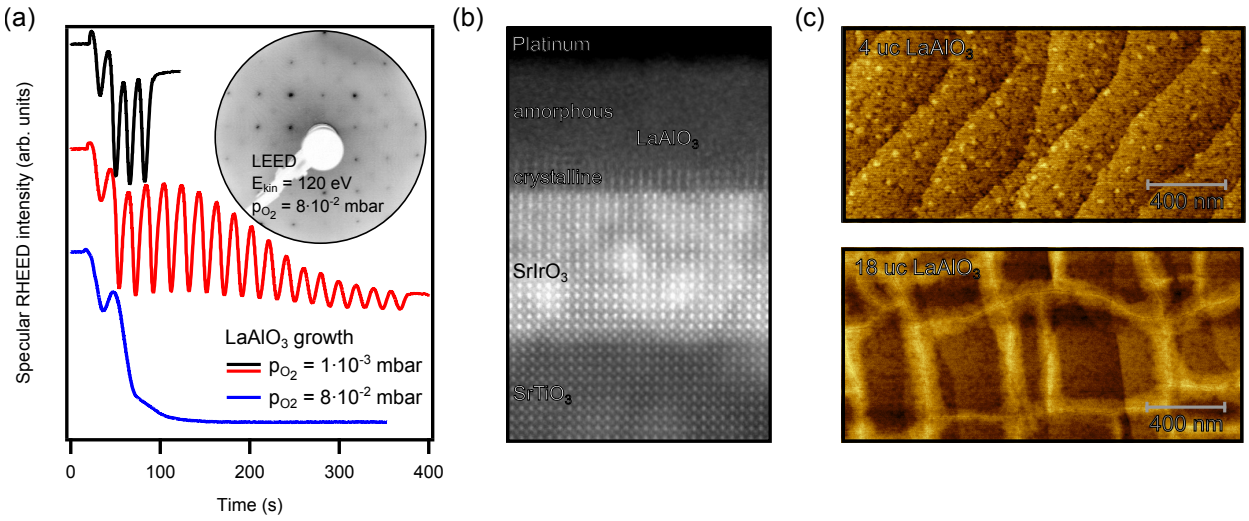

Figure 6.32: (a) Specular RHEED intensity oscillations during $LaAlO_3$ growth on a $SrIrO_3$ film. The oxygen partial pressure has to be reduced after the growth of $SrIrO_3$ ($p_{O_2} = 8 \cdot 10^{-2}$ mbar) to avoid the amorphization of $LaAlO_3$ above the first 1-2 unit cells. (b) HAADF-STEM displays the crystalline-amorphous transition in the $LaAlO_3$ film. (c) For moderately thick $LaAlO_3$ films a homogenous coverage with unit-cell steps, indicating layer-by-layer growth, is observed, whereas the large in-plane strain between $LaAlO_3$ and $SrTiO_3$ (via strained $SrIrO_3$) of $\approx 3\,\%$ leads to a strain relaxation by cracking above a certain thickness [325].

$SrIrO_3$ interface. However, in a first approximation doping of either holes or electrons into the half-filled $J_{\text{eff}} = 1/2$ band is expected to drive a band filling-controlled Mott transition into a correlated-metal regime.

Hence, the growth of $LaAlO_3$ on $SrIrO_3$ films has been established to test for changes of the electronic structure of $SrIrO_3$, which originate from a polar discontinuity-induced charge transfer to/from the $LaAlO_3/SrIrO_3$ interface. As shown in Fig. 6.32 (a) employing

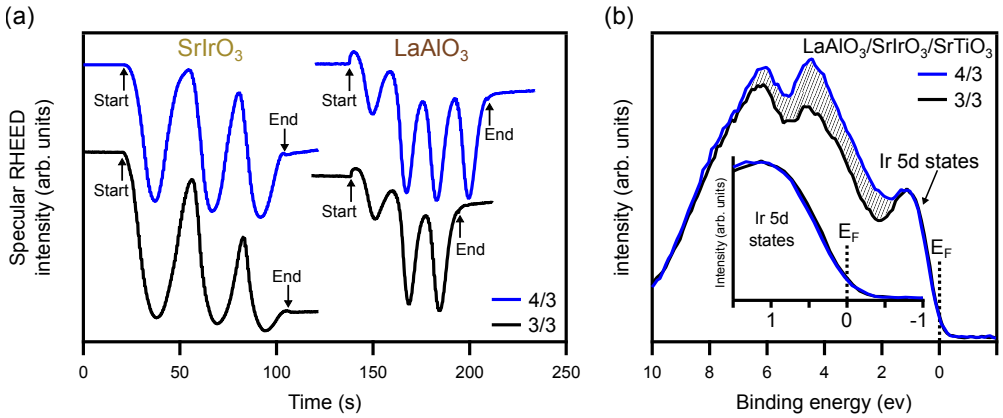

Figure 6.33: (a) Specular RHEED intensity oscillations during the growth of a 4/3 and a 3/3 $LaAlO_3/SrIrO_3/SrTiO_3$ heterostructure. (b) No significant changes are observed in the valence-band spectra near the chemical potential. The $LaAlO_3$ O $2p$ valence states lie in the higher binding energy region and are the reason for the (shaded) extra spectral weight.

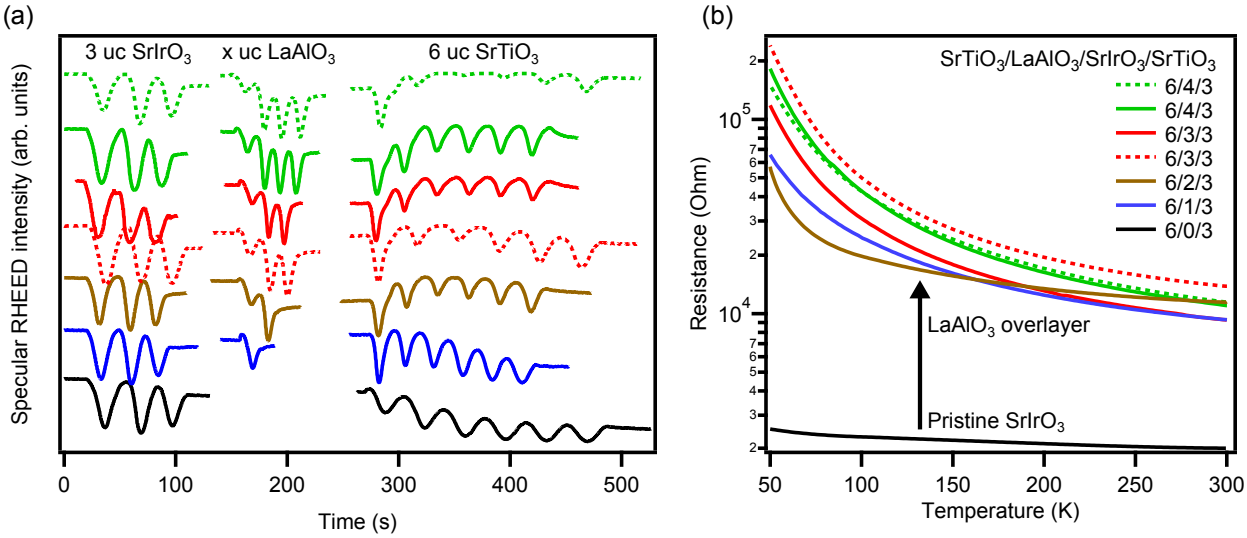

Figure 6.34: (a) Specular RHEED intensity oscillations during the growth of $SrTiO_3/LaAlO_3/SrIrO_3/SrTiO_3$ heterostructures for transport measurements, i.e., with an additional protective capping of 6 uc $SrTiO_3$. (b) R vs. T curves of several $SrTiO_3/LaAlO_3/SrIrO_3/SrTiO_3$ heterostructures with a constant $SrIrO_3$ (3 uc) and $SrTiO_3$ (6 uc), but variable $LaAlO_3$ thicknesses (0-4 uc). While all samples are insulating ($dR/dT < 0$), the specimens incorporating a $LaAlO_3$ layer exhibit an increased electrical resistance by one order of magnitude.

the rather high oxygen partial pressure necessary to achieve the correct oxidation state of iridium in $SrIrO_3$ ($p_{O_2} = 8 \cdot 10^{-2}$ mbar) for the growth of $LaAlO_3$ results in the rapid amorphization of $LaAlO_3$ after deposition of 1-2 unit cells. The transition from crystalline to amorphous $LaAlO_3$ is clearly resolved in a HAADF-STEM image in Fig. 6.32 (b), where $LaAlO_3$ adopts the perovskite structure for the first layers, but becomes disordered away from the interface. Aluminium is well-known for being extremely susceptible to oxidation and can even be exploited as reducing agent for the oxygen depletion of oxide surfaces [326]. For this reason, a reduction of the oxygen partial pressure by two orders of magnitude is required for persistent layer-by-layer growth on a $SrIrO_3$ film as seen in Fig. 6.32 (a) resulting in well-ordered and atomically flat $LaAlO_3$ for moderately thick films as shown by LEED (inset) and AFM (Fig. 6.32 (c)), respectively. However, despite the observation of more than 18 RHEED intensity oscillations, the significant in-plane strain of $\approx 3\,\%$ between $LaAlO_3$ and $SrTiO_3$ (via strained $SrIrO_3$) results in a strain relaxation by cracking above a certain thickness [325], hence limiting the accessible $LaAlO_3$ thickness range.

In the prototypical $LaAlO_3/SrTiO_3$ system, the critical thickness for the formation of a 2DES at the $SrTiO_3$ side of the heterointerface is 4 unit cells (uc) of $LaAlO_3$ [315]. Coincidentally, as shown in Fig. 6.1, the threshold thickness of the film thickness-induced metal-insulator transition in $SrIrO_3$ thin films is also 4 uc, although the physical origin is fundamentally different. For these reasons, two heterostructures with a $SrIrO_3$ thickness of 3 uc, i.e., close to the threshold for metallicity, and a $LaAlO_3$ thickness of 3 and 4 uc, i.e., below and above the expected critical thickness for a charge transfer, were grown on TiO_2-terminated $SrTiO_3$ (Fig. 6.33 (a)). In contrast to the itinerant Ti $3d$ states at the

$LaAlO_3/SrTiO_3$ interface, the number of Ir $5d$ electrons per site and the photoionization cross section of the Ir $5d$ valence states is sufficiently large for XPS measurements. However, within the energy resolution of XPS, no spectral changes are observed near the chemical potential as shown in Fig. 6.33 (b). Moreover, the presence of an screened-unscreened doublet structure impedes the indirect detection of additional charge by looking for a chemically shifted core-level component.

For these reasons the effect of a variable $LaAlO_3$ overlayer thickness on the transport behavior of $SrIrO_3$ films is systematically investigated. Since bare $SrIrO_3$ films are subject to degradation in air, a further protective crystalline $SrTiO_3$ overlayer is necessary for *ex situ* transport measurements [225]. As shown in Fig. 6.34 (a) persistent RHEED oscillations evidence the controlled layer-by-layer deposition of the complex heterostructures, during which the $SrTiO_3$ (6 uc) and $SrIrO_3$ (3 uc) thickness is kept constant, whereas the $LaAlO_3$ thickness ranges from 0 to 4 uc (denoted 6/x/3). Nonetheless, all samples stay in the insulating regime as characterized by a decreasing resistance with temperature ($dR/dT < 0$) shown in Fig. 6.34 (b). Interestingly, upon introduction of a $LaAlO_3$ overlayer and independent of its thickness the resistance reproducibly increases by an order of magnitude, with no significant deviation at the critical $LaAlO_3$ thickness of 4 uc. For these reason, in summary a polar discontinuity-induced charge transfer and concomitant band filling-induced Mott transition can be eliminated as driving mechanism for the observed changes in the resistance. Rather, the introduction of disorder by the $a^-a^-a^-$ octahedral rotations in bulk $LaAlO_3$, cation interdiffusion or the creation of oxygen vacancies acting as scattering centers within the $SrIrO_3$ may induce the observed increase of the resistance.

6.4 Summary

The importance of dimensionality on the electronic properties of iridates has been realized soon after the discovery of a metal-insulator transition in the bulk Ruddlesden-Popper strontium iridates $Sr_{n+1}Ir_nO_{3n+1}$ via n [16] and was further emphasized by the observation of a metal-insulator and concurrent magnetic transition in artificially synthesized superlattice structures ($[SrIrO_3]_m$,$[SrTiO_3]_k$), that mimic the layered perovskites. However, the hitherto-investigated materials should not be considered as two-dimensional in a strict sense since a finite interlayer coupling remains across the SrO or $SrTiO_3$ blocking layers. For this reason, the electronic properties of ultrathin $SrIrO_3$ films, deposited in a controlled layer-by-layer fashion with atomic precision, are investigated in this chapter. The opening of a charge gap at the chemical potential upon reduction of the film thickness below a threshold thickness of four unit cells evidences a metal-insulator transition. In a complementary study of the magnetoconductance properties of samples identical to ours, Groenendijk *et al.* similarly observe a metal-insulator transition, accompanied by enhanced spin fluctuations [248].

The energy- and momentum-resolved electronic structure of a thin film at the brink of the phase transition (3 uc) and in the two-dimensional limit (1 uc) was investigated by soft x-ray angle-resolved photoemission spectroscopy (SX-ARPES) and compared to the metallic band structure discussed in Chap. 5. Although the coherent $J_{\text{eff}} = 1/2$ band dispersion at the chemical potential is absent in the photoemission data of the insulating sample, the lower-

lying occupied $J_{\text{eff}} = 3/2$ bands continue to exhibit the characteristic dispersion observed also in the metallic case. Hence, the metal-insulator transition seems to be well-described by a single-band Mott transition induced by a reduction of the $J_{\text{eff}} = 1/2$ band width as a result of the reduced dimensionality. However, the expected characteristic transfer of spectral weight into an incoherent lower Hubbard band is not observed unequivocally, due to the presence of dispersive $J_{\text{eff}} = 3/2$ states in the same energy range. Although a clear discrimination is not possible, a broad non-dispersive peak at $\approx -1.5\,\text{eV}$ is consistently found throughout the reciprocal space and may be tentatively assigned to the lower Hubbard band. The faint dispersion discerned in the photoemission data of $SrIrO_3$ in the two-dimensional limit is in accordance with the band structure from magnetic DFT+U supercell calculations of a monolayer $SrIrO_3$. Since the DFT+U ground state in the presence of magnetic order is insulating irrespective of the $SrIrO_3$ thickness, while DFT+U calculations without magnetism yield a metal, a magnetic transition is expected to play an important role in the metal-insulator transition. As the band structure of the $SrIrO_3$ monolayer exhibits a striking similarity to bulk Sr_2IrO_4, the investigation of its evolution upon charge carrier doping promises valuable insights into the physics of Sr_2IrO_4 with respect to potential unconventional superconductivity.

The pronounced spin-orbit interaction in iridates strongly couples the electronic and structural degrees of freedom [65]. In the three-dimensional limit $SrIrO_3$ films adopt a distorted $GdFeO_3$-type structure with a $a^-b^+a^-/b^+a^-a^-$ domain structure as discussed in Sec. 4.5. Of these octahedral tiltings, only rotations about the surface normal prevail in the thin-film limit as a result of the octahedral connectivity between the $SrIrO_3$ film and the cubic perovskite substrate $SrTiO_3$. This structural transition to a $a^0a^0c^-$ pattern is reflected in a transition from a 2×2 to a $\sqrt{2} \times \sqrt{2}$ periodicity in surface electron diffraction and occurs at the same threshold thickness as the metal-insulator transition. Interestingly, the nonmetallic bulk Ruddlesden-Popper iridates Sr_2IrO_4 and $Sr_3Ir_2O_7$ also exclusively exhibit octahedral rotations about the c-axis [59, 88, 90, 327]. Since the hopping between neighboring iridium sites is mediated by the oxygen ligands, the transfer integral t is susceptible to changes of the bonding geometry [132]. Therefore, the structural transition may strongly affect the effective electronic correlations U/t and play a part in driving the Mott transition.

Since modifications of the lattice structure of crystals with ionic character inevitably precipitate changes of the electrostatic site potentials in the film, the observed structural transition was further investigated by introducing a simple lattice model with the tilting angle of the rigid IrO_6 octahedra as only degree of freedom. The site-dependent Madelung potential was found to be highly susceptible to octahedral tilting, with changes of $\approx -2\,\text{eV}$ for the strontium and $\approx 0.5\,\text{eV}$ for the iridium and oxygen sites. Indeed, this opposite trend observed for strontium and oxygen sites was found to be reflected in the relative binding energy shifts of strontium and oxygen core levels in the XPS spectra of bare $SrTiO_3$ and $SrIrO_3$ films with variable thicknesses. However, the simple model exclusively considers a hypothetical bulk crystal with variable tilting and can therefore not ultimately discriminate between the effects of the observed structural transition and dimensionality in ultrathin films. A comprehensive theoretical analysis of a realistic thin-film geometry including the semi-infinite substrate may serve to disentangle these contributions.

The multipeak structure in the Ir $4f$ core-level photoemission spectra of iridates is commonly attributed to the presence of a screened and unscreened final state and can be taken as measure for the strength of the effective electronic correlations, as evidenced by the intensity loss of the unscreened component when going from the Mott insulator Sr_2IrO_4 to the correlated metal $SrIrO_3$ and the Fermi-liquid system IrO_2 [296,297]. Similarly, the metal-insulator transition in $SrIrO_3$ thin films is accompanied by a suppression of the screened component as function of dimensionality. However, in contrast to bulk Sr_2IrO_4, the screened component is almost extinct in the two-dimensional thin-film limit. In comparison to monolayer $SrIrO_3$, where no perpendicular hopping channels are of avail, the finite hopping amplitude across the SrO double layers therefore appears to reduce the effective on-site Coulomb repulsion U/t in the Ruddlesden-Popper iridates.

The Ir $4f$ core-level spectra of ultrathin $SrIrO_3$ films is found to change upon storage in the UHV chamber on a time scale of several days. In this process oxygen sites in the SrO surface layer are found to be slowly substituted by fluorine atoms from the residual gas in the chamber which effectively act as electron dopants. Since the resulting chemically shifted Ir^{3+} component may be easily mistaken as a screened final state, care must be taken to measure a pristine $SrIrO_3$ surface. Regarding the similarity between monolayer $SrIrO_3$ and the predicted parent material for superconductivity Sr_2IrO_4, the unintentional fluorine doping may be utilized as electron-doping mechanism similar to cuprate superconductors [310]. However, no evidence of a band filling-induced Mott transition is found, although the observation of an increasing Ir $5d$ spectral weight attests the addition of electrons into Ir $5d$ states. Two possible scenarios for the absence of metallicity despite significant doping of up to one additional electron per iridium site are discussed. On the one hand, a strong charge disproportionation due to the presence of two spatially separated electronic phases with $5d^5$ Mott-insulating and $5d^6$ band-insulating configuration may serve as explanation. On the other hand, the effective positive charge of the fluorine impurity may lower the single-particle energy of its adjacent transition metal site and thereby act as charge trap for the doped electron, resulting in what has been called an alloy Mott-insulating phase.

As an alternative route to chemical substitution, which is not found to release itinerant charge carriers that trigger a band filling-controlled Mott transition, the thin-film geometry offers a minimally invasive possibility to achieve charge-carrier doping without the introduction of significant disorder. Most well-known from the paradigmatic $LaAlO_3/SrTiO_3$ system, the polar discontinuity at the polar/nonpolar heterointerface may result in a potential gradient in the $LaAlO_3$ film, which is canceled by a transfer of charge to the $SrTiO_3$ interface if a critical thickness of four unit cells is reached [261]. In the $LaAlO_3/SrTiO_3$ system the usually empty Ti $3d^0$ band becomes filled with electrons that form an itinerant two-dimensional electron system in the vicinity of the interface. For this reason, the influence of a variable $LaAlO_3$ overlayer thickness on the electronic properties of a $SrIrO_3$ film at the brink of the phase transition (3 uc) was investigated. Unfortunately, irrespective of its thickness the $LaAlO_3$ overlayer merely caused an increased resistivity rather than metallic behavior in the $SrIrO_3$ film. Therefore, structural or chemical instead of polar discontinuity-induced effects are held responsible for the observed minor changes of the transport properties.

In summary, a number of complex effects contribute to the metal-insulator transition

observed in $SrIrO_3$ films as function of dimensionality. In agreement with the general conception of the metal-insulator transition in the strontium iridate bulk layered perovskites, Mott localization appears to be the driving mechanism. Since the electronic and structural degrees of freedom are strongly intertwined, the leading factor cannot be ultimately determined. In the following chapter, the magnetic properties of $SrIrO_3$ thin films are investigated to test the theoretical predictions of a magnetically ordered phase in the two-dimensional limit.

Chapter 7

Spectroscopic footprints of magnetic order in $SrIrO_3$

In the last decade the magnetic properties of iridium oxides have been the subject of intense research efforts as the entanglement of spin and orbital degrees of freedom due to strong spin-orbit coupling (SOC) results in unconventional magnetic exchange interactions [6, 328]. In particular, the $J_{\text{eff}} = 1/2$ ground state found in spin-orbit-coupled Mott-Hubbard systems with a low-spin d^5-configuration is a coherent superposition of orbital and spin states of different symmetries with an inherent quantum phase and hence very different from the spin $S = 1/2$ state found in conventional Mott insulators [1, 8, 9]. These peculiarities result in multidirectional magnetic exchange interactions and, depending on the lattice geometry, may lead to a suppression of the isotropic Heisenberg interaction via destructive interference [8]. For example, when realized in a honeycomb lattice structure the $J_{\text{eff}} = 1/2$ low-energy physics is captured by the Kitaev model, which may host a spin-liquid ground state relevant for quantum computing [8, 329, 330].

In the Ruddlesden-Popper family of layered perovskite iridates $Sr_{n+1}Ir_nO_{3n+1}$ the IrO_6 octahedra form a corner-shared network, in which the isotropic antiferromagnetic exchange term competes with anisotropic terms driven by Hund's coupling and Dzyaloshinsky-Moriya interactions [8, 88]. Experimentally, a wide variety of magnetic orders is found in the perovskite iridates, for example, the quasi-two-dimensional Mott insulator Sr_2IrO_4 (n = 1) hosts a square lattice of antiferromagnetically coupled $J_{\text{eff}} = 1/2$ pseudospins with a weak ferromagnetic component due to canting, reminiscent of the high-T_C superconducting cuprate parent material La_2CuO_4 [9, 65, 133]. In contrast, the narrow-gap bilayer system $Sr_3Ir_2O_7$ (n = 2) hosts a G-type collinear antiferromagnetic structure with an easy c-axis [87, 88, 91], while the three-dimensional semimetal $SrIrO_3$ displays paramagnetic behavior [99].

In an attempt to mimic the layered Ruddlesden-Popper structure, a magnetic transition has been observed in artificially tailored ($[SrIrO_3]_m$,$SrTiO_3$) superlattices, where the intercalated SrO layers were substituted with $SrTiO_3$ monolayers [128]. While for m = 1 − 3 in-plane antiferromagnetism with a weak canted ferromagnetic component reminiscent of bulk Sr_2IrO_4 is observed, a dimensionality-driven transition to a paramagnetic metallic state takes place at m = 4. However, the lowered antiferromagnetic transition temperature observed upon increasing the number k of $SrTiO_3$ blocking layers in ($SrIrO_3$,$[SrTiO_3]_k$) superlattices evidences the persistent magnetic coupling between neighboring $[SrIrO_3]_m$ blocks across the $SrTiO_3$ blocking layers [130]. Hence, ultrathin $SrIrO_3$ films represent a considerably better-defined approach to the two-dimensional limit than superlattices.

The observation of enhanced spin fluctuations in magnetoconductance measurements near the thickness-driven metal-insulator transition (MIT) in $SrIrO_3$ thin films [248] and the density functional theory (DFT+U) analysis by D. Di Sante (cf. Fig. 6.9) indicate, that the MIT may also be accompanied by a magnetic transition resulting in a magnetically ordered ground state similar to bulk Sr_2IrO_4. However, an experimental investigation of the magnetic properties using a global magnetometric probe like a superconducting quantum interference device (SQUID) is impeded by the minute signal strength of a single atomic layer against the diamagnetic background of the $SrTiO_3$ substrate [331]. For this reason the atomic selectivity intrinsic to x-ray absorption spectroscopy (XAS) is exploited in this chapter to investigate the microscopic magnetic properties of $SrIrO_3$ thin films by means of x-ray magnetic circular dichroism (XMCD) measurements at the Ir M_3- and O K-absorption edges.

7.1 Data acquisition and correction

X-ray absorption spectroscopy (XAS), x-ray linear dichroism (XLD) and x-ray magnetic circular dichroism (XMCD) measurements at the O K and Ir M_3-absorption edges were performed at the soft x-ray beamline BOREAS (BL29) and high-field vector magnet end-station HECTOR of the Alba synchrotron in Barcelona, Spain, which offer full control of the light polarization at high photon flux and energy resolution. The O K-edge at $h\nu \approx 520-560\,\mathrm{eV}$ was measured using the 1^{st} undulator harmonic and a 800 lines/mm plane grating monochromator (MEG1 + SM1), while the Ir M_3-edge at $h\nu \approx 2510-2600\,\mathrm{eV}$ was measured using the 7^{th} harmonic and a 1200 lines/mm grating (HEG + SM2). The Ir M_2-absorption edge at $h\nu \approx 2880-2950\,\mathrm{eV}$ was not accessible with reasonable statistics due to the significant reduction of the photon flux in the high-energy limit, hence impeding the application of sum rules to disentangle the spin and orbital contribution to the magnetic moment by XMCD [196–198, 332]. As measure for the x-ray absorption, the total electron yield (TEY) and fluorescence yield (FY) were acquired as function of photon energy. Superconducting split-coils were used to generate a maximum magnetic field of $\pm 6\,\mathrm{T}$ directed along the incoming photon beam. All measurements were performed within a ultra-high vacuum (UHV)-compatible cryostat with a base pressure of $< 1 \times 10^{-10}\,\mathrm{mbar}$ and at a temperature $T = 25\,\mathrm{K}$ if not stated otherwise. After pulsed laser deposition (PLD) growth in Würzburg the samples were shipped to Barcelona in a vacuum vessel at a base pressure of $< 5 \times 10^{-9}\,\mathrm{mbar}$ and moved into the cryostat without exposure to ambient conditions.

Following data acquisition, the TEY and FY was normalized to the photocurrent of a gold mesh to account for synchrotron- or energy-dependent variations of the photon flux. For XLD and XMCD measurements, spectra with opposite polarization (a/b) were acquired consecutively in octets (a-b-b-a-b-a-a-b) or quartets (a-b-b-a) to compensate for potential time-dependent changes. The linear (LH, LV) or circular (C^+, C^-) dichroism $\Delta I(h\nu)$ of two data sets $I_{LV,C^+}(h\nu)$ and $I_{LH,C^-}(h\nu)$ is extracted by calculating

$$\Delta I(h\nu) = I_{LV/C^+}(h\nu) - (k + m \cdot h\nu) \cdot I_{LH/C^-}(h\nu), \tag{7.1}$$

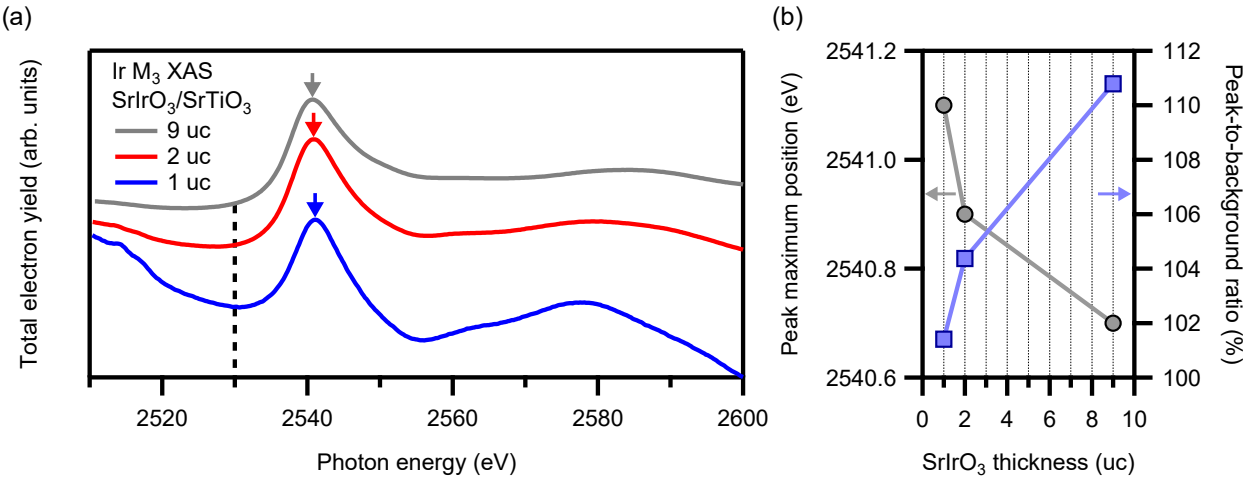

Figure 7.1: (a) Ir M_3-edge x-ray absorption spectra of three $SrIrO_3/SrTiO_3$ heterostructures with $SrIrO_3$ thicknesses 1,2 and 9 unit cells (arbitrarily scaled and offset). Due to an increasing contribution from lower-energy absorption edges the overall spectral line shape changes dramatically as the $SrIrO_3$ thickness decreases. (b) Peak maximum position (denoted by arrows in (a)) and peak-to-background ratio (background at $h\nu = 2530\,\mathrm{eV}$) of the three spectra.

where the parameters k and m are chosen such that

$$\int \left[I_{LV/C^+}(h\nu) - (k + m \cdot h\nu) \cdot I_{LH/C^-}(h\nu) \right]^2 d\,h\nu \tag{7.2}$$

in a defined pre- and post-edge region becomes minimized. In all spectra the pre- and post-edge region is denoted by a yellow line and background color.

7.2 Ir *M*-edge x-ray absorption spectroscopy

The BOREAS beamline offers access to a photon energy range from $h\nu = 80\,\mathrm{eV}$ to $h\nu = 4000\,\mathrm{eV}$, but the photon flux drops by more than an order of magnitude above $h\nu \approx 2500\,\mathrm{eV}$. In contrast to the L-edge of $3d$ transition metal oxides, XAS at the Ir $L_{2,3}$-absorption edge requires the use of dedicated hard x-ray beamlines as the needed photon energies lie between $h\nu = 11\,\mathrm{keV}$ and $13\,\mathrm{keV}$. For this reason, rather than using the $L_{2,3}$-absorption edges like most previous XMCD experiments on iridate compounds [133, 333–337], absorption experiments were performed at the Ir M_3-edge (Ir $3p_{3/2} \rightarrow$ Ir $5d$).

Figure 7.1 (a) shows the Ir M_3-edge TEY x-ray absorption spectra of three $SrIrO_3/SrTiO_3$ heterostructures with film thickness 1, 2 and 9 unit cells (uc). The Ir M absorption spectra are exclusively measured in TEY mode, since the x-ray fluorescence yield at the Ir M-edge is an order of magnitude smaller than at the Ir L-edge and hardly measurable [338]. The overall spectral line shape changes drastically with decreasing $SrIrO_3$ thickness due to the increasing contribution of the extended x-ray absorption fine structure from lower-energy absorption edges, in particular, the Sr $L_{2,3}$-edge at $h\nu \approx 2000\,\mathrm{eV}$ and the Ir $M_{4,5}$-edge at $h\nu \approx 2100\,\mathrm{eV}$ [339]. Specifically, the peak-to-background ratio drops from $\approx 110\,\%$ to below

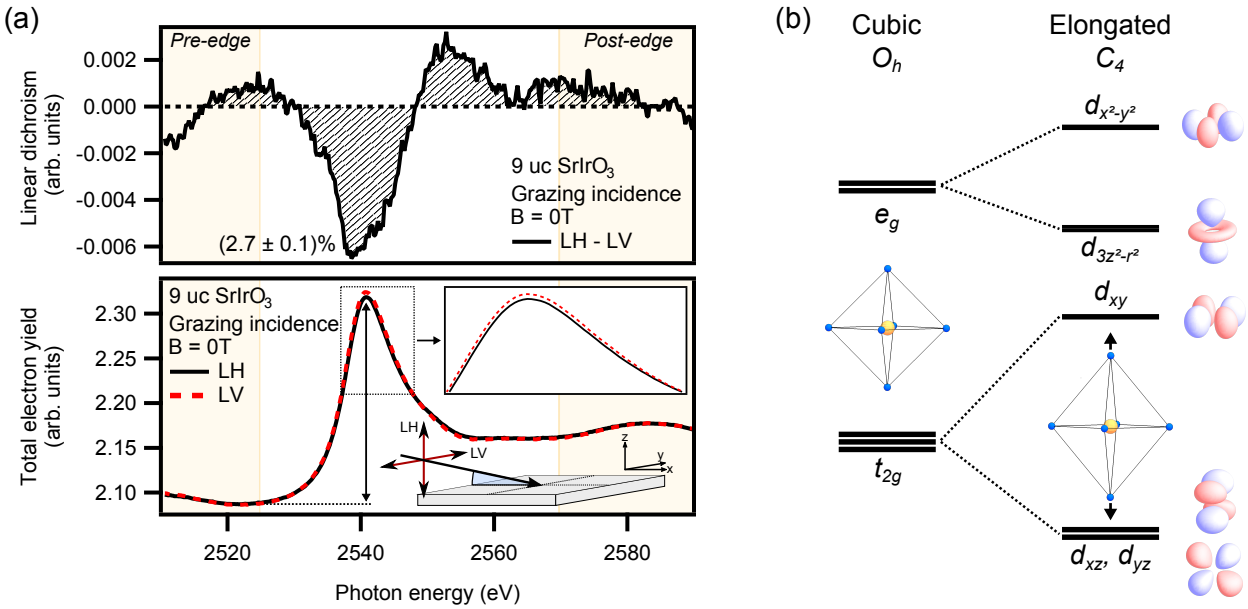

Figure 7.2: (a) Ir M_3-edge x-ray absorption spectra for linear horizontal (LH) and vertical (LV) light polarization and linear dichroism of a 9 uc $SrIrO_3$ sample in grazing incidence. The increased absorption for in-plane polarization (LV) indicates the presence of more holes in the in-plane orbitals. (c) Transition metal $5d$ splitting for a tetragonal distortion of the oxygen octahedron in the absence of strong spin-orbit coupling. Elongation along the c-axis lowers the energy of the out-of-plane orbitals $d_{xz/yz}$ and d_{z^2}.

$\approx 102\,\%$ in the monolayer limit, where the pre-peak signal at $h\nu = 2530\,\mathrm{eV}$ (dashed line) is taken as background. Furthermore, the changing background signal causes a shift of the peak maximum by $\approx 0.4\,\mathrm{eV}$ across the thickness-induced MIT (cf. Fig. 7.1 (b)).

7.2.1 X-ray linear dichroism at the Ir M-absorption edge

Polarization-dependent near-edge XAS is a powerful method to determine the local electronic structure of the transition metal ion in an oxide, as it is element specific and the dipole transition imposes strict selection rules [185]. Figure 7.2 (a) shows the Ir M_3-edge x-ray absorption spectra and linear dichroism of a 9 uc $SrIrO_3$ film in grazing light incidence and zero magnetic field. Since XLD yields information on the empty Ir $5d$ states, the larger absorption for in-plane polarization (LV) indicates the presence of more empty in-plane states [340, 341]. This finding is in line with the expected splitting of the t_{2g} and e_g energy levels in tetragonal C_4 symmetry due to an elongated octahedral crystal field in the absence of SOC as depicted in Fig. 7.2 (b). However, as reflected in the large peak width of $\approx 10\,\mathrm{eV}$, the short lifetime of the Ir $3p$ core hole due to the large number of possible Auger decay channels washes out the multiplet details, thereby impeding the discrimination of absorption features into the crystal-field-split t_{2g} and e_g states [25].

In the presence of strong SOC, the t_{2g} orbitals are split into a $J_{\mathrm{eff}} = 1/2$ doublet and a $J_{\mathrm{eff}} = 3/2$ quartet, but noncubic distortions will lead to a destruction of the spin-orbit entanglement and a restoration of the t_{2g} orbitals if the crystal-field strength is of the same

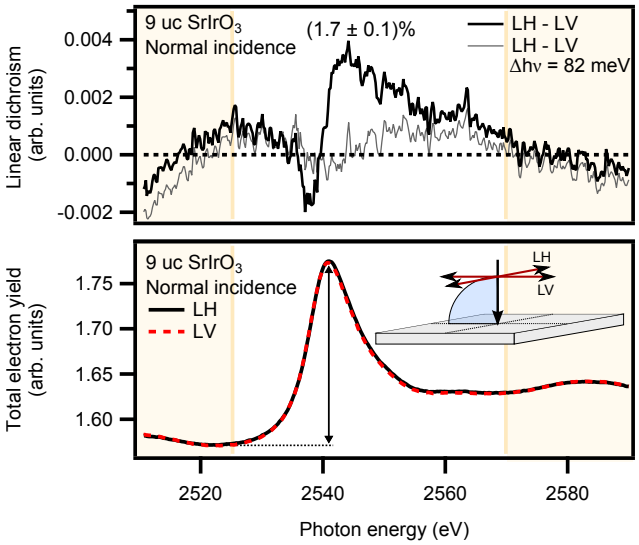

Figure 7.3: Ir M_3-edge x-ray absorption spectra for linear horizontal (LH) and vertical (LV) light polarization and linear dichroism of a 9 uc $SrIrO_3$ sample in normal incidence. Surprisingly, a sizeable dichroism is observed despite the nominal equivalence of *a*- and *b*-axis. Upon introduction of a photon energy shift between LV and LH the dichroic signal almost vanishes. Here and hereafter, the size of the dichroic signal is given relative to the difference between the maximum signal and the background signal, as indicated by an arrow.

order of magnitude as SOC [8, 25]. To what extent the $J_{\text{eff}} = 1/2$ state is materialized in iridate compounds has been the matter of intense debate in the past years [74,133,342–344]. By exploiting the larger Ir 3*d* core-hole lifetime in core-to-core resonant inelastic x-ray scattering (RIXS), Agrestini *et al.* showed that the d_{z^2} orbital is, as expected for the e_g manifold, indeed about 0.5 eV lower in energy than the $d_{x^2-y^2}$ orbital [25]. In contrast, the t_{2g} orbitals are found to be nearly degenerate as the tetragonal splitting is canceled by an imbalance between ligand hopping for in-plane and out-of-plane t_{2g} orbitals resulting from the large covalency of the 5*d* orbitals and the layered structure of Sr_2IrO_4 [25]. Whether or not the e_g and t_{2g} manifolds both exhibit a crystal field splitting due to the tetragonal distortion of the unit cell remains elusive and may be resolved by core-to-core RIXS measurements.

Intriguingly, as shown in Fig. 7.3 a dichroic signal is also found in normal light incidence, although the *a*- and *b*-axes are equivalent in first approximation. The octahedral pattern due to IrO_6 rotations discussed in Sec. 4.5 does break the tetragonal symmetry and would in principle allow for a dichroic signal. However, the approximate domain size of 50 nm observed in transmission electron microscopy (cf. Fig. 4.10) is several orders of magnitudes smaller than the beam size ($100 \times 100\,\mu m^2$) and is expected to result in a vanishing average dichroic signal. Furthermore, the symmetry breaking by the vicinal steps of the $SrTiO_3$ substrate cannot account for the dichroic signal of $(1.7 \pm 0.1)\,\%$ as the step size of 200 nm exceeds the lattice parameter by a factor of 500. The derivative-like shape of the dichroic signal, i.e., a zero-crossing at the maximum amplitude, is an indication that the dichroic signal is a measurement artifact rather than of physical origin. Indeed, an artificially introduced photon energy shift (≈ 80 meV) between LH and LV almost completely cancels the dichroism and

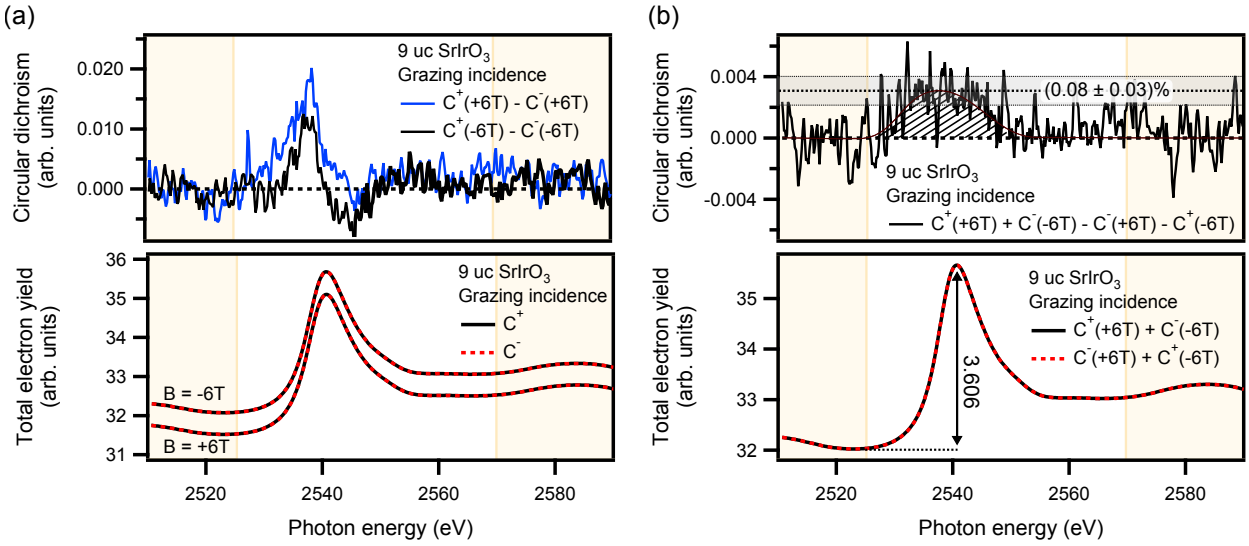

Figure 7.4: (a) Ir M_3-edge x-ray absorption spectra for circular right (C^+) and left (C^-) light polarization and circular dichroism ($C^+ - C^-$) of a 9 uc $SrIrO_3$ sample in grazing light incidence for positive and negative magnetic field $B = \pm 6$ T. The observed dichroic signal does not change sign with the magnetic field and is hence not (entirely) due to the sample magnetization, but a measurement artifact caused by an asymmetry between the optical paths of circular right and left beam. (b) Subtracting the spectra for $B = +6$ T and $B = -6$ T compensates the spurious dichroic signal and reveals the true, albeit tiny, magnetic dichroism.

may result from different optical paths of the different polarizations. In contrast, a similar shift does not result in a complete cancellation for grazing incidence.

7.2.2 X-ray circular magnetic dichroism at the Ir M-absorption edge

By using photons with defined helicity, i.e., circular polarization, the x-ray absorption process becomes spin-dependent and hence sensitive to the sample magnetization. While antiferromagnetic order cannot be detected due to symmetry constraints, it has been shown that the canted net ferromagnetic moment in Sr_2IrO_4, which differs from the local moment, can in principle be measured as function of magnetic field and temperature by XMCD at the Ir L_3-absorption edge [133].

Figure 7.4 shows the Ir M_3-absorption edge spectra of a 9 uc $SrIrO_3$ film in grazing incidence for circular right (C^+) and left (C^-) polarization in a magnetic field $B = \pm 6$ T and the respective magnetic circular dichroic signal. Interestingly, the dichroic signal does not change sign with the magnetic field and is hence not (entirely) due to a magnetization of the sample, but a measurement artifact caused by an asymmetry between the optical paths of circular right and left beam. Nonetheless, the different amplitude of the dichroic signal for $B = \pm 6$ T indicates the presence of a *pristine* XMCD, which can be extracted by

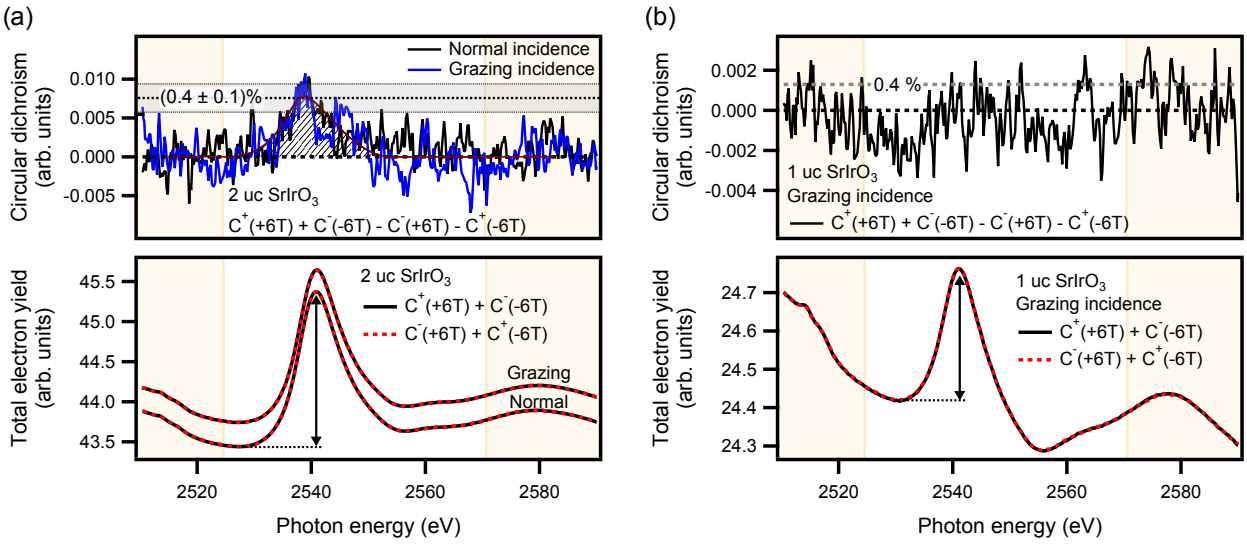

Figure 7.5: (a) Ir M_3-edge x-ray absorption spectra and circular dichroism of a 2 uc $SrIrO_3$ sample in grazing and normal light incidence. Subtracting $B = \pm 6\,\mathrm{T}$ reveals the true magnetic dichroic signal, which is of similar magnitude for normal and grazing incidence, i.e., in- and out-of-plane magnetization by the external magnetic field, hence indicating the absence of an easy axis for the magnetization (within the limited experimental resolution). (b) For the monolayer $SrIrO_3$ sample, no magnetic dichroism can be discerned within the rather large noise level due to the tiny iridium signal (cf. Fig. 7.1 (b)).

subtracting the two light polarizations:

$$\Delta I_{\pm} = I_{C^+}(+6T) + I_{C^-}(-6T) - [I_{C^-}(+6T) + I_{C^+}(-6T)] \tag{7.3}$$

The resulting signal reveals the true magnetic dichroism of the sample, albeit tiny ($(0.08 \pm 0.03)\,\%$ relative to the white line intensity denoted by an arrow in the absorption spectrum). The observation of a finite film magnetization at $B = \pm 6\,\mathrm{T}$ does not necessarily imply a persisting magnetic order at zero magnetic field and can be explained by the alignment of (Pauli) paramagnetic moments within the 9 uc thick metallic film [17, 99]. Due to the minute signal strength despite a total acquisition time of 12 hours, no efforts were made to check for a zero-field remanent signal at the Ir M-edge.

Since the thickness threshold for the MIT in $SrIrO_3$ films is 3 uc, the XMCD was also checked for $SrIrO_3$ films with 1 and 2 uc thickness. Figure 7.5 (a) and (b) show the respective absorption and extracted XMCD spectra using Eq. 7.3 for $B = \pm 6\,\mathrm{T}$ at grazing and normal light incidence. In the bilayer sample (Fig. 7.5 (a)), the dichroic signal is found to be five times stronger ($(0.4 \pm 0.1)\,\%$) than for the thick, metallic film and independent of the light incidence, hence indicating the absence of a pronounced easy axis for the magnetization. In contrast, no significant dichroic signal is observed for the monolayer $SrIrO_3$ (Fig. 7.5 (b)). However, a signal of the same order of magnitude as for the bilayer (0.4 %) would not be discernible within the noise level and hence, the presence of a paramagnetic response cannot be ultimately ruled out.

In summary, the presence of an increased (saturation) magnetization at $B = 6\,\mathrm{T}$ in the

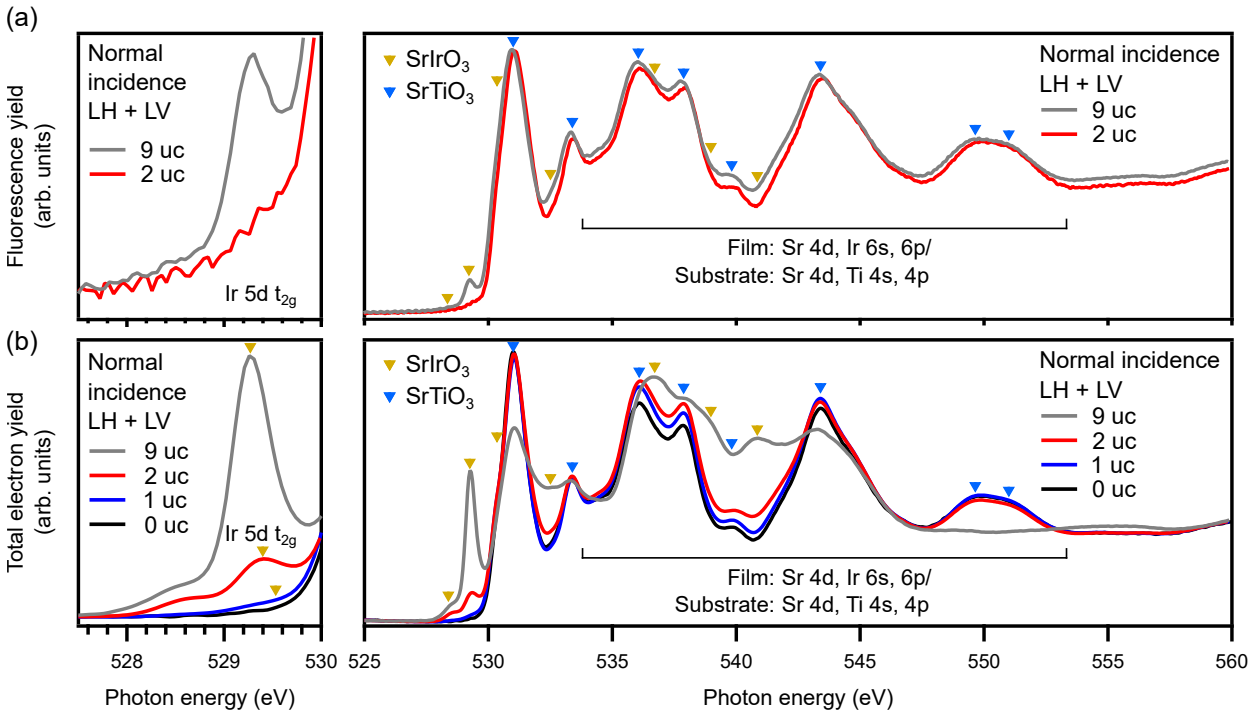

Figure 7.6: (a) Fluorescence yield x-ray absorption spectra of a 2 uc and 9 uc $SrIrO_3$ film on $SrTiO_3$. (b) Total electron yield x-ray absorption spectra of a 1, 2 and 9 uc $SrIrO_3$ film on $SrTiO_3$ and bare $SrTiO_3$. By comparison between the bulk- and surface-sensitive FY and TEY spectra to the $SrTiO_3$ reference, the $SrIrO_3$ (yellow triangles) and $SrTiO_3$ (blue triangles) features are identified. In the pre-peak region of $SrTiO_3$ a pronounced $SrIrO_3$ double-feature is observed which is identified as O $2p$ – Ir $5d$ t_{2g} hybridized state.

bilayer film indicates an increased magnetic susceptibility in the insulating limit. However, the overall small iridium signal strength for thin $SrIrO_3$ films in combination with the tiny magnetic circular dichroic signal necessitates extremely long acquisition times ($>$ 12 hours), which impede the systematic investigation of the temperature or magnetic field dependence of the magnetization. Hence, no direct conclusions can be drawn about the magnetic ground state and whether a long-range order persists in the absence of an external magnetic field.

7.3 O *K*-edge x-ray absorption spectroscopy

X-ray absorption at the oxygen K-edge takes advantage of the dipole transition from the O $1s$ to the O $2p$ state [184]. In a purely ionic crystal, the electronic configuration of an O^{2-} ion would be $1s^2 2s^2 2p^6$ and hence the absorption into the fully occupied $2p$ shell would be forbidden. However, in real materials (e.g., transition metal oxides) the covalency effect due to orbital hybridization between O $2p$ and cationic states effectively reduces the number of filled states with O $2p$ character, thereby opening the $1s \rightarrow 2p$ channel [184,345]. O K-edge XAS hence selectively measures the unoccupied density of states with O $2p$ symmetry.

Figure 7.6 shows the O K-edge absorption spectra of three $SrIrO_3/SrTiO_3$ heterostructures (1, 2 and 9 uc $SrIrO_3$) in comparison to bare $SrTiO_3$. The fluorescence yield (FY)

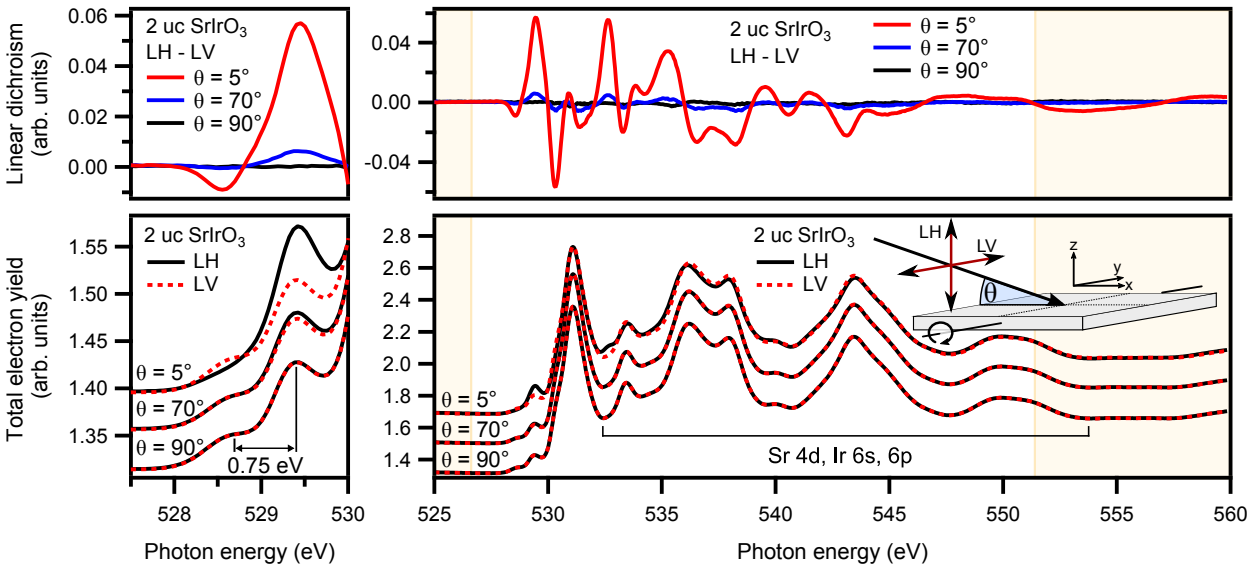

Figure 7.7: X-ray absorption spectra and linear dichroism of a 2 uc $SrIrO_3$ film on $SrTiO_3$ as function of the angle of light incidence Θ. A pronounced linear dichroism is observed, when Θ is tuned away from normal incidence ($\Theta = 90°$). Interestingly, the two pre-edge peaks exhibit a linear dichroism of opposite sign.

spectra in Fig. 7.6 (a) are dominated by the absorption of $SrTiO_3$, as the photons created during the fluorescent decay of the core hole have a mean free path similar to the incoming x-rays ($\approx 100\,\text{nm}$) [185]. In contrast, the $SrIrO_3$ contribution in the TEY spectra shown in Fig. 7.6 (b) is significant, since TEY probes the drain current of the sample which essentially originates from secondary Auger decay and therefore has a probing depth similar to the maximum $SrIrO_3$ thickness ($9\,\text{uc} \approx 36\,\text{Å}$) [185]. By comparison of the FY and TEY spectra to the $SrTiO_3$ reference spectrum, the $SrTiO_3$ (blue triangles) and $SrIrO_3$ (yellow triangles) contributions are easily identified. Nonetheless, a clear discrimination between substrate and film contribution is only possible in the pre-edge region of $SrTiO_3$ (left panels), where a pronounced $SrIrO_3$ double-feature is found.

In general, the transition metal oxide O K-edges can be divided into two regions: the first features near the onset of the edge ($h\nu < 534\,\text{eV}$) represent O $2p$ states hybridized with the unoccupied transition metal d states, while the features at higher photon energies originate from hybridization with the higher unoccupied states of the cations, i.e., Sr $4d$, Ir $6s$, Ir $6p$ for $SrIrO_3$ and Sr $4d$, Ti $4s$, Ti $4p$ for $SrTiO_3$ [185]. Hence, the double-feature in the pre-peak region is identified as an O $2p$ state hybridized with the lowest unoccupied Ir $5d$ state, i.e., the single hole in the $J_{\text{eff}} = 1/2$ (i.e., t_{2g}) states [20, 343].

In a recent XAS study on $SrRu_{1-x}Ir_xO_3$ thin films, Seong *et al.* observe a similar double-peak structure [346]. Here, the weak low-energy structure is assigned to the coherent quasi-particle state at the Fermi energy, while the higher-energy peak is interpreted as unoccupied upper Hubbard band (UHB) of $J_{\text{eff}} = 1/2$ states.[13] However, as shown in Fig. 7.6, the low-energy peak is clearly observed in the bilayer $SrIrO_3$ sample despite the total absence of

[13] The absolute peak energies in Ref. [346] are $h\nu \approx 526\,\text{eV}$ and $h\nu \approx 527\,\text{eV}$ and differ from ours by $\approx 2\,\text{eV}$. This discrepancy may however be due to calibration errors.

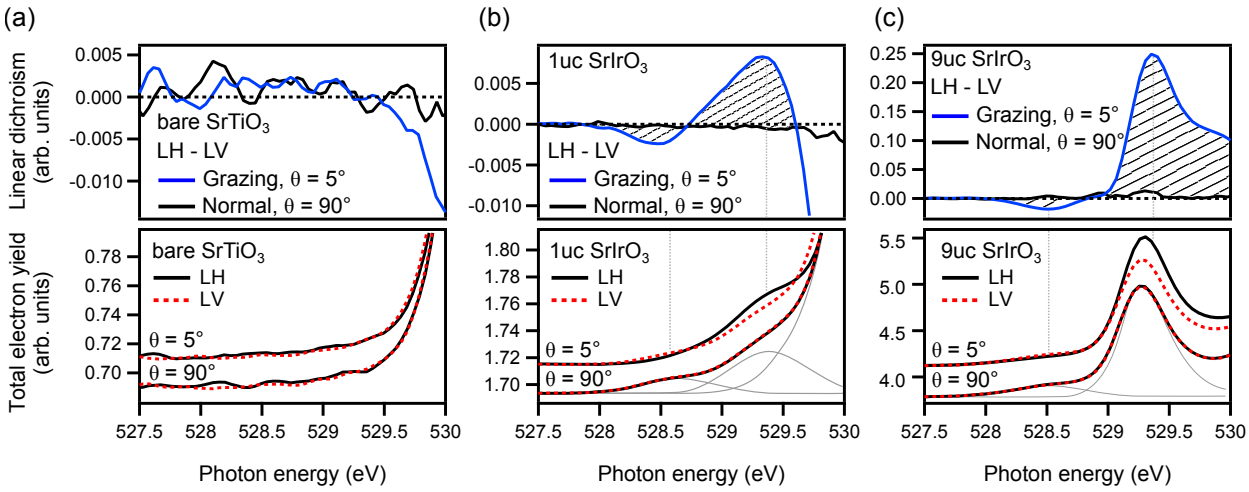

Figure 7.8: Pre-edge x-ray absorption spectra and linear dichroism in grazing and normal light incidence of (a) a bare $SrTiO_3$ substrate, (b) a 1 uc $SrIrO_3$ film and (c) a 9 uc $SrIrO_3$ film on $SrTiO_3$. While no signal is observed in the pre-edge region of $SrTiO_3$, the two pre-edge features exhibit a linear dichroism of opposite sign for all film thicknesses. The gray peaks are guides-to-the-eye.

coherent weight at the Fermi level in photoemission spectroscopy as discussed in detail in Chap. 6. Furthermore, the intensity of the alleged quasiparticle signal relative to the alleged UHB signal decreases with increasing film thickness, although the formation of a quasiparticle peak in photoemission evidences the transition from a Mott-insulating to a correlated-metal phase. For these reasons, the interpretation in Ref. [346] is questioned. In the following chapter, the physical origin of the double-peak structure is revealed by means of XLD measurements and DFT+U simulations.

7.3.1 Signatures of surface and bulk oxygen sites — x-ray linear dichroism at the O *K*-absorption edge

The polarization and angular dependence of O K-edge XLD is governed by the dipole matrix elements for the $1s \rightarrow 2p_i$ (i $= x, y, z$) transitions, which are fully determined by the relative orientation of the dipole vector and the $2p_i$ orbitals due to the isotropy of the $1s$ state [184]. Figure 7.7 shows the polarization-dependent O K-edge absorption spectra and linear dichroism of the 2 uc $SrIrO_3$ film as function of the angle of light incidence Θ relative to the substrate (see inset). The linear dichroism is zero for normal incidence ($\Theta = 90°$) and increases upon changing Θ to grazing incidence ($\Theta \approx 5°$). Intriguingly, as shown in the left panels, the two pre-edge features, which are separated by ≈ 0.75 eV exhibit a linear dichroism of opposite sign. In particular, the low-energy peak vanishes for out-of-plane polarization in grazing incidence. The same applies for the double-peak features in 1 uc and 9 uc $SrIrO_3$ films shown in Fig. 7.8, whereas the bare $SrTiO_3$ substrate exhibits neither XAS nor XLD in this region.

This behavior is reminiscent of the low-energy O K-absorption features in Sr_2IrO_4 [7, 20], Ba_2IrO_4 [343], $La_{2-x}Sr_xCuO_4$ [347], Sr_2RuO_4 [348] and Ca_2RuO_4 [349, 350]. Exemplarily,

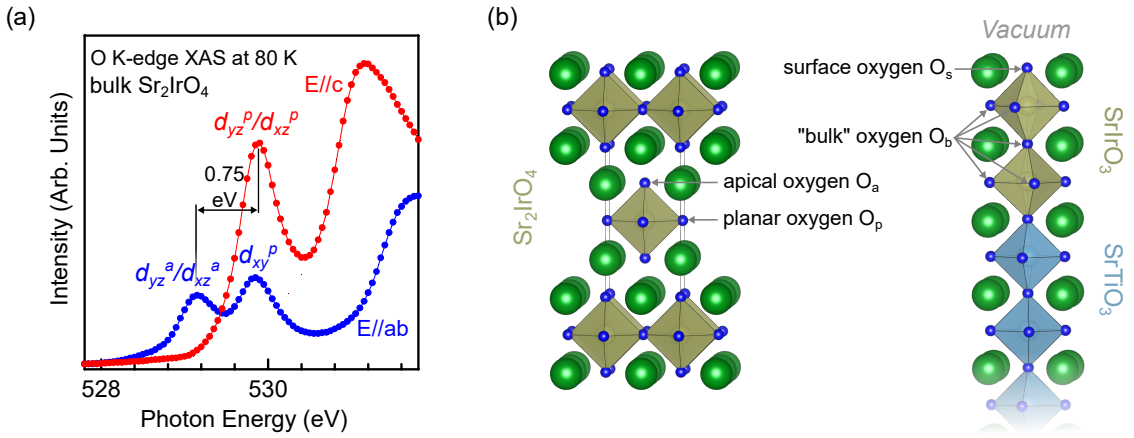

Figure 7.9: (a) O K-edge x-ray absorption spectra of bulk Sr_2IrO_4 for in- (E||ab) and out-of-plane (E||c) polarization. A similar energy splitting and polarization dependence as for $SrIrO_3$ thin films is observed. (b) The presence of two inequivalent oxygen sites with different binding energies in the n = 1 Ruddlesden-Popper structure of Sr_2IrO_4 explains the double-peak XAS structure. In contrast, the oxygen sites in bulk $SrIrO_3$ are equivalent (in the first approximation). However, the symmetry breaking at the surface may account for a large difference in O 1s binding energies. *Figure (a) adapted with permission from Ref. [7]. Copyright © (2008) by the American Physical Society. All rights reserved.*

the XAS of Sr_2IrO_4 (adopted from Ref. [7]) is shown in Fig. 7.9 (a). For out-of-plane polarization (E||c, LH) the low-energy feature is completely suppressed, while for in-plane polarization (E||a, LV) the two features are of roughly the same intensity. All mentioned examples have in common the quasi-two-dimensional n = 1 Ruddlesden-Popper structure shown in Fig. 7.9 (b), which hosts two inequivalent oxygen sites with very different local chemical environment. The accordingly different binding energies of apical (O_a) and planar (O_p) oxygen sites affect the energies of the O 1s core holes created during x-ray absorption and causes an energy shift between the absorption peaks [351]. Under this premise, the polarization dependence is easily understood, as the three t_{2g} orbitals have a strong directional dependence and therefore form different bonds with planar and apical oxygen $2p_i$ orbitals as shown in Fig. 7.10. For out-of-plane polarization the apical peak vanishes, because only $1s \rightarrow 2p_z$ transitions are allowed, while the apical O $2p_z$ orbital does not hybridize with any t_{2g} orbital due to symmetry constraints and hence is fully occupied [349, 350].

The n = ∞ member of the Ruddlesden-Popper series, i.e., the three-dimensional perovskite structure, does not host apical oxygen sites. As discussed in Chap. 6 the investigated $SrIrO_3$ films adopt a modified perovskite structure, which is tetragonally strained to the substrate and hosts a complex pattern of octahedral rotations that vary as function of the film thickness. In the thin-film limit $SrIrO_3$ exclusively hosts octahedral rotations about the c-axis and, as discussed in Sec. 6.2.2, the corresponding $a^0a^0c^-$ bulk structure hosts two inequivalent oxygen sites with a Madelung potential difference of less than 0.25 eV, which cannot account for the XAS double-peak structure observed in the 2 uc $SrIrO_3$ film. However, the Madelung potential calculation in Sec. 6.2.2 does not include the broken translational

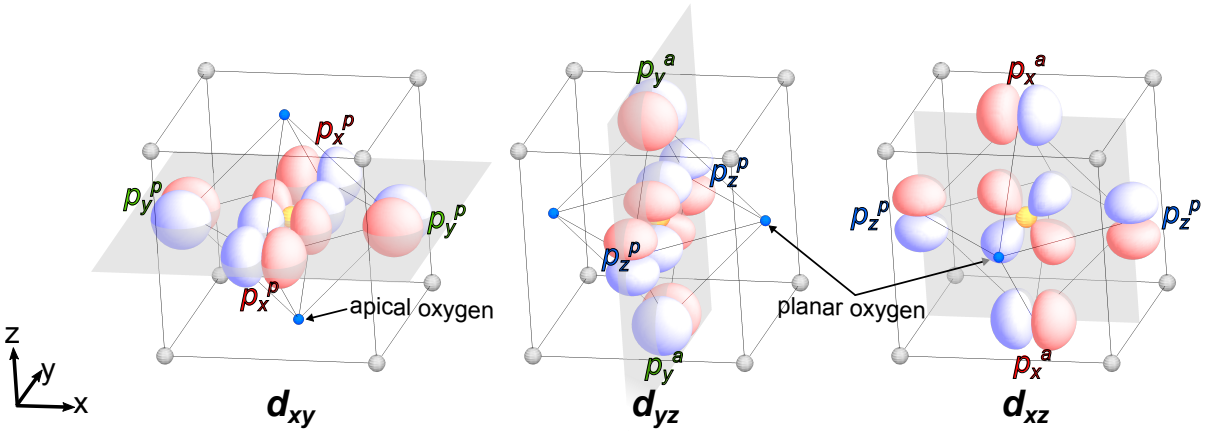

Figure 7.10: Symmetry-allowed O $2p$ – Ir t_{2g} orbital bonding geometries in an IrO_6 octahedron [349, 350].

symmetry at the surface (and interface), which drastically alters the nearest-neighbor chemical environment of the surface oxygen (O_s) in comparison to the subsurface ("bulk") oxygen sites (O_b). For this reason, the site-dependent O $1s$ core-hole energies for bulk Sr_2IrO_4 and the $1//4$ $SrIrO_3/SrTiO_3$ slab introduced in Sec. 6.1 were compared quantitatively by D. Di Sante. The DFT+U computations were performed using the functional and basis set described in Sec. 5.1 and the core-hole energy difference between the respective oxygen sites was extracted from the calculations as described in Refs. [352] and [353]. Indeed, the calculated difference between the O $1s$ core-hole energy of apical and planar oxygen in Sr_2IrO_4 amounts to 0.65 eV and is hence almost identical to the observed energy difference of 0.75 eV in Fig. 7.9 (a). In accordance, the difference in O $1s$ core-hole energy of surface and bulk oxygen in the $SrIrO_3$ monolayer is found to be 0.63 eV, in good agreement with bulk Sr_2IrO_4 and experiment. The lowest-energy peak in the x-ray absorption spectra of $SrIrO_3$ is therefore identified as O $2p_x/2p_y$ orbital of a surface oxygen in the terminating SrO layer which hybridizes with the adjacent Ir $5d_{xz}/5d_{yz}$ orbitals. The increasing bulk-to-surface ratio for thicker films naturally explains the increasing intensity ratio between high- and low-energy peak in Fig. 7.6.

7.3.2 Circular magnetic dichroism at the O *K*-absorption edge

X-ray absorption spectroscopy at the $L_{2,3}$-edges of transition metal oxides has attracted much attention due to the strong dependence of the XMCD on the exchange-splitting and SOC of the initial $2p$ core levels and the final states of d character. Less effort has been made to investigate the XMCD at the O K-edge of magnetic oxides, because the SOC of light elements is typically small due to the weak gradient of the core Coulomb potential. However, it has been shown that pronounced O K-edge XMCD can be induced by strong p–d hybridization in CrO_2 [354, 355], $LaMnO_3$ and $La_{1-x}Sr_xMnO_{3+\delta}$ [356]. In a comprehensive theoretical study Koide *et al.* have shown that the contribution of SOC at the absorbing oxygen atom is negligible for the O K-edge XMCD of CrO_2, whereas the SOC at the nearest-neighbor Cr site is found to strongly polarize the oxygen spin and orbital degrees of freedom

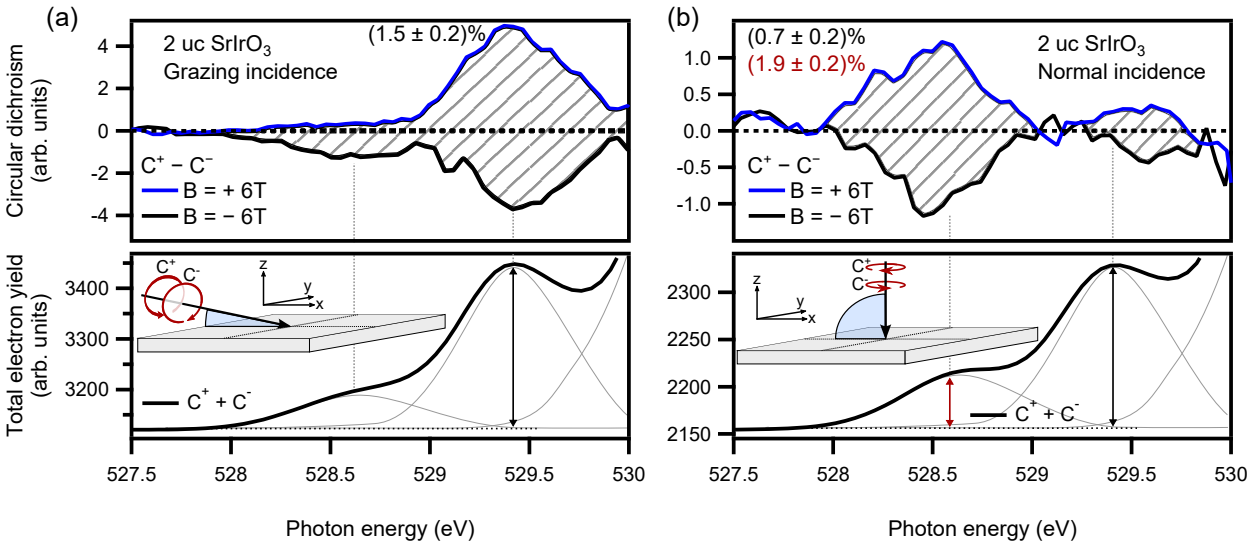

Figure 7.11: O K-edge XAS and XMCD of a 2 uc $SrIrO_3$ film on $SrTiO_3$ in a magnetic field $B = \pm 6\,\mathrm{T}$ in (a) grazing and (b) normal incidence. The sign change of the dichroic signal upon reversal of the magnetic field direction evidences its true magnetic origin.

via the O $2p$ – Cr $3d$ hybridization [357].

In comparison to $3d$ transition metal oxides like CrO_2, the hybridization between oxygen ligand and transition metal d states is known to be stronger in the $5d$ transition metal oxides due to the larger spatial extent of $5d$ orbitals [25]. Furthermore, the magnitude of the SOC is significantly enlarged at the heavy $5d$ transition metal site [9]. For these reasons the O K-edge XMCD of $SrIrO_3/SrTiO_3$ heterostructures was investigated with focus on the low-energy Ir $5d$ t_{2g}-derived features.

Figure 7.11 shows the O K-edge XAS and XMCD of a 2 uc $SrIrO_3$ film grown on $SrTiO_3$ in a magnetic field $B = \pm 6\,\mathrm{T}$. In grazing incidence the bulk-oxygen feature exhibits a significant dichroic signal, which changes sign upon reversal of the magnetic-field direction and is therefore of true magnetic origin. Intriguingly, the dichroism becomes zero in normal incidence, although no indication of an easy axis for magnetism is found in Ir M_3-edge XMCD. However, the Ir M_3-edge does not allow for a discrimination between absorption into the unoccupied t_{2g} and e_g states and hence the easy axis may exclusively hold for the $J_{\mathrm{eff}} = 1/2$ (i.e., t_{2g}) magnetic order in bilayer $SrIrO_3$. Interestingly, the surface-oxygen feature exhibits an inverse behavior, i.e., a finite magnetic dichroic signal in normal and zero dichroic signal in grazing incidence. However, on the basis of the current data set, it remains speculative whether the symmetry breaking at the surface results in a localized out-of-plane magnetization. A more systematic investigation of the O K-edge XMCD as function of the angle of incidence, $SrIrO_3$ thickness, magnetic field strength and temperature may shed light on this question in future measurements.

The observation of a magnetic circular dichroic signal in an external magnetic field does not necessarily imply the presence of a magnetically ordered phase, but may originate from an alignment of paramagnetic moments. Rather, the observation of a magnetic hysteresis as function of the external magnetic field serves as experimental fingerprint for ferromagnetism.

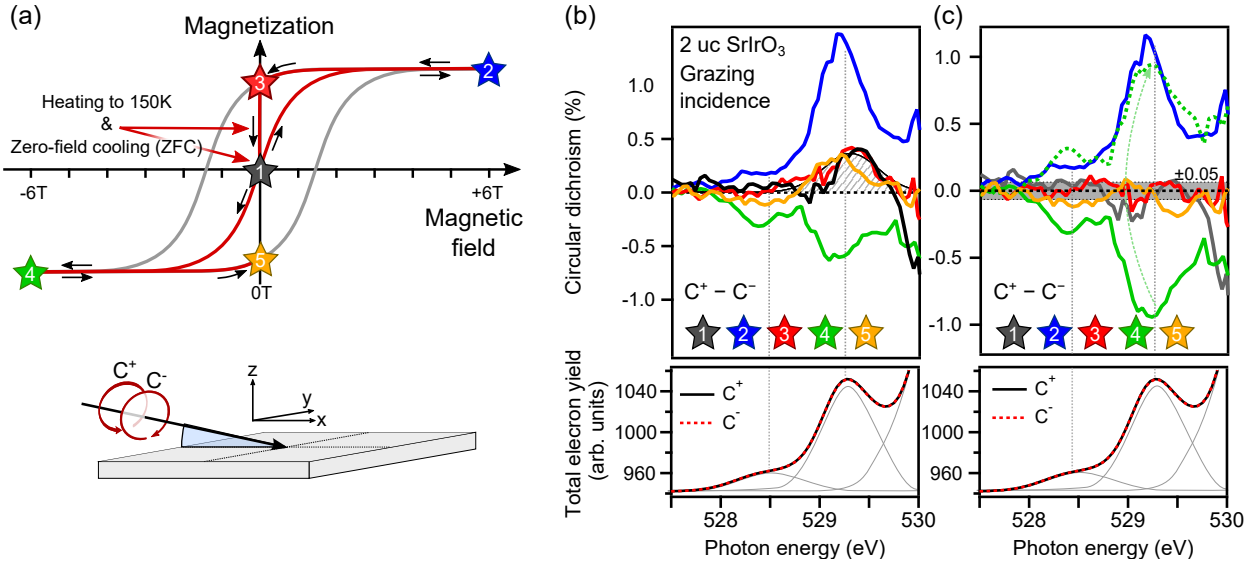

Figure 7.12: (a) Sketch of the magnetic hysteresis loop of a ferromagnetic material. When cooled down in zero external magnetic field (from above the Curie temperature) the net magnetization is zero due to the random alignment of ferromagnetic domains. After reaching the saturation magnetization upon increasing the external magnetic field, a finite remanent magnetization remains at zero field. The numbered stars along the red path denote the sampling points, where the XMCD spectra shown in (b) were measured. The dashed signal is superimposed over all XMCD spectra and is taken as measurement artifact. (c) After subtraction of the artifact the XMCD spectra are symmetric with respect to the external magnetic field (cf. green dashed curve). The noise level in spectra 1, 3 and 5, highlighted in gray, determines the upper boundary of the remanent magnetization to $\approx 5\,\%$ of the saturation magnetization.

Figure 7.12 (a) depicts an oversimplified sketch of a ferromagnetic hysteresis loop. When cooled down in zero magnetic field (zero-field cooling - ZFC) the ferromagnetic patches will align randomly and result in a zero net magnetization (1). With increasing magnetic field the ferromagnetic patches align until the saturation magnetization is reached (2). When decreasing the external magnetic field to zero, a finite net remanent magnetization M_R persists (3). In Ir L_3-edge XMCD measurements of bulk Sr_2IrO_4 a remanence magnetization $M_R(0\,\mathrm{T}) \approx 60\% \cdot M(0.75\,\mathrm{T})$ at $T = 6\,\mathrm{K}$ and a Curie temperature $T_C \approx 240\,\mathrm{K}$ are found in agreement with bulk magnetic susceptibility measurements [61, 133] and the saturation magnetization M_S is reached at $B \approx 0.5\,\mathrm{T}$. For ($[SrIrO_3]_m$, $SrTiO_3$) superlattices the Curie temperature is $T_C \approx 140\,\mathrm{K}$ ($m = 1$) and $T_C \approx 100\,\mathrm{K}$ ($m = 2$) [128].

As the acquisition time necessary to obtain an acceptable signal-to-noise ratio of the XMCD signal is on the order of 2 hours, the XMCD was only measured at five sampling points along the red path on the hysteresis loop in Fig. 7.12 (a). As shown in Fig. 7.12 (b) the dichroic signal in saturation ($B = \pm 6\,\mathrm{T}$) exhibits a clear sign reversal for opposite external magnetic field. However, the signal amplitude for $\pm 6\,\mathrm{T}$ is not equal and a reproducible, small positive dichroic signal is observed in all spectra taken at $B = 0\,\mathrm{T}$, irrespective of the sample history (ZFC or not). This residual signal may be a measurement artifact due to slightly different optical paths of the two circular light polarizations within the beamline,

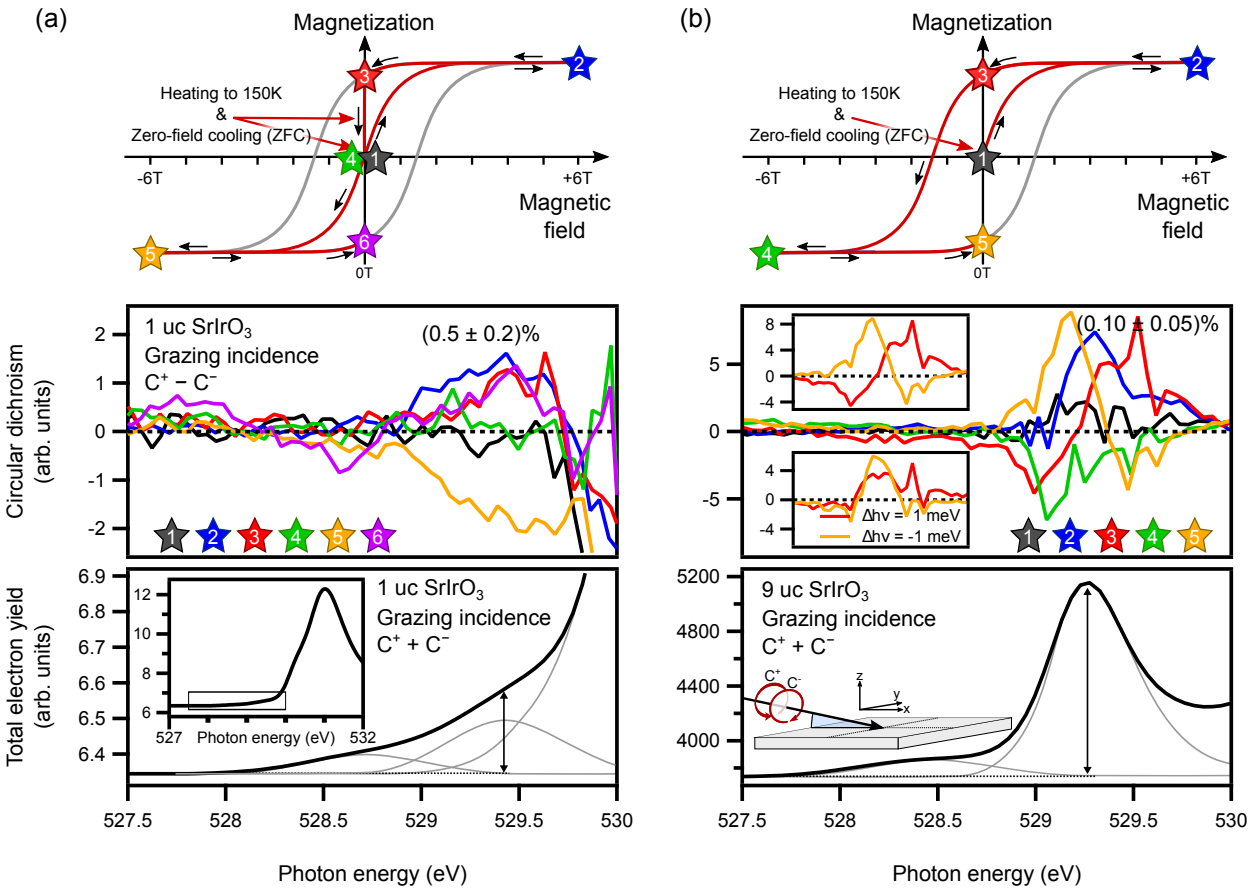

Figure 7.13: O K-edge XAS and XMCD measurements of (a) a 1 uc and a (b) 9 uc thick $SrIrO_3$ film on $SrTiO_3$ at different sampling points along the red path in a ferromagnetic hysteresis loop.

which is also observed for the Ir M_3 XMCD. Alternatively, it may be a true magnetic dichroism originating from magnetic moments pinned to impurities within the film, which survive the heating to $T = 150\,\mathrm{K}$ prior to ZFC. In any case, the dashed peak is therefore subtracted from all spectra, resulting in symmetric curves with respect to the magnetic field (cf. Fig. 7.12 (c)). Accordingly, an upper boundary of $\approx 5\,\%$ of the saturation magnetization at $B = \pm 6\,\mathrm{T}$ – corresponding to the noise level in Fig. 7.12 (c) – is found for the remanent magnetization. Hence, no clear manifestation of a magnetically ordered phase is observed.

Figure 7.13 shows similar measurements for the 1 uc and 9 uc $SrIrO_3$ films. However, for the monolayer the O K-edge XMCD is pushed to the limit of the experimental resolution, as the dichroic signal amounts to only 0.5 % of the pre-edge XAS signal, which is by itself overshadowed by the $SrTiO_3$ background (see inset). While a sign reversal is observed for $B = \pm 6\,\mathrm{T}$ (spectra 2 and 5), the $B = 0\,\mathrm{T}$ curves (spectra 3 and 6) do not show a systematic trend towards a significant remanence magnetization. In case of the 9 % $SrIrO_3$ film, the $B = \pm 6\,\mathrm{T}$ XMCD signal exhibits a sign reversal (spectra 2 and 4), but amounts to only 0.1 % of the total XAS signal. The $B = 0\,\mathrm{T}$ spectra (3 and 5) show a similarly large signal with a derivative shape, that is almost nullified by the introduction of a energy shift

of 1 meV (see insets). Accordingly, zero remanence magnetization is found in agreement with the expected paramagnetic behavior in the metallic phase. The overall quantitative difference to the rather large XMCD signals observed for the 2 uc (1.5 %) and 1 uc (0.5 %) films is an indication, that the magnetic susceptibility may be enlarged in the insulating phase. However, a more systematic study of the thickness and magnetic field dependence is necessary for a definite answer.

7.4 Summary

The dimensionality-driven metal-insulator transitions found in the Ruddlesden-Popper series $Sr_{n+1}Ir_nO_{3n+1}$ [16] and artificially tailored ($[SrIrO_3]_m$,$SrTiO_3$) superlattices [128] are accompanied by transitions from paramagnetic [99] to complex antiferromagnetically ordered phases [9, 88, 130, 133]. The enhanced spin fluctuations observed in magnetoconductance measurements of $SrIrO_3$ thin films in proximity to the thickness-driven MIT [248] and the good agreement between the SX-ARPES band structure and magnetic DFT+U calculations in the monolayer limit (cf. Sec. 6.1.3) advert to the possibility of a similar magnetic transition in $SrIrO_3$ thin films. In contrast, according to the Mermin-Wagner theorem the long-range ordering of an antiferromagnetic state is unstable against thermal fluctuations at arbitrarily low temperatures in a truly two-dimensional system, i.e., in the absence of interlayer coupling perpendicular to the plane [358]. Therefore, the magnetic properties of $SrIrO_3$ in the thin-film limit are investigated in this chapter.

The magnetic characterization of atomically thin layers is challenging, since conventional magnetometry using global probes (e.g. SQUID) predominantly picks up the diamagnetic response of the $SrTiO_3$ substrate (or of magnetic impurities therein) rather than the tiny signal from the $SrIrO_3$ film. For this reason, the inherent elemental selectivity and surface sensitivity of x-ray absorption spectroscopy in TEY mode was exploited to investigate the magnetic and electronic structure of $SrIrO_3$ thin films above and below the threshold thickness. To this end, the linear and magnetic circular dichroism at the Ir M_3- and O K-absorption edge of three films (1, 2 and 9 unit cells) were studied as function of magnetic field, angle of light incidence and/or temperature.

At the Ir M_3-edge the thin, insulating $SrIrO_3$ film is found to exhibit a larger magnetic circular dichroism in an external field $B = \pm 6$ T than its thick, metallic counterpart. Although this can be tentatively interpreted as indication for a stronger magnetic susceptibility in the insulating phase, the minute dichroic signal and photon flux at the M_3-edge necessitate acquisition times exceeding 12 hours and hence impede a systematic investigation as function of the external magnetic field. Therefore, it is not feasible to confirm the presence of a ferromagnetic order by searching for a magnetic hysteresis and/or a remanent magnetization at zero field.

Despite the presence of oxygen ions in the whole heterostructure, information about the film can be deduced from the linear and magnetic circular dichroism at the O K-absorption edge. By exploiting the different depth information inherent to absorption spectra acquired in fluorescence and total electron yield mode and by comparison to reference spectra of bare $SrTiO_3$, two spectral features in the pre-edge region of $SrTiO_3$ are clearly identified as

unoccupied states in the $SrIrO_3$ film. They arise from a hybridization of O $2p$ ligand states with the lowest unoccupied Ir $5d\,t_{2g}$ states and exhibit an opposite linear dichroism in grazing light incidence. This phenomenology is highly reminiscent of the quasi-two-dimensional Sr_2IrO_4 (and other transition metal oxides with the same Ruddlesden-Popper structure), where the photon energy offset is commonly explained by the different core-hole energies of apical and planar oxygen sites in the layered crystal structure. The angular dependence of the linear dichroism is readily explained by that of the $s \rightarrow p_i$ dipole matrix element and the symmetry-allowed bonds between the respective O $2p_i$ and Ir t_{2g} sub-orbitals. Due to the absence of apical oxygen sites in the cubic $SrIrO_3$ structure, the surface oxygen site is identified as origin of the lower-energy feature as confirmed by oxygen core-hole energies extracted from DFT+U calculations of a $SrIrO_3$//$SrTiO_3$ supercell and bulk Sr_2IrO_4.

Surprisingly, a circular magnetic dichroism is observed at the O K-absorption edge, most likely induced by a combination of strong spin-orbit coupling at the iridium site and the strong Ir $5d-$O $2p$ hybridization. Its true magnetic origin is evidenced by its changing sign upon reversal of the magnetic field. Since, to our knowledge, this is the first documented XMCD effect observed at the O K-edge of iridium oxides, these findings open a promising avenue towards a better understanding of the orbital character of the low-energy states in iridates and the magnetism of the $J_{\text{eff}} = 1/2$ pseudospin state. Interestingly, the magnetic dichroism of the bulk and surface oxygen features is found to vanish for normal and grazing light incidence, respectively. In light of the strong phenomenological similarities with Sr_2IrO_4, O K-edge XMCD measurements of bulk Sr_2IrO_4 samples may therefore be extremely beneficial for a deeper insight into its magnetic properties. However, a correct interpretation of the experimental data calls for strong theoretical support, e.g., by multiple scattering theory [357], which captures the complex interplay between $5d-2p$ hybridization and on-site SOC at the iridium cation site.

Similar to the Ir M_3-edge XMCD, in an external field of $B = \pm 6\,\text{T}$ the thin, insulating film is found to exhibit a significantly stronger dichroic signal at the O K-edge than the thick, metallic one. The comparatively strong dichroic signal of the 2 uc thick $SrIrO_3$ sample and the higher photon flux at the O K-edge furthermore allow for XMCD measurements at zero magnetic field to check for signs of remanence. However, no clear sign of a remanent magnetization exceeding an upper boundary of $\approx 5\%$ of the saturation magnetization at $B = \pm 6\,\text{T}$ is found in this study. Whether or not this translates into the absence of magnetic order in the two-dimensional limit, i.e., a confirmation of the Mermin-Wagner theorem, remains an open question and requires further dedicated XMCD measurements at the O K-edge with better measurement statistics and a more systematic investigation of the dependence on the external magnetic field, temperature and photon angle of incidence.

Chapter 8

Summary

In this thesis, the interplay between strong spin-orbit coupling and electron-electron interactions upon transition from the three- to the two-dimensional regime is investigated by state-of-the-art x-ray spectroscopy techniques. For this purpose, the evolution of the structural, electronic and magnetic properties of the $5d$ transition metal oxide $SrIrO_3$ is studied whilst undergoing a dimensional crossover. $SrIrO_3$ is the $n = \infty$ end member of the $Sr_{n+1}Ir_nO_{3n+1}$ Ruddlesden-Popper series, which has attracted substantial attention in the last decade due to observations of an exotic spin-orbit-entangled ground state. However, in contrast to its layered counterparts experimental data on $SrIrO_3$ has been scarce, since its perovskite phase is thermodynamically metastable at ambient conditions and only emerges upon application of high pressure and temperature.

In an alternative approach the cubic phase can be stabilized in a thin-film geometry by effectively substituting the external pressure by epitaxial strain to an underlying perovskite substrate. This thesis therefore sets out to establish the synthesis of single-crystalline perovskite $SrIrO_3$ films on $SrTiO_3$ by pulsed laser deposition (PLD). For this purpose the appropriate thermodynamic conditions for persistent layer-by-layer growth of high-quality, stoichiometric $SrIrO_3$ films are identified. A recurring theme is the tendency of iridium to form volatile IrO_3 at excessive substrate temperature and/or oxygen partial pressure. The formation and evaporation of IrO_3 leads to a cation off-stoichiometry and – depending on its magnitude – either results in the growth of other Ruddlesden-Popper phases or iridium-deficient $SrIrO_3$ with Ruddlesden-Popper-like stacking faults. However, even in fully stoichiometric films the iridium cations in the topmost IrO_2 layer remain prone to over-oxidation and, as a result, a conversion from B- to A-site surface termination is observed during PLD growth in contradiction with the expected conservation of the perovskite AO-BO_2 stacking order.

The crystal structure of the thus-optimized thin films exhibits two distinct deviations from the ideal cubic perovskite structure. On the one hand the cubic symmetry is broken by a tetragonal out-of-plane distortion due to epitaxial strain to the substrate, while on the other hand a collective rotational pattern of the IrO_6 octahedra is found to enlarge the crystalline unit cell by $\sqrt{2} \times \sqrt{2} \times 2$. Of the enlarged unit cell's three possible orientations, only two are observed and form orthogonally aligned domains.

Layer-by-layer growth is a prerequisite for the deposition of a predetermined number of atomic layers and hence for the investigation of the effects of dimensionality. The homogeneity and chemical composition of the target material, in particular the presence of $SrIrO_3$ rather than a mix of IrO_2 and hydroxylated $Sr(OH)_2$ is found to be crucial for this pur-

pose. Due to the unavailability of adequate commercial targets a manufacture process for high-quality $SrIrO_3$ targets was established, thereby facilitating reproducible layer-by-layer growth of phase-pure $SrIrO_3$ films.

In a combined experimental and theoretical approach the electronic structure of perovskite $SrIrO_3$ is thereupon investigated by soft x-ray angle-resolved photoelectron spectroscopy and *ab initio* density functional theory. Its metallic ground state exhibits coherent quasiparticle peaks with a well-defined Fermi surface and is reasonably well described by density functional theory in the presence of strong spin-orbit coupling. However, at variance with experiment the Fermi surface is comprised of $J_{\text{eff}} = 1/2$, $J_{\text{eff}} = 3/2$ and e_g states in the absence of electron-electron interactions. The introduction of a sizeable local Coulomb repulsion removes the latter from the chemical potential and renders a single metallic half-filled band that is well described by the effective total angular momentum $J_{\text{eff}} = 1/2$. Therefore, the Coulomb interaction yields an electron system which is susceptible to Mott localization given a sufficiently small kinetic energy. The tetragonal strain causes a tubular distortion of the Fermi surface, while backfolded shadow bands reflect the broken symmetry due to octahedral rotations.

Upon reduction of the film thickness below a threshold of four unit cells the opening of a charge gap at the chemical potential evidences a metal-insulator transition. Since the hopping term t is diminished upon transition into the two-dimensional regime the enhanced effective Coulomb repulsion U/t drives a Mott localization of the $J_{\text{eff}} = 1/2$ conduction electrons. The observation of the characteristic transfer of spectral weight into a lower Hubbard band by soft x-ray angle-resolved photoemission spectroscopy is impeded by the presence of dispersing $J_{\text{eff}} = 3/2$ bands below the chemical potential. The striking similarity between the electronic structures of SrO-terminated $SrIrO_3$ in the monolayer limit and the bulk Mott insulator Sr_2IrO_4 underlines the importance of dimensionality. With regard to predictions of exotic superconductivity in Sr_2IrO_4 upon electron doping, this finding potentially opens new avenues towards unconventional superconductivity in iridium oxides.

The metal-insulator transition is accompanied by a concurrent structural transition as the corner-shared octahedral network between substrate and film imposes constraints upon the octahedral rotations in the thin-film limit. Since the electron hopping in transition metal oxides is mediated by the oxygen ligands via $d-p$ hybridization, the structural transition is expected to concomitantly influence the metal-insulator transition by readjusting the balance between Coulomb repulsion U and hopping t.

In an effort to investigate the interfacial band alignment between substrate and film across the metal-insulator transition the photoemission core-level energies are traced as function of film thickness. The observed binding energy shifts evidence the formation of a Schottky barrier within the interfacial region of the $SrTiO_3$ substrate. However, as evidenced by divergent trends for the oxygen and strontium core levels, the concept of a global energy shift breaks down for the $SrIrO_3$ film because the site-dependent electrostatic Madelung potentials are highly susceptible to structural changes. Indeed, a quantitative estimate of the Madelung potentials upon introduction of variable octahedral rotations in strained $SrIrO_3$ yields changes between -0.5 and $+2\,\text{eV}$.

The iridium $4f$ core-level spectra indirectly reflect the metal-insulator transition, because

the final-state screening of the core hole by itinerant charge carriers becomes eliminated upon the opening of a charge gap. Since the screened-unscreened peak ratio is commonly taken as measure for the strength of electronic correlations, the total suppression of the screened component in the monolayer limit indicates a stronger prevalence of the Coulomb interaction than in bulk Sr_2IrO_4. Experimentally, the observation of the intrinsic screening process is complicated by the presence of an extrinsic surface contamination by fluorine. Despite the absence of a band filling-induced Mott transition, the correlation between the total Ir $5d$ spectral weight, the chemically shifted Ir^{3+} core-level component and the observed fluorine signal strongly suggests a charge carrier doping via chemical substitution of oxygen for fluorine at the very surface.

Finally, the magnetic properties of $SrIrO_3$ are investigated because of experimental and theoretical indications for a remanent magnetic order in atomically thin $SrIrO_3$. For this purpose, the elemental selectivity and surface sensitivity of x-ray absorption spectroscopy in total electron yield mode at the Ir M_3- and O K-absorption edge is exploited. Whereas the former is found to be unsuited for a systematic analysis, surprisingly, a circular magnetic dichroism is observed at the O K-absorption edge. The two dichroic features in the pre-edge region of $SrTiO_3$ are found to originate from the orbital hybridization of the lowest unoccupied Ir $5d$ states with the O $2p$ ligand states of the surface and bulk oxygen sites, respectively. Although the magnetic dichroism in an external magnetic field is found to be larger in the insulating limit, no evidence for a remanent magnetization in zero external field (exceeding an upper boundary of 5% of the saturation signal) is found in any $SrIrO_3$ thin film.

Bulk Sr_2IrO_4 is known to host a canted antiferromagnetically ordered ground state and exhibits a similar double-peak feature at the O K-edge as a result of the presence of apical and planar oxygen sites in its layered perovskite structure. In light of the unprecedented finding of an x-ray magnetic dichroism at the O K-edge of an iridium oxide and the striking phenomenological similarities, a comparative study of bulk Sr_2IrO_4 and $SrIrO_3$ thin films as function of external magnetic field, temperature and light incidence promises new insights into the intricate connection between the $J_{\text{eff}} = 1/2$ pseudospin state, its hybridization with the oxygen ligand states and the magnetic ordering phenomena in iridates.

In conclusion, the complex interplay between spin-orbit coupling, electronic correlations, magnetic order and structural degrees of freedom in epitaxially stabilized perovskite $SrIrO_3$ thin films has been investigated upon transition from the three- into the two-dimensional limit. It is demonstrated that the film thickness can be used as experimental control parameter to tune three physical properties, which cooperatively determine the system's ground state. First, the effective Coulomb interaction U/t increases upon reduction of the thickness since the coordination of iridium sites becomes smaller, hence providing less hopping channels (smaller t) and less screening (bigger U). Second, in the two-dimensional limit the crystalline structure due to the IrO_6 rotations deviates from the rotational pattern of bulk $SrIrO_3$, since the octahedral network with the cubic $SrTiO_3$ imposes constraints upon the in-plane rotations. Finally, the onset of an insulating state may be associated with magnetic correlations, although the actual stabilization of a long-range magnetic order remains a delicate issue.

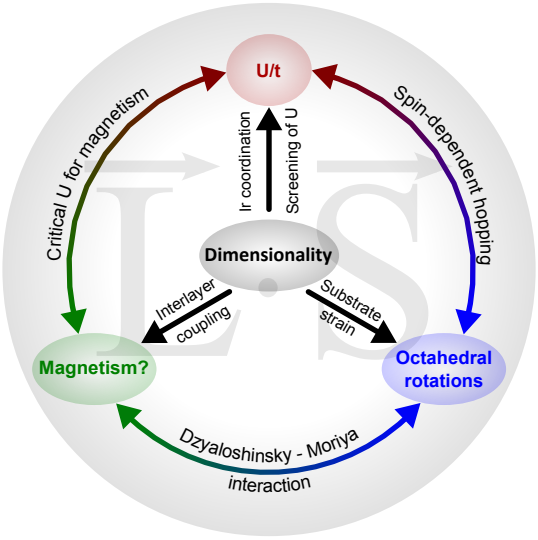

Figure 8.1: In conclusion, the film thickness, i.e., dimensionality is used as experimental control parameter to tune the effective Coulomb interaction U/t, the cooperative octahedral rotations and possibly the magnetic interactions. The cooperative interplay between these degrees of freedom constitutes the complexity of the system and complicates the identification of a leading parameter mechanism.

The strong cooperative interplay between these degrees of freedom constitutes the complexity of the system. Specifically, octahedral rotations strongly affect the magnetic coupling in iridates due to pseudodipolar and Dzyaloshinsky-Moriya-exchange interactions. In turn, the symmetry breaking due to octahedral rotations provides further spin-dependent hopping terms in the J_{eff} basis that will increase the hopping integral t. On the other hand, changes in U/t affect the magnetic ordering by altering the required critical on-site Coulomb repulsion U for the transition to an antiferromagnetic ground state.

The underlying reason for this extraordinary dimensionality dependence is the spatially three-dimensional $J_{\text{eff}} = 1/2$ Kramers doublet wave function, which results from the mixing of orbitals with different symmetries with the spin degrees of freedom due to the strong spin-orbit coupling in $5d$ systems. With regard to Sr_2IrO_4 as a potential parent material for exotic superconductivity, the analogy between monolayer $SrIrO_3$ and bulk Sr_2IrO_4 may open a promising experimental avenue towards electron doping without the introduction of disorder, thereby possibly pushing the system into a novel, spin-orbit-driven superconducting phase.

Appendix

Madelung potential

In an ionic crystal the electrostatic or Madelung energy due to the long-range Coulomb interaction is the main contributor to the total lattice energy. The electrostatic potential ϕ_i at any crystal site i, when approximating the ionic charge densities as point charges, is given by

$$\phi_i = \sum_{j \neq i} \phi_{ij} = \sum_{j \neq i} \frac{1}{4\pi\epsilon_0} \frac{q_j}{r_{ij}}, \tag{A.1}$$

where $q_j = Z_j e$ is the ionic charge at site j and $r_{ij} = |\vec{r_i} - \vec{r_j}|$ is the distance between the ions i and j. The site-dependent electrostatic potential and associated energy is unambiguous, but dependent on the lattice dimensions, ion positions and charges, and hence unique to any given crystalline material.

Often a dimensionless geometric factor α, known as Madelung constant is defined by introducing a characteristic distance R

$$\phi_i = \frac{e}{4\pi\epsilon_0 R} \sum_{j \neq i} \underbrace{\frac{Z_j}{r_{ij}/R}}_{\alpha}. \tag{A.2}$$

The Madelung constant α has a fixed value for any given crystal structure and is equal for all materials with identical symmetry. However, the choice of R is somewhat arbitrary (closest cation-anion distance, a lattice constant, the cube-root of the formula-unit volume, ...), resulting in possible confusion.

The evaluation of the lattice sum is not trivial because it is only conditionally convergent [359], as already addressed by Madelung in the early 20th century [360]. A prominent method to calculate the lattice potential based on the Fourier transformation of the crystal charge distribution was described by Ewald [289]. Here, the total electrostatic potential ϕ_i of the referential ion i in the field of all other ions in the crystal is given by

$$\phi_i = \sum_l \frac{q_l}{r_l} F\left(\eta^{1/2} r_l\right) + \frac{4\pi}{\Delta} \sum_{\vec{G}} S\left(\vec{G}\right) G^{-2} \exp\left(-\frac{G^2}{4\eta}\right) - 2q_i \left(\frac{\eta}{\pi}\right)^{1/2}, \tag{A.3}$$

where

$$F(x) = \frac{2}{\sqrt{\pi}} \int_x^\infty \exp\left(-s^2\right) ds, \tag{A.4}$$

Δ is the unit cell volume and $S\left(\vec{G}\right)$ is the structure factor. In Ewald's method, the charge density of an ion of charge q_i at point $\vec{r_i}$ is approximated as Gaussian distribution

$$\rho\left(\vec{r_i}\right) = q_0 \left(\eta/\pi\right)^{3/2} \exp\left(-\eta r^2\right), \tag{A.5}$$

where η describes the width and acts as a parameter, which has to be chosen correctly for rapid convergence. In Eq. A.3 the first and second term correspond to a summation in real and reciprocal space, respectively, with the third as correction term. The limit $\eta \to 0$ corresponds to a direct summation.[14]

For the numerical evaluation of the Ewald sum and the associated Madelung potential, the Python code shown in Listing A.1 was adopted from Ref. [362]. As input it requires a list r of three-dimensional vectors $\vec{r_i}$ describing the lattice sites of ion i, a list q of scalars q_i describing the ionic point charges of ion i and two lists *cell* and *invcell* of three vectors describing the real and reciprocal space unit cell, respectively. The output electrostatic potentials ϕ_i in the program are expressed in Å^{-1}, since charges are introduced as charge numbers and distances are expressed in Å. Multiplication with a factor $\frac{e}{4\pi\epsilon_0} \approx 14.4\,\text{VÅ}$ yields the electrostatic potential in V.

The code was tested with several benchmark compounds discussed by van Gool & Piken [363]. As shown in Tab. A.1 the calculated values coincide with the reference values within a margin of error below 0.02%, independent of the chosen unit cell. Since the main objective of this study was the interpretation of experimental core-level binding energies, the focus is put on the site-dependent Madelung potential of specific compounds rather than the dimensionless Madelung constant of certain crystal structures. However, α can be obtained from these values by

$$\alpha = -a \sum_i \frac{q_i p_i \phi_i}{2\kappa} \tag{A.6}$$

where $a = R$ is the length of the unit cell, q_i is the total charge number of ion i, p_i the frequency of occurrence of ion i in the unit cell and κ the total number of the formula unit in the unit cell.

[14] For a detailed derivation of Ewald's formula see Ref. [361], App. B.

Material	Setting	Input	i	Site	$\phi_{i,\mathrm{cal}}$ (Å^{-1})	$\phi_{i,\mathrm{Lit}}$ (Å^{-1})
CsCl	Cubic	`CsCl_Cubic(i)`	0	Cs^+	−0.4937	−0.4936
	Single unit cell		1	Cl^-	+0.4937	+0.4936
	Orthorhombic	`CsCl_Ortho(i)`	0-2	Cs^+	−0.4937	−0.4936
	(3 CsCl)		3-6	Cl^-	+0.4937	+0.4936
NaCl	Cubic	`NaCl(i)`	0	Na^+	−0.6210	−0.621
			1	Cl^-	+0.6210	+0.621
$SrTiO_3$	Cubic	`SrTiO3_single(i)`	1	Sr^{2+}	−1.3795	−1.380
	$1 \times 1 \times 1$		1	Ti^{4+}	−3.1696	−3.170
	unit cell		2-4	O^{2-}	+1.6532	+1.653
	$2 \times 2 \times 2$	`SrTiO3_double(i)`	0-7	Sr^{2+}	−1.3796	−1.380
	unit cell		8-15	Ti^{4+}	−3.1696	−3.170
			15-39	O^{2-}	+1.6532	+1.653

Table A.1: Madelung potentials ϕ_i of the benchmark compounds CsCl, NaCl and $SrTiO_3$. $\phi_{i,\mathrm{cal}}$: calculated with the Python code in Listing A.1 and A.2. $\phi_{i,\mathrm{Lit}}$: reference values by Van Gool & Piken in Ref. [363]. For CsCl and $SrTiO_3$ the Madelung potential was calculated using the primitive and an enlarged unit cell. The deviation between the calculated values and the reference values is below 0.02%.

```
#The MIT License (MIT)
#
#Copyright (c) 2015 Luke Olson
#
#Permission is hereby granted, free of charge, to any person obtaining a copy
#of this software and associated documentation files (the "Software"), to deal
#in the Software without restriction, including without limitation the rights
#to use, copy, modify, merge, publish, distribute, sublicense, and/or sell
#copies of the Software, and to permit persons to whom the Software is
#furnished to do so, subject to the following conditions:
#
#The above copyright notice and this permission notice shall be included in all
#copies or substantial portions of the Software.

from numpy import dot, sqrt
from numpy.linalg import norm
from scipy.special import erfc
from scipy import exp, pi

def energy():
    pass

def potential(i, r, q, cell, area, invcell, alpha=5, nmax=3, mmax=9):
    """
    i : potential location
    r : list of radii
    q : list of charges
    alpha : Ewald parameter
    nmax : real space box cutoff
    mmax : Fourier space box cutoff
    """
    Vr = potential_realsum(i, r, q, cell, alpha, nmax)
    Vf = potential_recipsum(i, r, q, invcell, alpha, mmax, area)
    Vs = potential_selfsum(i, r, q, cell, alpha)
    return Vr+Vf+Vs

def potential_realsum(i, r, q, cell, alpha, nmax):
    Vr = 0
    for j in range(0, len(q)):
        rij = r[i, :] - r[j, :]
        Vrloc = 0
        for n2 in range(-nmax, nmax+1):
            for n1 in range(-nmax, nmax+1):
                for n0 in range(-nmax, nmax+1):
                    if max([abs(n0), abs(n1), abs(n2)]):
                        n = n0*cell[0, :]+n1*cell[1, :]+n2*cell[2, :]
                        rn = norm(rij - n)
                        Vrloc += erfc(alpha*rn)/rn
        Vr += q[j]*Vrloc
    return Vr
```

```
def potential_recipsum(i, r, q, cell, alpha, mmax, area):
    Vf = 0
    for j in range(0, len(q)):
        rij = r[i, :] - r[j, :]
        Vfloc = 0
        for n2 in range(-mmax, mmax+1):
            for n1 in range(-mmax, mmax+1):
                for n0 in range(-mmax, mmax+1):
                    if max([abs(n0), abs(n1), abs(n2)]):
                        m = 2*pi*(n0*cell[0, :]+n1*cell[1, :]+n2*cell[2, :])
                        Vfloc += exp(1.j * dot(m, rij) - dot(m, m) /
                                     (alpha**2 * 4))/(dot(m, m)/(4*pi**2))

        Vf += q[j]/(pi*area) * Vfloc.real
    return Vf

def potential_selfsum(i, r, q, cell, alpha):
    Vs = 0
    for j in range(0, len(q)):
        if i == j:
            Vs -= 2*q[j]*alpha/sqrt(pi)
        else:
            rn = norm(r[i, :] - r[j, :])
            Vs += q[j]*erfc(alpha*rn)/rn
    return Vs
```

Listing A.1: Python code for the Ewald summation of the Madelung potential. *Adopted from Ref. [362]. Copyright © (2015) by Luke Olson.*

```
from pyewald import ewaldsum
from numpy import array, diag, sqrt, concatenate, dot
from numpy.linalg import det, inv

def CsCl_Cubic(i):
    a = b = c = 4.123
    cell = diag((a, b, c))
    invcell = inv(cell).T
    r = array([[0.1*a,  0.1*b,  0.1*c],
               [0.6*a,  0.6*b,  0.6*c]])
    q = array([1, -1])
    area = abs(det(cell))
    alpha = 5./sqrt((cell**2).sum(1).max())
    return ewaldsum.potential(i, r, q, cell, area, invcell, alpha)


def CsCl_Ortho(i):
    a = 4.123
    b = 4.123
    c = 12.369
    cell = diag((a, b, c))
    invcell = inv(cell).T
    r = array([[0.6*a,  0.6*b,  (4/15)*c],
               [0.6*a,  0.6*b,  0.6*c],
               [0.6*a,  0.6*b,  (14/15)*c],
               [0.1*a,  0.1*b,  0.1*c],
               [0.1*a,  0.1*b,  (13/30)*c],
               [0.1*a,  0.1*a,  (23/30)*c]
              ])
    q = array([1, 1, 1, -1, -1, -1])
    area = abs(det(cell))
    alpha = 5./sqrt((cell**2).sum(1).max())
    return ewaldsum.potential(i, r, q, cell, area, invcell, alpha)


def NaCl(i):
    a = b = c = 5.62779
    cell = diag((a, b, c))
    invcell = inv(cell).T
    r = array([[0,      0,      0],
               [0.5*a,  0.5*b,  0],
               [0.5*a,  0,      0.5*c],
               [0,      0.5*b,  0.5*c],
               [0.5*a,  0,      0],
               [0,      0.5*b,  0],
               [0,      0,      0.5*c],
               [0.5*a,  0.5*b, 0.5*c]])
    q = array([1, 1, 1, 1, -1, -1, -1, -1])
    area = abs(det(cell))
    alpha = 5./sqrt((cell**2).sum(1).max())
    return ewaldsum.potential(i, r, q, cell, area, invcell, alpha)
```

```
def SrTiO3_Single(i):
    a = 3.9051
    b = 3.9051
    c = 3.9051
    cell = diag((a, b, c))
    invcell = inv(cell).T
    r = array([[0,      0,      0],
               [0.5*a,  0.5*b,  0.5*c],
               [0.5*a,  0.5*b,  0],
               [0,      0.5*b,  0.5*c],
               [0.5*a,  0,      0.5*c]])
    q = array([+2, +4, -2, -2, -2])
    area = abs(det(cell))
    alpha = 5./sqrt((cell**2).sum(1).max())
    return ewaldsum.potential(i, r, q, cell, area, invcell, alpha)


def SrTiO3_Double(i):
    a = b = c = 2*3.905
    qA = +2
    qB = +4
    qO = -2
    Basis = array([[0, 0, 0],
                   [1, 0, 0],
                   [1, 1, 0],
                   [0, 1, 0],
                   [0, 0, 1],
                   [1, 0, 1],
                   [1, 1, 1],
                   [0, 1, 1]])
    A = array([0.0, 0.0, 0.0])
    B = array([0.5, 0.5, 0.5])
    O1 = array([0.0, 0.5, 0.5])
    O2 = array([0.5, 0.0, 0.5])
    O3 = array([0.5, 0.5, 0.0])
    q = array([qA, qA, qA, qA, qA, qA, qA, qA,
               qB, qB, qB, qB, qB, qB, qB, qB,
               qO, qO, qO, qO, qO, qO, qO, qO,
               qO, qO, qO, qO, qO, qO, qO, qO,
               qO, qO, qO, qO, qO, qO, qO, qO])
    Sites = concatenate((Basis+A, Basis+B, Basis+O1, Basis+O2, Basis+O3))
    cell = diag((a, b, c))
    invcell = inv(cell).T
    area = abs(det(cell))
    alpha = 5./sqrt((cell**2).sum(1).max())
    for j, Site in enumerate(Sites):
        Sites[j] = 0.5*dot(cell, Site)
    return ewaldsum.potential(i, Sites, q, cell, area, invcell, alpha)
```

```
def SrIrO3_Bulk(i, delta):
    a=5.5909
    b=7.8821
    c=5.5617

    cell = diag((a, b, c))
    invcell = inv(cell).T

    AtomA = "Sr"
    AtomB = "Ir"
    AtomO = "O"

# Positions from original paper by Zhao et al.
# (J. Appl. Physics 103, 103706 (2008))
#    Sr = Wyckoff_Pnma_4c(0.4901,0.25,0.5085)
#    Ir = Wyckoff_Pnma_4b(0,0,0.5)
#    O1 = Wyckoff_Pnma_4c(0.073,0.25,0.506)
#    O2 = Wyckoff_Pnma_8d(0.714,0.044,0.292)

# Revised positions from Comment to Zhao et al.
# by Puggioni & Rondinelli (J. Appl. Phys. 119, 086102 (2016))
    Sr = Wyckoff_Pnma_4c(0.5085,0.25,0.4901)
    Ir = Wyckoff_Pnma_4b(0.5,0,0)
    O1 = Wyckoff_Pnma_4c(0.506,0.25,0.073)
    O2 = Wyckoff_Pnma_8d(0.292,0.044,0.714)

    Types = array([AtomA,AtomA,AtomA,AtomA,
                   AtomB,AtomB,AtomB,AtomB,
                   AtomO,AtomO,AtomO,AtomO,
                   AtomO,AtomO,AtomO,AtomO,
                   AtomO,AtomO,AtomO,AtomO,])
    r = concatenate((Sr, Ir,O1,O2))

    qA = +2
    qB = +4 - delta
    qO = -2 + (delta/3)

    q = array([qA, qA, qA, qA,
               qB, qB, qB, qB,
               qO, qO, qO, qO,
               qO, qO, qO, qO,
               qO, qO, qO, qO ])

    for j,Site in enumerate(r):
        r[j] = dot(cell, Site)

    area = abs(det(cell))
    alpha = 5./sqrt((cell**2).sum(1).max())

    return ewaldsum.potential(i,r,q,cell,area,invcell, alpha)
```

```
# WYCKOFF POSITIONS of point group Pnma (NO.62)
def Wyckoff_Pnma_8d(x,y,z):
    W8d = array([[x,y,z],
                 [-x+0.5, -y, z+0.5],
                 [-x, y+0.5, -z],
                 [x+0.5, -y+0.5, -z+0.5],
                 [-x,-y,-z],
                 [x+0.5, y, -z+0.5],
                 [x,-y+0.5,z],
                 [-x+0.5, y+0.5, z+0.5]
                ])
    return W8d

def Wyckoff_Pnma_4c(x,y,z):
    W4c = array([[x,0.25,z],
                  [-x+0.5,0.75,z+0.5],
                  [-x,0.75,-z],
                  [x+0.5, 0.25,-z+0.5]
                ])
    return W4c

def Wyckoff_Pnma_4b(x,y,z) :
    W4b = array([[0,0,0.5],
                  [0.5,0,0],
                  [0,0.5,0.5],
                  [0.5,0.5,0]
                ])
    return W4b
```

Listing A.2: Structural definitions for the calculation of the Madelung potential, for details see Tab. A.1.

Bibliography

[1] M. Imada, A. Fujimori and Y. Tokura, Reviews of Modern Physics **70**, 1039 (1998).

[2] M. Z. Hasan and C. L. Kane, Reviews of Modern Physics **82**, 3045 (2010).

[3] P. A. Lee, N. Nagaosa and X.-G. Wen, Reviews of Modern Physics **78**, 17 (2006).

[4] C. L. Kane and E. J. Mele, Science **314**, 1692 (2006).

[5] P. A. Dirac and R. H. Fowler, Proceedings of the Royal Society of London A **117**, 610 (1928).

[6] W. Witczak-Krempa, G. Chen, Y. B. Kim and L. Balents, Annual Review of Condensed Matter Physics **5**, 57 (2014).

[7] B. Kim, H. Jin, S. Moon, J.-Y. Kim, B.-G. Park, C. Leem, J. Yu, T. Noh, C. Kim, S.-J. Oh, J.-H. Park, V. Durairaj, G. Cao and E. Rotenberg, Physical Review Letters **101**, 076402 (2008).

[8] G. Jackeli and G. Khaliullin, Physical Review Letters **102**, 017205 (2009).

[9] B. J. Kim, H. Ohsumi, T. Komesu, S. Sakai, T. Morita, H. Takagi and T. Arima, Science **323**, 1329 (2009).

[10] J. G. Bednorz and K. A. Müller, Zeitschrift für Physik B **64**, 189 (1986).

[11] F. Wang and T. Senthil, Physical Review Letters **106**, 136402 (2011).

[12] H. Watanabe, T. Shirakawa and S. Yunoki, Physical Review Letters **110**, 027002 (2013).

[13] Y. K. Kim, O. Krupin, J. D. Denlinger, A. Bostwick, E. Rotenberg, Q. Zhao, J. F. Mitchell, J. W. Allen and B. J. Kim, Science **345**, 187 (2014).

[14] Y. K. Kim, N. H. Sung, J. D. Denlinger and B. J. Kim, Nature Physics **12**, 37 (2016).

[15] S. N. Ruddlesden and P. Popper, Acta Crystallographica **10**, 538 (1957).

[16] S. J. Moon, H. Jin, K. W. Kim, W. S. Choi, Y. S. Lee, J. Yu, G. Cao, A. Sumi, H. Funakubo, C. Bernhard and T. W. Noh, Physical Review Letters **101**, 226402 (2008).

[17] J. M. Longo, J. A. Kafalas and R. J. Arnott, Journal of Solid State Chemistry **3**, 174 (1971).

[18] A. Georges, G. Kotliar, W. Krauth and M. J. Rozenberg, Reviews of Modern Physics **68**, 13 (1996).

[19] F. Hund, Zeitschrift für Physik **33**, 345 (1925).

[20] S. J. Moon, M. W. Kim, K. W. Kim, Y. S. Lee, J.-Y. Kim, J.-H. Park, B. J. Kim, S.-J. Oh, S. Nakatsuji, Y. Maeno, I. Nagai, S. I. Ikeda, G. Cao and T. W. Noh, Physical Review B **74**, 113104 (2006).

[21] K. Momma and F. Izumi, Journal of Applied Crystallography **44**, 1272 (2011).

[22] B. Keimer, A. Aharony, A. Auerbach, R. J. Birgeneau, A. Cassanho, Y. Endoh, R. W. Erwin, M. A. Kastner and G. Shirane, Physical Review B **45**, 7430 (1992).

[23] B. Andlauer, J. Schneider and W. Tolksdorf, Physica Status Solidi B **73**, 533 (1976).

[24] S. Sugano, *Multiplets of Transition-Metal Ions in Crystals*, Elsevier (2012).

[25] S. Agrestini, C.-Y. Kuo, M. Moretti Sala, Z. Hu, D. Kasinathan, K.-T. Ko, P. Glatzel, M. Rossi, J.-D. Cafun, K. O. Kvashnina, A. Matsumoto, T. Takayama, H. Takagi, L. H. Tjeng and M. W. Haverkort, Physical Review B **95**, 205123 (2017).

[26] F. Bloch, Zeitschrift für Physik **57**, 545 (1929).

[27] F. Bloch, Zeitschrift für Physik **52**, 555 (1929).

[28] A. Sommerfeld, Zeitschrift für Physik **47**, 1 (1928).

[29] J. H. d. Boer and E. J. W. Verwey, Proceedings of the Physical Society **49**, 59 (1937).

[30] N. F. Mott and R. Peierls, Proceedings of the Physical Society **49**, 72 (1937).

[31] N. F. Mott, Proceedings of the Physical Society. Section A **62**, 416 (1949).

[32] N. F. Mott, Canadian Journal of Physics **34**, 1356 (1956).

[33] N. F. Mott, Philosophical Magazine **6**, 287 (1961).

[34] J. Hubbard, Proceedings of the Royal Society of London A **276**, 238 (1963).

[35] M. C. Gutzwiller, Physical Review Letters **10**, 159 (1963).

[36] J. Kanamori, Progress of Theoretical Physics **30**, 275 (1963).

[37] R. Bulla, *private communication with Michael Sing* (2001).

[38] W. F. Brinkman and T. M. Rice, Physical Review B **2**, 4302 (1970).

[39] J. M. Luttinger, Physical Review **119**, 1153 (1960).

[40] J. M. Luttinger and J. C. Ward, Physical Review **118**, 1417 (1960).

[41] J. Zaanen, G. A. Sawatzky and J. W. Allen, Physical Review Letters **55**, 418 (1985).

[42] P. M. Woodward, Acta Crystallographica B **53**, 32 (1997).

[43] P. M. Woodward, Acta Crystallographica B **53**, 44 (1997).

[44] V. M. Goldschmidt, Naturwissenschaften **14**, 477 (1926).

[45] R. D. Shannon, Acta Crystallographica A **32**, 751 (1976).

[46] C. J. Howard and H. T. Stokes, Acta Crystallographica B **54**, 782 (1998).

[47] A. M. Glazer, Acta Crystallographica B **28**, 3384 (1972).

[48] A. M. Glazer, Acta Crystallographica A **31**, 756 (1975).

[49] C. H. Kronbo, M. B. Nielsen, S. M. Kevy, P. Parisiades and M. Bremholm, Journal of Solid State Chemistry **238**, 74 (2016).

[50] M. B. Nielsen, D. Ceresoli, P. Parisiades, V. B. Prakapenka, T. Yu, Y. Wang and M. Bremholm, Physical Review B **90**, 214101 (2014).

[51] C.-Q. Jin, J.-S. Zhou, J. B. Goodenough, Q. Q. Liu, J. G. Zhao, L. X. Yang, Y. Yu, R. C. Yu, T. Katsura, A. Shatskiy and E. Ito, Proceedings of the National Academy of Sciences **105**, 7115 (2008).

[52] J.-G. Cheng, J. A. Alonso, E. Suard, J.-S. Zhou and J. B. Goodenough, Journal of the American Chemical Society **131**, 7461 (2009).

[53] J.-G. Cheng, T. Ishii, H. Kojitani, K. Matsubayashi, A. Matsuo, X. Li, Y. Shirako, J.-S. Zhou, J. B. Goodenough, C. Q. Jin, M. Akaogi and Y. Uwatoko, Physical Review B **88**, 205114 (2013).

[54] M. Murakami, K. Hirose, K. Kawamura, N. Sata and Y. Ohishi, Science **304**, 855 (2004).

[55] F. Lichtenberg, A. Herrnberger, K. Wiedenmann and J. Mannhart, Progress in Solid State Chemistry **29**, 1 (2001).

[56] F. Lichtenberg, A. Herrnberger and K. Wiedenmann, Progress in Solid State Chemistry **36**, 253 (2008).

[57] S. N. Ruddlesden and P. Popper, Acta Crystallographica **11**, 54 (1958).

[58] Q. Huang, J. L. Soubeyroux, O. Chmaissem, I. N. Sora, A. Santoro, R. J. Cava, J. J. Krajewski and W. F. Peck, Journal of Solid State Chemistry **112**, 355 (1994).

[59] M. K. Crawford, M. A. Subramanian, R. L. Harlow, J. A. Fernandez-Baca, Z. R. Wang and D. C. Johnston, Physical Review B **49**, 9198 (1994).

[60] C. Dhital, T. Hogan, Z. Yamani, C. de la Cruz, X. Chen, S. Khadka, Z. Ren and S. D. Wilson, Physical Review B **87**, 144405 (2013).

[61] G. Cao, J. Bolivar, S. McCall, J. E. Crow and R. P. Guertin, Physical Review B **57**, R11039 (1998).

[62] S. Boseggia, R. Springell, H. C. Walker, H. M. Rønnow, C. Rüegg, H. Okabe, M. Isobe, R. S. Perry, S. P. Collins and D. F. McMorrow, Physical Review Letters **110**, 117207 (2013).

[63] S. Fujiyama, H. Ohsumi, K. Ohashi, D. Hirai, B. J. Kim, T. Arima, M. Takata and H. Takagi, Physical Review Letters **112**, 016405 (2014).

[64] F. Ye, S. Chi, B. C. Chakoumakos, J. A. Fernandez-Baca, T. Qi and G. Cao, Physical Review B **87**, 140406 (2013).

[65] S. Boseggia, H. C. Walker, J. Vale, R. Springell, Z. Feng, R. S. Perry, M. M. Sala, H. M. Rønnow, S. P. Collins and D. F. McMorrow, Journal of Physics: Condensed Matter **25**, 422202 (2013).

[66] M. Ge, T. F. Qi, O. B. Korneta, D. E. De Long, P. Schlottmann, W. P. Crummett and G. Cao, Physical Review B **84**, 100402 (2011).

[67] S. Chikara, O. Korneta, W. P. Crummett, L. E. DeLong, P. Schlottmann and G. Cao, Physical Review B **80**, 140407 (2009).

[68] I. Dzyaloshinsky, Journal of Physics and Chemistry of Solids **4**, 241 (1958).

[69] T. Moriya, Physical Review Letters **4**, 228 (1960).

[70] T. Moriya, Physical Review **120**, 91 (1960).

[71] J. F. Mitchell, APL Materials **3**, 062404 (2015).

[72] J. Kim, D. Casa, M. H. Upton, T. Gog, Y.-J. Kim, J. F. Mitchell, M. van Veenendaal, M. Daghofer, J. van den Brink, G. Khaliullin and B. J. Kim, Physical Review Letters **108**, 177003 (2012).

[73] M. Guarise, B. Dalla Piazza, M. Moretti Sala, G. Ghiringhelli, L. Braicovich, H. Berger, J. N. Hancock, D. van der Marel, T. Schmitt, V. N. Strocov, L. J. P. Ament, J. van den Brink, P.-H. Lin, P. Xu, H. M. Rønnow and M. Grioni, Physical Review Letters **105**, 157006 (2010).

[74] J. Kim, M. Daghofer, A. H. Said, T. Gog, J. van den Brink, G. Khaliullin and B. J. Kim, Nature Communications **5**, 4453 (2014).

[75] Z. Y. Meng, Y. B. Kim and H.-Y. Kee, Physical Review Letters **113**, 177003 (2014).

[76] Y. Yang, W.-S. Wang, J.-G. Liu, H. Chen, J.-H. Dai and Q.-H. Wang, Physical Review B **89**, 094518 (2014).

[77] A. Damascelli, Z. Hussain and Z.-X. Shen, Reviews of Modern Physics **75**, 473 (2003).

[78] A. de la Torre, S. McKeown Walker, F. Y. Bruno, S. Riccó, Z. Wang, I. Gutierrez Lezama, G. Scheerer, G. Giriat, D. Jaccard, C. Berthod, T. K. Kim, M. Hoesch, E. C. Hunter, R. S. Perry, A. Tamai and F. Baumberger, Physical Review Letters **115**, 176402 (2015).

[79] V. Brouet, J. Mansart, L. Perfetti, C. Piovera, I. Vobornik, P. Le Fèvre, F. Bertran, S. C. Riggs, M. C. Shapiro, P. Giraldo-Gallo and I. R. Fisher, Physical Review B **92**, 081117 (2015).

[80] Y. Cao, Q. Wang, J. A. Waugh, T. J. Reber, H. Li, X. Zhou, S. Parham, S.-R. Park, N. C. Plumb, E. Rotenberg, A. Bostwick, J. D. Denlinger, T. Qi, M. A. Hermele, G. Cao and D. S. Dessau, Nature Communications **7**, 11367 (2016).

[81] X. Liu, M. P. M. Dean, Z. Y. Meng, M. H. Upton, T. Qi, T. Gog, Y. Cao, J. Q. Lin, D. Meyers, H. Ding, G. Cao and J. P. Hill, Physical Review B **93**, 241102 (2016).

[82] I. Battisti, K. M. Bastiaans, V. Fedoseev, A. de la Torre, N. Iliopoulos, A. Tamai, E. C. Hunter, R. S. Perry, J. Zaanen, F. Baumberger and M. P. Allan, Nature Physics **13**, 21 (2017).

[83] J. Cheng, X. Sun, S. Liu, B. Li, H. Wang, P. Dong, Y. Wang and W. Xu, New Journal of Physics **18**, 093019 (2016).

[84] S. Chikara, G. Fabbris, J. Terzic, G. Cao, D. Khomskii and D. Haskel, Physical Review B **95**, 060407 (2017).

[85] J. S. Lee, Y. Krockenberger, K. S. Takahashi, M. Kawasaki and Y. Tokura, Physical Review B **85**, 035101 (2012).

[86] O. B. Korneta, T. Qi, S. Chikara, S. Parkin, L. E. De Long, P. Schlottmann and G. Cao, Physical Review B **82**, 115117 (2010).

[87] S. Boseggia, R. Springell, H. C. Walker, A. T. Boothroyd, D. Prabhakaran, S. P. Collins and D. F. McMorrow, Journal of Physics: Condensed Matter **24**, 312202 (2012).

[88] J. W. Kim, Y. Choi, J. Kim, J. F. Mitchell, G. Jackeli, M. Daghofer, J. van den Brink, G. Khaliullin and B. J. Kim, Physical Review Letters **109**, 037204 (2012).

[89] H. Matsuhata, I. Nagai, Y. Yoshida, S. Hara, S.-i. Ikeda and N. Shirakawa, Journal of Solid State Chemistry **177**, 3776 (2004).

[90] G. Cao, Y. Xin, C. S. Alexander, J. E. Crow, P. Schlottmann, M. K. Crawford, R. L. Harlow and W. Marshall, Physical Review B **66**, 214412 (2002).

[91] S. Boseggia, R. Springell, H. C. Walker, A. T. Boothroyd, D. Prabhakaran, D. Wermeille, L. Bouchenoire, S. P. Collins and D. F. McMorrow, Physical Review B **85**, 184432 (2012).

[92] T. Hogan, L. Bjaalie, L. Zhao, C. Belvin, X. Wang, C. G. Van de Walle, D. Hsieh and S. D. Wilson, Physical Review B **93**, 134110 (2016).

[93] I. Nagai, Y. Yoshida, S. I. Ikeda, H. Matsuhata, H. Kito and M. Kosaka, Journal of Physics: Condensed Matter **19**, 136214 (2007).

[94] S. Fujiyama, K. Ohashi, H. Ohsumi, K. Sugimoto, T. Takayama, T. Komesu, M. Takata, T. Arima and H. Takagi, Physical Review B **86**, 174414 (2012).

[95] C. Dhital, S. Khadka, Z. Yamani, C. de la Cruz, T. C. Hogan, S. M. Disseler, M. Pokharel, K. C. Lukas, W. Tian, C. P. Opeil, Z. Wang and S. D. Wilson, Physical Review B **86**, 100401 (2012).

[96] B. Kim, P. Liu and C. Franchini, Physical Review B **95**, 024406 (2017).

[97] R. D. Burbank and H. T. Evans, Acta Crystallographica **1**, 330 (1948).

[98] G. Cao, V. Durairaj, S. Chikara, L. E. DeLong, S. Parkin and P. Schlottmann, Physical Review B **76**, 100402 (2007).

[99] J. G. Zhao, L. X. Yang, Y. Yu, F. Y. Li, R. C. Yu, Z. Fang, L. C. Chen and C. Q. Jin, Journal of Applied Physics **103**, 103706 (2008).

[100] D. Puggioni and J. M. Rondinelli, Journal of Applied Physics **119**, 086102 (2016).

[101] P. E. R. Blanchard, E. Reynolds, B. J. Kennedy, J. A. Kimpton, M. Avdeev and A. A. Belik, Physical Review B **89**, 214106 (2014).

[102] A. Biswas, K.-S. Kim and Y. H. Jeong, Journal of Applied Physics **116**, 213704 (2014).

[103] A. Biswas, K.-S. Kim and Y. H. Jeong, Journal of Magnetism and Magnetic Materials **400**, 36 (2016).

[104] B. L. Altshuler, D. Khmel'nitzkii, A. I. Larkin and P. A. Lee, Physical Review B **22**, 5142 (1980).

[105] R. M. Hill, Physica Status Solidi A **34**, 601 (1976).

[106] J. H. Gruenewald, J. Nichols, J. Terzic, G. Cao, J. W. Brill and S. S. Seo, Journal of Materials Research **29**, 2491 (2014).

[107] F.-X. Wu, J. Zhou, L. Y. Zhang, Y. B. Chen, S.-T. Zhang, Z.-B. Gu, S.-H. Yao and Y.-F. Chen, Journal of Physics: Condensed Matter **25**, 125604 (2013).

[108] P. W. Anderson, Physical Review **109**, 1492 (1958).

[109] A. Biswas, K.-S. Kim and Y. H. Jeong, *Metal–Insulator Transitions and Non-Fermi Liquid Behaviors in 5d Perovskite Iridates*, in *Perovskite Materials - Synthesis, Characterisation, Properties, and Applications*, Intech Open (2016).

[110] K. Byczuk, Physical Review B **71**, 205105 (2005).

[111] M. A. Zeb and H.-Y. Kee, Physical Review B **86**, 085149 (2012).

[112] J.-M. Carter, V. V. Shankar, M. A. Zeb and H.-Y. Kee, Physical Review B **85**, 115105 (2012).

[113] Y. Chen, Y.-M. Lu and H.-Y. Kee, Nature Communications **6** (2015).

[114] K. A. Müller, W. Berlinger and F. Waldner, Physical Review Letters **21**, 814 (1968).

[115] P. A. Fleury, J. F. Scott and J. M. Worlock, Physical Review Letters **21**, 16 (1968).

[116] K. v. Benthem, C. Elsässer and R. H. French, Journal of Applied Physics **90**, 6156 (2001).

[117] M. I. Cohen and R. F. Blunt, Physical Review **168**, 929 (1968).

[118] C. Lin, C. Mitra and A. A. Demkov, Physical Review B **86**, 161102 (2012).

[119] C. Lin and A. A. Demkov, Physical Review Letters **111**, 217601 (2013).

[120] J. N. Eckstein, Nature Materials **6**, 473 (2007).

[121] D. Kan, T. Terashima, R. Kanda, A. Masuno, K. Tanaka, S. Chu, H. Kan, A. Ishizumi, Y. Kanemitsu, Y. Shimakawa and M. Takano, Nature Materials **4**, 816 (2005).

[122] A. Spinelli, M. A. Torija, C. Liu, C. Jan and C. Leighton, Physical Review B **81**, 155110 (2010).

[123] K. A. Müller and H. Burkard, Physical Review B **19**, 3593 (1979).

[124] C. S. Koonce, M. L. Cohen, J. F. Schooley, W. R. Hosler and E. R. Pfeiffer, Physical Review **163**, 380 (1967).

[125] P. Moetakef, J. R. Williams, D. G. Ouellette, A. P. Kajdos, D. Goldhaber-Gordon, S. J. Allen and S. Stemmer, Physical Review X **2**, 021014 (2012).

[126] M. Kawasaki, K. Takahashi, T. Maeda, R. Tsuchiya, M. Shinohara, O. Ishiyama, T. Yonezawa, M. Yoshimoto and H. Koinuma, Science **266**, 1540 (1994).

[127] G. Koster, B. L. Kropman, G. J. H. M. Rijnders, D. H. A. Blank and H. Rogalla, Applied Physics Letters **73**, 2920 (1998).

[128] J. Matsuno, K. Ihara, S. Yamamura, H. Wadati, K. Ishii, V. V. Shankar, H.-Y. Kee and H. Takagi, Physical Review Letters **114**, 247209 (2015).

[129] S. Y. Kim, C. H. Kim, L. J. Sandilands, C. H. Sohn, J. Matsuno, H. Takagi, K. W. Kim, Y. S. Lee, S. J. Moon and T. W. Noh, Physical Review B **94**, 245113 (2016).

[130] L. Hao, D. Meyers, C. Frederick, G. Fabbris, J. Yang, N. Traynor, L. Horak, D. Kriegner, Y. Choi, J.-W. Kim, D. Haskel, P. J. Ryan, M. P. M. Dean and J. Liu, Physical Review Letters **119**, 027204 (2017).

[131] H. Zhang, K. Haule and D. Vanderbilt, Physical Review Letters **111**, 246402 (2013).

[132] B. Kim, P. Liu and C. Franchini, Physical Review B **95**, 115111 (2017).

[133] D. Haskel, G. Fabbris, M. Zhernenkov, P. P. Kong, C. Q. Jin, G. Cao and M. van Veenendaal, Physical Review Letters **109**, 027204 (2012).

[134] C. Rayan Serrao, J. Liu, J. T. Heron, G. Singh-Bhalla, A. Yadav, S. J. Suresha, R. J. Paull, D. Yi, J.-H. Chu, M. Trassin, A. Vishwanath, E. Arenholz, C. Frontera, J. Železný, T. Jungwirth, X. Marti and R. Ramesh, Physical Review B **87**, 085121 (2013).

[135] R. K. Singh and J. Narayan, Physical Review B **41**, 8843 (1990).

[136] J. A. Venables, G. D. T. Spiller and M. Hanbucken, Reports on Progress in Physics **47**, 399 (1984).

[137] G. Koster, *Reflection high-energy electron diffraction for in situ characterization of thin film growth*, in *In Situ Characterization of Thin Film Growth*, Woodhead Publishing (2011).

[138] A. Ichimiya, *Reflection High-Energy Electron Diffraction*, Cambridge University Press (2004).

[139] Y. Horio, Y. Hashimoto and A. Ichimiya, Applied Surface Science **100-101**, 292 (1996).

[140] A. Ichimiya, Journal of the Physical Society of Japan **35**, 213 (1973).

[141] S. Nishikawa and S. Kikuchi, Nature **121**, 1019 (1928).

[142] G. J. H. M. Rijnders, G. Koster, D. H. A. Blank and H. Rogalla, Applied Physics Letters **70**, 1888 (1997).

[143] T. Terashima, Y. Bando, K. Iijima, K. Yamamoto, K. Hirata, K. Hayashi, K. Kamigaki and H. Terauchi, Physical Review Letters **65**, 2684 (1990).

[144] S. Stoyanov, Surface Science **199**, 226 (1988).

[145] S. Clarke and D. D. Vvedensky, Physical Review B **36**, 9312 (1987).

[146] S. Clarke and D. D. Vvedensky, Physical Review Letters **58**, 2235 (1987).

[147] G. Rijnders, G. Koster, V. Leca, D. H. A. Blank and H. Rogalla, Applied Surface Science **168**, 223 (2000).

[148] E. Abbe, Archiv für Mikroskopische Anatomie **9**, 413 (1873).

[149] M. Knoll and E. Ruska, Zeitschrift für Physik **78**, 318 (1932).

[150] H. Busch, Annalen der Physik **386**, 974 (1926).

[151] D. B. Williams and C. B. Carter, *Transmission Electron Microscopy*, Springer (2009).

[152] E. Kvaalen, *Licensed under Creative Commons BY-SA 4.0*, https://commons.wikimedia.org/wiki/File:Schematic_view_of_imaging_and_diffraction_modes_in_TEM.tif (2020).

[153] J. C. H. Spence, *High-Resolution Electron Microscopy*, Oxford University Press (2017).

[154] P. Hartel, H. Rose and C. Dinges, Ultramicroscopy **63**, 93 (1996).

[155] D. O. Klenov and S. Stemmer, Ultramicroscopy **106**, 889 (2006).

[156] W. Y. Kwong and W. Y. Zhang, International Symposium on Semiconductor Manufacturing (2005).

[157] T. Tao, J. Ro, J. Melngailis, Z. Xue and H. D. Kaesz, Journal of Vacuum Science & Technology B **8**, 1826 (1990).

[158] H. Hertz, Annalen der Physik **267**, 983 (1887).

[159] A. Einstein, Annalen der Physik **322**, 132 (1905).

[160] K. Siegbahn, Reviews of Modern Physics **54**, 709 (1982).

[161] P. W. Anderson, Physical Review Letters **18**, 1049 (1967).

[162] P. Nozières and C. T. De Dominicis, Physical Review **178**, 1097 (1969).

[163] S. Hüfner, *Photoelectron Spectroscopy: Principles and Applications*, Springer (2003).

[164] S. Suga and A. Sekiyama, *Photoelectron Spectroscopy: Bulk and Surface Electronic Structures*, Springer (2014).

[165] W. Schattke, Progress in Surface Science **54**, 211 (1997).

[166] P. J. Feibelman and D. E. Eastman, Physical Review B **10**, 4932 (1974).

[167] T. Fujikawa, Journal of Electron Spectroscopy and Related Phenomena **173**, 51 (2009).

[168] C. N. Berglund and W. E. Spicer, Physical Review **136**, A1030 (1964).

[169] T. Miller, W. E. McMahon and T.-C. Chiang, Physical Review Letters **77**, 1167 (1996).

[170] E. D. Hansen, T. Miller and T.-C. Chiang, Physical Review B **55**, 1871 (1997).

[171] S. Moser, Journal of Electron Spectroscopy and Related Phenomena **214**, 29 (2017).

[172] J. J. Yeh and I. Lindau, Atomic Data and Nuclear Data Tables **32**, 1 (1985).

[173] E. A. Kraut, R. W. Grant, J. R. Waldrop and S. P. Kowalczyk, Physical Review Letters **44**, 1620 (1980).

[174] E. A. Kraut, R. W. Grant, J. R. Waldrop and S. P. Kowalczyk, Physical Review B **28**, 1965 (1983).

[175] H. Wadati, A. Maniwa, A. Chikamatsu, H. Kumigashira, M. Oshima, T. Mizokawa, A. Fujimori and G. A. Sawatzky, Physical Review B **80**, 125107 (2009).

[176] O. Gunnarsson and K. Schönhammer, Physical Review B **31**, 4815 (1985).

[177] M. P. Seah and W. A. Dench, Surface and Interface Analysis **1**, 2 (1979).

[178] S. Tanuma, C. J. Powell and D. R. Penn, Surface and Interface Analysis **35**, 268 (2003).

[179] M. Sing, G. Berner, K. Goß, A. Müller, A. Ruff, A. Wetscherek, S. Thiel, J. Mannhart, S. A. Pauli, C. W. Schneider, P. R. Willmott, M. Gorgoi, F. Schäfers and R. Claessen, Physical Review Letters **102**, 176805 (2009).

[180] S. Tanuma, T. Shiratori, T. Kimura, K. Goto, S. Ichimura and C. J. Powell, Surface and Interface Analysis **37**, 833 (2005).

[181] S. Tougaard and B. Jørgensen, Surface and Interface Analysis **7**, 17 (1985).

[182] D. A. Shirley, Physical Review B **5**, 4709 (1972).

[183] J. Wong, Materials Science and Engineering **80**, 107 (1986).

[184] F. de Groot, M. Grioni, J. C. Fuggle, J. Ghijsen, G. A. Sawatzky and H. Petersen, Physical Review B **40**, 5715 (1989).

[185] F. de Groot, Journal of Electron Spectroscopy and Related Phenomena **67**, 529 (1994).

[186] F. de Groot, Chemical Reviews **101**, 1779 (2001).

[187] F. de Groot and A. Kotani, *Core Level Spectroscopy of Solids*, CRC Press (2008).

[188] M. Haverkort, *Spin and orbital degrees of freedom in transition metal oxides and oxide thin films studied by soft x-ray absorption spectroscopy*, Ph.D. thesis, Universität zu Köln (2005).

[189] F. de Groot, Nature Chemistry **4**, 766 (2012).

[190] J. Fink, N. Nücker, E. Pellegrin, H. Romberg, M. Alexander and M. Knupfer, Journal of Electron Spectroscopy and Related Phenomena **66**, 395 (1994).

[191] D. Pesquera Herrero, *Strain and interface-induced charge, orbital and spin orderings in transition metal oxide perovskites*, Ph.D. thesis, Universitat Autònoma de Barcelona, (2014).

[192] G. Schütz, W. Wagner, W. Wilhelm, P. Kienle, R. Zeller, R. Frahm and G. Materlik, Physical Review Letters **58**, 737 (1987).

[193] H. Ebert, Reports on Progress in Physics **59**, 1665 (1996).

[194] U. Fano, Physical Review **184**, 250 (1969).

[195] U. Fano, Physical Review **178**, 131 (1969).

[196] B. T. Thole, P. Carra, F. Sette and G. van der Laan, Physical Review Letters **68**, 1943 (1992).

[197] P. Carra, B. T. Thole, M. Altarelli and X. Wang, Physical Review Letters **70**, 694 (1993).

[198] G. van der Laan and B. T. Thole, Physical Review Letters **60**, 1977 (1988).

[199] K. Szot and W. Speier, Physical Review B **60**, 5909 (1999).

[200] J. M. Huijbregtse, J. H. Rector and B. Dam, Physica C: Superconductivity **351**, 183 (2001).

[201] T. Ohnishi, K. Shibuya, M. Lippmaa, D. Kobayashi, H. Kumigashira, M. Oshima and H. Koinuma, Applied Physics Letters **85**, 272 (2004).

[202] S. N. Magonov, V. Elings and M. H. Whangbo, Surface Science **375**, L385 (1997).

[203] R. García, R. Magerle and R. Perez, Nature Materials **6**, 405 (2007).

[204] R. Bachelet, F. Sánchez, J. Santiso, C. Munuera, C. Ocal and J. Fontcuberta, Chemistry of Materials **21**, 2494 (2009).

[205] G. Koster, L. Klein, W. Siemons, G. Rijnders, J. S. Dodge, C.-B. Eom, D. H. A. Blank and M. R. Beasley, Reviews of Modern Physics **84**, 253 (2012).

[206] J. M. Huijbregtse, B. Dam, J. H. Rector and R. Griessen, Journal of Applied Physics **86**, 6528 (1999).

[207] T. Ohnishi, M. Lippmaa, T. Yamamoto, S. Meguro and H. Koinuma, Applied Physics Letters **87**, 241919 (2005).

[208] T. Ohnishi, K. Shibuya, T. Yamamoto and M. Lippmaa, Journal of Applied Physics **103**, 103703 (2008).

[209] J. H. Song, T. Susaki and H. Y. Hwang, Advanced Materials **20**, 2528 (2008).

[210] H. K. Sato, C. Bell, Y. Hikita and H. Y. Hwang, Applied Physics Letters **102**, 251602 (2013).

[211] A. Ohtomo, D. A. Muller, J. L. Grazul and H. Y. Hwang, Applied Physics Letters **80**, 3922 (2002).

[212] Y. Hotta, Y. Mukunoki, T. Susaki, H. Y. Hwang, L. Fitting and D. A. Muller, Applied Physics Letters **89**, 031918 (2006).

[213] P. Scheiderer, M. Schmitt, J. Gabel, M. Zapf, M. Stübinger, P. Schütz, L. Dudy, C. Schlueter, T.-L. Lee, M. Sing and R. Claessen, Advanced Materials **0**, 1706708 (2018).

[214] S. Ohashi, M. Lippmaa, N. Nakagawa, H. Nagasawa, H. Koinuma and M. Kawasaki, Review of Scientific Instruments **70**, 178 (1999).

[215] T. Ohnishi and K. Takada, Applied Physics Express **4**, 025501 (2011).

[216] W. E. Bell and M. Tagami, The Journal of Physical Chemistry **67**, 2432 (1963).

[217] E. H. P. Cordfunke and G. Meyer, Recueil des Travaux Chimiques des Pays-Bas **81**, 670 (1962).

[218] E. H. P. Cordfunke and G. Meyer, Recueil des Travaux Chimiques des Pays-Bas **81**, 495 (1962).

[219] Y. K. Kim, A. Sumi, K. Takahashi, S. Yokoyama, S. Ito, T. Watanabe, K. Akiyama, S. Kaneko, K. Saito and H. Funakubo, Japanese Journal of Applied Physics **45**, L36 (2005).

[220] K. Nishio, H. Y. Hwang and Y. Hikita, APL Materials **4**, 036102 (2016).

[221] Y. Tokuda, S. Kobayashi, T. Ohnishi, T. Mizoguchi, N. Shibata, Y. Ikuhara and T. Yamamoto, Applied Physics Letters **99**, 173109 (2011).

[222] C. S. Lent and P. I. Cohen, Surface Science **139**, 121 (1984).

[223] S. Stoyanov and M. Michailov, Surface Science **202**, 109 (1988).

[224] C. Jin-Seok, J. Seung Yup, M. Soon Jae and J. Byung Chul, Journal of the Korean Physical Society **56**, 1814 (2010).

[225] D. J. Groenendijk, N. Manca, G. Mattoni, L. Kootstra, S. Gariglio, Y. Huang, E. van Heumen and A. D. Caviglia, Applied Physics Letters **109**, 041906 (2016).

[226] S. M. Antao and I. Hassan, The Canadian Mineralogist **47**, 1245 (2009).

[227] A. A. Bolzan, C. Fong, B. J. Kennedy and C. J. Howard, Acta Crystallographica B **53**, 373 (1997).

[228] S. R. Foltyn, R. C. Dye, K. C. Ott, E. Peterson, K. M. Hubbard, W. Hutchinson, R. E. Muenchausen, R. C. Estler and X. D. Wu, Applied Physics Letters **59**, 594 (1991).

[229] G. Rijnders, D. H. A. Blank, J. Choi and C.-B. Eom, Applied Physics Letters **84**, 505 (2004).

[230] M. Nakahara, S. Tsunekawa, K. Watanabe, T. Arai, T. Yunogami and K. Kuroki, Journal of Vacuum Science & Technology B **19**, 2133 (2001).

[231] Y. Okada, S.-Y. Shiau, T.-R. Chang, G. Chang, M. Kobayashi, R. Shimizu, H.-T. Jeng, S. Shiraki, H. Kumigashira, A. Bansil, H. Lin and T. Hitosugi, Physical Review Letters **119**, 086801 (2017).

[232] D. I. Woodward and I. M. Reaney, Acta Crystallographica B **61**, 387 (2005).

[233] Y. F. Nie, P. D. C. King, C. H. Kim, M. Uchida, H. I. Wei, B. D. Faeth, J. P. Ruf, J. P. C. Ruff, L. Xie, X. Pan, C. J. Fennie, D. G. Schlom and K. M. Shen, Physical Review Letters **114**, 016401 (2015).

[234] V. N. Strocov, T. Schmitt, U. Flechsig, T. Schmidt, A. Imhof, Q. Chen, J. Raabe, R. Betemps, D. Zimoch, J. Krempasky, X. Wang, M. Grioni, A. Piazzalunga and L. Patthey, Journal of Synchrotron Radiation **17**, 631 (2010).

[235] V. N. Strocov, X. Wang, M. Shi, M. Kobayashi, J. Krempasky, C. Hess, T. Schmitt and L. Patthey, Journal of Synchrotron Radiation **21**, 32 (2013).

[236] G. Kresse and J. Furthmüller, Physical Review B **54**, 11169 (1996).

[237] P. E. Blöchl, Physical Review B **50**, 17953 (1994).

[238] G. Kresse and D. Joubert, Physical Review B **59**, 1758 (1999).

[239] J. P. Perdew, K. Burke and M. Ernzerhof, Physical Review Letters **77**, 3865 (1996).

[240] S. Steiner, S. Khmelevskyi, M. Marsmann and G. Kresse, Physical Review B **93**, 224425 (2016).

[241] A. I. Liechtenstein, Physical Review B **52**, R5467 (1995).

[242] A. Yamasaki, H. Fujiwara, S. Tachibana, D. Iwasaki, Y. Higashino, C. Yoshimi, K. Nakagawa, Y. Nakatani, K. Yamagami, H. Aratani, O. Kirilmaz, M. Sing, R. Claessen, H. Watanabe, T. Shirakawa, S. Yunoki, A. Naitoh, K. Takase, J. Matsuno, H. Takagi, A. Sekiyama and Y. Saitoh, Physical Review B **94**, 115103 (2016).

[243] Z. Hussain, C. S. Fadley, S. Kono and L. F. Wagner, Physical Review B **22**, 3750 (1980).

[244] R. C. White, C. S. Fadley, M. Sagurton and Z. Hussain, Physical Review B **34**, 5226 (1986).

[245] L. Plucinski, J. Minár, B. C. Sell, J. Braun, H. Ebert, C. M. Schneider and C. S. Fadley, Physical Review B **78**, 035108 (2008).

[246] W. Ku, T. Berlijn and C.-C. Lee, Physical Review Letters **104**, 216401 (2010).

[247] Z. T. Liu, M. Y. Li, Q. F. Li, J. S. Liu, W. Li, H. F. Yang, Q. Yao, C. C. Fan, X. G. Wan, Z. Wang and D. W. Shen, Scientific Reports **6**, 30309 (2016).

[248] D. J. Groenendijk, C. Autieri, J. Girovsky, M. C. Martinez-Velarte, N. Manca, G. Mattoni, A. M. R. V. L. Monteiro, N. Gauquelin, J. Verbeeck, A. F. Otte, M. Gabay, S. Picozzi and A. D. Caviglia, Physical Review Letters **119**, 256403 (2017).

[249] D. C. Licciardello and D. J. Thouless, Physical Review Letters **35**, 1475 (1975).

[250] R. Aso, D. Kan, Y. Shimakawa and H. Kurata, Scientific Reports **3**, 2214 (2013).

[251] R. Aso, D. Kan, Y. Shimakawa and H. Kurata, Advanced Functional Materials **24**, 5177 (2014).

[252] R. Aso, D. Kan, Y. Fujiyoshi, Y. Shimakawa and H. Kurata, Crystal Growth & Design **14**, 6478 (2014).

[253] C. L. Jia, M. Lentzen and K. Urban, Science **299**, 870 (2003).

[254] C.-L. Jia, M. Lentzen and K. Urban, Microscopy and Microanalysis **10**, 174 (2004).

[255] J.-M. Carter, V. Shankar V. and H.-Y. Kee, Physical Review B **88**, 035111 (2013).

[256] G. Shirane and Y. Yamada, Physical Review **177**, 858 (1969).

[257] H. Kroemer, Reviews of Modern Physics **73**, 783 (2001).

[258] Z. Zhong and P. Hansmann, Physical Review X **7**, 011023 (2017).

[259] H. Takagi and H. Y. Hwang, Science **327**, 1601 (2010).

[260] J. Mannhart and D. G. Schlom, Science **327**, 1607 (2010).

[261] A. Ohtomo and H. Y. Hwang, Nature **427**, 423 (2004).

[262] X. R. Wang, C. J. Li, W. M. Lü, T. R. Paudel, D. P. Leusink, M. Hoek, N. Poccia, A. Vailionis, T. Venkatesan, J. M. D. Coey, E. Y. Tsymbal, Ariando and H. Hilgenkamp, Science **349**, 716 (2015).

[263] J. E. Kleibeuker, Z. Zhong, H. Nishikawa, J. Gabel, A. Müller, F. Pfaff, M. Sing, K. Held, R. Claessen, G. Koster and G. Rijnders, Physical Review Letters **113**, 237402 (2014).

[264] J. Garcia-Barriocanal, F. Y. Bruno, A. Rivera-Calzada, Z. Sefrioui, N. M. Nemes, M. Garcia-Hernández, J. Rubio-Zuazo, G. R. Castro, M. Varela, S. J. Pennycook, C. Leon and J. Santamaria, Advanced Materials **22**, 627 (2010).

[265] J. Garcia-Barriocanal, J. C. Cezar, F. Y. Bruno, P. Thakur, N. B. Brookes, C. Utfeld, A. Rivera-Calzada, S. R. Giblin, J. W. Taylor, J. A. Duffy, S. B. Dugdale, T. Nakamura, K. Kodama, C. Leon, S. Okamoto and J. Santamaria, Nature Communications **1**, 82 (2010).

[266] H. Chen, A. J. Millis and C. A. Marianetti, Physical Review Letters **111**, 116403 (2013).

[267] I. González, S. Okamoto, S. Yunoki, A. Moreo and E. Dagotto, Journal of Physics: Condensed Matter **20**, 264002 (2008).

[268] S. Okamoto, J. Nichols, C. Sohn, S. Y. Kim, T. W. Noh and H. N. Lee, Nano Letters **17**, 2126 (2017).

[269] J. Nichols, X. Gao, S. Lee, T. L. Meyer, J. W. Freeland, V. Lauter, D. Yi, J. Liu, D. Haskel, J. R. Petrie, E.-J. Guo, A. Herklotz, D. Lee, T. Z. Ward, G. Eres, M. R. Fitzsimmons and H. N. Lee, Nature Communications **7**, 12721 (2016).

[270] L. C. Seitz, C. F. Dickens, K. Nishio, Y. Hikita, J. Montoya, A. Doyle, C. Kirk, A. Vojvodic, H. Y. Hwang, J. K. Norskov and T. F. Jaramillo, Science **353**, 1011 (2016).

[271] A. R. Akbashev, L. Zhang, J. T. Mefford, J. Park, B. Butz, H. Luftman, W. C. Chueh and A. Vojvodic, Energy & Environmental Science **11**, 1762 (2018).

[272] G. Berner, A. Müller, F. Pfaff, J. Walde, C. Richter, J. Mannhart, S. Thiess, A. Gloskovskii, W. Drube, M. Sing and R. Claessen, Physical Review B **88**, 115111 (2013).

[273] G. Berner, M. Sing, H. Fujiwara, A. Yasui, Y. Saitoh, A. Yamasaki, Y. Nishitani, A. Sekiyama, N. Pavlenko, T. Kopp, C. Richter, J. Mannhart, S. Suga and R. Claessen, Physical Review Letters **110**, 247601 (2013).

[274] J. Gabel, M. Zapf, P. Scheiderer, P. Schütz, L. Dudy, M. Stübinger, C. Schlueter, T.-L. Lee, M. Sing and R. Claessen, Physical Review B **95**, 195109 (2017).

[275] P. Schütz, F. Pfaff, P. Scheiderer, Y. Z. Chen, N. Pryds, M. Gorgoi, M. Sing and R. Claessen, Physical Review B **91**, 165118 (2015).

[276] Y. Hikita, Y. Kozuka, T. Susaki, H. Takagi and H. Y. Hwang, Applied Physics Letters **90**, 143507 (2007).

[277] R. Schafranek and A. Klein, Solid State Ionics **177**, 1659 (2006).

[278] R. Schafranek, S. Payan, M. Maglione and A. Klein, Physical Review B **77**, 195310 (2008).

[279] N. Ohashi, H. Yoshikawa, Y. Yamashita, S. Ueda, J. Li, H. Okushi, K. Kobayashi and H. Haneda, Applied Physics Letters **101**, 251911 (2012).

[280] K. G. Rana, V. Khikhlovskyi and T. Banerjee, Applied Physics Letters **100**, 213502 (2012).

[281] B. S. Y. Kim, Y. A. Birkhölzer, X. Feng, Y. Hikita and H. Y. Hwang, Applied Physics Letters **114**, 133504 (2019).

[282] W. Meevasana, P. D. C. King, R. H. He, S.-K. Mo, M. Hashimoto, A. Tamai, P. Songsiriritthigul, F. Baumberger and Z.-X. Shen, Nature Materials **10**, 114 (2011).

[283] S. M. Walker, F. Y. Bruno, Z. Wang, A. de la Torre, S. Riccó, A. Tamai, T. K. Kim, M. Hoesch, M. Shi, M. S. Bahramy, P. D. C. King and F. Baumberger, Advanced Materials **27**, 3894 (2015).

[284] A. F. Santander-Syro, O. Copie, T. Kondo, F. Fortuna, S. Pailhès, R. Weht, X. G. Qiu, F. Bertran, A. Nicolaou, A. Taleb-Ibrahimi, P. Le Fèvre, G. Herranz, M. Bibes, N. Reyren, Y. Apertet, P. Lecoeur, A. Barthélémy and M. J. Rozenberg, Nature **469**, 189 (2011).

[285] L. Dudy, M. Sing, P. Scheiderer, J. D. Denlinger, P. Schütz, J. Gabel, M. Buchwald, C. Schlueter, T.-L. Lee and R. Claessen, Advanced Materials **28**, 7443 (2016).

[286] P. Schütz, D. V. Christensen, V. Borisov, F. Pfaff, P. Scheiderer, L. Dudy, M. Zapf, J. Gabel, Y. Z. Chen, N. Pryds, V. A. Rogalev, V. N. Strocov, C. Schlueter, T.-L. Lee, H. O. Jeschke, R. Valentí, M. Sing and R. Claessen, Physical Review B **96**, 161409 (2017).

[287] T. Yamamoto, S. Suzuki, K. Kawaguchi and K. Takahashi, Japanese Journal of Applied Physics **37**, 4737 (1998).

[288] J. Li, N. Ohashi, H. Okushi and H. Haneda, Physical Review B **83**, 125317 (2011).

[289] P. P. Ewald, Annalen der Physik **369**, 253 (1921).

[290] I. I. Mazin, H. O. Jeschke, K. Foyevtsova, R. Valentí and D. I. Khomskii, Physical Review Letters **109**, 197201 (2012).

[291] S. Doniach and M. Sunjic, Journal of Physics C: Solid State Physics **3**, 285 (1970).

[292] A. Kotani, Journal of Electron Spectroscopy and Related Phenomena **78**, 7 (1996).

[293] A. Yamasaki, O. Kirilmaz, A. Irizawa, A. Higashiya, T. Muro, H. Fujiwara, F. Pfaff, P. Scheiderer, J. Gabel, M. Sing, M. Yabashi, K. Tamasaku, A. Hloskovskyy, H. Okabe, H. Yoshida, M. Isobe, J. Akimitsu, W. Drube, T. Ishikawa, S. Imada, A. Sekiyama, R. Claessen and S. Suga, Proceedings of the International Conference on Strongly Correlated Electron Systems **3**, 013001 (2014).

[294] J. M. Kahk, C. G. Poll, F. E. Oropeza, J. M. Ablett, D. Céolin, J.-P. Rueff, S. Agrestini, Y. Utsumi, K. D. Tsuei, Y. F. Liao, F. Borgatti, G. Panaccione, A. Regoutz, R. G. Egdell, B. J. Morgan, D. O. Scanlon and D. J. Payne, Physical Review Letters **112**, 117601 (2014).

[295] V. Pfeifer, T. E. Jones, J. J. V. Vélez, C. Massué, M. T. Greiner, R. Arrigo, D. Teschner, F. Girgsdies, M. Scherzer, J. Allan, M. Hashagen, G. Weinberg, S. Piccinin, M. Hävecker, A. Knop-Gericke and R. Schlögl, Physical Chemistry Chemical Physics **18**, 2292 (2016).

[296] J. K. Kawasaki, M. Uchida, H. Paik, D. G. Schlom and K. M. Shen, Physical Review B **94**, 121104 (2016).

[297] H.-D. Kim, H.-J. Noh, K. H. Kim and S.-J. Oh, Physical Review Letters **93**, 126404 (2004).

[298] M. A. van Veenendaal and G. A. Sawatzky, Physical Review Letters **70**, 2459 (1993).

[299] M. van Veenendaal, Physical Review B **74**, 085118 (2006).

[300] J. Kim, J.-Y. Kim, B.-G. Park and S.-J. Oh, Physical Review B **73**, 235109 (2006).

[301] H. Guo, Y. Li, D. Urbina, B. Hu, R. Jin, T. Liu, D. Fobes, Z. Mao, E. W. Plummer and J. Zhang, Physical Review B **81**, 155121 (2010).

[302] E. B. Guedes, M. Abbate, K. Ishigami, A. Fujimori, K. Yoshimatsu, H. Kumigashira, M. Oshima, F. C. Vicentin, P. T. Fonseca and R. J. O. Mossanek, Physical Review B **86**, 235127 (2012).

[303] A. Chainani, A. Yamamoto, M. Matsunami, R. Eguchi, M. Taguchi, Y. Takata, H. Takagi, S. Shin, Y. Nishino, M. Yabashi, K. Tamasaku and T. Ishikawa, Physical Review B **87**, 045108 (2013).

[304] Y. Z. Chen, N. Bovet, F. Trier, D. V. Christensen, F. M. Qu, N. H. Andersen, T. Kasama, W. Zhang, R. Giraud, J. Dufouleur, T. S. Jespersen, J. R. Sun, A. Smith, J. Nygård, L. Lu, B. Büchner, B. G. Shen, S. Linderoth and N. Pryds, Nature Communications **4**, 1371 (2013).

[305] A. Chikina, F. Lechermann, M.-A. Husanu, M. Caputo, C. Cancellieri, X. Wang, T. Schmitt, M. Radovic and V. N. Strocov, ACS Nano **12**, 7927 (2018).

[306] N. P. Armitage, P. Fournier and R. L. Greene, Reviews of Modern Physics **82**, 2421 (2010).

[307] P. Ruffieux, P. Schwaller, O. Gröning, L. Schlapbach, P. Gröning, Q. C. Herd, D. Funnemann and J. Westermann, Review of Scientific Instruments **71**, 3634 (2000).

[308] M. B. Trzhaskovskaya, V. I. Nefedov and V. G. Yarzhemsky, Atomic Data and Nuclear Data Tables **77**, 97 (2001).

[309] M. B. Trzhaskovskaya, V. I. Nefedov and V. G. Yarzhemsky, Atomic Data and Nuclear Data Tables **82**, 257 (2002).

[310] A. C. W. P. James, D. W. Murphy and S. M. Zahurak, Nature **338**, 240 (1989).

[311] C. Greaves and M. G. Francesconi, Current Opinion in Solid State and Materials Science **3**, 132 (1998).

[312] J. Sugiyama, R. Itti, H. Yamauchi, N. Koshizuka and S. Tanaka, Physical Review B **45**, 4952 (1992).

[313] M. Sing, S. Glawion, M. Schlachter, M. R. Scholz, K. Goß, J. Heidler, G. Berner and R. Claessen, Physical Review Letters **106**, 056403 (2011).

[314] N. Nakagawa, H. Y. Hwang and D. A. Muller, Nature Materials **5**, 204 (2006).

[315] S. Thiel, G. Hammerl, A. Schmehl, C. W. Schneider and J. Mannhart, Science **313**, 1942 (2006).

[316] A. Kalabukhov, R. Gunnarsson, J. Börjesson, E. Olsson, T. Claeson and D. Winkler, Physical Review B **75**, 121404 (2007).

[317] Z. Q. Liu, C. J. Li, W. M. Lü, X. H. Huang, Z. Huang, S. W. Zeng, X. P. Qiu, L. S. Huang, A. Annadi, J. S. Chen, J. M. D. Coey, T. Venkatesan and Ariando, Physical Review X **3**, 021010 (2013).

[318] N. C. Bristowe, P. B. Littlewood and E. Artacho, Physical Review B **83**, 205405 (2011).

[319] Y. Li, S. N. Phattalung, S. Limpijumnong, J. Kim and J. Yu, Physical Review B **84**, 245307 (2011).

[320] N. Pavlenko, T. Kopp, E. Y. Tsymbal, G. A. Sawatzky and J. Mannhart, Physical Review B **85**, 020407 (2012).

[321] M. P. Warusawithana, C. Richter, J. A. Mundy, P. Roy, J. Ludwig, S. Paetel, T. Heeg, A. A. Pawlicki, L. F. Kourkoutis, M. Zheng, M. Lee, B. Mulcahy, W. Zander, Y. Zhu, J. Schubert, J. N. Eckstein, D. A. Muller, C. S. Hellberg, J. Mannhart and D. G. Schlom, Nature Communications **4** (2013).

[322] P. R. Willmott, S. A. Pauli, R. Herger, C. M. Schlepütz, D. Martoccia, B. D. Patterson, B. Delley, R. Clarke, D. Kumah, C. Cionca and Y. Yacoby, Physical Review Letters **99**, 155502 (2007).

[323] P. Scheiderer, F. Pfaff, J. Gabel, M. Kamp, M. Sing and R. Claessen, Physical Review B **92**, 195422 (2015).

[324] L. Yu and A. Zunger, Nature Communications **5** (2014).

[325] S. Thiel, *Study of Interface properties in $LaAlO_3/SrTiO_3$ heterostructures*, Ph.D. thesis, Universität Augsburg (2009).

[326] T. C. Rödel, F. Fortuna, S. Sengupta, E. Frantzeskakis, P. L. Fèvre, F. Bertran, B. Mercey, S. Matzen, G. Agnus, T. Maroutian, P. Lecoeur and A. F. Santander-Syro, Advanced Materials **28**, 1976 (2016).

[327] M. A. Subramanian, M. K. Crawford and R. L. Harlow, Materials Research Bulletin **29**, 645 (1994).

[328] D. Pesin and L. Balents, Nature Physics **6**, 376 (2010).

[329] J. Chaloupka, G. Jackeli and G. Khaliullin, Physical Review Letters **105**, 027204 (2010).

[330] Y. Singh, S. Manni, J. Reuther, T. Berlijn, R. Thomale, W. Ku, S. Trebst and P. Gegenwart, Physical Review Letters **108**, 127203 (2012).

[331] M. Khalid, A. Setzer, M. Ziese, P. Esquinazi, D. Spemann, A. Pöppl and E. Goering, Physical Review B **81**, 214414 (2010).

[332] W. L. O'Brien and B. P. Tonner, Physical Review B **50**, 12672 (1994).

[333] C. Donnerer, M. M. Sala, S. Pascarelli, A. D. Rosa, S. N. Andreev, V. V. Mazurenko, T. Irifune, E. C. Hunter, R. S. Perry and D. F. McMorrow, Physical Review B **97**, 035106 (2018).

[334] J.-W. Kim, Y. Choi, S. H. Chun, D. Haskel, D. Yi, R. Ramesh, J. Liu and P. J. Ryan, Physical Review B **97**, 094426 (2018).

[335] L. S. I. Veiga, M. Etter, K. Glazyrin, F. Sun, C. A. Escanhoela, G. Fabbris, J. R. L. Mardegan, P. S. Malavi, Y. Deng, P. P. Stavropoulos, H.-Y. Kee, W. G. Yang, M. van Veenendaal, J. S. Schilling, T. Takayama, H. Takagi and D. Haskel, Physical Review B **96**, 140402 (2017).

[336] M. A. Laguna-Marco, D. Haskel, N. Souza-Neto, J. C. Lang, V. V. Krishnamurthy, S. Chikara, G. Cao and M. van Veenendaal, Physical Review Letters **105**, 216407 (2010).

[337] S. Agrestini, C.-Y. Kuo, K. Chen, Y. Utsumi, D. Mikhailova, A. Rogalev, F. Wilhelm, T. Förster, A. Matsumoto, T. Takayama, H. Takagi, M. W. Haverkort, Z. Hu and L. H. Tjeng, Physical Review B **97**, 214436 (2018).

[338] J. H. Hubbell, P. N. Trehan, N. Singh, B. Chand, D. Mehta, M. L. Garg, R. R. Garg, S. Singh and S. Puri, Journal of Physical and Chemical Reference Data **23**, 339 (1994).

[339] J. A. Bearden and A. F. Burr, Reviews of Modern Physics **39**, 125 (1967).

[340] A. Tebano, C. Aruta, S. Sanna, P. G. Medaglia, G. Balestrino, A. A. Sidorenko, R. De Renzi, G. Ghiringhelli, L. Braicovich, V. Bisogni and N. B. Brookes, Physical Review Letters **100**, 137401 (2008).

[341] D. Pesquera, G. Herranz, A. Barla, E. Pellegrin, F. Bondino, E. Magnano, F. Sánchez and J. Fontcuberta, Nature Communications **3**, 1189 (2012).

[342] M. Moretti Sala, M. Rossi, A. Al-Zein, S. Boseggia, E. C. Hunter, R. S. Perry, D. Prabhakaran, A. T. Boothroyd, N. B. Brookes, D. F. McMorrow, G. Monaco and M. Krisch, Physical Review B **90**, 085126 (2014).

[343] M. Moretti Sala, M. Rossi, S. Boseggia, J. Akimitsu, N. B. Brookes, M. Isobe, M. Minola, H. Okabe, H. M. Rønnow, L. Simonelli, D. F. McMorrow and G. Monaco, Physical Review B **89**, 121101 (2014).

[344] N. A. Bogdanov, V. M. Katukuri, J. Romhányi, V. Yushankhai, V. Kataev, B. Büchner, J. van den Brink and L. Hozoi, Nature Communications **6**, 7306 (2015).

[345] J. Suntivich, W. T. Hong, Y.-L. Lee, J. M. Rondinelli, W. Yang, J. B. Goodenough, B. Dabrowski, J. W. Freeland and Y. Shao-Horn, The Journal of Physical Chemistry C **118**, 1856 (2014).

[346] S. Seong, D. H. Kim, E. Lee, A. Biswas, Y. H. Jeong, B. I. Min, B. Kim, Y. Kim, J. Baik and J.-S. Kang, Journal of Applied Physics **124**, 205102 (2018).

[347] C. T. Chen, F. Sette, Y. Ma, M. S. Hybertsen, E. B. Stechel, W. M. C. Foulkes, M. Schulter, S.-W. Cheong, A. S. Cooper, L. W. Rupp, B. Batlogg, Y. L. Soo, Z. H. Ming, A. Krol and Y. H. Kao, Physical Review Letters **66**, 104 (1991).

[348] M. Schmidt, T. R. Cummins, M. Bürk, D. H. Lu, N. Nücker, S. Schuppler and F. Lichtenberg, Physical Review B **53**, R14761 (1996).

[349] T. Mizokawa, L. H. Tjeng, G. A. Sawatzky, G. Ghiringhelli, O. Tjernberg, N. B. Brookes, H. Fukazawa, S. Nakatsuji and Y. Maeno, Physical Review Letters **87**, 077202 (2001).

[350] H.-J. Noh, S.-J. Oh, B.-G. Park, J.-H. Park, J.-Y. Kim, H.-D. Kim, T. Mizokawa, L. H. Tjeng, H.-J. Lin, C. T. Chen, S. Schuppler, S. Nakatsuji, H. Fukazawa and Y. Maeno, Physical Review B **72**, 052411 (2005).

[351] D. J. Singh, Physical Review B **52**, 1358 (1995).

[352] S. Lizzit, A. Baraldi, A. Groso, K. Reuter, M. V. Ganduglia-Pirovano, C. Stampfl, M. Scheffler, M. Stichler, C. Keller, W. Wurth and D. Menzel, Physical Review B **63**, 205419 (2001).

[353] L. Köhler and G. Kresse, Physical Review B **70**, 165405 (2004).

[354] E. Goering, A. Bayer, S. Gold, G. Schütz, M. Rabe, U. Rüdiger and G. Güntherodt, Europhysics Letters **58**, 906 (2002).

[355] V. Kanchana, G. Vaitheeswaran and M. Alouani, Journal of Physics: Condensed Matter **18**, 5155 (2006).

[356] T. Koide, H. Miyauchi, J. Okamoto, T. Shidara, T. Sekine, T. Saitoh, A. Fujimori, H. Fukutani, M. Takano and Y. Takeda, Physical Review Letters **87**, 246404 (2001).

[357] A. Koide and T. Yokoyama, Physical Review B **96**, 144419 (2017).

[358] N. D. Mermin and H. Wagner, Physical Review Letters **17**, 1133 (1966).

[359] J. P. Buhler and R. E. Crandall, Journal of Physics A: Mathematical and General **23**, 2523 (1990).

[360] E. Madelung, Physikalische Zeitschrift **19**, 524 (1919).

[361] C. Kittel, *Introduction to Solid State Physics*, Wiley (2004).

[362] L. Olson, *PyEwald*, https://github.com/lukeolson/pyewald (2015).

[363] W. Van Gool and A. G. Piken, Journal of Materials Science **4**, 95 (1969).

List of publications

- **P. Schütz**, M. Kamp, D. Di Sante, A. Lubk, B. Büchner, G. Sangiovanni, M. Sing and R. Claessen, Electronic structure of epitaxial perovskite films in the two-dimensional limit: Role of the surface termination, Appl. Phys. Lett. **116**, 201601 (2020).
- P. Scheiderer, M. Schmitt, J. Gabel, M. Zapf, M. Stübinger, **P. Schütz**, L. Dudy, C. Schlueter, T.-L. Lee, M. Sing, and R. Claessen, Tailoring materials for Mottronics: Excess oxygen doping of a prototypical Mott insulator, Adv. Mat. **30**, 1706708 (2018).
- D.V. Christensen,Y. Frenkel, **P. Schütz**, F. Trier, S. Wissberg, R. Claessen, B. Kalisky, A. Smith, Y.Z. Chen, and N. Pryds, Electron mobility in γ-Al_2O_3/$SrTiO_3$, Phys. Rev. Applied **9**, 054004 (2018).
- **P. Schütz**, D. Di Sante, L. Dudy, J. Gabel, M. Stübinger, M. Kamp, Y. Huang, M. Capone, M.-A. Husanu, V.N. Strocov, G. Sangiovanni, M. Sing, and R. Claessen, Dimensionality-driven metal-insulator-transition in spin-orbit coupled $SrIrO_3$, Phys. Rev. Lett. **119**, 256404 (2017).
- **P. Schütz**, D.V. Christensen, V. Borisov, F. Pfaff, P. Scheiderer, L. Dudy, M. Zapf, J. Gabel, Y.Z. Chen, N. Pryds, V. Rogalev, V. Strocov, C. Schlueter, T.-L. Lee, V. Borisov, H.O. Jeschke, R. Valentí, M. Sing, and R. Claessen, Microscopic origin of the mobility enhancement at a spinel/perovskite oxide heterointerface revealed by photoemission spectroscopy, Phys. Rev. B **96**, 161409(R) (2017).
- J. Gabel, M. Zapf, P. Scheiderer, **P. Schütz**, L. Dudy, M. Stübinger, C. Schlueter, T.-L. Lee, M. Sing, and R. Claessen, Disentangling specific and generic doping mechanisms for oxide heterostructures, Phys. Rev. B **95**, 195109 (2017).
- L. Dudy, M. Sing, P. Scheiderer, J.D. Denlinger, **P. Schütz**, J. Gabel, M. Buchwald, C. Schlueter, T.-L. Lee, and R. Claessen, In situ control of separate electronic phases on $SrTiO_3$-surfaces by oxygen dosing, Adv. Mat. **28**, 7443 (2016).
- **P. Schütz**, F. Pfaff, P. Scheiderer, Y.Z. Chen, N. Pryds, M. Gorgoi, M. Sing, and R. Claessen, Band bending and alignment at the spinel/perovskite γ-Al_2O_3/$SrTiO_3$ heterointerface, Phys. Rev. B **91**, 165118 (2015).
- **P. Schütz**, F. Pfaff, P. Scheiderer, M. Sing, and R. Claessen, Monitoring non-pseudomorphic epitaxial growth of spinel/perovskite oxide heterostructures by reflection high-energy electron diffraction, Appl. Phys. Lett. **106**, 063108 (2015).

Danksagung

An dieser Stelle möchte ich mich bei all denen bedanken, die zum Gelingen dieser Arbeit und dem erfolgreichen Abschluss meiner Promotion beigetragen haben. Mein besonderer Dank richtet sich an folgende Personen:

- Prof. Dr. Ralph Claessen, für die Betreuung dieser Arbeit und die Möglichkeit sie am Lehrstuhl für Experimentelle Physik IV anfertigen zu dürfen. Vielen Dank für das freundliche Arbeitsklima, das immer konstruktive Feedback, sowie die erfolgreiche Zusammenarbeit beim Erstellen wissenschaftlicher Publikationen und der Organisation von Lehrveranstaltungen! Besonderen Dank für die Bereitstellung der Rahmenbedingungen, die die erfolgreiche Forschung im Labor in Würzburg, aber auch an internationalen Großforschungseinrichtungen erst möglich machen. Darüberhinaus Danke für die vielen Gelegenheiten an Tagungen (Kyoto, Paris, Trieste, ...) und Schulen (Les Houches, Cargese) teilzunehmen. Ich hoffe ich bin weiterhin ein gern gesehener Gast bei Verteidigungen und Weihnachtsfeiern des Lehrstuhls!

- Prof. Dr. Michael Sing, zuerst für das Korrekturlesen dieser Arbeit und vieler weiterer Manuskripte und Strahlzeitanträge. Darüberhinaus vielen Dank für unzählige Bürogespräche und Kaffeepausen, sowie die gemeinsam verbrachte Zeit auf der Strahlzeit in Barcelona und dem Workshop in Kyoto. Die Karaoke-Feier anlässlich meines Poster-Preises wird mir noch lange in Erinnerung bleiben!

- Alle Lehrstuhlkollegen mit denen ich in den letzten Jahren während und nach der Arbeit Zeit verbringen durfte. Besonderen Dank gehen dabei an meine Bürokollegen Felix Reis und Raúl Stühler, an Philipp Scheiderer und Michael Zapf für viele Gespräche, sowie an Florian Pfaff für die Betreuung meiner Masterarbeit und das Einlernen im Labor. Darüberhinaus vielen Dank an Judith Gabel, Ozan Kirilmaz, Martin Stübinger, Matthias Schmitt und Berengar Leikert für die große Hilfe im Labor in Würzburg und die (Wo-)Manpower bei Strahlzeiten! Vielen Dank an die ehemaligen Post-Docs Lenart Dudy und Markus Scholz für zahlreiche Hilfestellungen und die großartige Musikauswahl! Vielen Dank außerdem an Julian Aulbach und Ozan Kirilmaz für die Angeldiskussionen am Lehrstuhl! Darüberhinaus vielen Dank an die EP4-Ehemaligen Götz Berner, Andreas Ruff und Alexey Shuvaev, die mir besonders in der Anfangszeit mit Rat und Tat zur Seite standen. Insbesondere auch vielen Dank an meine Masterandin Lisa Mündlein und meinen Bacheloranden Thomas Übelacker, die mir beim Etablieren des Filmwachstums geholfen haben. Vielen Dank auch an meinen Mit-Pilzenthusiasten Thomas Demarczyk für viele AFM Aufnahmen!

- Dr. Domenico Di Sante, Prof. Dr. Giorgio Sangiovanni and Dr. Massimo Capone for the strong theoretical support and many physical discussions! Without your efforts the successful interpretation of the experimental data would not have been possible!

- Dr. Martin Kamp und Dr. Axel Lubk für die Transmissionselektronenmikroskopie-Aufnahmen und die Hilfe bei deren Interpretation! Außerdem vielen Dank an Prof. Dr. Jens Pflaum für die Unterstützung bei den Pulverdiffraktometrie-Messungen. Furthermore, I would like to thank Dr. Yingkai Huang for his advice and help with the preparation of the $SrIrO_3$ targets.

- Dr. Vladimir Strocov, Dr. Marius-Adrian Husanu, Dr. Stefano Agrestini, Dr. Javier Herrero-Martín and Dr. Eric Pellegrin for the great support during the ARPES and XAS beam times at the Swiss Light Source and the ALBA synchrotron!

- Monika Seifer für ihre herzliche Art und die enorme Hilfsbereitschaft bei eigentlich allen nicht-physikalischen Problemen die während meiner Promotion aufgetreten sind! Vielen Dank auch für die Hilfe bei der Organisation der Fall School und Konferenz in Würzburg.

- Meinen Kommilitonen und guten Freunden Simon, Felix, Manu, Stöpsel, Martin, Julian und Hermann und allen anderen Würzburgern, die mir unvergessliche Jahre in Würzburg geschenkt haben. Ich werde es vermissen und hoffe, dass wir noch viele schöne Stunden zusammen verbringen werden!

- Meinen Eltern und meiner restlichen Familie, die mich immer bedingungslos unterstützt haben. Danke, dass ich darauf vertrauen kann, dass ihr immer für mich da seid!

- Zu guter Letzt meiner Frau Jacqueline, die mit mir durch alle Höhen und Tiefen geht. Vielen Dank für alles, ich liebe dich!